POLITECNICO DI MILANO

Facoltà di Ingegneria Industriale

Corso di Laurea in Ingegneria Spaziale

Design of a Planar Autonoumos Spacecraft Docking Simulator Using Vision Navigation

Relatore: Prof. Michèle Lavagna

Correlatore: Ing. Giuseppe di Mauro

Tesi di laurea di:

Nicola CORTIGIANI Matr. 721244

Anno Accademico 2009-2010

Sommario

1. **Introduzione: definizione del problema**
   Il progetto Smart Flyer prevede l'analisi e lo sviluppo delle risorse necessarie a realizzare manovre di precisione, che possono essere rendezvous, ispezione, operazioni di prossimità, volo in formazione e docking in maniera autonoma. Da questo punto di vista ci sarebbe un'elevata riduzione dei rischi legati a quelle fasi che coinvolgono esseri umani nel processo, ed un elevato risparmio di capitali stanziati fin ora per l'addestramento del personale altamente specializzato.

2. **Motivazioni ed obiettivi del lavoro**
   Lo scopo di questo lavoro è quello di analizzare le criticità e le tecnologie necessarie per manovre di prossimità e volo in formazione di microsatelliti, con l'obiettivo di dimostrare la possibilità di effettuare una manovra di rendezvous e docking, tra lo Smart Flyer ed un satellite target non collaborante. Questa tesi in particolare si occupa della progettazione di un flyer analogo allo Smart flyer, dello sviluppo di un simulatore con cui testare le diverse tecniche di controllo e dello sviluppo ed implementazione dei software di visione artificiale usati nella manovra di final docking.

3. **Tecniche e metodi sviluppati ed impiegati**
   E' stato realizzato un simulatore in ambiente Simulink capace di riprodurre la dinamica dei satelliti chaser e target su un piano a basso attrito presente nel laboratorio del Dipartimento di Ingegneria Aerospaziale presso il Politecnico di Milano. Grazie a tale software è stato quindi possibile testare la fattibilità di manovre di prossimità e final docking mediante tre differenti controllori: PD, LQR ed uno con legge di controllo non lineare.

4. **Stato dell'arte relativo alle tecniche di controllo**
   Allo stato attuale le tecniche di controllo di sistemi lineari come quello considerato in questo elaborato, sono molto ben sviluppate, compresa la parte di osservazione dello stato grazie al filtro di Kalman o ai filtri ricorsivi ai minimi quadrati utilizzati.

5. **Contributi innovativi**
   Le innovazioni apportate al progetto Smart Flyer riguardano sicuramente:

   - il sistema di posizionamento inerziale, che prevede l'utilizzo di una telecamera fissa, avente direzione di vista normale al piano del tavolo e collegata ad un desktop PC che fornisce la posizione e l'assetto assoluto ai due flyers;
   - il sistema propulsivo con l'utilizzo di sole quattro ventole per la movimentazione in modo da risparmiare potenza, peso e semplicità nel sistema di attuazione
   - la scelta di una legge di controllo non lineare, come candidata per il confronto con i classici PD ed LQR;

- l'implementazione in tutti e tre i sistemi di controllo di una tecnica di compensazione dei disturbi legati alla deformazione del tavolo per effetto del peso proprio;
- l'ideazione di un algoritmo approssimato per la determinazione dell'assetto e della distanza relativa tra i due flyers a partire dal riconoscimento di un immagine piana sul target.

6. **Analisi dei risultati ottenuti**
   Dal punto di vista numerico l'ADS (Autonomous Docking Simulator) sviluppato dimostra che settando opportunamente le matrici dei pesi ed i guadagni la manovra di docking viene correttamente svolta con tutti e tre i sistemi di controllo implementati, con diverse caratteristiche di velocità e di efficienza. Mentre dal punto di vista sperimentale solo i programmi di visione artificiale sono stati testati e hanno mostrato risultati in accordo con le aspettative. Il sistema di controllo in anello chiuso infatti non è stato ancora soggetto ad alcuna verifica sperimentale a causa di problemi legati alla scheda di acquisizione.

Abstract

Nowadays autonomous proximity and docking maneuvering in space represents one of the key techniques to make several space missions feasible: in orbit re-fueling, debris mitigation, large orbiting structures building, planetary specimen collection an return to Earth, humans space transportation, in space system reconfigurations, formation flying control are just some of the applicative examples which would benefit of any enhancement in the underlined technological field.
Apart from the International Space Station related experience, which still sees the human operator in the control loop, actual autonomous docking maneuvering applications in space lack, although the correspondent scientific research and on ground testing is quite active in many of the involved technical areas. Among the fundamental aspects such a maneuvering has to deal with, precise state reconstruction and fine control are two challenging topics, strongly dependent on the selected docking mechanism.
At Politecnico di Milano, Dipartimento di Ingegneria Aerospaziale a dedicated facility to test proximity and docking control algorithms is being implemented.
The thesis highlights both the testbed design and realization and the closed loop control implemented to simulate autonomous proximity maneuvering. The project includes two vehicles floating on air pads on a frictionless glass surface. Each vehicle is equipped with a camera and four fans, as actuators. The vehicle brain is represented by a PC104+ unit. An inertial camera fixed on the frictionless table is cabled to a desktop PC which provide to supply via wireless to the flyers, their attitude and position in the inertial frame. The target vehicle is provided with a set of LEDs and features to further guide the chaser to the correct docking.
The vehicles are completely autonomous: a compressed air tank each to feed the pads, Ion-Lithium batteries for power supply and a wireless board for TMTC. The overall mass is about 15 kg while a 30 Wh energy supply allows an experimental campaign of 20 min. A quite simple docking mechanism has been implemented made of a passive male-plate on the target, and an active female-clamp actuated by a linear motor on the chaser. A discrete Kalman filter has been implemented in the observer module, part of software control chain, in order to propagate and filter the desktop PC output. The final approaching phases are supported by the vision sensor too and relative position and attitude are gained by means of triangulation.
A PD, LQR and Non-Linear controllers have been separately implemented to perform a critical trade-off before selection according to speed and fluctuations criteria, during the final docking phase. Both software simulations and preliminary experimental results are presented and discussed in the work.

Acknowledgments

The author would like to thank the following people for their invaluable assistance in the completion of this thesis:

Professor Michèle Lavagna for her guidance.

Engineer Giuseppe di Mauro, for his friendship and partnership in this project.

And last, but not least...

My fiancé, Betty, for listening to every story I have ever told her about those crazy, autonomously docking, battle robots, and for her love and support as we made it through our university programs together.

Contents

List of Figures

List of Tables

Acronyms

DOF: Degree of Freedom The independent displacements and/or rotations that specify the orientation of the system.

CS: Coordinate System The system which uses a set of numbers, or coordinates, to uniquely determine the position of a point or other geometric element.

SF: Smart Flyer The chaser flyer.

TF: Target Flyer The target flyer.

INS: Inertial Navigation System The set of inertial sensors and computer that calculates position and attitude.

IMU: Inertial Measurement Unit The set of inertial sensors.

PIC: Programmable Intelligent Computer The microcontroller used in the old version of Smart FLyer to control the actuators.

PSD: Power Spectral Density The power spectral density of a signal that represent statistically its variations.

RMS: Root Mean Square Also known as the quadratic mean, is a statistical measure of the magnitude of a varying quantity.

ADS: Autonomous Docking Simulator Is the Simulink simulator developed.

PD: Proportional and derivative The controller that give control action proportional to error and to its derivative.

LQR: Linear quadratic regulator The controller that provides the best solution in terms of maximizing the performances introduced in the quadratic functional.

NL: Non linear The controller that uses a non-linear control law, generating control forces with a gain matrix that depends by the state error.

PWM: Pulse width modulation. The technique used to control a power device through a series of pulses at constant frequency but with variable duty cycle.

TOF: Time of flight The duration in which a satellite is traveling along its transfer orbit.

Chapter 1

Introduction

One of the most difficult issues in the development of an automated rendezvous system is the problem of gaining sufficient confidence prior to flight that the system will perform in orbit as required by the mission objectives and as intended in the design. In order to arrive at an acceptable level of confidence that the final product will fulfil its tasks, an high number of analysis must be done.
Demonstration in orbit will provide in the first isnstance experience concerning the behaviour of an item under orbit dynamic and zero-g conditions. Further, depending on the demonstration item and the objectives, it may also provide experience concerning other environmental conditions, e.g. survival under launch load conditions, performance under real measurement environment conditions, motion in 6 degree of freedom etc. A particular problem of using the results of a demonstration in orbit with two spacecraft for verification and validation purposes, is the fact that this would require an indipendent measurement capability which is better than the performance of the item or process that is to be verified. For instance, the performance of a GNC system is mainly determined by the accuracy of its sensors, which have been selected because they are the best available for the purpose. For this reason it will generally not be possible to verify the performance of a GNC system and of its sensors in orbit by comparing it with independent measurament of higher accuracy. Therefore many verification facility and experimental simulator has been developed. Such facilities are required for the verification of the GNC control software implemented in the onboard computer and for verification of trajectory sensor equipment together with the navigation function of the GNC system.
In addition a verification facility will have to provide a number of function for the interface with the test item, for running the simulation environment and integration of the dynamics equations, for data inputs and outputs and for pre and post processing such data.

1.1 State of the art: in orbit applilcations

The problem of rendezvous and docking in space keeps being interest for the last four decades. Spacecraft rendezvous and docking (RVD) has important applications such as

ferry of cargo to manned space stations, in-orbit servicing of low Earth orbit spacecraft, assembly in orbit of larger units, re-supply of orbital platforms and stations, repair of spacecraft in orbit, re-joining and orbiting vehicle using a lander in the case of lunar and planetary return missions and also the capture of orbital debris.
Rendezvous and docking problem requires adequate modeling, estimation and control of the relative motion between the two spacecraft, namely a chaser and a target. With the cancellation of the Titan rocket program, the United States no longer has a heavy-lift capability that would allow a single vehicle to launch from Earth and travel to Mars (and beyond). Therefore, any interplanetary spacecraft would have to be broken down into separate components, launched by separated launches, and require in-orbit assembly through autonomous docking exploitation. Furthermore, from a spacecraft servicing perspective, docking and robotic capabilities will be necessary for any in-orbit spacecraft requiring component replacement or propellant refilling. The ability to perform these missions effectively will extend these spacecraft's mission life, saving millions of dollars in launching replacing spacecraft.
Adding autonomy to docking and servicing further enhances the usefulness of this technology. Human-in-the-loop systems mean costs for training and execution time to perform tasks, not taking into account that, whenever EVA are involved, safety exposing man to the dangerous environments of outer space. The Russian Soyuz capsule had and has the ability to autonomously dock with the Mir Space Station and International Space Stations [54]. The U.S. Air Force, NASA, and Defense Advanced Research Projects Agency (DARPA) have all been investigating technologies which support autonomous docking missions through the use of experimental small satellites [55]. The Air Force Research Laboratory (AFRL) launched the XSS-11 in 2005 to experiment with proximity operations of a small satellite to an upper stage of a Minatour I launch vehicle [56]. NASA launched their Demonstration of Autonomous Rendezvous Technology (DART) in 2005 and had mixed results [57]. DARPA conducted the Orbital Express mission in 2006 in order to demonstrate a satellite being autonomously docked and refueled.

1.2 State of the art: existent test facilities

The primary function of the facility is to provide the simulation run environment i.e. the real time execution of the integration of the differential equations describing the dynamic processes to be simulated. other features required for a verification facility are the introduction of failure conditions in the test run and the capability to stop and re-start the simulation. A second test item may be connected to the facility e.g. a sensor like the GPS receive, which may be physically simulated by external device. To the other many requirements are already difficult to implement in a laboratory facilities such as the six DOF motion capability, the correct mass and inertia of the spacecraft, the compensation of the gravity effect, the correct contact velocities, etc. The combination of all these requirements is pratically impossible to achieve without reduction of the degree of freedom and without a problem scaling.

In order to further the technologies that will enable autonomous spacecraft docking to take place, several laboratories in the world have developed on the ground experimental test-beds. It's out of the purpose of this work doing a review of the verfication facilities so only the reference work has been briefly described.
Stanford University's Aerospace Robotics Laboratory has a state of the art research program in free-flying space robotics. ARL has experimentally developed enabling technologies such as object acquisition and manipulation, adaptive identification of unknown payloads, and docking of massive objects by one or more free-flying robots (see figure 1.1) in a free-floating, zero-drag environment. The robots realized in 1993 serve as a testbed for spacecraft formation flight sensing, planning and control research. The

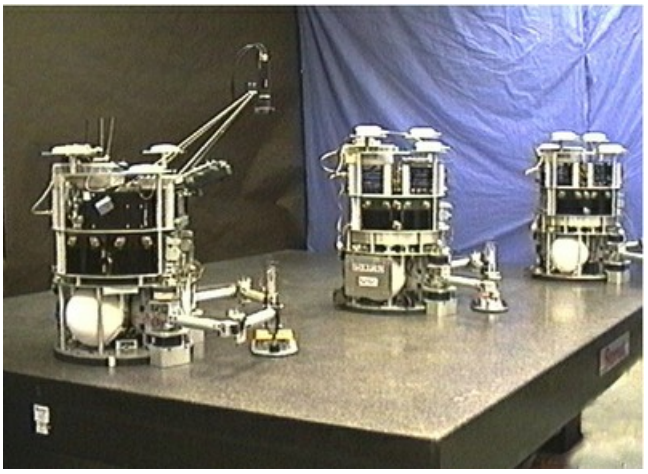

Figure 1.1: Stanford University's Free-Flying Space Robot

ARL's space robotics facility involve three autonomous self-contained free-flying space robots. A space environment is simulated in two dimensions using an air bearing over a 2x2 [m], frictionless granite table. The robots are equipped with cold-gas thrusters with which they may move about in their zero-drag environment. Other characteristics include two direct-current motor-driven manipulators with pneumatic grippers, on-board vision CCD camera, wireless ethernet communications, on-board computing, power and gas reserves, and momentum wheels on two of the three robots. Robot position and attitude are tracked either by an overhead vision system or by the indoor pseudolite-based GPS system that allow inertial navigation skills. No infos has been founded about the control methods but it uses an high bandwidth: about 100[Hz]. Research at ARL has focused both on developing the capabilities of individual robots to perform complex, extended tasks, and on multiple robot systems to perform tasks that are impossible, for a single robot to perform alone [53].
The Astronaut Reference Flying Robot (ARFR), built by Japan's MITI Electrotechincal Laboratory (see figure 1.2) in 1992, is a laboratory version of flying telerobotics system [6]. The research could potentially replace the work of an astronaut who performs extravehicular activities. Moreover, as astronauts sometimes attach a grappling device to the MMU, the robot has an anchor device. The AFRF also operates on 16 square meters frictionless floor, floating on a cushion of air by means of air bearings.

Two flexible manipulators provided of proximity sensors at each end effector constitute the catching mechanism. The proximity sensors used are two tiny CCD camera. Attitude and vehicle motion control is obtained thanks of gas jet thrusters feeded by the 2 on board gas tanks. AFRF uses accelerometers and a rate gyros for inertial sensors, and uses the video-tracker for position calibration tentatively. The robot is a completely stand-alone system with an energy source, intelligent control system, and communication system on board. Its dimension are about 70x70x70 [cm] with a total mass about 150 [kg] and an energy source of 180 [Wh].

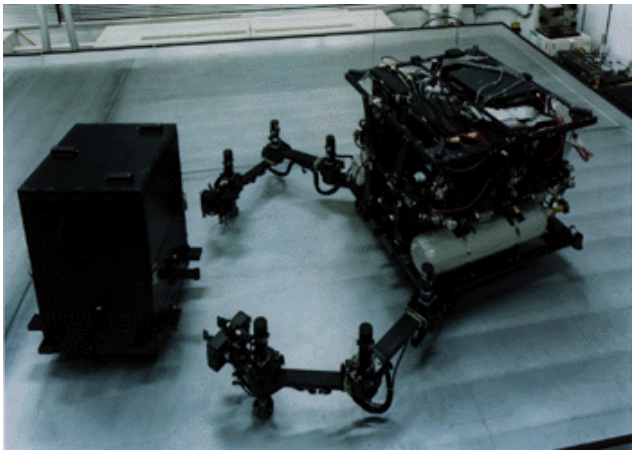

Figure 1.2: Astronaut Reference Flying Robot

The damping coefficients of PID control used, are changed adaptively in accordance with the maneuvers. In fact, overdamping is promised near the target to avoid collisions. The proximity maneuvering system alternately executes two controls, the rotation control and translation control, every 40ms. Consequently, the control cycle of the proximity maneuvering system becomes 80ms.

NASA Marshall Space Flight Center (MSFC) Flight Robotics Laboratory testbed has a large, 353 square meters surface. A 1361 kg airsled that fluctuate on the floor (see figure 1.3) has been realized in 2006 in order to develope a relative navigation sensor database, tests and model indeed it is still operative [57]. The robot floats on three large air-bearings; about 20 times larger than the previous examples. Propulsion and attitude control is accomplished through the use of 16 thrusters feeded by onboard tank. The ACVS (AutoTRAC Computer Vision System), which is the key aspect of the facility, is a camera-based system that employs the use of light emitting diodes (LEDs) and specific targets composed of either mirrors or reflective surfaces to determine a relative state (range, azimuth, elevation, and roll, pitch, and yaw).

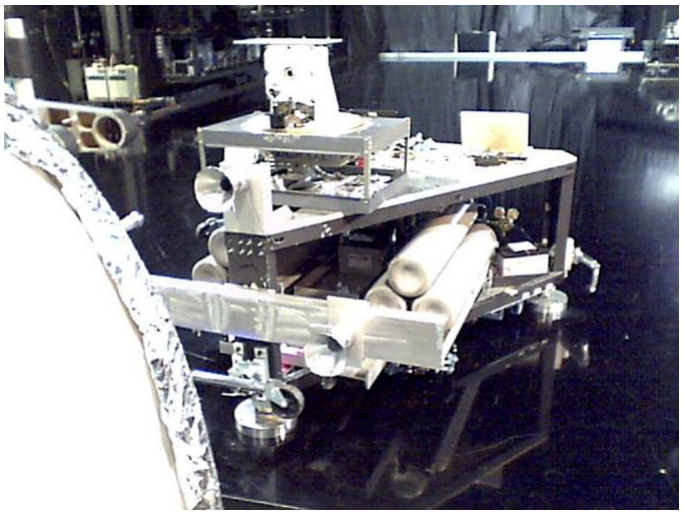

Figure 1.3: MSFC Flight Robotics Laboratory Airsled

Self-Training Autonomous Neural Network Objects(STANNOs) and *Creativity Machines* have already been developed to a high level of capability through many years of experimentation. One major strength of STANNOs is ability to build, in software form, extremely large, multilayer ANNs (artificial neural networks) capable of processing millions of bytes streaming from relatively highresolution video sources (640 x 480). A modestly appointed computer is thereby capable of completing both forward and back-propagation steps on millisecond time scales. The ability to train and execute multi-billion-weight ANNs on digital computers has enabled nearly instantaneous translation of input camera frames from a robot to navigational fields for the robot to follow toward pre-designated targets.
The Naval Postgraduate School's Planar Autonomous Docking and Servicing Simulator II (AUDASS II) chaser vehicle was constructed in 2005 and replaced the legacy AUDASS as the SRL's primary vehicle for performing autonomous docking research [17]. The older vehicle was converted into the target vehicle in the docking simulation[18],[19]. The AUDASS II has a single mechanism integrated into its structure that is capable of performing docking maneuvers and fluid transfer. It uses computer vision to obtain relative position. At NPS is used an epoxy frictionless floor about 21 square meters. Each of two 40x40x85 [cm] flyers realized has a mass of 63 kg and an energy reservoir about 336 Wh. It has eight fas jet thrusters for propulsion, four air bearings to float on an epoxy surface, a reaction wheel for attitude control. Two different computer are used onboard: one is used to determine attitude, relative position to the target vehicle, and laboratory position for the chaser vehicle. The other computer receives sensor inputs, executes a control algorithm based on PID algorithm, and transmits commands to the vehicle's actuators. The IMU senses both angular rates and accelerations, and provides a signal to the control computer.

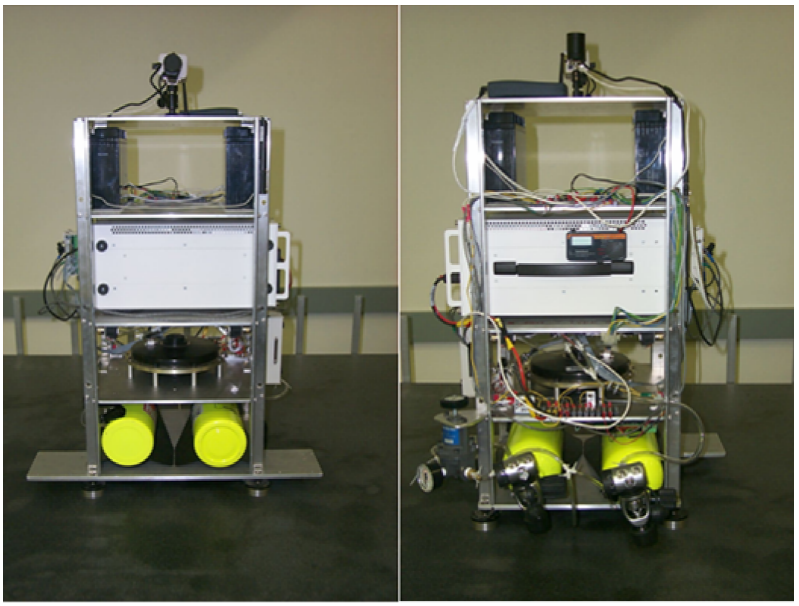

Figure 1.4: NPS Planar Autonomous Docking Simulator

In Europe there is also a laboratory facility for simulation of planar formation flying dynamics is being developed at Zentrum fur Angewandte Raumfahrttechnologie und Mikrogravitation (ZARM) in Bremen in 2008, which is intended to be used to test algorithms to control the orientation and position of satellites using pulse motors and to develop algorithms for determining the orientation of the satellite imagery of the star chamber [52]. The low power robot (figure 1.5) has only a 11 Wh energy reservoir and the diameter of its layout not exceed 30 cm, while the height does not exceed half of its diameter. For plane motions 6 air compressed thruster are controlled by valves. The compressed air is spent not only for the actuators but also for the airbearings. The angular velocity sensor and accelerometer in real time provides an estimate of the full state vector. Adjustment of assessment of the state vector model using a web-camera and the sky simulator (the ceiling with luminous LEDs). Using a map of the LEDs on the ceiling, according to pictures from a web camera mounted on the top cover layout, we can calculate the position and orientation of the layout, and thus adjust the score vector state model obtained from the angular velocity sensors and accelerometers. However, adjustments can be made only with some time lag due to too much time required to process one image.

The control system position and orientation of the layout consists of an onboard computer and microcontroller. The actuators system functioning follow this principles: every 100 ms computer sends a value to the microcontroller regard how in the next 100 ms should work each actuator. The microcontroller in turn, gives a command to open the valves on the thruster.

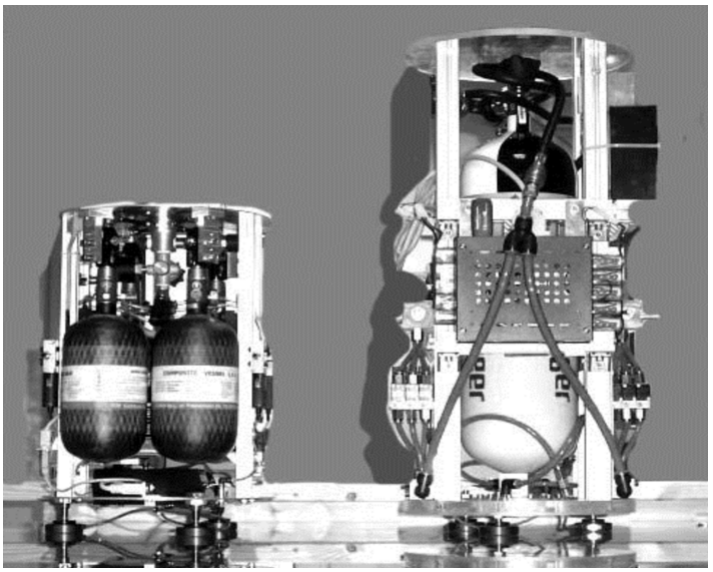

Figure 1.5: Zarm LuVex mock-up

1.3 Scope of the work

The here presented study relates to the enhancement of the already existing test bed for orbital maneuvering simulations at DIA - Politecncio di Milano. A fan propelled, axial symmetric robot, named Smart-Flyer (SF) was designed and build in previous work to test zero-gravity maneuvers, on the frictionless table available at DIA (figure 1.6). In particular the work focuses on three different but greatly interdependent aspects:

- the design and implementation of a closed loop control chain for proximity and docking maneuvering between a chaser and a non-collaborative target;
- the target hardware design and the existing chaser vehicle critical review and possible upgrading;
- the testing campaing in lab is fitted in the study of the feasibility and on the necessary technology to realize spacecraft proximity operation and formation flying.

More in details the work is focused on:

1. Checking of the Smart Flyer health status and definining possible modifications and improvements.
2. Designing, sizing and possibly integrating a second vehicle, that represents the non colaborative docking target, as far as possible similar to the existing test bed.
3. Development of a software simulator to simulate the two vehicles controlled dynamics, sensors and actuators included. The simulator is the fundamental tool to test and critically compare different control laws and philosophies and to finally select the fittest to be settled on board.

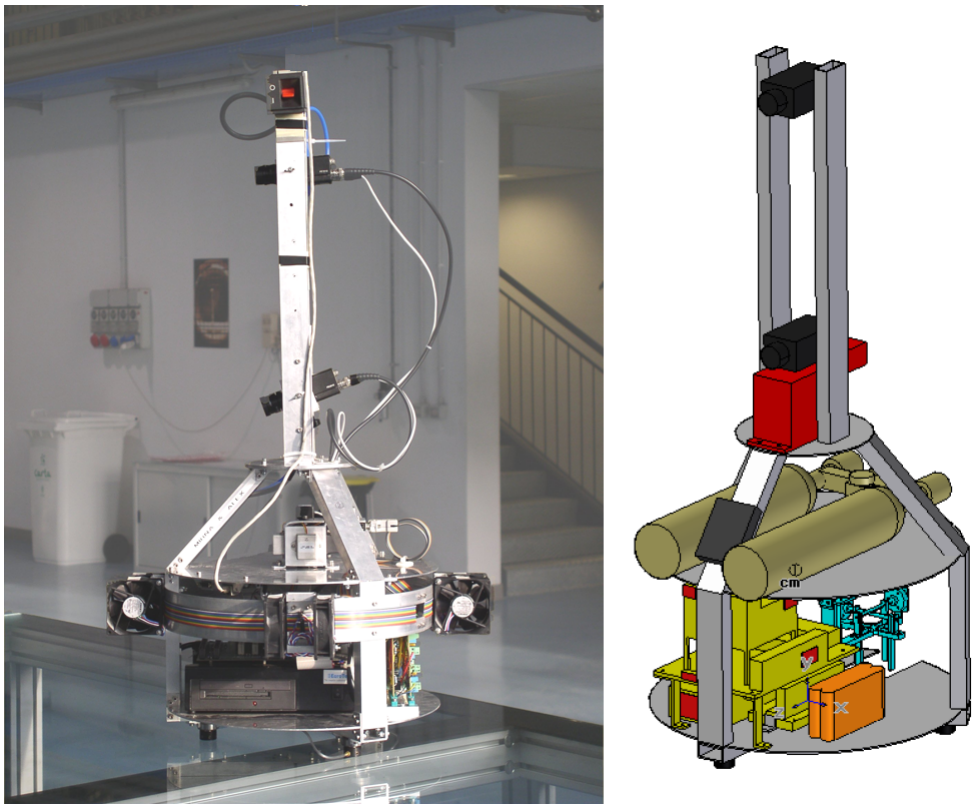

Figure 1.6: Smart Flyer initial configuration

4. Image processing architectures devoted to manage the relative and absolute chaser state vector respectively; the relative motion identification exploits the on board camera, while the absolute state vector knolwedge comes from a inertially fixed camera, linked with the destop PC;

5. Implementation of the selected control philosophy on chaser's PC104+ onboard computer and an experimental testing campaign management.

Chapter 2

The test bed

In the following chapter will be discussed the current status of the laboratory facility, that include only the chaser flyer and frictionless table.

2.1 Low friction support

In the documentation produced before [7] a low friction surface has been designed in order to allow microgravity simulation.

2.1.1 Concavity problem

The frictionless table is needed to simulate a microgravity environment the proximity and docking maneuver occur in. To assure frictionless condition a smooth glass plane has been selected and the vehicles must be equipped with air bearings to create a sustaining air film between the robot and the table itself.
The glass surface has been preferred to be free to select the operating surface dimensions. Besides it's possible to obtain with the glass a very high durable superficial finishing compared with other materials [7].
Despite the Young's module of the glass is high, about 70 [GPa] and the sheet is reinforced with a polymeric layer distributed along the mean plane, its weight may cause planarity loosing; therefore an apposite metal structure that divide the glass sheet in 4 quadrants. Figure 2.1 shows the overall glass table structure.

Dimension	3 [m] x 3 [m] x 10.5 [mm]
Weight	225 [kg]

Table 2.1: Frictionless table properties

Unfortunately it has been experienced that, even with such a support, each quadrant still inflects. It should be underlined that inflection is not annoying per se but according to th moving vehcile control synthesis. In [2] a maximum displacement at the center of each quadrant equal to 1 [mm] it's reported that affects the vehicles' acceleration component normal to the local horizontal plane.

Figure 2.1: Low friction table

2.2 Resolutive actions

The problem presented above can be solved in two ways:

- by setting a well suited control law that tunes the actuators according to the vehicle position with the respect to the table inflected shape;
- by adding 4 further supports in order to reduce the glass displacement.

The first action is here suggested as the better, but the second alternative is sized anyway in the followings. The structural analysis highlighted that a 0.2 mm of inflection at each quadrant centre, caused by the weight, is experienced (figure 2.2). With an inverse approach it's been computed the elasticity modulus necessary to have a 1 [mm] maximum displacement, and it's been found a value equal to 7 [GPa] that appear really far from glass typical value that are about 70 [GPa].

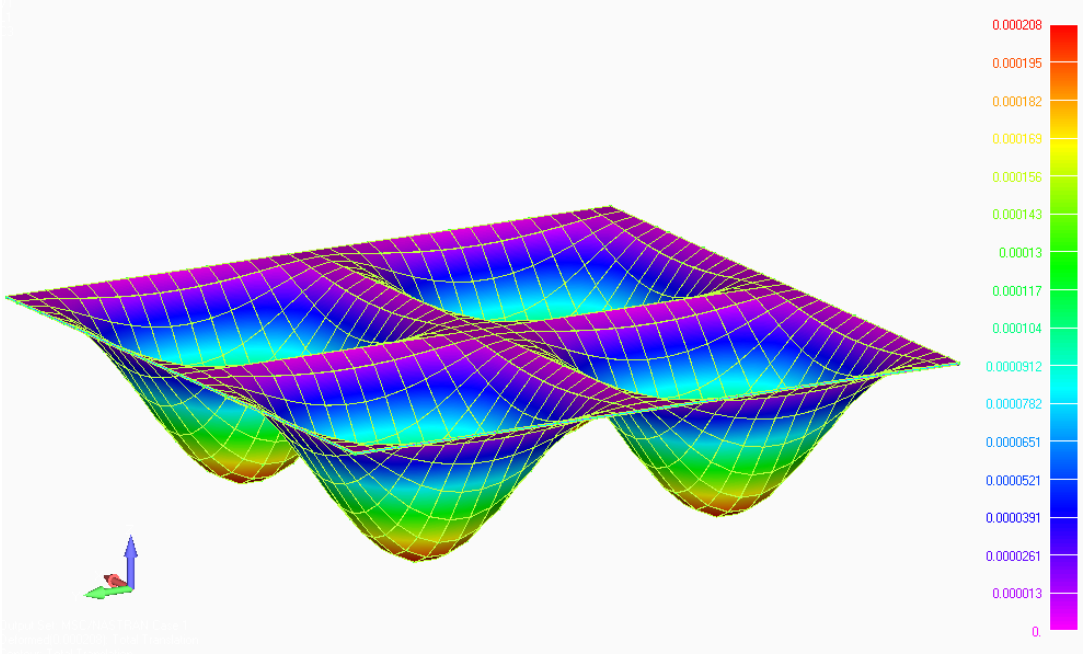

Figure 2.2: Table deformation: MSC Nastran analysis; results expressed in meters

Metal supports can be still adopted (figure 2.3) placed under the center of each quadrant, in order to constrain the central zone to remain on the same plane of the table borders. Each support should be provided with a thick plate that distribute the constrain around the geometric center of the quadrant, and a lining to not ruin the superficial finishing of the crystal. The maximum displacement can be reduced of an order of magnitude, as shown in figure 2.4.

Figure 2.3: Adjustable support

In this work the solution adopted to face the inflection problem is the suited controller described in section 5.13 and 5.12.

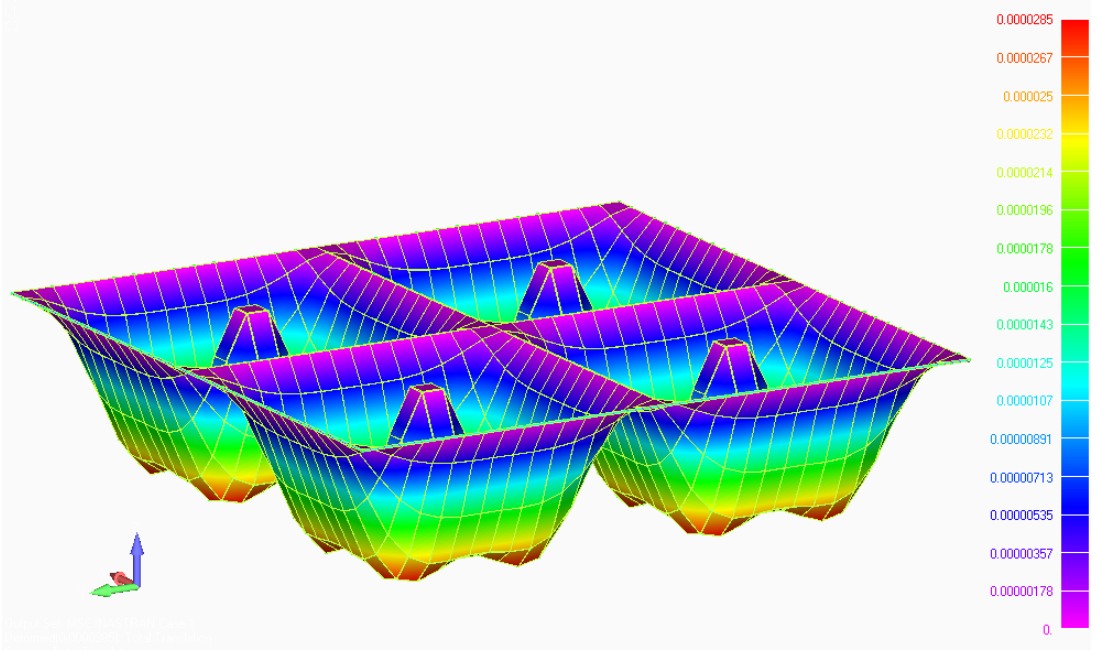

Figure 2.4: Reinforced table deformation: MSC Nastran analysis; results expressed in meters

2.3 The existing vehicle: state of the art

The prototype, assembled some years ago at DIA - Politecnico di Milano laboratory, is a 3 degrees of freedom robot which moves on the glass table, as already mentioned, thanks to three airpads.
In the following paragraphs will be described in detail the Smart Flyer subsystems, which are already designed in previous works [7].

2.3.1 Floating system

Three NelsonAir (FPC-10) airbearings, feeded with 4 [atm] compressed air assure the microgravity conditions to the vehicle. They are binded to ball bearings with orientable axis produced by SKF (model 1201ETN9) to guarantee the perfect alignment with the table plane; figure 2.5 offers a floating system detail.

For an autonomous flotation system SF use two Scubatec compressed air tank, linked with tap that synchronize the output air. The system performance is reported in table 2.1(a).

Figure 2.5: Nelson air airbearing binded to SKF ball bearing

(a) Flotation system property

Tank pressure	200 $[bar]$
Tank capacity	0.85 $[l]$
Dimension	440[mm]x90[mm]
Mass	4.5 [kg]
Airpad pressure	4 $[atm]$
Discharge time	19 $[min]$
Efficiency	0.43

(b) Scubatec tanks

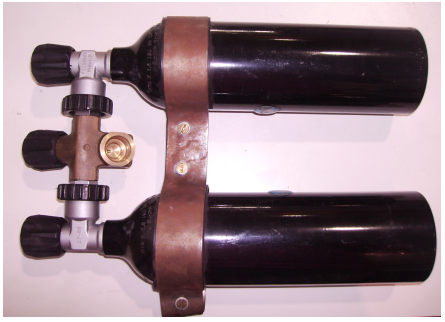

Table 2.2: Flotation system

2.3.2 On board sensors

The SF is equipped with an inertial platform made of 3 piezoelectric gyroscopes ENV-05D-52, produced by Murata and 3 accelerometers ADXL105EM produced by Analog Devices (figure 2.6). The features of the available sensors are reported in tables 2.3 and 2.4.

(a) ADXL05EM-1 characteristics

Analog Devices ADXL05	
Bandwidth	100 $[Hz]$
Nonlinearity	$\pm 0.2[\%FS]$
Random walk	$5[mg\ rms]$
Cross Sensitivity	$\pm 3.5[\%FS]$
Accuracy	0.02 $[m/s^2]$
Power	0.075 $[W]$

(b) ADXL05EM-1 Accelerometer

Table 2.3: Analog Devices ADXL05EM-1 accelerometer

(a) Gyrostar ENV-05D-52 characteristics

Gyrostar ENV-05D-52	
Bandwidth	7 $[Hz]$
Nonlinearity	$\pm 0.5[\%FS]$
Random walk	$0.9[^\circ/s\ rms]$
Accuracy	1 $[^\circ/s]$
Power	0.04 $[W]$

(b) ENV-05D-52 gyroscope

Table 2.4: ENV-05D-52 Gyroscope

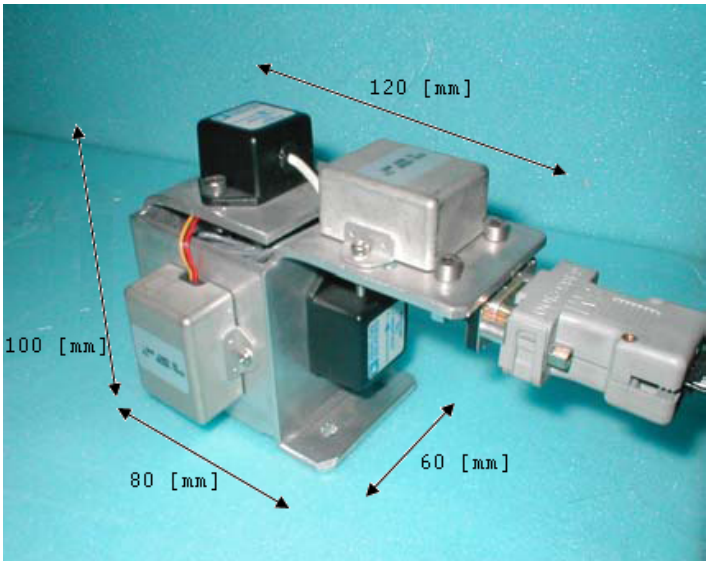

Figure 2.6: Smart Flyer strapdown platform

2.3.3 Artificial vision system

The prototype use only one CCD Pulnix PE2010 camera (figure 2.7) for monocular vision. The image is acquired with the Sensoray 311 PC104+ frame grabber to convert the analogic camera signal into digital, necessary for further computer elaboration.

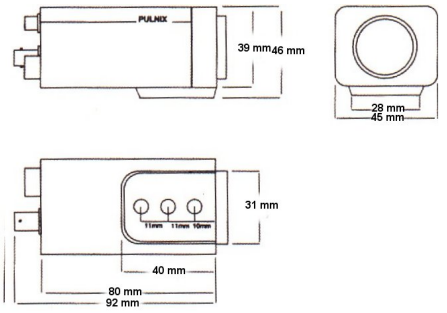

2.7.1: Pulnix PE2010 envelope

2.7.2: Pulnix PE2010

Figure 2.7: Smart Flyer cameras

(a) Pulnix PE2010 camera

Pulnix PE2010	
CCD	1/3”
Pixel	752x582
Cell dimension	6.5x6.25[μm^2]
Power	2.4 [W]
Mass	228 [g]

(b) Rapitron D0214M lens

Rapitron D0214M	
Focal length	2.8 [mm]
View angle	95.6° x 72.6°
Dimensions	30[mm]x36[mm]
Weight	58 g

Table 2.5: Pulnix PE 2010 and Rapitron lens features

The board (figure 2.8) use 2 converters: one for the color and the other for the brightness. Each converter samples the input signal and filters it, to reduce the aliasing problem. The board provides a 30 frame per seconds in NTSC mode and 25 frame per second in PAL (or SECAM mode).

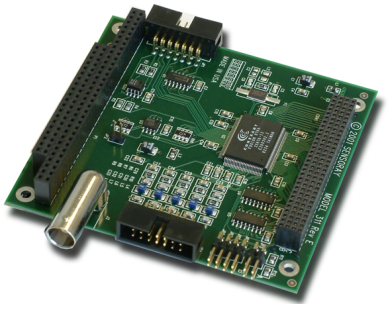

Figure 2.8: Sensoray 311 PC104+ frame grabber

2.3.4 Computer system

The extreme versatility of the Smart Flyer is given by the onboard electronic unit:

- PC/104+ computer with 1432 CPU module;
- ACS-9071-06 RJ45 Ethernet adapter;
- Scidyne GPIO-104 acquisition board;
- Sensoray 311 PC104+ frame grabber, that allows the capture of monochrome and color images from a variety of analog video sources into computer memory;
- Mc Lennan MSE422 that can control 4 electric motors;
- Hitachi DK23DA-40F 10 [Gb] hard disk.

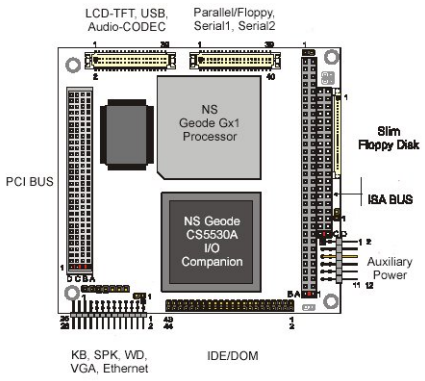

2.9.1: PC104+ Mother board

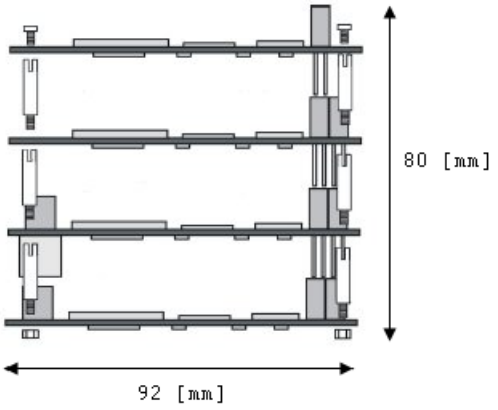

2.9.2: PC104+ assembly diagram

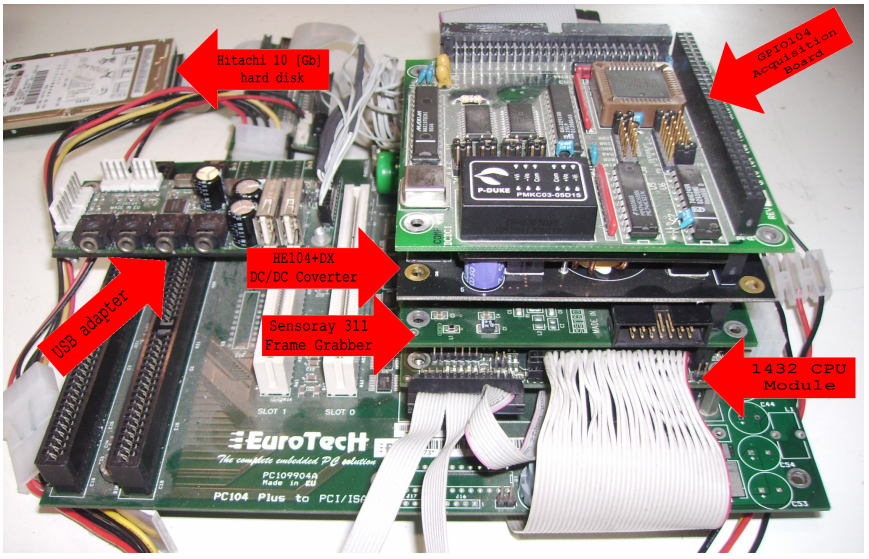

2.9.3: PC104+ assembly

Figure 2.9: Smart Flyer onboard computer

The most important features in the choice of onboard computer are the dimension, reduced mass, low power requirement (10 W) and the limited computational power. Furthermore, in [7] the author took care other aspects in the choice of the onboard computer such as possibility to connect the PC/104+ to other computers by means of a router, and to connect other peripherals like mouse, keyboard and monitor useful for the software test. The operative system installed is the Gentoo Linux version.

2.3.5 The actuators

The bidimensional motion is obtained with 8 cooling computer fans, produced by Thermaltake [61] (figure 2.10.1). Translation is obtained whenever two corresponding couples are activated (eg. 2 and 5 with 3 and 8 in figure 2.10), while whenever two alternate couples(eg. 1 and 5 with 3 and 7) are switched on rotation is achieved.

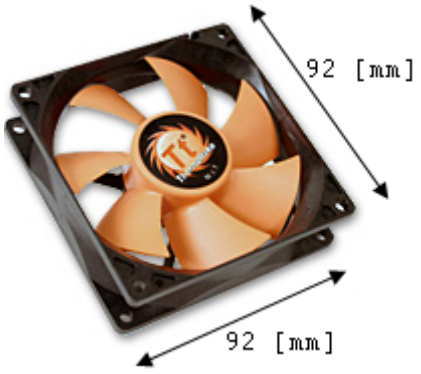

2.10.1: A2028 Thermaltake fan

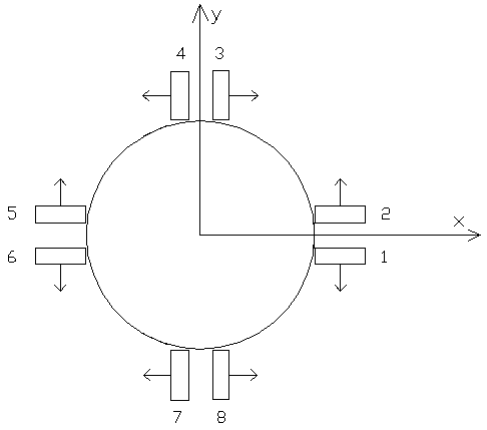

2.10.2: Fans disposition

Figure 2.10: Smart Flyer initial propulsive system

The fans can supply thrust only in the direction reported in figure 2.10. The propulsion system architecture involve also the use of an integrated boards, with a PIC,that process the 4 (-5 or +5 [V]) acquisition board output in order to decide which fans must be activated. This is necessary also because each fan need a power about 6 W that the acquisition board can't supply.

Unfortunately with the years 3 of the 8 PC fans has been lost, indeed in the section 3.3 un upgrade is necessary.

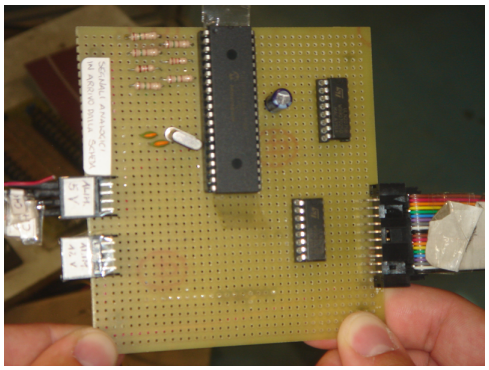

Figure 2.11: Smart Flyer actuators control boards

2.3.6 Communication system

The Smart Flyer communication system must guarantee the possibility to communicate with desktop PC its attitude and position data without cable that can obstacle the plane motion. For this reason vehicle is provided with an access point that links the onboard PC104+, via wireless with external devices. The maximum speed in transmission is 11 Mbps, that is surely lower than normal LAN connection, but it is enough for the data transmission needs; indeed the mini-router must be able to transfer attitude and position information to the desktop PC. Such data must be written in a shared folder and their size is usually less than 10 Kb, so a controller bandwidth greater than 100 [Hz] can be used. The power consumption of the Dlink access point is about 6 W while

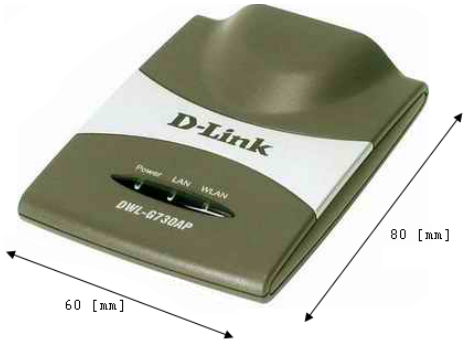

2.12.1: DWL-G730AP Dlink access point

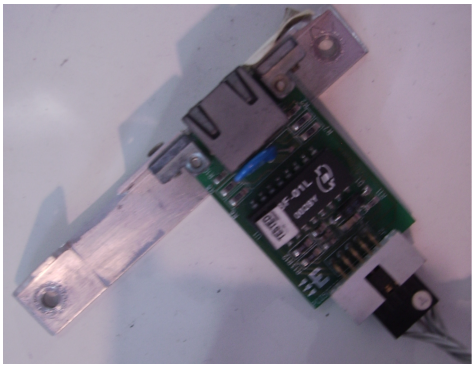

2.12.2: Ethernet adapter

Figure 2.12: Smart Flyer communication system

its mass is lower than 0.1 kg.

2.3.7 The docking mechanism

The Smart Flyer is provided with a docking system that consist of a plier that is the male of the passive target plate. The plier (figure 2.13.1) is made of an horizontal support on which a piston pushed by a linear actuator can run. The stator of the electric motor

that activates the linear actuator is fixed with the horizontal support.
Two levers are hinged with the support respectively in A and B and with the sledge in C and D: such a constraint translates the sledge linear montion into the levers rotation around the hinges.
The electric motor is controlled by the MSE422 McLennan board mentioned in the 2.3.4. As far as the levers stay opened, the robot maneuver to get the correct position and attitude with respect to the passive plate to be clamped (figure 2.13.2).

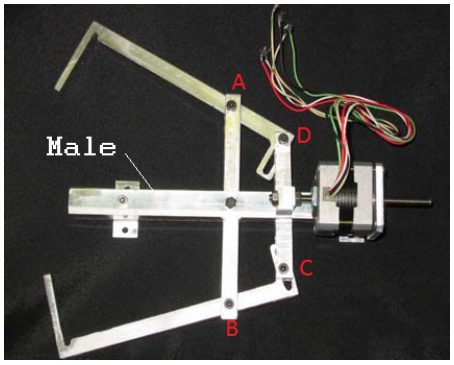

2.13.1: Active docking plier

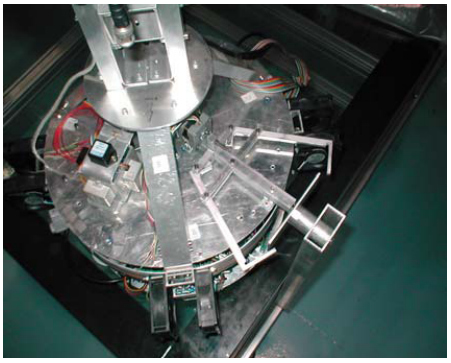

2.13.2: Docking test

Figure 2.13: Smart Flyer doking system

2.3.8 The supply system

In table 2.6 is reported the older power budget that in the following chapter will be revise.

Component	Producer	Model	Voltage [V]	Current [A]	Power [W]
PC104+	Eurotech	CPU 1432	5	1.9	9.5
Hard disk	Hitachi	DK23DA10F	5	0.9	4.5
Lan adapter	Eurotech	ACS-907106	5	0.6	3
Acquisition board	Scidyne	GPIO-104	5	0.34	1.7
Motors control board	McLennan	MSE422	12	0.6	7.2
Access point	D-link	DWLG730AP	5	1.2	6
Camera	Pulnix	PE2010	12	0.2	2.4
Accelerometers	Analog Device	ADXL05EM-1	5	0.015	0.225
Gyroscopes	Murata Electronics	ENV-05D72	5	0.008	0.12
Frame grabber	Sensoray	311	5	0.3	1.5
PIC board	Microchip	PIC18F2431	5	0.025	0.125
Fans[1]	Thermaltake	A2028	12	0.5	24
Total					60.27

Table 2.6: Old SF power budget

Then the older battery requirements are reported in table 2.7.

Required power	60.27 $[W]$
Simulation time	30 $[min]$
Dept of discharge	50 [%]

Table 2.7: Battery pack requirements

The elementary module chosen for the battery pack is the MP176065 produced by SAFT and sold by ELTEC that supplies also the battery charger. The cell main features are reported in the table 2.7(a).

(a) Battery cell MP176065 property

Battery cell MP176065	
Medium voltage	3.6 $[V]$
Voltage at end of charge	2.7 $[V]$
Nominal capacity	6.0 $[Ah]$
Medium capacity	5.6 $[Ah]$
Cell capacity	15.12 $[Wh]$
Thickness	18 $[mm]$
Width	60 $[mm]$
Height	65 $[mm]$
Weight	150 $[g]$

(b) Battery cell envelope

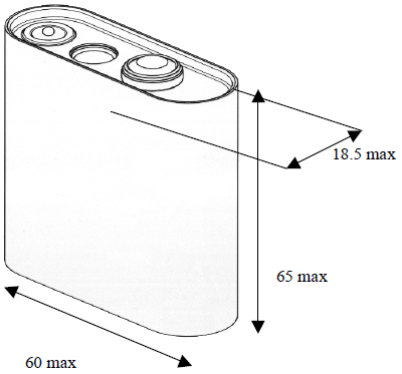

Table 2.8: Battery cell MP176065

$$n = \frac{P_{req} \cdot time}{C_r \cdot DOD} = 3.986 \approx 4 \tag{2.1}$$

A series of 4 battery cells provides 14.4 [V] nominal voltage, that allows feeding the vehcile for 30 minutes; the sizing process assumed a 50%depth of discharge to provide a battery lifetime greater than 500 cycles. This choice allow that the battery life is greater than 500 cycles.

All vehicle loads required a feeding voltage of 5 or 12 [V], therefore a DC-DC converter to stabilize the battery output voltage. The selected converter [7] chosen assures the correct feeding to the loads even when the battery is at the the minimum voltage; the converter properties are reported in table 2.9.

(a) HE104+DX DC-DC Converter property

HE104+DX DC-DC Converter	
Input voltage	6-40 $[V]$
Output voltage	3.3, $\pm$ 5, $\pm$ 12 $[V]$
Max output power	60 $[W]$
Efficiency	$>$ 95% [%]
Dimension	90x90 $[mm]$
Weight	173 $[g]$

(b) HE104+DX DC-DC

Table 2.9: Smart Flyer DC-DC Converter

Unfortunately with the years the battery pack has been lost, indeed in the section 3.5 a new power budget with the added devices must be done.

2.3.9 Structure and configuration

The Smart Flyer structure (figure 2.14) is made of the Al 6060 aluminum alloy that assures lightness and it is easy to process.

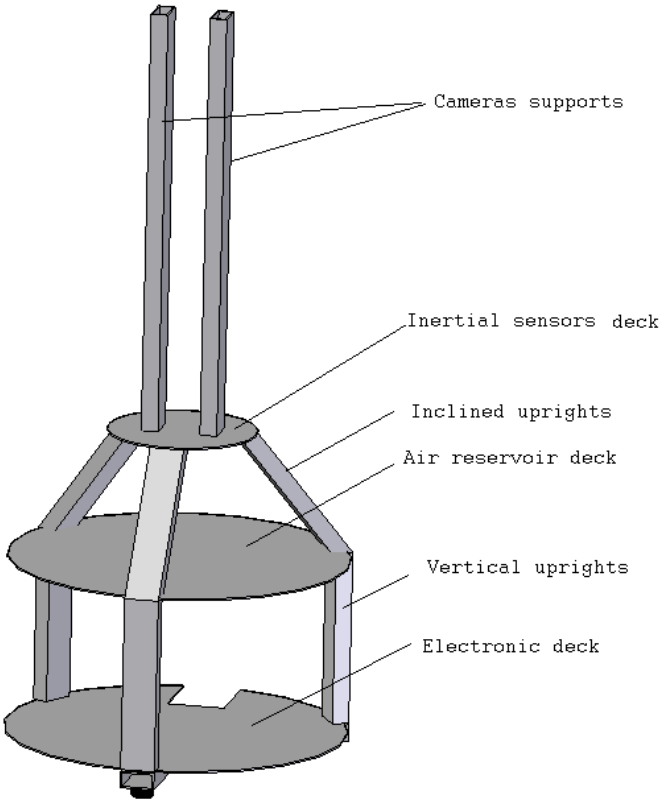

Figure 2.14: Smart Flyer structure

Two circular bases and 3 uprights represents the main structure to transfer the overall load to the airpads.

The structure is represented in figure (figure 2.15): it is possible to see that there are other 3 supports in order to bind the airbearings to the bottom of the lower deck.

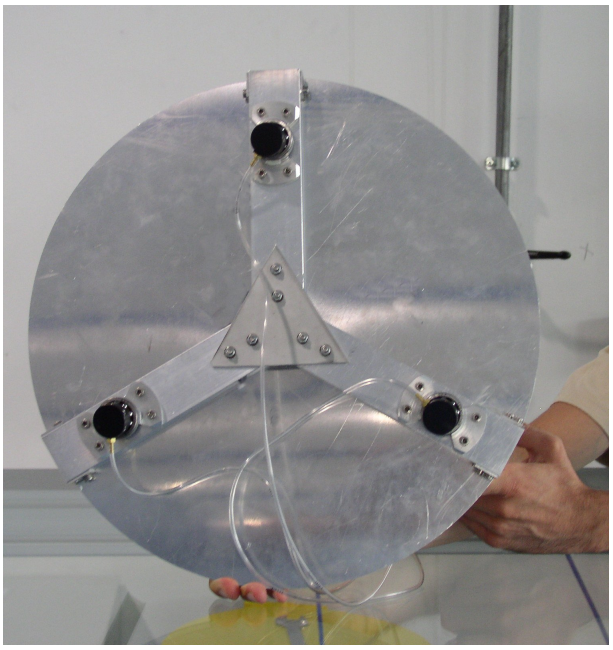

Figure 2.15: Smart Flyer lower basis

The upper and lower circular plates thickness is 2 [mm], while for the plate supporting the camera the thickness doubles, and is binded with the upper basis with other 3 diagonal uprights in order to contrast the bending moment of the 2 stirrups that support the two cameras: figure 2.14.
A double ring to support the 8 fans are loked up to the vertical support. The ring can slide along the vertical axes to get the thrust aligned with the SF's center of mass and avoid pitch moment.
The height of the camera can changed thanks to 2 other vertical uprights that allow to place the camera at a maximum height of 90 [cm].

The initial SF configuration is presented in table 2.10 without the docking plier, so one of the first upgrade is a configuration reanalysis in order to find the allocation for the docking system.

Total mass	14.86 $[kg]$
Center of mass position	
x	-10 $[mm]$
y	28.3 $[mm]$
z	206 $[mm]$
Moments of inertia	
I_x	1156953 $[mm_4]$
I_y	281274 $[mm_4]$
I_z	1099636 $[mm_4]$
I_{xy}	-5952 $[mm_4]$
I_{xz}	-4510 $[mm_4]$
I_{yz}	68162 $[mm_4]$

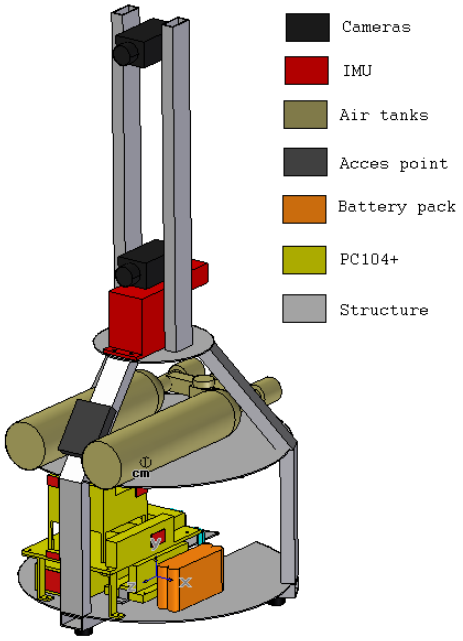

Table 2.10: Smart Flyer initial configuration without docking system

Moreover cause of the ages some devices like battery pack and fans actuators have been lost, others like the docking plier doesn't work very well. This are the main reasons of the upgrades described in the following chapter.

Chapter 3

The chaser vehicle upgrade

3.1 The navigation problem

In this section will be discuss the uselessness of the IMU available, the possibility to install a newer and more accurate inertial navigation system and the final choice about the use of a fixed camera that translate the image acquired in flyers absolute position.
The navigation is the process focused on outputting the the position and attitude of the vehicle starting from sensors' information. A IMU is typically installed to obtain those information and, as reported in 2.3.2, an IMU is installed on the SF too.
The gyroscopes provide measures of angular speed, while the accelerometers measure the acceleration, both devices measure absolute quantities but they are often expressed in a reference frame fixed with sensors. It is very common that the three measurements axes chosen for the sensors coincide with the axes of the local reference system of the robot.
The measurements provided by the gyroscopes are used to determine the attitude of the body reference system such that it is possible to express the measurements of the accelerometers in the inertial reference to be further integrated over time to get the absolute position and velocity. The inertial navigation systems (INS) requires knowledge of position and attitude at the beginning of navigation (initial conditions), which are the constants of integration: they can be accurately measured before to start the simulation.
Since an INS integrates the differential equations of motion containing inertial measurements, systematic errors cause errors in velocity and position that increase with the integration time. So the most common INS are unable to perform accurate autonomous navigation for long time and then are often associated with other instruments of a different nature: integrated navigation or assisted navigation. Currently the more used aiding system in outdoor applications is the GPS and the integrated system is indicated by INS/GPS (or IMU/GPS).
In the following paragraphs will be briefly presented the errors that afflict the inertial sensors and the requirements for the precise navigation of the flyers. Such requirements are derived by the numerical simulation described in chapter 5.

3.1.1 Strapdown platform

In strapdown configuration the sensors are tightly bounded to the vehicle to perceive the whole dynamic: the relations between the local reference system, and the inertial one must be analytically obtained. The strapdown configuration is most popular nowadays: the Smart Flyer mounts a similar platform.
Strapdown systems can be classified according to on their performance in autonomous navigation mode:

1. Strategic grade: positioning error less than $30[m/h]$, gyroscopes drift rate less than $0.0001[\,^\circ/h]$ and accelerometers bias about $1\mu g$;
2. Navigation grade: positioning error about $3-4[km/h]$, gyroscopes drift rate less than $10^{-2}[\,^\circ/h]$ and accelerometers bias between $50-100[\mu g]$;
3. Tactical grade: positioning error less than $20-40[km/h]$, gyroscopes drift rate about $1-10[\,^\circ/h]$ and accelerometers bias between $100-1000[\mu g]$.

Inertial systems with lower performance exist, called low accuracy INS, they are normally used in assisted mode only and not included in the former taxonomy.
For the current tesbed the first strapdown represents the best suited solution: more specifically, as the aim is to obtain a platform with positioning error less than $0.5[m/h]$, the lower bound of the first is suggested.

3.1.2 Errors description

The inertial sensors drawback, as mentioned, is that they are affected by various errors. In the inertial measurements there is always a bias, that is equal to the output supplied with a null input. In the case of the gyroscopes is called drift (or drift rate). The scale factor is instead the ratio between the variation of output and input signal. The scale factor is not an error, but its value is only known with some precision, so an error in its esteem entails a residual error in the output. There are also other errors, specific to the different sensors. Each error has one or more constants or recoverable components such as: changes induced by temperature changes, in run-to-run (between two series on-off) and changes in-run (between two measures within the same power). The inertial sensors performances depend substantially on the ability to compensate the systematic errors, therefore they are usually tested to evaluate the error parameters and calibrate the output in various environmental conditions. The calibration is done by comparing the output of the sensors with the input that should be known.

Nonlinearity error

The transfer function between the sensor's input and output is not perfectly linear. This nonlinearity represents the maximum deviation of output voltage from the line of perfect linear regression. It is usually expressed as a percentage of full scale, and a good instrument calibration can reduce the effect of nonlinearity.

Offset error

The sensors usually do not provide a perfectly null output when the analogue input signal is zero, but show an offset voltage that can be subtracted from measures to increase the accuracy. The problem is that this error can vary from sensor to sensor[1], and also with changes in temperature, and then offset detection must be done before any simulation.

Sensitivity drift with temperature

This drift represents the variation in the instrument sensitivity due to temperature changes during the test. Fortunately the temperature in the laboratory where it will be performed the simulations is kept constant, then the effect of this variation can be neglected.

Cross axis sensitivity

The output provided by the accelerometer (similar is the case of the gyroscope) is influenced by the acceleration (or angular velocities) along the other two axes perpendicular to the current measurement. This sensitivity is expressed as a percentage of the sensitivity along the axis of measurement. Then it is possible to multiply this percentage for lateral accelerations to know the increase in output that will be measured by the sensor. Once calibrated, it is simple to eliminate this error component by solving the following linear system:

$$\begin{aligned} a_x^{meas} &= a_x^{real} + S_y a_y^{real} + S_z a_z^{real} \\ a_y^{meas} &= a_y^{real} + S_x a_x^{real} + S_z a_z^{real} \\ a_z^{meas} &= a_z^{real} + S_x a_x^{real} + S_y a_y^{real} \end{aligned} \tag{3.1}$$

where S_x, S_y, S_z are the cross axis sensitivity of the instrument while a_{real} and a_{meas} are respectively the real and the measured acceleration components.

Ratiometric error

Usually the sensors are ratiometric that means that the output offset and sensitivity of the sensor will be linearly scaled to the power supply. This type of error can not be modeled (only statistical model is possible) because DC-DC converter has voltage fluctuations about $20[mV]$ around the provides output.

Noise Density

The density spectral power of the measured signal is measured often in $[g/\sqrt{Hz}]$ for accelerometers and $[\,^\circ/s/\sqrt{Hz}]$ for gyros. When this value is multiplied by the root of the acquisition frequency gives the root mean square (RMS) acceleration (or angular

[1] Even between two identical sensors: the same manufacturer and same model, it is possible to have different offset errors.

velocity) sensor noise. It is usually difficult to measure a signal with magnitudes lower than this value because the probability density function takes the form:

$$P(x) = \frac{2a_{RMS}}{\sqrt{2\pi}\sigma} e^{-\frac{x^2}{2\sigma^2}} \tag{3.2}$$

Table 3.1 reports the probability that the measure doubles, become four times etc., than the a_{RMS}.

$2a_{RMS}$	32%
$4a_{RMS}$	4.6%
$6a_{RMS}$	0.27%
$8a_{RMS}$	0.006%

Table 3.1: Noise density probability

Although this type of error can not be eliminated, it can be, at least reduced by filtering; it is advisable that the minimum acceleration observed is at least double than the a_{RMS} sensor. It appears clear that it is possible to reduce the noise level, lowering the acquisition frequency, even if this solution has a lower limit dictated by the Shannon theorem.

Resolution

The smallest detectable measure increase is the instrument resolution. This quantity is closely related to the noise level and therefore the acquisition frequency of the instrument: $R = N\sqrt{1.6 \cdot BW}$ where N is the PSD of noise while BW is the frequency in $[Hz]$. It is important that the resolution of A/D converter in the acquisition board is less than that one computed for the sensor, otherwise it will be overestimating the acquisition system performance [2].

Drift error

In addition to what has been said there are also numerical problems, due to the fact that the sensors measures must be integrated once or twice depending on whether the measure is either angular velocity or accelerations. This procedure, which must occur at discrete time in the computer, is a further source of error that can not be offset except through integrator reset, with a more accurate estimate resulting from outside. This error also increases over time and this is the main cause of the fact that the INS are unable to accuracy navigation for long periods.

3.1.3 Available sensors

In the followings requirements for the current application and performances of the available sensors presented in 2.3.2 are discussed. The main features of accelerometers and gyros are reported in 2.2(a) and 2.3(a) while the acquisition board characteristics are listed in table 3.2.

[2] Also the chosen acquisition frequency must be compatible with the acquisition board skill.

GPIO-104	
Channels	12 SE
A/D resolution	12 bit
Input ranges	$\pm 5, \pm 10, +5, +10[V]$
Nonlinearity	$\pm$ 1LSB
Sampling	max 100000$[samples/s]$
LSB@ $+5[V]$	$1.2207[mV]$
LSB@ $+10[V]$	$2.4414[mV]$
LSB@ $\pm 5[V]$	$2.4414[mV]$
LSB@ $\pm 10[V]$	$4.8828[mV]$

Table 3.2: SF acquisition board performances

3.1.4 Signal to be acquired

The performance required to the sensors can be easily identified by looking at the signals to be acquired, depitched, in terms of accelerations and angular velocity in figures 3.1. Such values are exctracted from the numerical simulation of the PD controller (section 5.13.1) described in chapter 5, in which the Smart Flyer starting from its parking orbit travel along a transfer orbit to the Target Flyer operative orbit, to perform the docking manoeuvre (chapter 5). The reference frame for the chaser vehicle (but is analogous the case of Target flyer) is shown in figure 5.3.

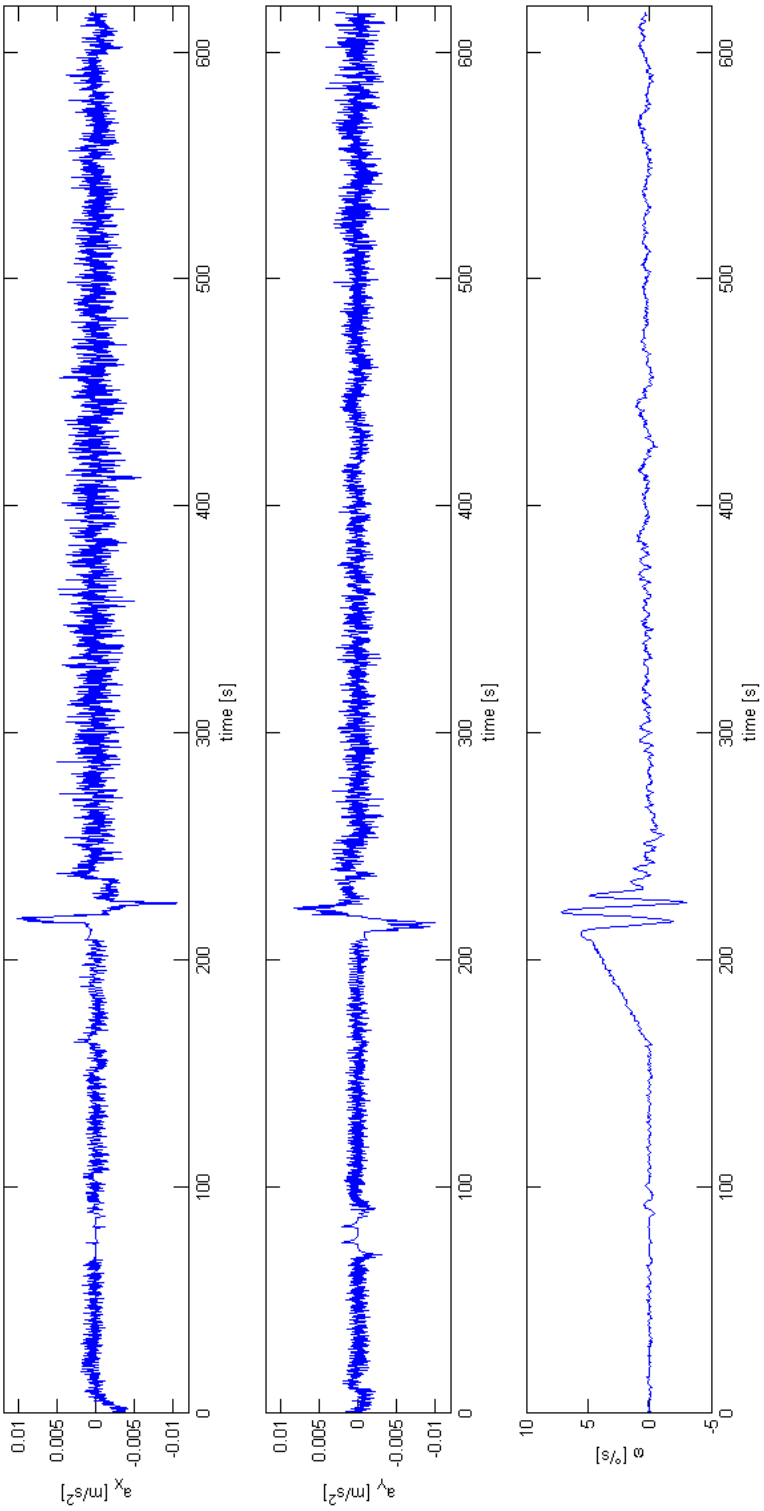

Figure 3.1: Real acceleration and angular velocity: SF - Simulation 1 - PD Controller

Figures 3.1 clearly highlight that the available accelerometers cannot measure even the maximum acceleration (about 0.01 $[m/s^2]$) as their accuracy is 0.02 $[m/s^2]$; the gyro too, are not suited to that because they must be more accurate than the accelerometers[3], is not able to catch the low angular speed of the flyer.
Due to the fact that the acceleration and angular velocity are very low, it is difficult to identify the minimum sensors resolution. Therefore, an estimation of maximum error has been carried out, by using different sensors with different accuracy characteristics. It was therefore decided to make a comparison between the actual position and attitude and those obtained by filtering[4] the measured signal, using different sensors with different accuracy characteristics.
Known also that the controller bandwidth[5] is $10[Hz]$, it is possible to compute the maximum noise level acceptable in order to choose the new sensors. It should be noted that according to that, only noise measurement and rounding errors due to sensor resolution are considered. The results obtained are shown in tables 3.3, 3.4 and 3.5 where R is the resolution of the sensor, $\widetilde{t}$ is the time spent to overcome the error threshold of $20[cm]$ for the position and 10 deg for the attitude. The simulation considered in the following tables provides the entire transfer orbit and docking maneuver with the Target Flyer, including the time needed to close the clamp, for a total of about $620[s]$.

R $[m/s^2]$	$PSD[g/\sqrt{Hz}]$	$a_{RMS}[m/s^2]$	$\lvert e_x\rvert_{max}$ $[m]$	$\lvert e_x\rvert_{t=620}$ $[m]$	$\widetilde{t}_{\lvert e_x\rvert=0.2}[s]$
10^{-6}	$2.6 \cdot 10^{-8}$	$7.9 \cdot 10^{-7}$	0.0219	0.003	-
10^{-5}	$2.6 \cdot 10^{-7}$	$7.9 \cdot 10^{-6}$	0.038	0.001	-
10^{-4}	$2.6 \cdot 10^{-6}$	$7.9 \cdot 10^{-5}$	2.173	1.268	160.15
10^{-3}	$2.6 \cdot 10^{-5}$	$7.9 \cdot 10^{-4}$	5.724	5.557	95.5

Table 3.3: Accelerometer X

R $[m/s^2]$	$PSD[g/\sqrt{Hz}]$	$a_{RMS}[m/s^2]$	$\lvert e_y\rvert_{max}$ $[m]$	$\lvert e_y\rvert_{t=620}$ $[m]$	$\widetilde{t}_{\lvert e_y\rvert=0.2}[s]$
10^{-6}	$2.6 \cdot 10^{-8}$	$7.9 \cdot 10^{-7}$	0.032	0.024	-
10^{-5}	$2.6 \cdot 10^{-7}$	$7.9 \cdot 10^{-6}$	0.051	0.036	-
10^{-4}	$2.6 \cdot 10^{-6}$	$7.9 \cdot 10^{-5}$	12.50	12.48	66.23
10^{-3}	$2.6 \cdot 10^{-5}$	$7.9 \cdot 10^{-4}$	14.405	14.405	49.02

Table 3.4: Accelerometer Y

The 10 deg threshold for attitude has been chosen not for the error magnitude itself, but for its spread in the rotation of acceleration vector in the inertial reference system.
In order to have an useful IMU accelerometers with a noise:
$PSD < 5 \cdot 10^{-7}[g/\sqrt{Hz}]$ that is $a_{RMS} < 1.6 \cdot 10^{-5}[m/s^2]$ should be selected; while the gyros should have: $PSD < 5 \cdot 10^{-4}[rad/s/\sqrt{Hz}]$ that is $\omega_{RMS} < 1.6 \cdot 10^{-3}[rad/s]$.
Then, it becomes essential to find more sensors that meet the newly imposed requirements.

[3] In fact the errors in angular speed estimation are propagated in the attitude matrix and so in the acceleration projection.

[4] The measures filtering is done by the discrete Kalman filter described in section 5.11.

[5] The choice of this value will be explained in chapter 5.

R $[rad/s]$	$PSD[rad/s/\sqrt{Hz}]$	$\omega_{RMS}[rad/s]$	$\lvert e_\alpha \rvert_{max}[°]$	$\lvert e_\alpha \rvert_{t=620}[°]$	$\widetilde{t}_{\lvert e_\alpha \rvert=10[^o]}$
10^{-5}	$2.5 \cdot 10^{-6}$	$7.9 \cdot 10^{-6}$	0.063	0.031	-
10^{-4}	$2.5 \cdot 10^{-5}$	$7.9 \cdot 10^{-5}$	0.155	0.069	-
10^{-3}	$2.5 \cdot 10^{-4}$	$7.9 \cdot 10^{-4}$	1.56	0.384	-
10^{-2}	$2.5 \cdot 10^{-3}$	$7.9 \cdot 10^{-3}$	15.6	2.94	53.94

Table 3.5: Gyroscope

3.1.5 Selection of new sensors

Among the many commercially available sensors the attention has been focused on those with very low noise level. In the following section only the sensors with features of interest,such as PSD noise (or RMS of the measure), sensitivity and acquisition frequency[6] will be shown.

Accelerometers

Model	$PSD[g/\sqrt{Hz}]$	$a_{RMS}[m/s^2]$	$B[Hz]$	Price [$]
COLIBRYS SF1500S.A	$3 \cdot 10^{-7}$	-	DC to 1500	600
HONEYWELL QA-3000	-	$1.7 \cdot 10^{-5}$	DC to 500	5500

Table 3.6: Ultra-precise accelerometers

Model	**S** $[mV/g]$	**R** $[\mu g]$	$S \cdot R[mV]$
COLIBRYS SF1500S.A	2400	5.62	0.014
HONEYWELL QA-3000	10000	$8.8 \cdot 10^{-5}$	0.09

Table 3.7: LSB Computation

In addition to the accelerometers an acquisition board able to measure those low voltages is needed, otherwise the ultra-precise sensors exploitation is unusefu. Between the two accelerometers presented the choice is inevitably the COLIBRYS for the lower price and also because it is the only one that operates with a supply voltage that can be provided with the SF battery pakcage.

Gyroscopes

Model	$PSD[rad/s/\sqrt{Hz}]$	$\omega_{RMS}[rad/s]$	$B[Hz]$	Price [$]
KVH DSP 3000-FOG	$2 \cdot 10^{-5}$	-	440	4000
HONEYWELL GG1320AN	10^{-6}	-	1600	27000
BAE SYSTEM VSG	-	$3.5 \cdot 10^{-3}$	> 70	1000

Table 3.8: Ultra-precise gyros

[6]So that known the resolution of the instrument it possible to detect if $R \cdot S > LSB$ of the available acquisition board.

Model	**S** $[mV/(rad/s)]$	**R** $[rad/s]$	$S \cdot R[mV]$
KVH DSP 3000-FOG	1145	$3.75 \cdot 10^{-4}$	0.43
HONEYWELL GG1320AN	5000	$1.88 \cdot 10^{-5}$	0.09
BAE SYSTEM VSG	1500	$1.74 \cdot 10^{-4}$	0.26

Table 3.9: LSB Computation

The gyro input voltage is compatible with the onboard batteries. The BAE Systems sensor, however, has a noise level slightly higher than the requirements, so for purely economic reason the choice is the KVH sensor.
Even the acquisition board has to be replaced with one that is able to measure a LSB voltage of $14[\mu V]$, so as said so far, and for the huge costs of sensors and board necessary, it has searched an alternative solution to strapdown platform.

3.1.6 Assisted navigation

A completely different solution that has been here considered to avoid the consistent expence for a new set of inertial sensors is the assisted navigation. Assisted navigation refers to the strategy of obtaining the state vector information from devices external to the vehicle. The most obvious support in that sense may be offered by GPS but, as simulations are not conducted outdoors, and in the laboratory equipment there isn't an indoor GPS, it was decided to use one or more fixed cameras on the table sides, in order to acquire the position of the two robot-flyers in an inertial reference, using the same algorithm of the camera mounted on SF and active during the final docking maneuvers, chapter 6. It is therefore necessary to provide a set of LEDs (or a different marker) on the chaser.
Just recalling that the accuracy of this recognition depends on the distance between the camera lens and the robot, it is opportune that the measure is carried out at the point of closest approach and this forces to use multiple cameras, with the cost increase that is however lower than the problem already underlined.
The problem has been easily solved by using a single camera positioned with the focal axis normal to the table plane at a distance that can cover the entire range of motion. This solution is the most advantageous not only in terms of cost of but also because it would remove the need to put LEDs on all sides of the Smart Flyer, in fact a simply marker light only on the upper surface would be suffices.
Results presented in the hereinafter refer to this last configuration.
The used camera is a compact webcam, with an high capturing frequency (30 [fps]). In table 3.10 the main features are shown:

(a) Trust webcam features

Camera	
Trust WB6250X	
Resolution	640×480 $[Pixel]$
Focal length	6 $[mm]$
Horizontal view angle	70 [°]
Vertical view angle	65 [°]

(b) Trust WB6250

Table 3.10: Fixed camera

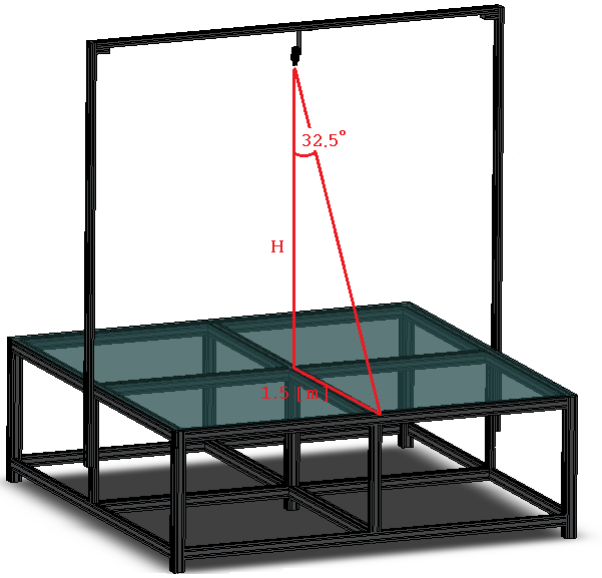

Figure 3.2: Fixed camera position

As illustrated in figure 3.2 it's evident that the necessary distance to observe the whole table is equal to:

$$H = \frac{1.5}{tan(32.5)} = 2.35[m] \tag{3.3}$$

The system just sized is presented in figure 3.3.

Literature related to similar assisted anvigation architectures [17] reports software to estimate distance and attitude with an error less than 5% on the position and about 2 deg on the attitude. These values are used to simulate the camera errors in ADS (see chapter 5). It should also take in account that acquisitions are made by the desktop computer, and processed with the recognition software, and then sent via wireless to both flyers (figure 3.4).

The computer vision algorithm used in this work will be explained in the section 6.2, but noting that the time taken by the recognition software in literature [25] and [27] are about 0.2 [s] with a 486 Pentium processor, it can be considered that a sampling time equal to 1 [s] is more than enough to include the delay due to data transmission.

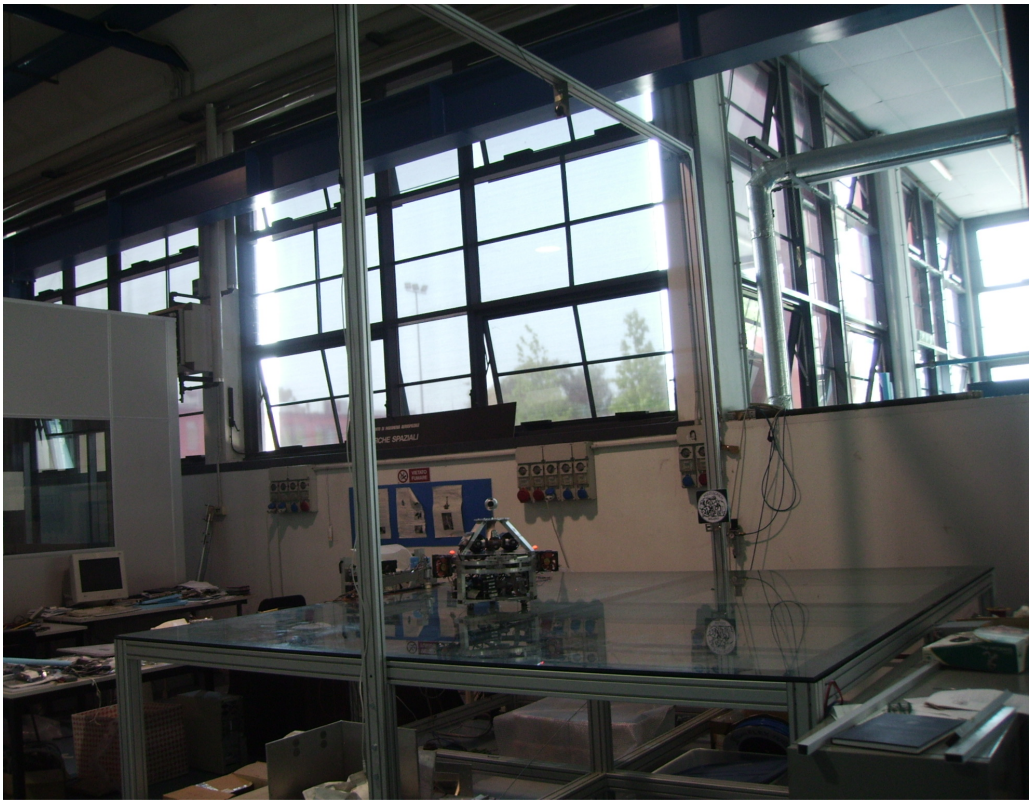

Figure 3.3: Fixed camera and its supports

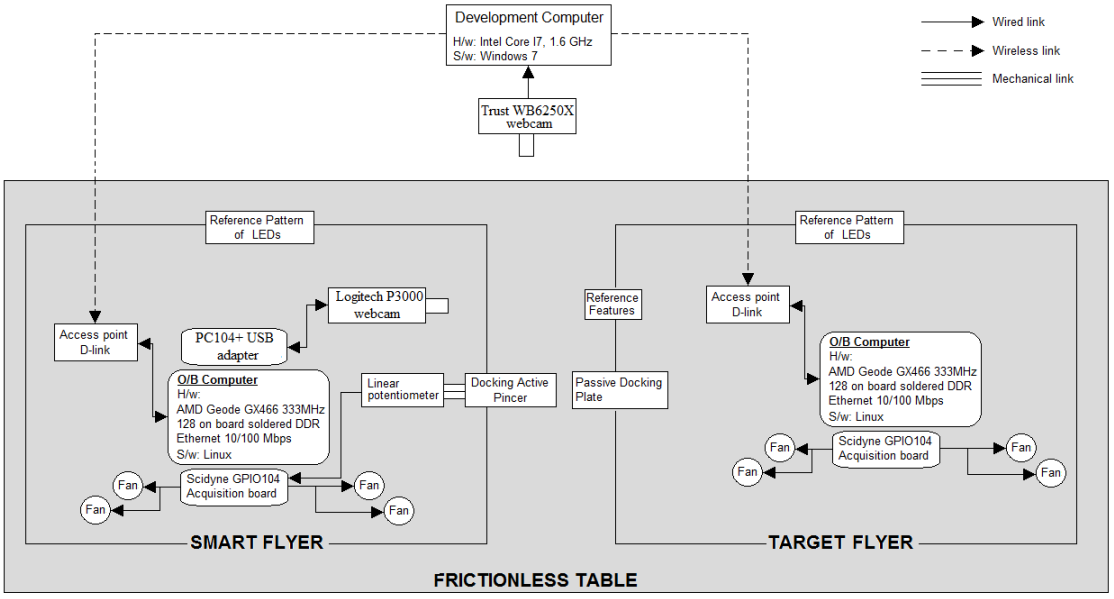

Figure 3.4: Testbed scheme

The mass and the power consumption of the 2 LEDs necessary to the inertial tracking (see section 6.2) are neglected.

3.2 Artificial vision system

During experimental test a Pulnix camera malfunctioning has been osbserved; in particular it stops to acquire with the small movement, and so is unuseful onboard. Then a compatible with PC104+ standard USB adapter has been installed, and a Logitech webcam has been used for the vision system. The performances of the relative camera is reported in table 3.10(a).

(a) Logitech webcam features

Camera	
Logitech Quickcam P3000	
Resolution	640×480 $[Pixel]$
Focal length	6 $[mm]$
Horizontal view angle	50 [°]
Vertical view angle	45 [°]

(b) Logitech P3000

Table 3.11: Relative camera

This configuration allows a power and mass reduction cause of the uselessness of the Sensoray frame grabber board and of the Pulnix camera, the details of this reduction are reported in the next sections.

3.3 The actuators

The definition of the fans number has been updated. Only four fans are actually needed for planar motion, yaw rotation included; depending on the four fans allocation either rotation maneuvers cannot be superimposed to translation maneuvers, or rototransaltional maneuvers are feasilble. Figures 3.6 and 3.5 show the baseline and back up solution, the baseline identified to assure the rototranslation maneuvering. More specifically, the baseline solutions, with fans placed at 45 deg, avoid rotations just making the SF capable of progessing in any direction. This means that in the orbital phase, when the onboard camera is deactivated the flyer can be translate and rotate without alignment need.

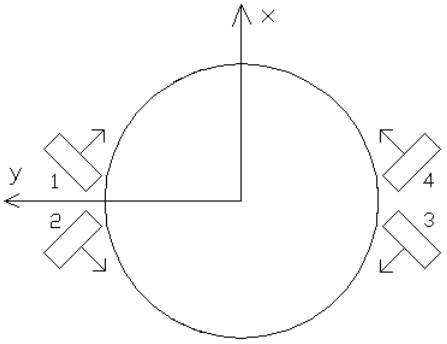

Figure 3.5: Smart Flyer fans re-disposition: primary solution

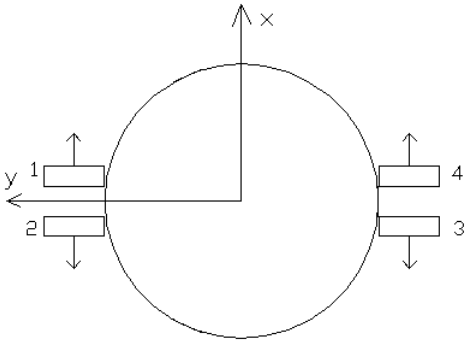

Figure 3.6: Smart Flyer fans re-disposition: backup solution

The main backup entailed by the baseline configugration is the reduced actions by a $\sqrt{2}/2$ factor. Therefore a check on the overall obtainable thrust to overcome the table concavity is needed. A check on the actuators effectivness for system stabilization under control has been done and discussed in chapter 5. At the center of each quadrant of the table there is a maximum deflection about 0.2 [mm] (see 2.2) while the side of the quadrant is 1.5 [m]: the slope due to the table inflection is approximately equal to the slope of the cone generatrix that has its vertex in the maximum inflection point.

$$\xi = \arctan\left(\frac{0.0002}{0.75}\right) = 0.015^{\circ} \tag{3.4}$$

The only acting force, apart from the control is the weight. Its component along the quadrant slope is:

$$a_d^{MAX} = g\sin(\xi) = 0.0026[m/s^2] \tag{3.5}$$

to be conservative, a margined mass of 20 [kg] has been considered. The disturbing force along the motion direction is 0.052 [N]. Cause of this actuators doesn't born as thruster no power-force curve is available, and the calibration operations has been performed: table 3.12. Assuming a fan powered with 1 [W] gives 0.0375 [N], two fans at the same power and inclined at 45°give $0.0375 \cdot \sqrt{2} = 0.053[N]$. This means that the table deflection is not an issue for this actuators configuration.

	Measured thrust [N]			
Power [W]	**Measure 1**	**Measure 2**	**Measure 3**	**Measure 4**
0.84	0.023544	0.022563	0.023544	0.025506
1.2	0.054936	0.054936	0.060822	0.05886
1.8	0.095157	0.097119	0.089271	0.10791
2.4	0.135378	0.126549	0.133416	0.131454
3	0.164808	0.157941	0.164808	0.159903
3.6	0.184428	0.184428	0.184428	0.192276
4.2	0.217782	0.21582	0.214839	0.216801
4.8	0.238383	0.23544	0.238383	0.236421
5.4	0.2668326	0.272718	0.266832	0.262908
5.64	0.275661	0.276642	0.276642	0.273699

Table 3.12: Thrust supplied by SF's fans actuators

The use of only 4 fans allows removing to eliminate the PIC circuit devoted to feed 8 actuators with only 4 analog outputs generated by the Scidyne acquisition board. Instead of the microcontroller an integrated circuit has been created. It include 4 relays to switch the actuators to apply the requested control profile.

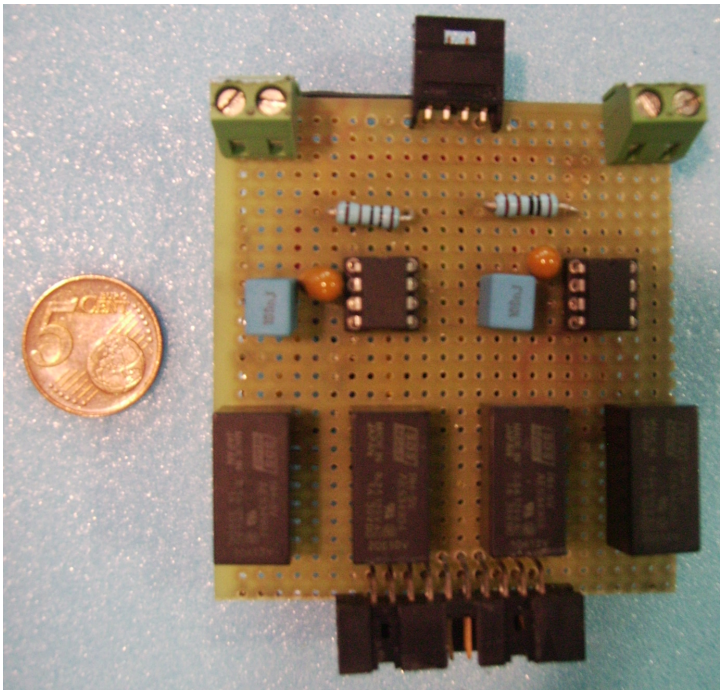

Figure 3.7: Integrated circuit with 4 relays

The benefit of such a design solutions stays in that no external power is required. The electric scheme of the integrated circuit is shown in figure 3.8

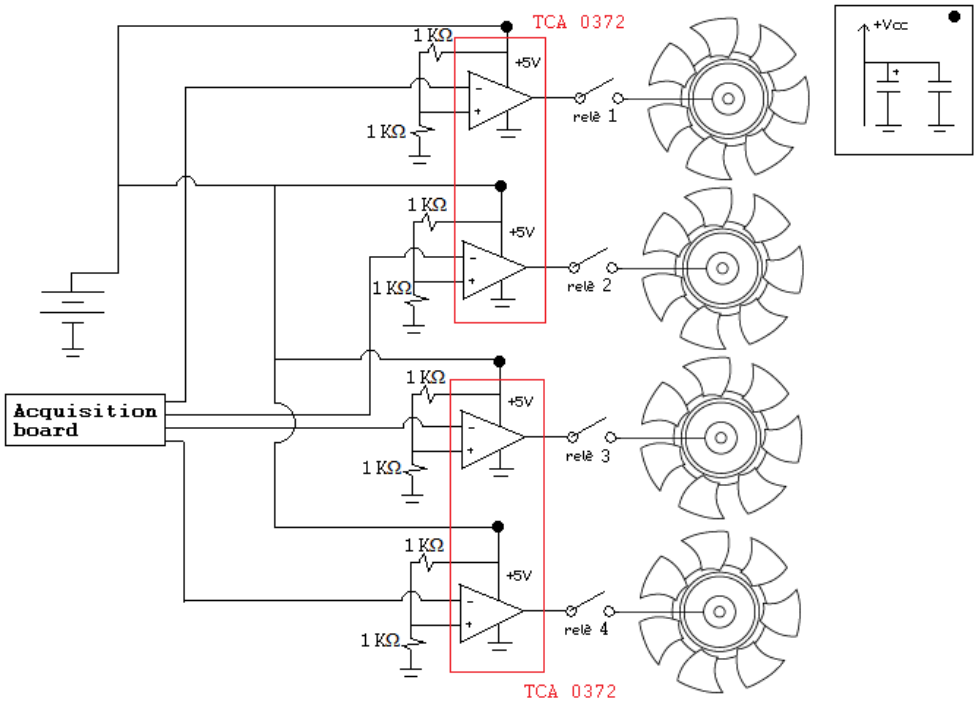

Figure 3.8: Integrated circuit scheme

3.4 The docking mechanism

Because of manufactoring and design errors, the docking plier doesn't work correctly. In particular the following problems have been noted:

- whenever the lever angle exceeds 20° the levers can't be closed;
- failure in docking phase may occur because the two levers are not in contact when they grasp the target plate.

To cope with the aforementioned issues two bolts have been inserted to limit the lever angle at 20° and an appropriate target plate has been designed to reduced the failure risk during the docking phase.

Alternatively, however, a backup solution has been designed too to keep alternatives during labs tests.
In order to simplify the docking mechanism, it is assumed there are no moving parts during the docking manouvre. To this end a passive target plate with an active spike has been preliminarly designed (figure 3.10).

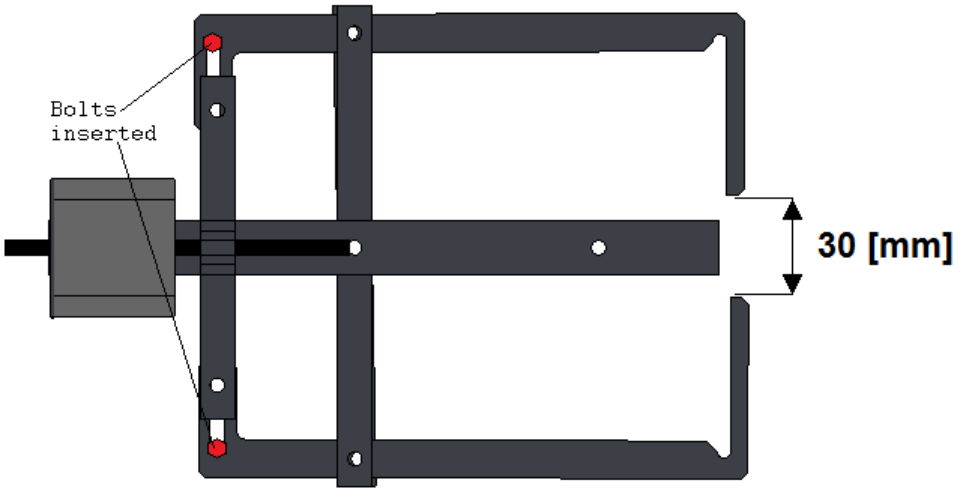

Figure 3.9: Active clamp closed

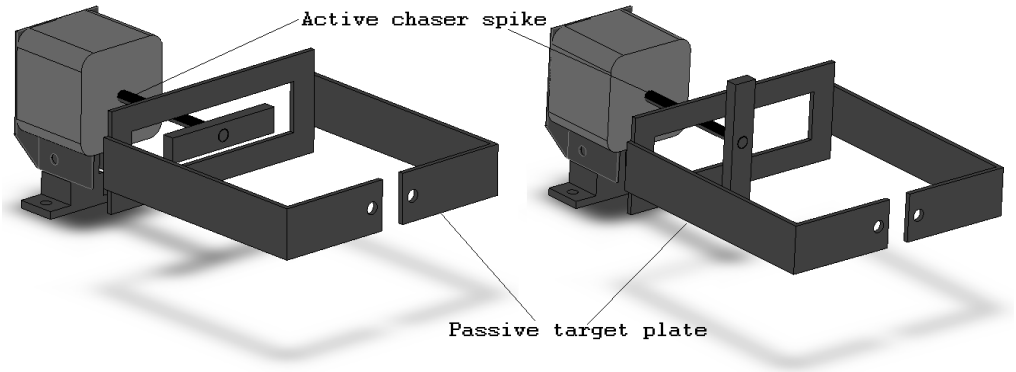

Figure 3.10: Open and close backup docking system

3.5 The supply system

In order to consider all changes described in the previous sections, a new power budget has been carried out. The power estimation is reported in table 3.13. The 20% margin

Component	Supplier	Model	Voltage [V]	Current [A]	Power [W]
PC104+	Eurotech	CPU 1432	5	1.9	9.5
Hard disk	Hitachi	DK23DA10F	5	0.9	4.5
Lan adapter	Eurotech	ACS-907106	5	0.6	3
Acquisition board	Scidyne	GPIO-104	5	0.34	1.7
USB Adapter	Eurotech	PC060104	5	0.1	0.5
Motors control board	McLennan	MSE422	12	0.6	7.2
Access point	D-link	DWL-G730AP	5	1.2	6
Webcam	Logitech	P3000	5	0.2	1
Potentiometer	Novotechnik	TR25	5	10^{-6}	$5 \cdot 10^{-6}$
Fans[7]	Thermaltake	A2028	12	0.5	18
Total					51.4
Total + 20%					61.7

Table 3.13: New SF power budget

has been considered in order to provide for future upgrades. Despite the 20% margin and the addition of other (low power devices) the power budget remains about 62 W then a 4 cells battery pack will be suffices to guarantee a feed of

$$time = \frac{n \cdot C_r \cdot DOD}{P_{req}} = 29[min] \tag{3.6}$$

Unfortunately the DC-DC converter is not able to work with an input power greater than 60 [W], see table 2.8(a). So a new DC-DC converter is necessary, but this old device can be re-used on TF board because the target needs a lower power than the chaser.
The new device chosen for the SF and compatible with the PC104+ is the TriM-Engineering HE-HP that has a maximum input power about 100 W, see table 3.14.

The gained power is computed in the table 3.15.

(a) HE-HP DC-DC converter property

Tri-M Engineering HE-HP	
Input voltage	6-40 $[V]$
Output voltage	5, 12 $[V]$
Max output power	100 $[W]$
Efficiency	$>$ 90% [%]
Dimension	95x89 $[mm]$
Weight	172 $[g]$

(b) HEHP DC-DC converter

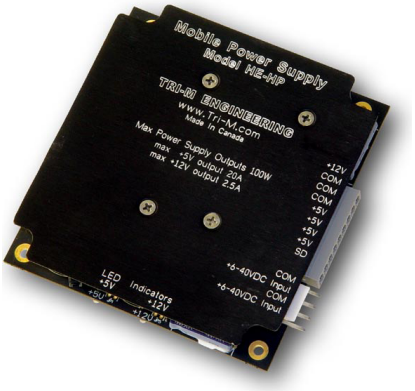

Table 3.14: New Smart Flyer DC-DC converter

Adding element	Power [W]	Removed element	Power [W]
Logitech P3000	1	Pulnix camera	2.4
USB adapter	0.5	Sensoray 311	1.5
		IMU	0.38
		4 Fans[8]	6
		PIC board	0.125
Power addition [W]	1.5	**Power gained [W]**	10.405
Power margin [W]	10.405 - 1.5 = 8.905		

Table 3.15: Power gained

3.6 Configuration

Given that the vision system doesn't use the Pulnix camera and the panoramical view isn't necessary, the vertical heavy supports are removed, and the Logitech webcam is placed on the upper base.
The gained mass is calculated in the table 3.16.

Adding element	Mass [kg]	Removed element	Mass [kg]
Logitech P3000	0.07	Pulnix camera	0.22
USB adapter	0.03	Sensoray 311	0.15
		IMU + support	1.27
		Vertical stirrups	0.67
		4 Fans	0.412
		PIC board	0.05
Mass addition [kg]	0.1	**Mass gained [kg]**	2.36
Mass margin [kg]	2.36 - 0.1 = 2.26		

Table 3.16: Mass gained

Besides the location of the docking plier and its relative control board and potentiometer has been chosen in order to align the docking device with the view direction. They are placed below the upper deck that is completely clear. The upgraded Smart Flyer configuration is showed in figure 3.11.

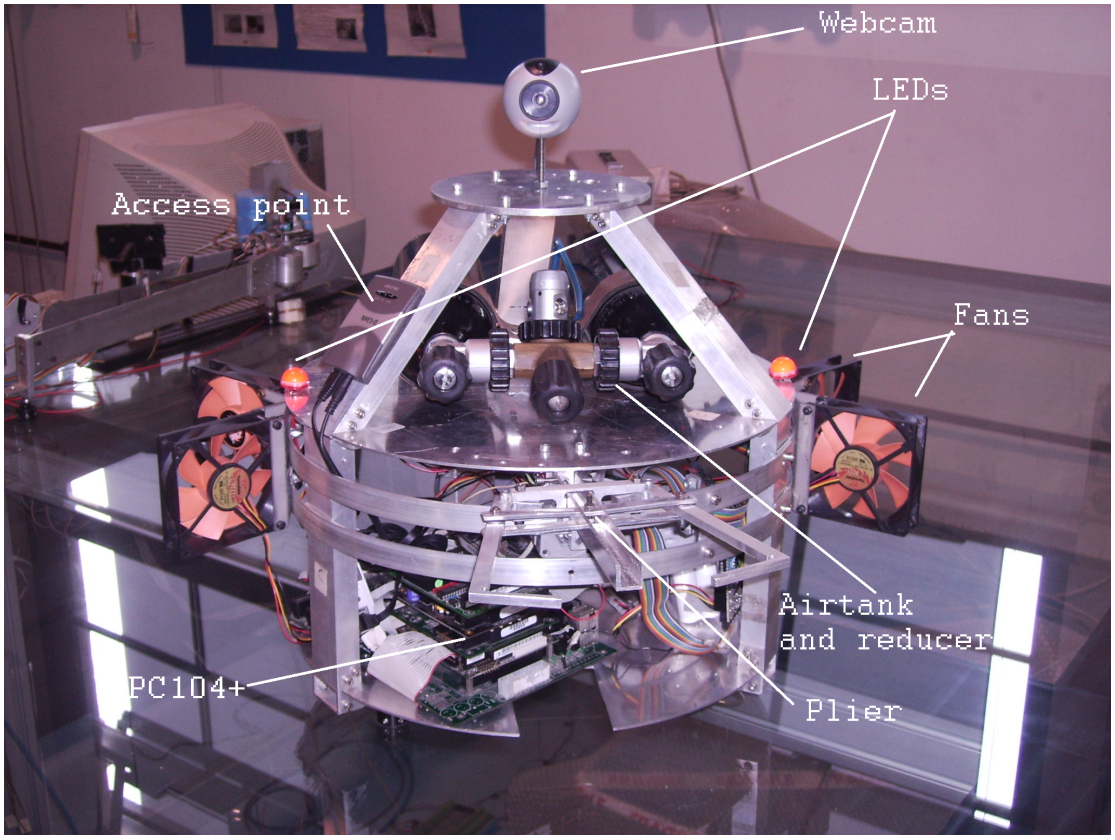

Figure 3.11: Smart Flyer upgraded configuration

Chapter 4

The Target flyer design

A key requirement for the Target flyer design is to build an autonomous floating robot able to move along a given path by means of a control system that allows it to reach desidered position, velocity and attitude in time. However it is possible to equip the TF with other devices that are useless (such as onboard camera) for the docking scope but could be useful in future if it will decide to do formation flying with the Smart Flyer.

4.1 Floating system

4.1.1 Requirements

In order to produce microgravity condition it's necessary an airbearings flotation system. Then a compressed air tank can assure autonomous flotation for all simulation time, about 20 minutes. Obviously the system should involve also a reducer that permit to feed the airpads with constant pressure.

4.1.2 Air tank

In order to realize a robot that isn't only a passive target and that is easily reusable in formation flying and active cooperation with Smart Flyer, it can be thought to begin the dimensioning of the various subsystems choosing an over sized air reservoir, like is showed in table 4.1.

(a) Luxfer bottle characteristic

Model	M25 x 2 ISO CP 10
Producer	Luxfer
Capacity	3 [lt]
Diameter	111 [mm]
Length	515 [mm]
Empty weight	4.5 [Kg]
Nominal pressure	230 [atm]

(b) Luxfer bottle and relative tap

Table 4.1: Target Flyer air tank and relative tap

4.1.3 Air bearings

Regarding the bearings to use on the TF, the same ones of SF can be used, since they are the smallest in sale. In the following pictures their characteristics are reported.

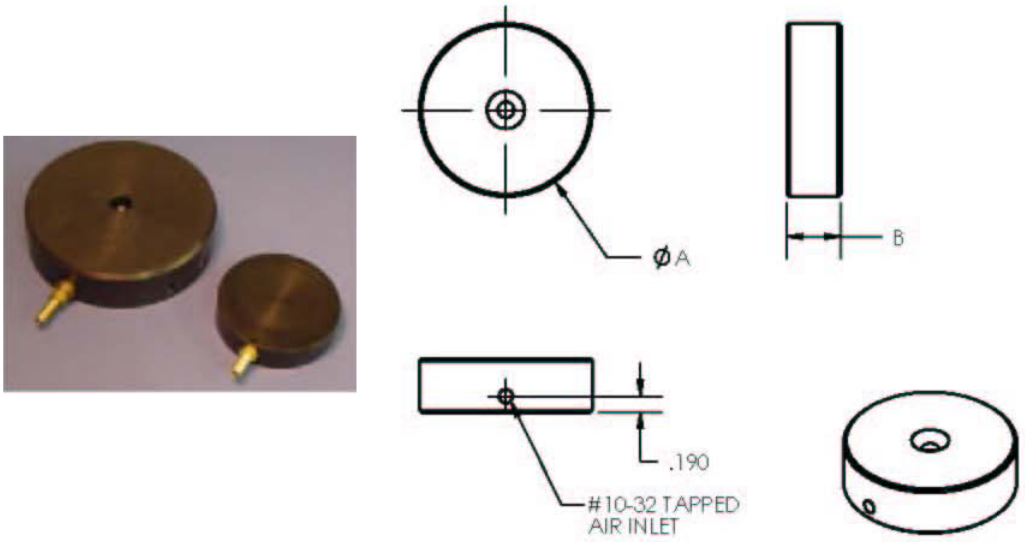

Figure 4.1: Target Flyer airpads

Model	A	B	D (in.sq.)	Load (lbs)	Stiffness (lbs/in)
FP-C-010	1.0"	0.5"	0.79	14	100,000
FP-C-015	1.5"	0.5"	1.76	32	160,000
FP-C-020	2.0"	0.625"	3.14	56	300,000
FP-C-025	2.5"	0.625"	4.91	88	450,000
FP-C-030	3.0"	0.875"	7.07	127	635,000
FP-C-040	4.0"	1.000"	12.56	226	1,000,000
FP-C-050	5.0"	1.250"	19.63	353	1,450,000
FP-C-060	6.0"	2.250"	28.2	508	2,000,000

D = Projected Area
.3 X PSIG X D = Approx. Load Limit
Load and Stiffness at .0005 Air Gap & 60 psi

All dimensions in inches. Air inlets are tapped 10-32.
A barbed fitting for 1/8" ID tygon tubing is supplied unless otherwise specified.
Bearings require approx. 30-90 psi - regulator - 10 micron filter.

Figure 4.2: Target Flyer airpads characteristics

4.1.4 Trade-off

A first sizing can foresee the use of the oversized tank shown in table 4.1, verifying that it assures a floatation time greater than 20 [min]. This choice might have the advantage to avoid the emptying synchronization problems deriving from the use of two bottles, and limit the barycentre excursions.
From the *NelsonAir* airbearings datasheet, a boost pressure of 60 [PSI] (about 4 atm) for each bearing guarantees to raise a limit load of 22 [kg] of 0.013 [mm]. Since the Target Flyer will have to be lighter than 66 [kg], it is possible to increase the gap air between table and bearings or to reduce the boost pressure, increasing the autonomy of the sustentation.
Furthermore assuming a length of 30 [cm] of the pipe that takes the compressed air from the reducer to the 3 bearings, and considering a required pressure of 4 atm at each bearings [60], the boost pressure can be estimated by the following expression:. In order to do this it is used an iterative cycle, where starting from an initial air condition it arrives to convergence doing a simple pressure budget:

$$\left(\frac{P}{\rho} + zg + \frac{1}{2}V^2\right)_{in} - \left(\frac{P}{\rho} + zg + \frac{1}{2}V^2\right)_{out} = K\frac{1}{2}V^2 \tag{4.1}$$

where $K = K_1 + K_2$ and $K_1 = \lambda l/d$ (where l is the length of the pipe and d its diameter), it represents the losses for friction, while $K_2 = 0.9$ represents the concentrated losses that is given by the splitting of the pipe at the pressure reducer, in order to feed each bearing.

The parameter λ depends on the material rugosity of the pipe and on the Reynolds number of the inside flow. Assuming a superficial rugosity of $5\,[\mu m]$ (typical for plastic tubes), and estimating the Reynold number by the following expression:

$$\begin{aligned} \lambda &= \frac{64}{Re} && Re \leq 4000 \\ \lambda &= \frac{1}{\left[-4log\left(0.27\frac{r}{d}+\frac{7}{Re}\right)^{0.9}\right]^2} && Re > 4000 \end{aligned} \tag{4.2}$$

a boost pressure of 4.083 [atm] is obtained. The usefullness of the calculation is in the possibility to find also the speed of the air, and therefore the pipe capacity in order to calculate the duration of the experiment with one single bottle. The regimen speed has resulted to be equal to 1.76 [m/s] in each of the 3 pipes with a total capacity equal to:

$$Q = 3\rho\left(\pi\frac{d^2}{4}\right)V = 2.1 \cdot 10^{-4}\left[\frac{kg}{s}\right] \tag{4.3}$$

Such value has been obtained under the incomprimibile fluid hypotheses, that is considering constant speed and density along all the tube[1].
The tank pressure is about 230 [atm] and the volume of the bottle is equal to $3 \cdot 10^{-3}$ $[m^3]$, then the air mass within the bottle can be calculate considering the system at the room temperature by the following equation:

$$\rho_0 = \frac{P_0}{R \cdot T_0} = 278\left[\frac{kg}{m^3}\right] \Rightarrow m_{air} = \rho_0 \cdot V_{bottle} = 0.835[kg] \tag{4.4}$$

At this point the necessary time to empty the bottle[2] is univocally determined:

$$t = \frac{m_{air}}{Q} = 3975[s] = 66.25[min] \tag{4.5}$$

The obtained time of floatation is sufficient to the simulation scope and could be ulteriorly increased feeding with lower pressure the bearings.

4.1.5 Mass Budget

In table 4.2 the necessary mass for the pneumatic floatation system is summarized.

Component	**Model**	**Mass [Kg]**
Bottle + air	Luxfer	4.5
Pressure reducer	Luxfer	0.25
Airbearings x 3	Nelson Air FP-C-010	0.1
Total		4.85
Total + 20% margin		5.82

Table 4.2: Floatation system mass budget

[1] Hypothesis verified from the result that show a $Mach$ number $<< 0.3$.

[2] The pressure inside the bottle can be assumed constant because it is much greater than the reducer output pressure.

4.2 Inertial positioning system

Also for the Target Flyer a wireless positioning system should be used. The facility is described in the subsection 3.1.6 and so any power and any mass must be allocated for this subsystem. Position and attitude information will be transfer to TF directly via wireless from the desktop PC, and will received thanks to the on board access point.
The mass and the power consumption of the 2 LEDs necessary to the inertial tracking (see section 6.2) are neglected.

4.3 Computer system

4.3.1 Requirements

Likewise to what has been done for Smart Flyer, it will be necessary to have:

- an onboard computer;
- a data acquisition board able to link the actuators and sensors with the onboard computer.

For the scopes of this work the TF's computer mustn't have the same high performances of the SF one, because it shouldn't acquire or process videos and/or images. Anyway, as it is described at the beginning of the chapter, it is preferable to provide the Target Flyer with the same equipment of the chaser.
Then, even if it isn't necessary, it will be mounted on TF also an USB adapter with a webcam and an hard disk device in order to permit the storage of the acquired images and/or videos.

4.3.2 Trade off

At this point must be identified the best solution in terms of architecture and operative system.
The use of PC/104 Plus module is investigated to satisfy the requirements. In fact, PC/104+ embedded computers have several advantages over standard PCs including being lightweight, compact, and stackable. Moreover, they have lower power requirements and have a higher resistance to shock and vibration than normal personal computers. For further capability, PC/104 Plus contains both an ISA and PCI bus which allows high speed processors to reach their full I/O bandwidth potential [51].
Today the 1432 CPU module used on the Smart Flyer is replaced with 1433 CPU module (figure 4.3). It is a fully RoHS compliant, fanless, low power Pentium MMX-class PC/104-Plus compliant CPU module. This +5V only module is based on the AMD Geode GX466 333MHz processor core with 128MB of on-board soldered DDR RAM. This single board embedded computer module is compatible with Windows CE and Linux. Integrated peripheral interfaces of the 1433 module include: 4 USB 2.0 ports, TFT and VGA, 2 serial ports, parallel port, IDE, AC97 audio port, AT keyboard, PS/2 mouse and fast Ethernet port, so no Ethernet adaptor is required for the Target Flyer.

Therefore starting from the bottom of the computer module it will be assembled:

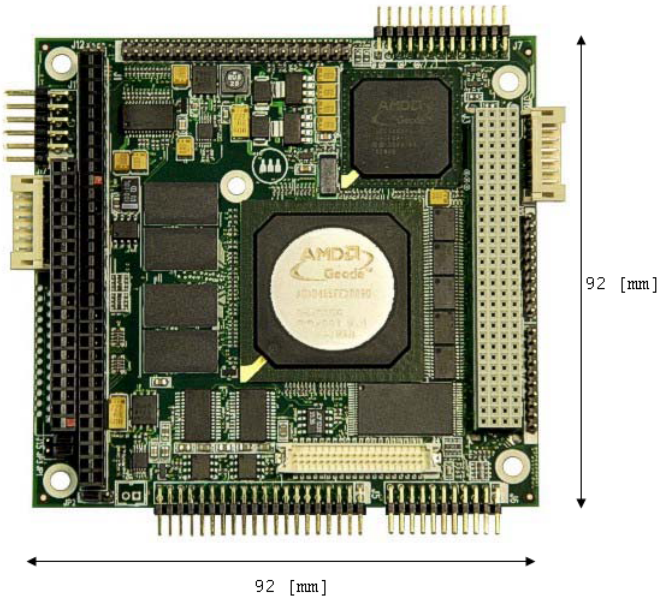

Figure 4.3: PC104+ 1433 CPU module

- the central processing unit (1433 CPU) module that controls the basic functions of the computer;
- over the CPU and attached through a standard PC/104 plus 4x30 pin interface is the I/O module;
- The next module on is the power supply DC-DC converter;
- The final module is the Scidyne GPIO-104 data acquisition board.

The I/O module has three connections that are used routinely throughout its preparation and operation. The first interface is the hard drive which memory must be sufficient for videos and images storage: an hard drive with 10 [Gb] or more space has surely more memory than the computer will ever use. The second connection on the board has connectors to a wide array of computer peripheries. These include one parallel port, two serial ports, keyboard and mouse ports, and one Ethernet port. The Ethernet port will be connected to the wireless router and is used during communication with the desktop computer. The keyboard interface is necessary during the computer's initial setup. The board's third interface goes to the CD and 3.5 inch floppy drive, that can be used to load the operating system and the drivers.
The data acquisition board is attached to the above computer through a PC/104+ connection. It has 8 analog input, 4 analog output and 24 digital input/output connections. The power supply module is also connected to the above module through a PC/104+ connection. One external connection allows for power to transfer from the DC/DC converter directly into the computer. The DC/DC choice will be discussed in section 4.8. At the moment no motors control board is selected for the Target Flyer.
For the operative system it must allow the video and image processing and the im-

plementation of the control software, so a reduced version of Gentoo Linux OS has been preferred for the possibility to download and install free updating software, for its stability and also for the multitasking property.

4.3.3 Mass and Power Budget

In the following tables, mass and power budget for the Target Flyer computer system are reported.

Component	Model	Voltage [V]	Current [A]	Power [W]
PC/104	Backplane BB2	5	0,9	4,5
	CPU 1433	5	1.08	5.4
Scidyne	GPIO104	5	0.34	1.7
Total				13.1
Total + 20%				15.7

Table 4.3: Computer system power budget

Component	Model	Mass [Kg]
PC/104	Backplane BB2	1.1
	CPU 1432	0.1
Scidyne	GPIO104	0.3
Total		1.8
Total + 20%		2.2

Table 4.4: Computer system mass budget

4.4 The actuators

4.4.1 Requirements

The propulsive system of the TF must allow the motion on the frictionless plane along a prefixed trajectory. As already explained in section 3.3 the target flyer, such as the SF, must be able to overcome, without any difficulty, the table deflection if it is equipped with at least 4 fans and weigh less than 20 kg.

4.4.2 Trade off

The alternatives for the sizing of the Target Flyer propulsive system are mainly 2, and in both the same Thermaltake fans are used because many calibration data are available for this actuators.

1. The primary solution consist to use the same number of actuators used for the Smart Flyer (figure 3.5) with the fans inclined at 45 [deg], in order to be able to translate and rotate without align the motion direction at each time;

2. The backup configuration uses 8 of the same fans of the SF disposed frontally (figure 4.4), in the case that the target become heavyer than the SF and require much thrust.

Obviously, the first configuration offers a saving in terms of mass and power, as well as being compatible with acquisition board.

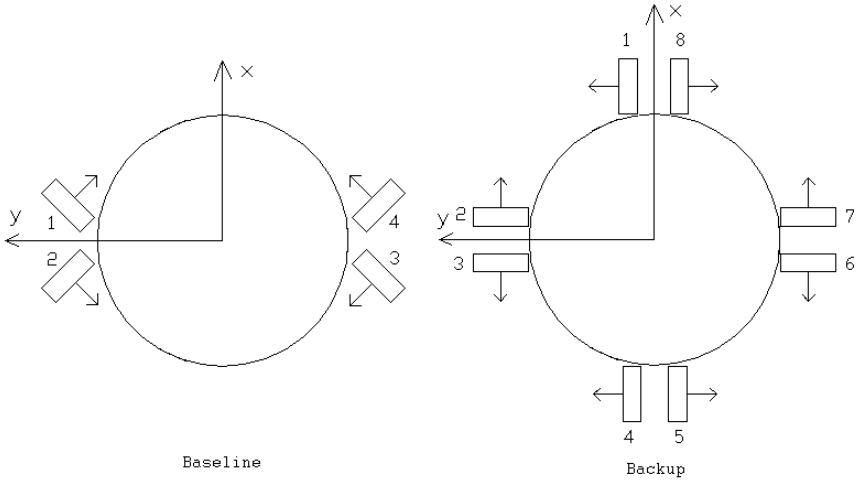

Figure 4.4: Target Flyer propulsive system: baseline and backup solution

4.4.3 Mass and Power Budget

In the following tables mass and power budget for the propulsion system are illustrated.

Model	A2028
Producer	THERMALTAKE
Dimension	92 x 92 x 25 [mm]
Air capacity	28.79 – 92.61 [CFM]
Weight	0.1 [Kg]
Total weight	0.4 [Kg]
Total weight + 20%	0.5 [Kg]

Table 4.5: Propulsive mass budget

Nominal voltage	12 [V]
Minimum voltage	7 [V]
Current	0.07 – 0.50 [A]
Input power	0.49 – 6 [W]
Rotation speed	$1300 \pm 10\% - 4800 \pm 10\%[RPM]$
Total power	18 [W]
Total power + 20%	21.6 [W]

Table 4.6: Propulsive power budget

4.5 Communication system

4.5.1 Requirements

The communication system must guarantee the possibility to communicate to the on-board computer, that manage the operations, telemetry and attitude data without any cable connection.

4.5.2 Trade off

Similarly to what done for the Smart Flyer is also possible to make independent the Target flyer from any cable connection by installing a wireless router (figure 2.12.1) compatible with onboard LAN board. The speed limit in trasmission for the Smart Flyer system is 11 Mbps, value certainly less than a LAN standard, but adequate to the data transmission needs that require less than 10 Kbs. Then the choice of this board for the TF is certainly conservative. It wouldn't be necessary to discuss other systems and/or configurations for problems related to cost and complication of other subsystems linked to this one.

4.5.3 Mass and Power Budget

The mass and power necessary for this subsystem are presented in tables 4.7 e 4.8.

Model	DWL-G730AP
Producer	D-Link
Dimension	143 x 95 x 25 [mm]
Total weight	50 [g]
Total weight + 20%	60 [g]

Table 4.7: Communication mass budget

No mass or power for LAN adapter is considered because it is integrated in the motherboard (see 4.3).

Model	DWL-G730AP
Producer	D-Link
Voltage	5 [V]
Current	1.2 [A]
Total power	6 [W]
Total power + 20%	7.2 [W]

Table 4.8: Communication power budget

4.6 Artificial vision system

4.6.1 Requirements

The vision system must permit the flyer the acquisition and consequently the processing of images and videos.

4.6.2 Trade off

For the acquisition a Logitech P3000 (figure 2.7) webcam is already avaiable at Politecnico di Milano, so has not sense to discuss about other alternatives.

4.6.3 Mass and Power Budget

The mass and power necessary for the artificial vision subsystem are presented in tables 4.9 e 4.10. No mass or power for the USB adapter are necessary because they are integrated in the mother board (see 4.3).

Model	P3000
Supplier	Logitech
Dimension	85 x 86 x 90 [mm]
Total weight	0.1 [kg]
Total weight + 20%	0.12 [kg]

Table 4.9: Artificial vision mass budget

Model	PE2010
Supplier	Pulnix
Voltage	5 [V]
Current	0.2 [A]
Total power	1 [W]
Total power + 20%	1.2 [W]

Table 4.10: Artificial vision power budget

4.7 The passive docking mechanism

4.7.1 Requirements

A passive docking mechanism must be made in order to realize a mechanical dock between the 2 flyers. The passive plate must be complementary with the active mechanism showed in figure 4.5.2.

4.7.2 Trade off

The primary solution to this problem is a passive plate with an hole that can to put up the plier spike: figure 4.5.1.

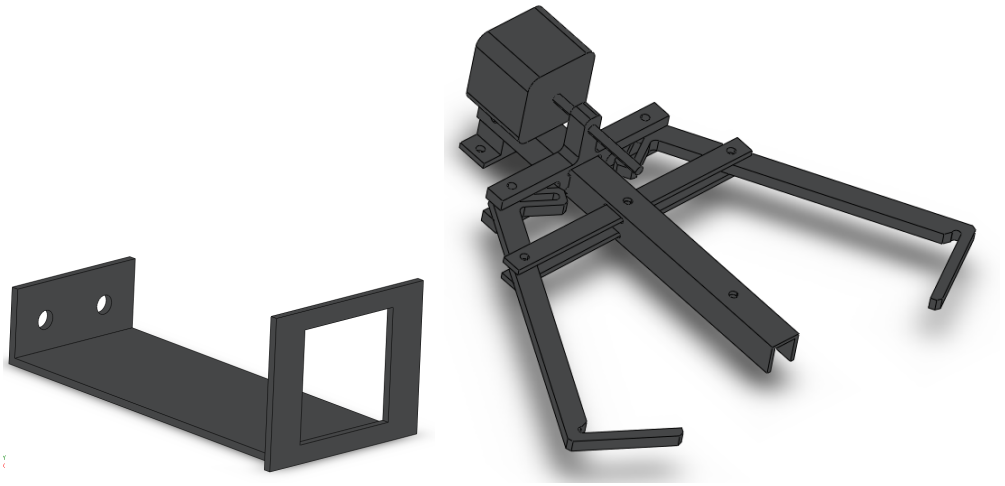

4.5.1: Passive docking plate 4.5.2: Active docking plier

Figure 4.5: Primary doking system

Another solution should be thought cause of the bad operation of the plier caused by realization mistakes[3] and it is showed in figure 4.6.

[3]The problem is discussed in section 3.4.

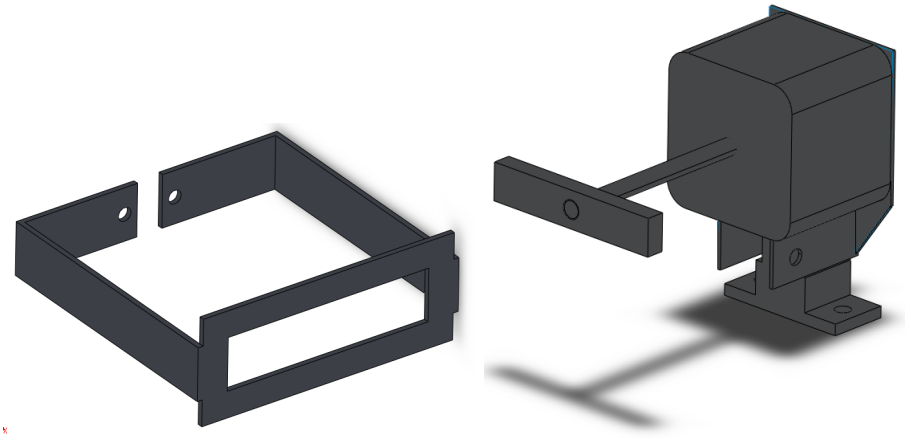

4.6.1: Backup passive docking plate 4.6.2: Backup active docking spike

Figure 4.6: Backup doking system

4.7.3 Leds and logos disposition

In order to estabilish the attitude and the Target Flyer relative position the camera mounted on SF must observe a feature on the target which size and shape is known. There are some conditions that improve the feature recognition software performance like:

- white and black image is better identifiable;
- definite line and surface instead shaded geometry increase software speed;
- well defined feature contours improve the software precision.

For this reasons a modified versions of the Politecnico di Milano logo (figure 4.7.1) has been chosen and it will be placed on the first face of TF. Each sides of the robot must present a different feature so the SF can understand which face it sees (figure 4.7.2 to 4.7.4).

4.7.1: Side1 4.7.2: Side2 4.7.3: Side3 4.7.4: Side4

Figure 4.7: Feature on TF's sides

4.7.4 Mass and Power Budget

Only the side 1 is provided with 4 LEDs for reasons that will be explained in the chapter 6, so the power budget for this subsystem is referred only to the 4 LEDs (see table 4.11 and 4.12). The mass of the passive docking plate is reported in section 4.9, while LED mass can be ignored in a total mass budget.

Model	RS-5V
Producer	RS
Dimension	4 x 5 x 20 [mm]
Quantity	4

Table 4.11: LEDs properties

Model	RS-5V
Producer	RS
Voltage	5 [V]
Current	0.05 [A]
Total power	1 [W]
Total power + 20%	1.2 [W]

Table 4.12: LEDs power budget

4.8 The supply system

4.8.1 Requirements

Also for the TF is not necessary to examine more operative condition in order to consider the power budget in the critical one because this flyer must only be able to follow a certain path along which will dock by SF.

Components	**Model**	**Quantity**	**Power with margin [W]**
PC/104+	Backplane BB2	1	13.9
	CPU 1433	1	
	Scidyne-GPIO104	1	
Wireless	Access point	1	7.2
Fans	ThermalTake A2028	3	21.6
Leds	RS-5V	4	1.2
Webcam	Logitech P3000	1	2.9
Total			46.8
Total + 20 %			56.16

Table 4.13: Power Budget

The total needed power is lower than 60 W and all devices require a voltage supply of 5-12 [V], therefore the old DC/DC converter can be used (see figure 2.8(b) and table

2.8(a)).

4.8.2 Trade off

In order to minimize the weight of needed batteries it is possible to assemble a cell lithium battery packs and study a configuration with a reasonable depth of discharge. Moreover, since the behavior of an assembled battery pack (equal to what happens in a traditional battery) is affected by a change in the nominal output voltage[4], it is necessary the addition of a DC/DC converter, that is capable to stabilize the input voltage providing a constant output.

4.8.3 Battery sizing

In table 4.13 the power budget in the operating mode is reported. Please note that all entries in the table below are already increased with a 20% margin in each subsystem, further a 20% margin of the total is applied.

The basic unit for battery pack is MP17-60-65, produced by SAFT and sold by the italian ELTEC, and its main feature are summarized in table 2.8. The number of cells necessary to allow an energy reservoir of 30 min is:

$$n = \frac{P_{req} \cdot time}{C_r \cdot DOD} = 3.7 \approx 4 \tag{4.6}$$

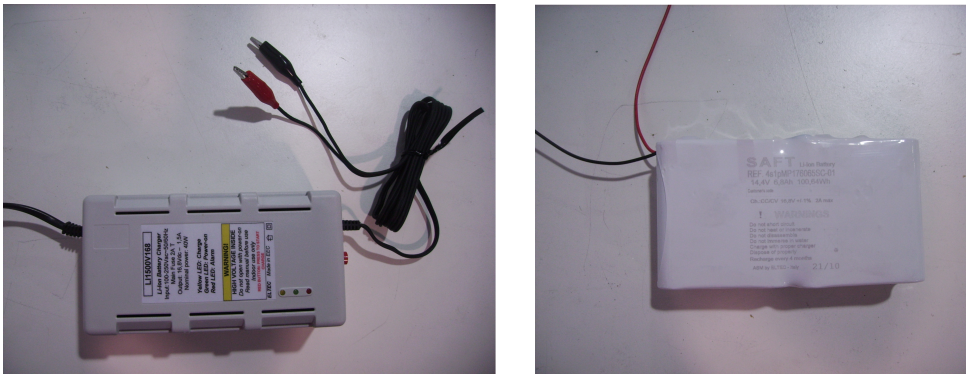

Figure 4.8: Battery pack and relative charger

For the battery pack dimensions it's possible to see the figure 2.7(b).

[4]Value that will be higher at the start of discharge and it decrease with increasing of depth of discharge.

4.8.4 Power distribution system

In figure 4.9 the power system scheme and the data links are shown.

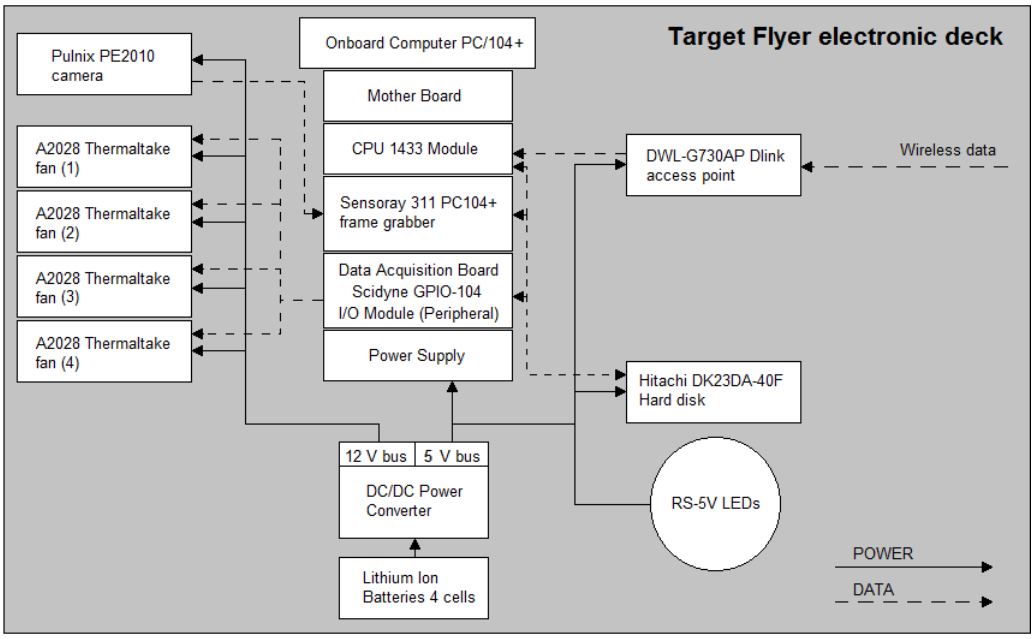

Figure 4.9: Data and Power Schematic of TF Electronics Deck Components

4.8.5 Mass Budget

The mass that must be allocated for the power system is evaluated and increased with margin of 20%: see table 4.14.

Thickness	19x4 [mm]
Width	60 [mm]
Height	65 [mm]
Weight	150 [g]
Number of cells	4
Total weight	0.6 [kg]
Total weight + 20%	0.72 [kg]

Table 4.14: Battery mass budget

4.9 Structure and configuration

4.9.1 Requirements

There are no particular requirements for the design of Target Flyer structure. . In particular, the only dimensioning loads are due to terrestrial gravity acceleration, given that the inertial accelerations due to TF motion are negligible.
The TF configuration has been chosen to satisfy the following aspects:

- the center of mass must be close to z axis (see figure 4.10);
- accessibility must be guaranteed;
- the actuators must be aligned with the center of gravity of TF.

4.9.2 Trade off

In the following section two possible solutions for assembling the TF with its geometric and inertial data are presented.
The first configuration has a square section with an intermediate level in order to mount other components and a center hole to place the compressed air tank.

This configuration limits the gravity center excursion due to the consumption of compressed air and allows the reduction of pressure losses, given that the reducer would be located near to the bearings. In table 4.15 the components dimensions and weights with margin are shown.
Table 4.16 shows the inertial characteristics and location of the TF's CG in this configuration.

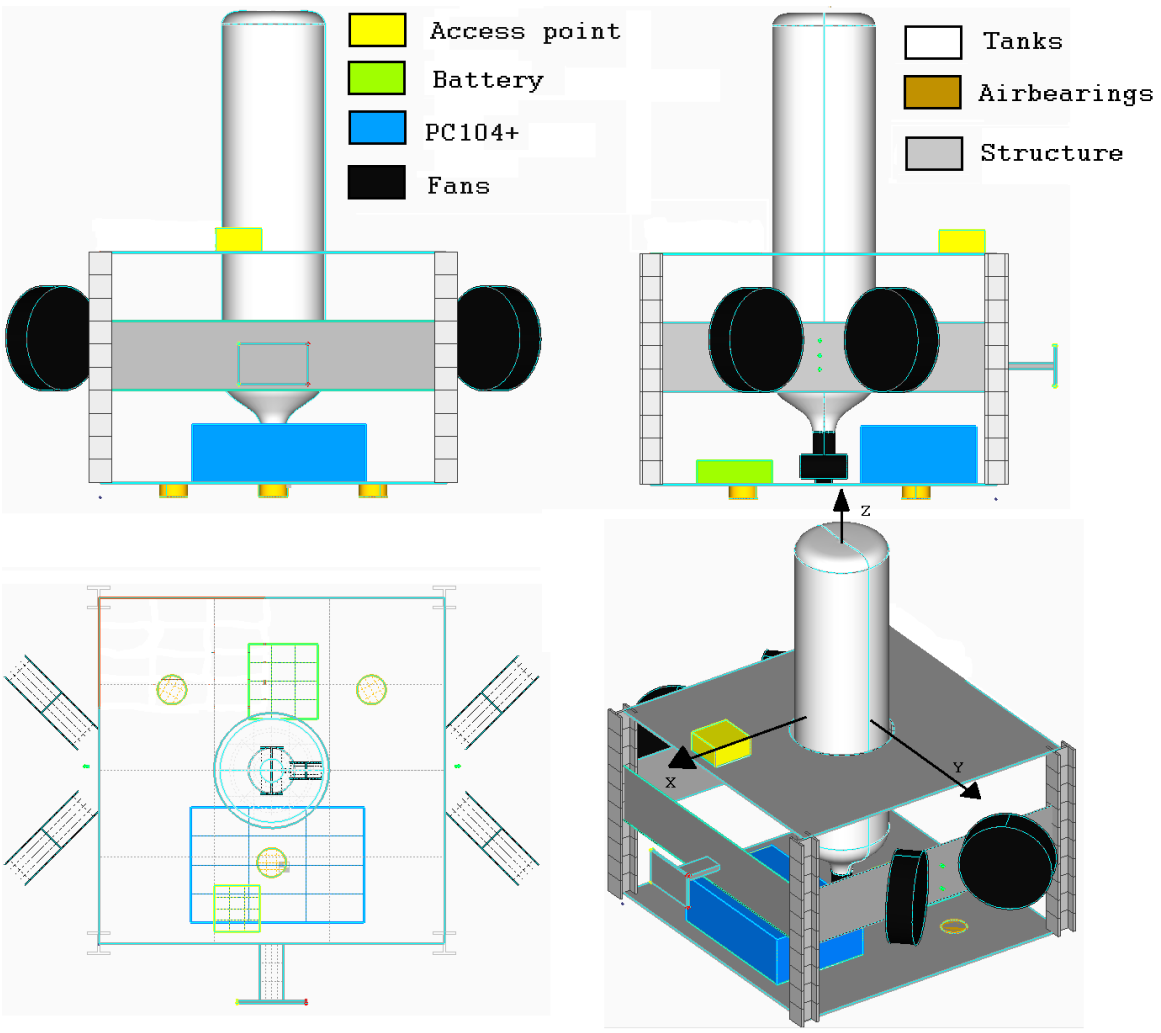

Figure 4.10: Target Flyer primary configuration

Component	Quantity	Dimension [mm]	Weight + margin [Kg]
Flotation system			
Tank	1	110 (d) x 515 (h)	5.4
Reducer	1	50 x 50 x 100	0.3
Airbearings	3	25 (d) x 13 (h)	0.12
OBDH			
Backplane BB2	1	150 x 100 x 30	1.8
CPU 1432	1		
Scidyne-GPIO104	1		
Propulsion system			
Fans A2028	4	90 x 90 x 25	0.5
Communication system			
Wireless router	1	144 x 95 x 25	0.06
Power system			
Battery pack	1	19 x 60 x 65	0.72
Payload			
Webcam	1	90 x 85 x 86	0.12
Total mass without structure			9.02
Structure mass + margin			7.37
Total mass			16.4
Total mass + 20%			19.67

Table 4.15: Weight and components cluttered in primary condition

Total mass [Kg]		
16.4		
Center of mass		
Xg [mm]	**Yg [mm]**	**Zg [mm]**
2.5	16	121
Moments of inertia		
Ixx [m^4]	**Iyy [m^4]**	**Izz [m^4]**
0.105	0.106	0.074

Table 4.16: Target Flyer inertial properties in primary configuration

The second configuration is the backup one and has a circular section structure, with a number of fans double respect the previous case but with the same housing for the compressed air cylinder (figure 4.11).
Table 4.18 shows the inertial characteristics and the CG position of TF in this configuration.

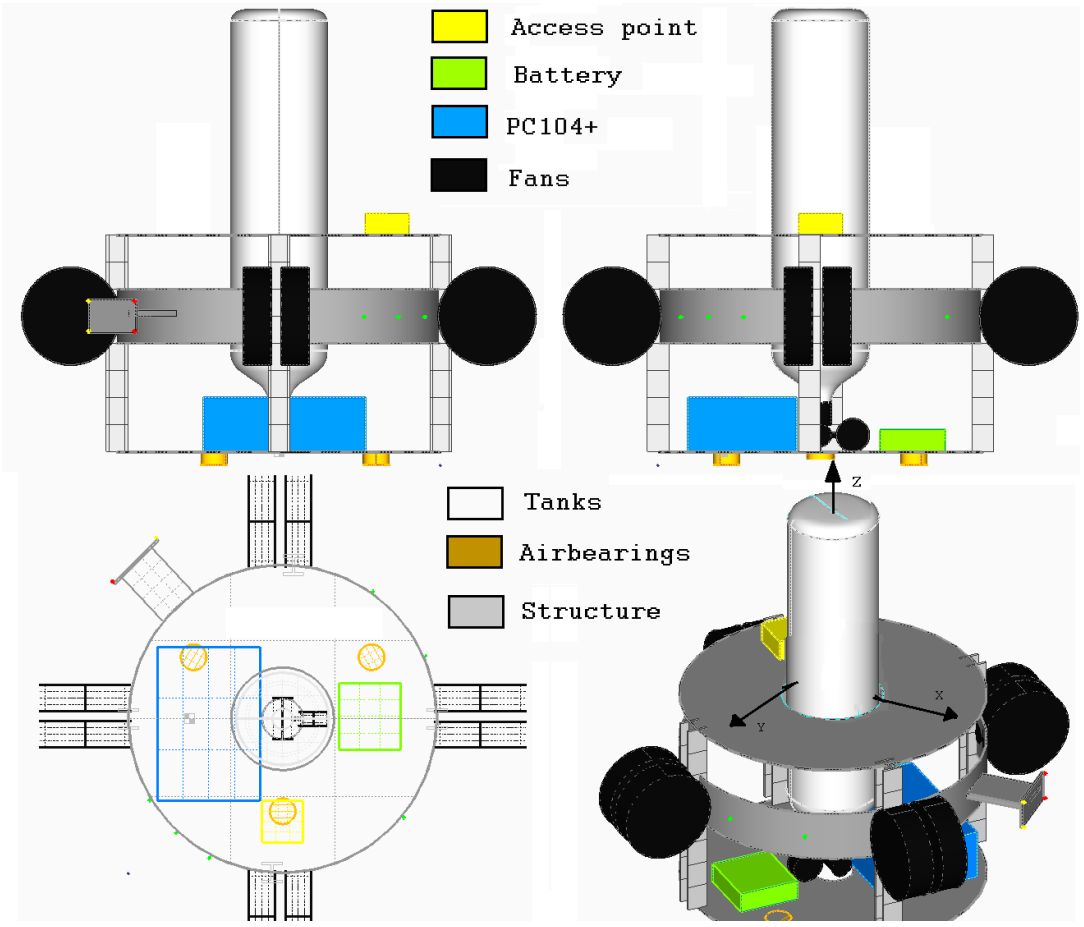

Figure 4.11: Target Flyer backup configuration

Component	Quantity	Dimension [mm]	Weight + margin [Kg]
Flotation system			
Bottle	1	90 (d) x 360 (h)	5.4
Reducer	1	50 x 50 x 100	0.3
Airbearings	3	25 (d) x 13 (h)	0.12
OBDH			
Backplane BB2	1	150 x 100 x 30	1.8
CPU 1432	1		
Scidyne-GPIO104	1		
Propulsion			
Fans A2028	8	90 x 90 x 25	1
Communication			
Wireless board	1	144 x 95 x 25	0.06
Power system			
Battery pack	1	19 x 60 x 65	0.72
Payload			
Webcam	1	90 x 85 x 86	0.12
Total mass without structure			9.52
Structure mass			7.37
Total mass			16.9
Total mass + 20%			20.23

Table 4.17: Weight and components cluttered in backup condition

Total mass [Kg]		
16.9		
Center of mass		
Xg [mm]	**Yg [mm]**	**Zg [mm]**
15.6	0.1	126
Moments of inertia		
Ixx [m^4]	**Iyy [m^4]**	**Izz [m^4]**
0.096	0.110	0.073

Table 4.18: Target Flyer inertial properties in backup configuration

4.9.3 Mass Budget

As for the thickness used for the structure in both configurations the thick aluminum equal to 3 [mm] for the 2 basis and 2 [mm] for all the others parts lead to a static deformation (due to the weight of the components) equal to 1.25 [mm] in primary configuration and equal to 0.3 [mm] in secondary configuration, (as can be seen from figures 4.12 and 4.13) which can be considered negligible for the purposes of this work.

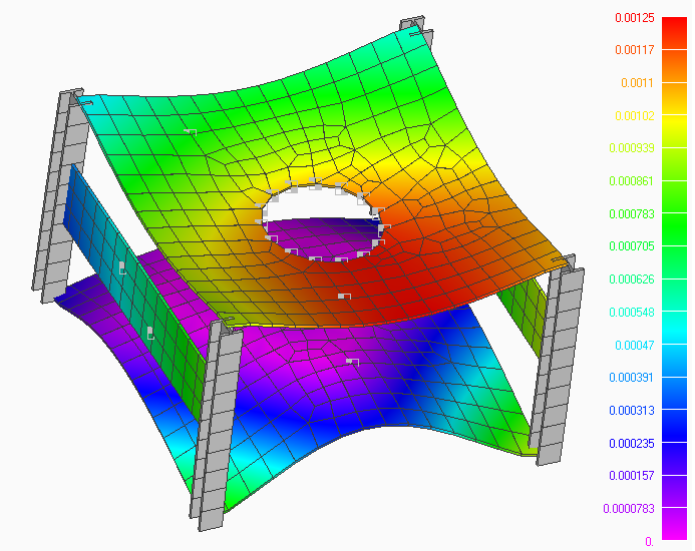

Figure 4.12: TF deformed condition in primary configuration

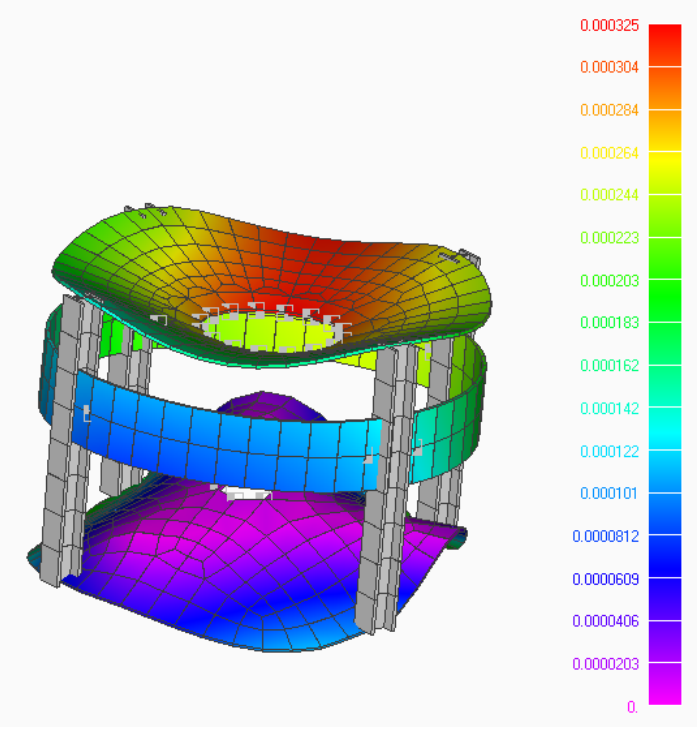

Figure 4.13: TF deformed condition in primary configuration

Aluminum alloy density	$2800[Kg/m^3]$
Aluminum volume	$2.19 \cdot 10^{-3}[m^3]$
Weight	6.132 [Kg]
Weight + 20%	7.37 [Kg]

Table 4.19: Structure mass budget in both configuration

4.10 Assembling disalignments

Any error in bottle positioning could cause an excursion of center of gravity that would cause an excessive and unequal distribution of weight force on the three bearings generating a pitch moment. As shown in table 4.16, in nominal condition the TF center of mass has a distance from the Z axis of 0.25 cm along x and 1.6 cm along y. In order to estimate the load distribution on bearings, 10° inclination of the bottle axis towards the nominal center of mass position has been assumed. Under this assumption, the maximum excursion of the center of mass from the nominal position occurs (about 2 cm), and the force distribution can be computed by the following expressions:

$$\begin{aligned} &F_1 + F_2 + F_3 = m_{TF} g \\ &F_1 x_1 + F_2 x_2 - F_3 x_3 = m_{TF} g x_G \\ &-F_2 y_2 + F_3 y_1 = m_{TF} g y_G \end{aligned} \tag{4.7}$$

where $x_1 = 0.065[m]$, $x_2 = -0.065[m]$, $x_3 = -0.065[m]$, $x_G = -0.036[m]$, $y_1 = 0[m]$, $y_2 = 0.075[m]$, $y_3 = -0.075[m]$ e $y_G = 0.0225[m]$ represent the coordinates of the points defined in figure 4.14.

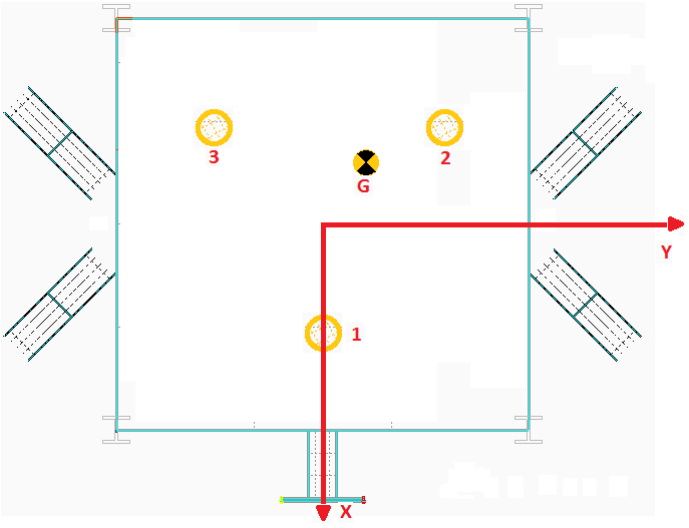

Figure 4.14: Airbearings and center of mass coordinates

The resulted redistribution of weight force is: $F_1/g = 3.94[kg]$, $F_2/g = 9.54[kg]$ e $F_3/g = 4.24[kg]$.
Despite bearing 2 is more loaded than the others, it will never touch the table: as explained in paragraph 4.1.3, with a 4 [atm] supply pressure the bearing can raise 22

[kg] mass up to 0.013 mm. Then even if all the flyer weight shifts on one of them there wouldn't be contact with the crystal.

Chapter 5

The Autonomous Docking Simulator

5.1 Simulator objectives

In the following the implemented software simulator is presented. The simulator is a powerful tool to design and check for the control chain before setting it with the hardware in the loop on the vehicles. Therefore three fundamental steps are needed to its finalization:

- the correct hardware modeling: sensors for navigation and actuators for control
- the vehicles dynamic modeling: each of the acting forces must be defined and modeled
- the guidance definition as a fundamental step for the control law synthesis

The guidance profile will directly be defined by the orbital proximity maneuvers the testbed is devoted to simulate. The planar motion dynamics of the target and the chaser for the final docking phase, a video-based measurement system and feasible position and attitude estimation and control schemes will be described and the simulation results of the study will be presented in the following chapter.
Three different control schemes (PD, LQR and NonLinear Control) are analyzed for the final docking phase control and a Kalman filter is exploited to filter and propagate the video-based measurements. The desired trajectory of the target is obtained by a PD controller. The perturbation forces due to the space environment are considered and appropriately scaled for experimental simulation. The control chains for both vehicles are reported in A.1 and A.2 The simulations described in the following section refer to scaled orbital manoeuvres which involve:

- a Lambert transfer from the chaser parking orbit to the target one;
- sighting, approach and final docking manoeuvre.

Furthermore, two conditions occurring in final approach will be discussed and simulation results are reported in the following section. After the sighting, when the chaser

starts with the approach and the Target flyer has its body between the chaser and the target plate, the chaser must turn around the target (condition 2) otherwise the Smart Flyer can align itself with the target and complete the final docking manoeuvre (condition 1): figure 5.1.

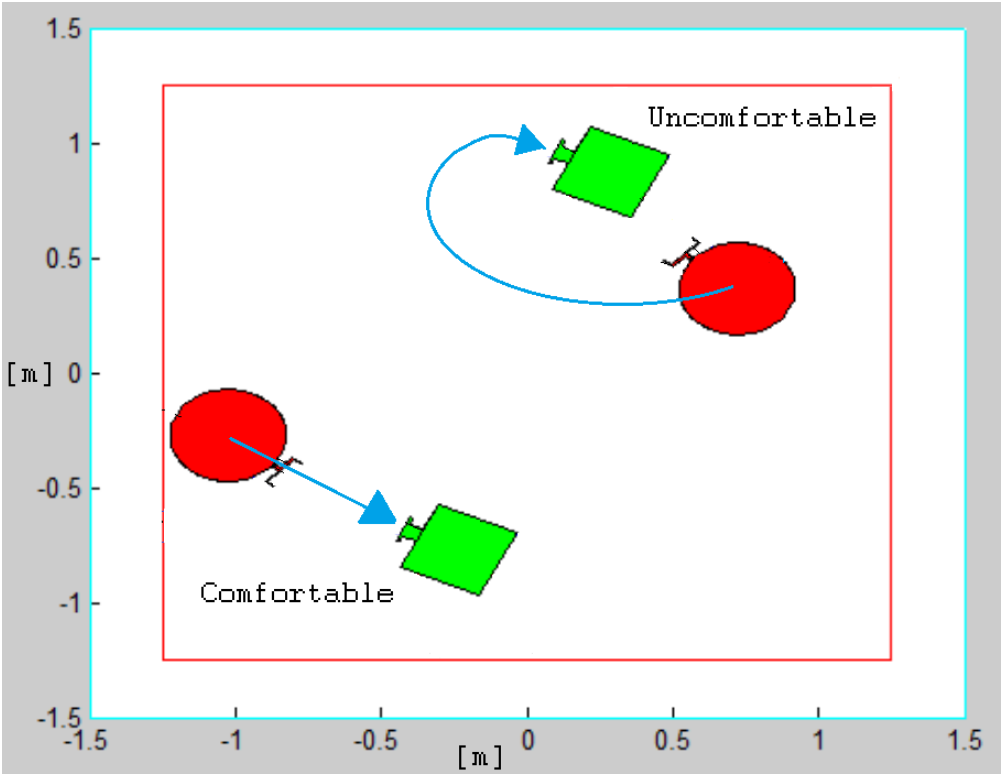

Figure 5.1: Comfortable and Uncomfortable manoeuvre

5.2 Parameters and initial conditions

The developed software simulator is tested according to the following input data. Therefore each of the simulations run refer to those parameters.

	Target Flyer		Smart Flyer	
	Real	**Scaled**	**Real**	**Scaled**
Simulation Parameters				
T_f	1200 $[s]$			
δt	0.1 $[s]$			
Inertial Parameters				
$Mass$	500 $[kg]$	10 $[kg]$	800 $[kg]$	16 $[kg]$
I_x	4 $[kg\ m^2]$	–	4 $[kg\ m^2]$	–
I_y	3.5 $[kg\ m^2]$	–	3.5 $[kg\ m^2]$	–
I_z	–	0.5 $[kg\ m^2]$	–	0.5 $[kg\ m^2]$
Ballistic Parameters				
$Area$	1 $[m^2]$	–	1 $[m^2]$	–
C_D	2	–	2	–
Optical Parameters				
c_d	0.6	–	0.6	–
c_s	0.2	–	0.2	–
Electromagnetic Parameters				
m_{rx}	0.05	–	0.5	–
m_{ry}	0.05	–	0.5	–

Table 5.1: Parameters and initial conditions

5.2.1 Comfortable manoeuvre

During *comfortable* docking manoeuvre the SF doesn't need to go beyond TF to grasp target plate (see figure 5.1). Table 5.2 shows the orbital parameter used in numerical simulation.

	Target Flyer	Smart Flyer
Orbital Parameters		
Ω	50 [deg]	
i	30 [deg]	
a	38000 $[km]$	10000 $[km]$
e	0.1	0.26
ω	30 [deg]	60 [deg]
ν	180 [deg]	45 [deg]
Initial Attitude		
α	90 [deg]	180 [deg]
$\dot{\alpha}$	0.3 [deg/s]	0 [deg/s]

Table 5.2: Orbital parameters: comfortable simulation

5.2.2 Uncomfortable manoeuvre

During "uncomfortable" docking manoeuvre the SF must go beyond TF to join to target plate (see figure 5.1). Table 5.3 shows the orbital parameter used in numerical simulation.

	Target Flyer	**Smart Flyer**
Orbital Parameters		
Ω	10 [deg]	
i	20 [deg]	
a	20000 $[km]$	16000 $[km]$
e	0.25	0.55
ω	30 [deg]	90 [deg]
ν	60 [deg]	270 [deg]
Initial Attitude		
α	180 [deg]	90 [deg]
$\dot{\alpha}$	0.3 [deg/s]	0 [deg/s]

Table 5.3: Orbital parameters: uncomfortable simulation

5.3 Reference systems

In the simulation the motion of two floating bodies on a low friction table is emulated. For this reason, it is useful to define some reference frames which will be described in details in the following sections.

5.3.1 The Target Flyer reference frame

As shown in figure 5.2, Target flyer reference frame has its origin coincident with the center of gravity of TF and the x axis direct as the passive plate for docking, the z axis normal to the table and the y-axis to form a right-handed reference. The attitude angle of the Target flyer α_{TF} is defined as the counterclockwise angle between the axis X of the table and X-axis of the flyer.

In figure 5.2 the fans (actuators) numeration is also reported. The lateral sides are also numbered counterclockwise from the face normal to X axes of the flyer.

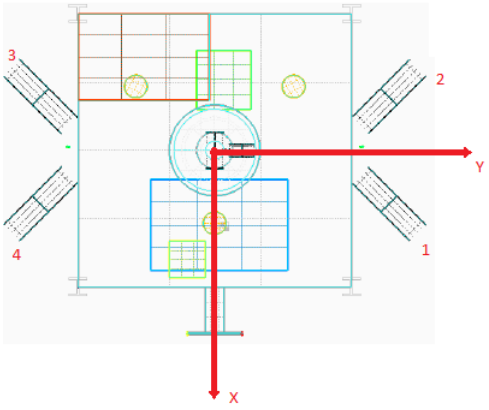

Figure 5.2: TF reference system

5.3.2 The Smart Flyer reference frame

Likewise to the TF choice, the SF reference frame is centered on the SF center of mass, with the x-axis directed as the plier for the docking[1]. The attitude angle of Smart Flyer α_{SF} is defined as the counterclockwise angle between the table X axis and the X-axis of the flyer.

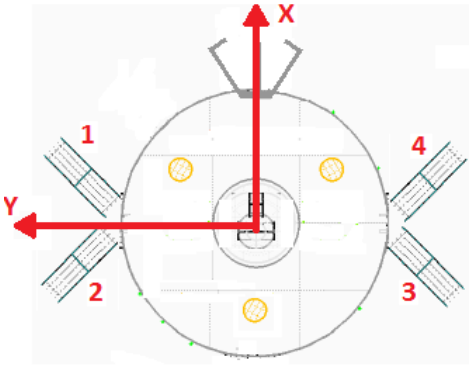

Figure 5.3: SF reference system

5.3.3 The Inertial reference frame

It is possible to define also a reference system fixed with the table whose origin coincides with the center of the crystal as shown in figure 5.4. As reported in figure 5.3, table plane coincides with the orbital plane and the axis X_{TABLE} coincides with the direction of the ascending nodes so that for each simulation the right ascension of the ascending node (Ω) and the argument of perigee orbit (ω) are uniquely defined. .

[1]Direction which also coincides with the pointing direction of the camera.

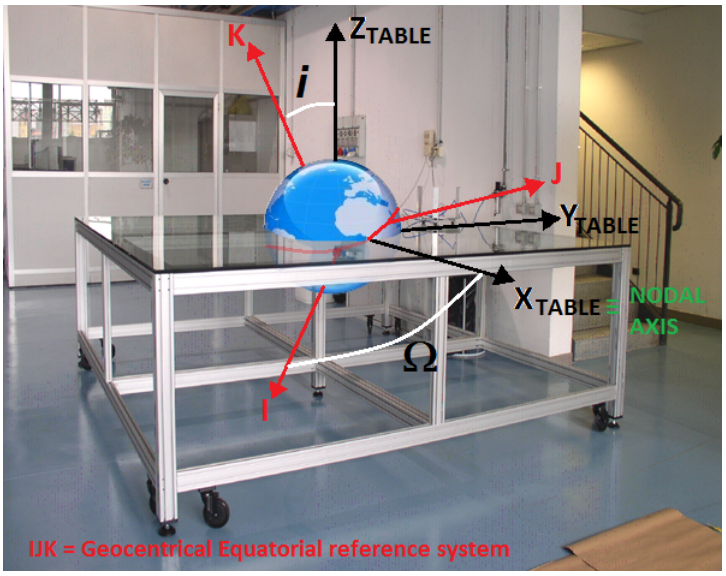

Figure 5.4: Inertial reference systems

5.3.4 Perifocal and Local orbital reference frame

Figure 5.5 highlights the perifocal PQW and the local RTN reference frames in order to match the real problem orbital parameters meaning into the laboratory environment.

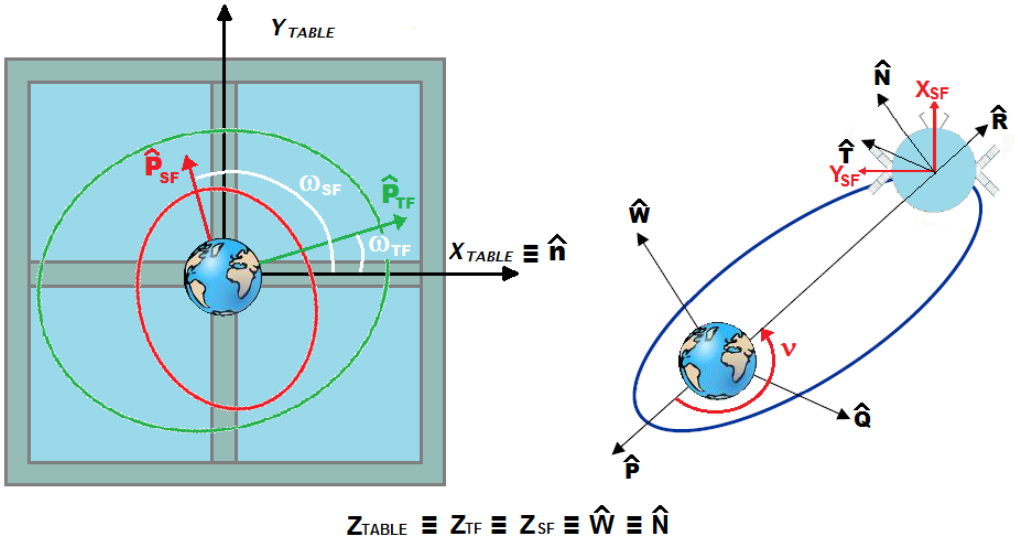

Figure 5.5: Perifocal and Local orbital reference systems

5.3.5 The Rotation matrix

Finally, the rotation matrices to transform any vector from a reference system to another are here reported:

$$\begin{aligned} a_{RTN} &= A_\nu a_{PQW} = A_\nu A_\omega a_{TABLE} = A_\nu A_\omega A_i A_\Omega a_{IJK} \\ a_{SF} &= A_{\alpha_{SF}} a_{TABLE} \\ a_{TF} &= A_{\alpha_{TF}} a_{TABLE} \end{aligned} \tag{5.1}$$

$$\text{where } A_\nu = \begin{bmatrix} cos(\nu) & sin(\nu) & 0 \\ -sin(\nu) & cos(\nu) & 0 \\ 0 & 0 & 1 \end{bmatrix} A_\omega = \begin{bmatrix} cos(\omega) & sin(\omega) & 0 \\ -sin(\omega) & cos(\omega) & 0 \\ 0 & 0 & 1 \end{bmatrix}$$

$$A_i = \begin{bmatrix} 1 & 0 & 0 \\ 0 & cos(i) & sin(i) \\ 0 & -sin(i) & cos(i) \end{bmatrix} A_\Omega = \begin{bmatrix} cos(\Omega) & sin(\Omega) & 0 \\ -sin(\Omega) & cos(\Omega) & 0 \\ 0 & 0 & 1 \end{bmatrix}$$

$$A_{\alpha_{SF}} = \begin{bmatrix} cos(\alpha_{SF}) & sin(\alpha_{SF}) & 0 \\ -sin(\alpha_{SF}) & cos(\alpha_{SF}) & 0 \\ 0 & 0 & 1 \end{bmatrix} A_{\alpha_{TF}} = \begin{bmatrix} cos(\alpha_{TF}) & sin(\alpha_{TF}) & 0 \\ -sin(\alpha_{TF}) & cos(\alpha_{TF}) & 0 \\ 0 & 0 & 1 \end{bmatrix}$$

5.4 Orbital Mechanic simulation

5.4.1 Scaling problem

One of the purpose of the ADS simulator is to reproduce the orbital motion from parking orbit of the chaser satellite to the target orbit, with only the assumption that they belong to the same orbital plane [2].

This requirements open a scaling necessity to make the orbit motion feasible on the experimental glass table. This subsection describes the choice of the scale variables and how the quantities vary accordingly to them. It is clear that the aim of representing the orbital motion, entails that the only quantities to scale are: time, length and mass. The scaling constants f, g, h can not be chosen arbitrarily because the scaled values must be reproduced in the laboratory and can not even be determined uniquely, because they will vary depending on the problem that will be simulated.

In any case, the scaling process always follows the same automated procedure that involves the following steps:

1. Determination of the space constant so that the apogee of the Target flyer is set to 1.15 [m] from the center of the table [3]. The problem cannot be scalable if the scaled periapsis radius of SF is less than 20$[cm]$ because it make difficult the motion of the chaser in such a small space.

$$f = 1.15/r_{A\ TF} \tag{5.2}$$

[2] This assumption does not damage the generality of the problem because is usually responsibility of the launcher to leave the chaser on the same orbital plane of the target.

[3] Although it is available a 3x3 table $[m]$ is considered a margin of 35$[cm]$ in order to prevent unwanted falls of the robots from the table.

$$f \cdot r_{P\ SF} \geq 0.2\ [m] \tag{5.3}$$

Typically, this condition occurs with TF in geostationary orbit and SF on a parking orbit with periapsis at 600 [km] altitude.

2. Determination of the time constant so that the Smart Flyer, which has speed much greater than the TF does not exceed the safe limit for the experimental test and the power limit of the fans. This is ensured by requiring that the Target flyer during the simulation [4] complete only one orbit. In this way it is determined the g constant and it is verfied that the scaled orbital period of the SF is at least greater than 1 minute.

$$g = T_{simulation}/T_{TF} \tag{5.4}$$

$$g \cdot T_{SF} \geq 60\ [s] \tag{5.5}$$

3. Determination of the mass constant so the mass of the Target flyer ($\approx 13\ [Kg]$) is the scaled mass of the satellite that really must be docked. In this way will lose the possibility to properly represent the mass of the chaser but this affects the satellite motion only for the calculation of the perturbation forces and they can be reasonably computed using the actual mass.ation of the perturbation forces and they can be reasonably computed using the actual mass.

$$h = m_{TF}/m_{real\ TF} \tag{5.6}$$

The table 5.4 shows the orbital parameters of both satellites at the initial time for simulation 1, the steps for the scale process are similar in the simulation 2:

	Target Flyer	**Smart Flyer**
Ω	50 [deg]	
i	30 [deg]	
a	38000 $[km]$	10000 $[km]$
e	0.1	0.36
ω	30 [deg]	60 [deg]
ν	180 [deg]	45 [deg]

Table 5.4: Orbital initial parameters: simulation 1

The scaling constants for the problem in exam is obtained by simple steps:

$$\begin{aligned} f &= 1.15/r_{A\ TF} = 2.73 \cdot 10^{-8} \\ g &= T_{simulation}/T_{TF} = 0.0075 \\ h &= m_{TF}/m_{real\ TF} = 0.026 \end{aligned} \tag{5.7}$$

where is assumed to be 500 [kg] the mass of the satellite to capture. The constraints are obviously respected in fact:

[4] Time that coincide with the duration of the floatation system.

$$\begin{array}{c} f \cdot r_{P\ SF} = 0.201\ > 0.2\ [m] \\ g \cdot T_{SF} = 166\ > 60\ [s] \end{array} \tag{5.8}$$

5.4.2 Smart Flyer transfer orbit

At the begin of the software simulation the propagation of the Target and Smart flyer orbits occurs in order to determine the point at which the SF has to initiate the transfer from its parking orbit to that where it performs the final docking manoeuvres. To this end a porkchop graph is created to search for the minimum ΔV needed to balistically transfer from the SF to the TF positions, the Δt between the start time of the simulation and the moment of departure for SF, and the TOF in transfer orbit; the computation is supported by a Lambert's problem solution [9].
The universal formulation used for the choice of the transfer orbit provides for each value of the starting time t_1 and for each value of TOF the resolution with Newton's method of more nonlinear equations to determine the SF and TF location respectively at the time t_1 and at the time $t_2 = t_1 + TOF$:

$$F(\chi)_{TF} = \chi^3 S + \frac{\underline{r}_{TF}(t_0) \cdot \underline{v}_{TF}(t_0)}{2\sqrt{\mu}}\chi^2 C + |\underline{r}_{TF}(t_0)|\chi(1 - zS) - \sqrt{\mu}(t_2 - t_0) = 0 \tag{5.9}$$

$$F(\chi)_{SF} = \chi^3 S + \frac{\underline{r}_{SF}(t_0) \cdot \underline{v}_{SF}(t_0)}{2\sqrt{\mu}}\chi^2 C + |\underline{r}_{SF}(t_0)|\chi(1 - zS) - \sqrt{\mu}(t_1 - t_0) = 0 \tag{5.10}$$

where t_0 is the moment at the simulator starting time, $z = \alpha\chi^2$ with $\alpha = 1/a$ while

$$C(z) = \frac{1 - cos(\sqrt{z})}{z} \tag{5.11}$$

$$S(z) = \frac{\sqrt{z} - sin\sqrt{z}}{\sqrt{z^3}} \tag{5.12}$$

It was proved that for the equations 5.9 and 5.10 the Newton's method converges for any initial value of χ_0 but this convergence is accelerated if the initial guess coincides with:

$$\chi_0 = \frac{\mu(t - t_0)^2}{r_P[F(\hat{\chi}) + \sqrt{\mu(t - t_0)}]} \tag{5.13}$$

where $\hat{\chi} = \sqrt{\mu(t - t_0)}/r_P$, $t = t_1$ or $t = t_2$ depending on whether the calculation regards TF or SF, lastly r_P is the periapsis radius of the orbit in exam. Founded the χ_{SF} and the χ_{TF} it is possible to determine the position and velocity vector for both satellites knowing that:

$$\begin{array}{c} f = 1 - \frac{\chi^2}{r_0}C(z) \\ g = t - t_0 - \frac{\chi^3}{\sqrt{\mu}}S(z) \end{array} \tag{5.14}$$

$$r = fr_0 + gv_0 \tag{5.15}$$

$$\begin{array}{c} \dot{f} = \frac{\sqrt{\mu}}{r_0 r}\chi[zS(z)-1] \\ \dot{g} = 1 - \frac{\chi^2}{r}C(z) \end{array} \tag{5.16}$$

$$v = \dot{f}r_0 + \dot{g}v_0 \tag{5.17}$$

Now it is possible to determine the transfer orbit solving the Lambert problem again with the universal variables [9].
The first operation is to determine the $\Delta\nu$ between the SF position at time t_1 that of TF at t_2:

$$\begin{array}{c} \underline{h}_{SF}(t_1) = \underline{r}_{SF}(t_1) \wedge \underline{v}_{SF}(t_1) \\ \underline{h}_{TF}(t_2) = \underline{r}_{TF}(t_2) \wedge \underline{v}_{TF}(t_2) \end{array} \tag{5.18}$$

$$\begin{array}{c} \underline{e}_{SF}(t_1) = \frac{\underline{v}_{SF}(t_1)\wedge\underline{h}_{SF}(t_1)}{\mu} - \frac{\underline{r}_{SF}(t_1)}{|\underline{r}_{SF}(t_1)|} \\ \underline{e}_{TF}(t_2) = \frac{\underline{v}_{TF}(t_2)\wedge\underline{h}_{TF}(t_2)}{\mu} - \frac{\underline{r}_{TF}(t_2)}{|\underline{r}_{TF}(t_2)|} \end{array} \tag{5.19}$$

$$\begin{array}{c} \hat{n}_{SF}(t_1) = \frac{\hat{k}\wedge\underline{h}_{SF}(t_1)}{|\hat{k}\wedge\underline{h}_{SF}(t_1)|} \\ \hat{n}_{TF}(t_2) = \frac{\hat{k}\wedge\underline{h}_{TF}(t_2)}{|\hat{k}\wedge\underline{h}_{TF}(t_2)|} \end{array} \tag{5.20}$$

$$\omega_{SF}(t_1) = \begin{cases} arccos\left(\frac{\hat{n}_{SF}(t_1)\cdot\underline{e}_{SF}(t_1)}{|\underline{e}_{SF}(t_1)|}\right) & se \quad \underline{e}_{SF}(t_1)\cdot\hat{k} > 0 \\ 2\pi - arccos\left(\frac{\hat{n}_{SF}(t_1)\cdot\underline{e}_{SF}(t_1)}{|\underline{e}_{SF}(t_1)|}\right) & se \quad \underline{e}_{SF}(t_1)\cdot\hat{k} < 0 \end{cases} \tag{5.21}$$

$$\omega_{TF}(t_2) = \begin{cases} arccos\left(\frac{\hat{n}_{TF}(t_2)\cdot\underline{e}_{TF}(t_2)}{|\underline{e}_{TF}(t_2)|}\right) & se \quad \underline{e}_{TF}(t_2)\cdot\hat{k} > 0 \\ 2\pi - arccos\left(\frac{\hat{n}_{TF}(t_2)\cdot\underline{e}_{TF}(t_2)}{|\underline{e}_{TF}(t_2)|}\right) & se \quad \underline{e}_{TF}(t_2)\cdot\hat{k} < 0 \end{cases} \tag{5.22}$$

$$\nu_{SF}(t_1) = \begin{cases} arccos\left(\frac{\underline{e}_{SF}(t_1)\cdot\underline{r}_{SF}(t_1)}{|\underline{e}_{SF}(t_1)||\underline{r}_{SF}(t_1)|}\right) & se \quad \underline{r}_{SF}(t_1)\cdot\underline{v}_{SF}(t_1) > 0 \\ 2\pi - arccos\left(\frac{\underline{e}_{SF}(t_1)\cdot\underline{r}_{SF}(t_1)}{|\underline{e}_{SF}(t_1)||\underline{r}_{SF}(t_1)|}\right) & se \quad \underline{r}_{SF}(t_1)\cdot\underline{v}_{SF}(t_1) < 0 \end{cases} \tag{5.23}$$

$$\nu_{TF}(t_2) = \begin{cases} arccos\left(\frac{\underline{e}_{TF}(t_2)\cdot\underline{r}_{TF}(t_2)}{|\underline{e}_{TF}(t_2)||\underline{r}_{TF}(t_2)|}\right) & se \quad \underline{r}_{TF}(t_2)\cdot\underline{v}_{TF}(t_2) > 0 \\ 2\pi - arccos\left(\frac{\underline{e}_{TF}(t_2)\cdot\underline{r}_{TF}(t_2)}{|\underline{e}_{TF}(t_2)||\underline{r}_{TF}(t_2)|}\right) & se \quad \underline{r}_{TF}(t_2)\cdot\underline{v}_{TF}(t_2) > 0 \end{cases} \tag{5.24}$$

$$\Delta\nu = \omega_{TF}(t_2) + \nu_{TF}(t_2) - \omega_{SF}(t_1) - \nu_{SF}(t_1) \tag{5.25}$$

The end point for the chaser transfer orbit can't be the actual position of the TF at time t_2 otherwise the collision between the two flyers would be unavoidable. So the radius vector $\underline{r}_{TF}(t_2)$ and the velocity vector $\underline{v}_{TF}(t_2)$ are computed by using an $\underline{r}_{TF}(t_0)$ and a $\underline{v}_{TF}(t_0)$ that are related to a true anomaly of $\nu_{TF}(t_0) - pi/3$, see figure 5.6 and 5.7. In this way it is as if the Target flyer travels with 60 [deg] in advance than the chaser believes: figure 5.6 and 5.7. This expedient will not be present in orbit but serves to prevent that the two vehciles get too close during transfer orbit.

So it's possible to solve the nonlinear equation in order to determine the variable z that uniquely defines the transfer orbit:

$$A = \frac{\sqrt{r_{SF} r_{TF}} sin(\Delta\nu)}{\sqrt{1 - cos(\Delta\nu)}} \tag{5.26}$$

$$y = r_{SF} + r_{TF} + A\frac{zS(z) - 1}{\sqrt{C(z)}} \tag{5.27}$$

$$\chi = \sqrt{\frac{y}{C(z)}} \tag{5.28}$$

$$F(z) = \frac{\chi^3}{\sqrt{\mu}} S(z) + \frac{A\sqrt{y}}{\sqrt{\mu}} - t_2 + t_1 = 0 \tag{5.29}$$

To exploit the Newton's method to solve the former equation, the derivative of $F(z)$ is needed; that can be defined as:

$$F'(z) = \frac{1}{\sqrt{\mu}} \left[\chi^3 \left(S'(z) - \frac{3S(z)C'(z)}{2C(z)} \right) + \frac{A}{8} \left(\frac{3S(z)\sqrt{y}}{C(z)} + \frac{A}{\chi} \right) \right] \tag{5.30}$$

where C (z) and S (z) are computed as shown in 5.11 and 5.12 while

$$\begin{aligned} S'(z) &= \tfrac{C(z) - 3S(z)}{2z} \\ C'(z) &= \tfrac{(1 - zS(z) - 2C(z))}{2z} \end{aligned} \tag{5.31}$$

Obtained the z is updated y through 5.27 and the necessary ΔV is evaluated:

$$\begin{aligned} f &= 1 - \tfrac{y}{r_{SF}(t1)} \\ g &= A\sqrt{\tfrac{y}{\mu}} \\ \dot{g} &= 1 - \tfrac{y}{r_{TF}(t2)} \\ \dot{f} &= \tfrac{-f\dot{g}+1}{g} \end{aligned} \tag{5.32}$$

$$\begin{aligned} \underline{v}(t_1) &= \tfrac{1}{g}(\underline{r}_{TF}(t_2) - f\underline{r}_{SF}(t_1)) \\ \underline{v}(t_2) &= \dot{f}\underline{r}_{SF}(t_1) + \dot{g}\underline{v}_{SF}(t_1)) \end{aligned} \tag{5.33}$$

$$\begin{aligned} \underline{\Delta v}(t_1) &= \underline{v}(t_1) - \underline{v}_{SF}(t_1) \\ \underline{\Delta v}(t_2) &= \underline{v}_{TF}(t_2) - \underline{v}(t_2) \end{aligned} \tag{5.34}$$

$$\begin{aligned} \Delta v_{TOT} = &\sqrt{|\underline{v}(t_1)|^2 + |\underline{v}_{SF}(t_1)|^2 - 2v(t_1)v_{SF}(t_1)cos(\gamma_1)} + \\ &+ \sqrt{|\underline{v}(t_2)|^2 + |\underline{v}_{TF}(t_2)|^2 - 2v(t_2)v_{TF}(t_2)cos(\gamma_2)} \end{aligned} \tag{5.35}$$

where γ_1 and γ_2 are the angles between the $\underline{v}(t_1)$ and $\underline{v}_{SF}(t_1)$ and between $\underline{v}_{TF}(t_2)$ and $\underline{v}(t_2)$ respectively.

Figures 5.6 and 5.7 show the parking and transfer orbits, while 5.8 and 5.9 depitch the evolution of ΔV versus time of departure and time of transfer for both simulations.

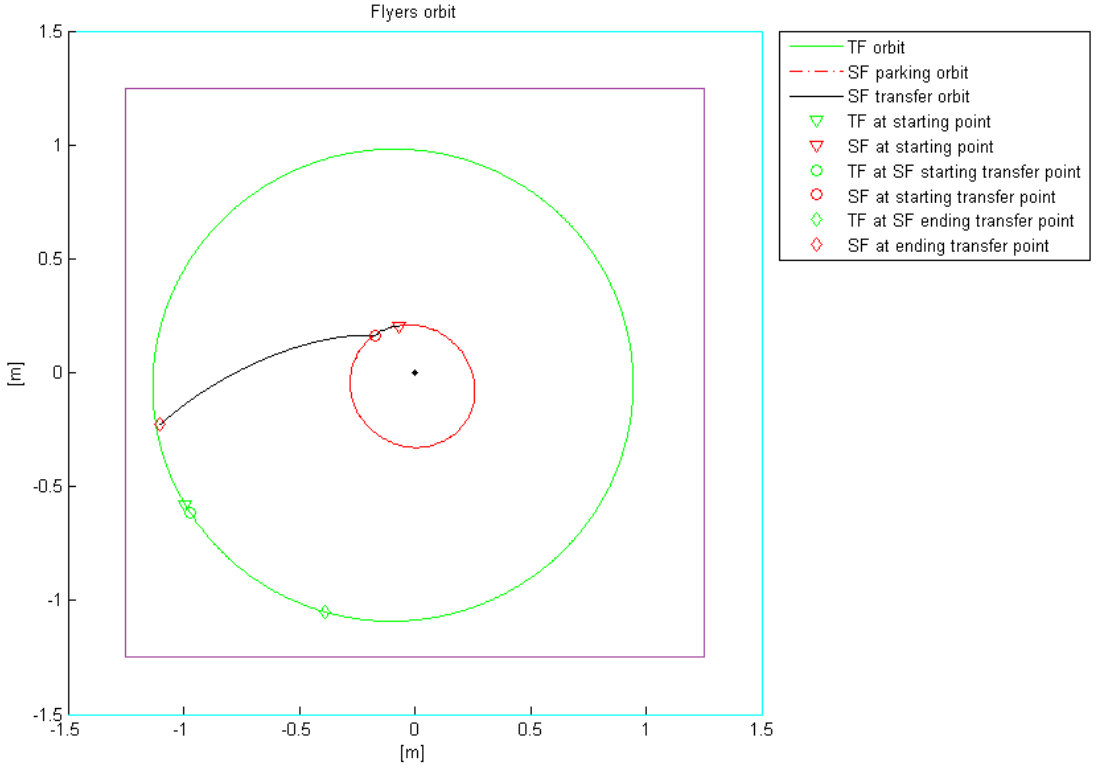

Figure 5.6: SF parking orbit and TF operative orbit: Simulation 1

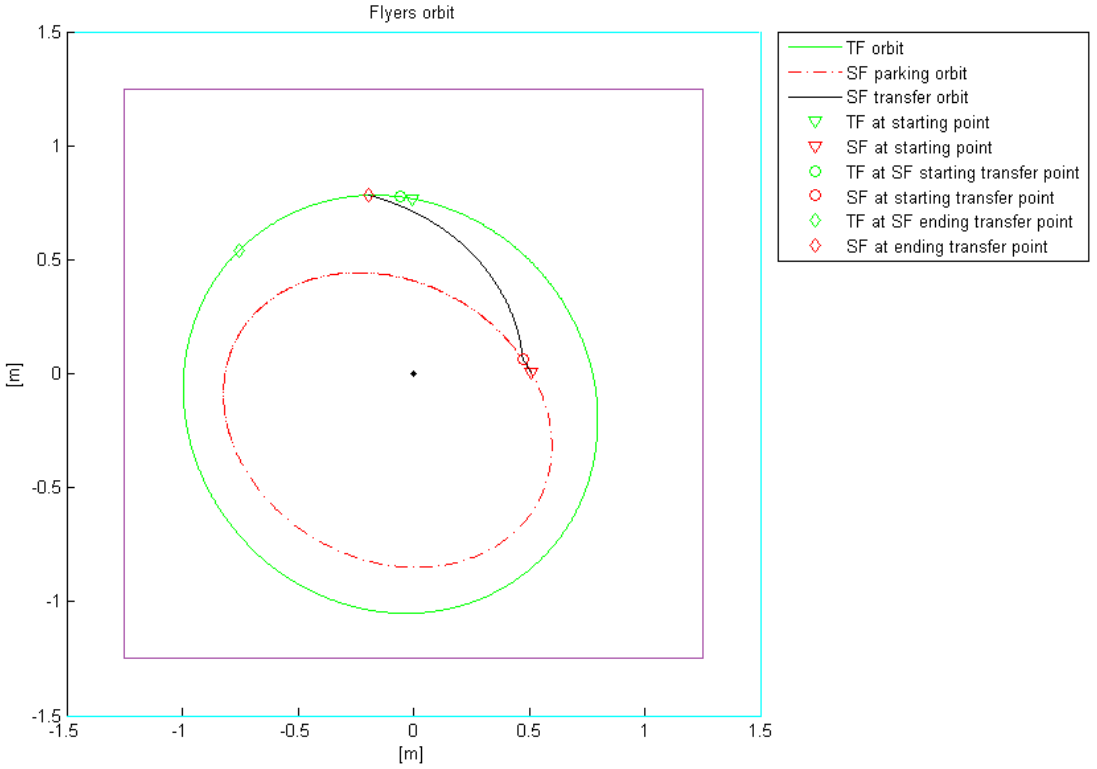

Figure 5.7: SF parking orbit and TF operative orbit: Simulation 2

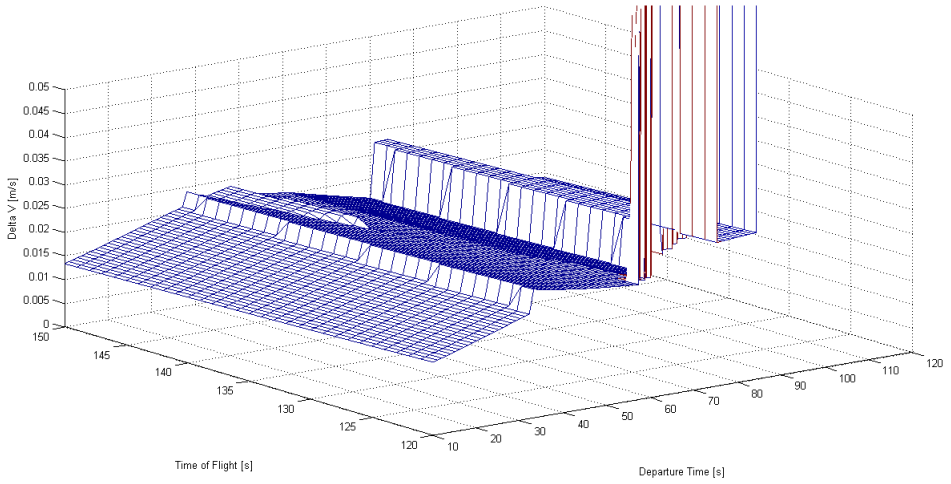

Figure 5.8: Transfer orbit porkchop: Simulation 1

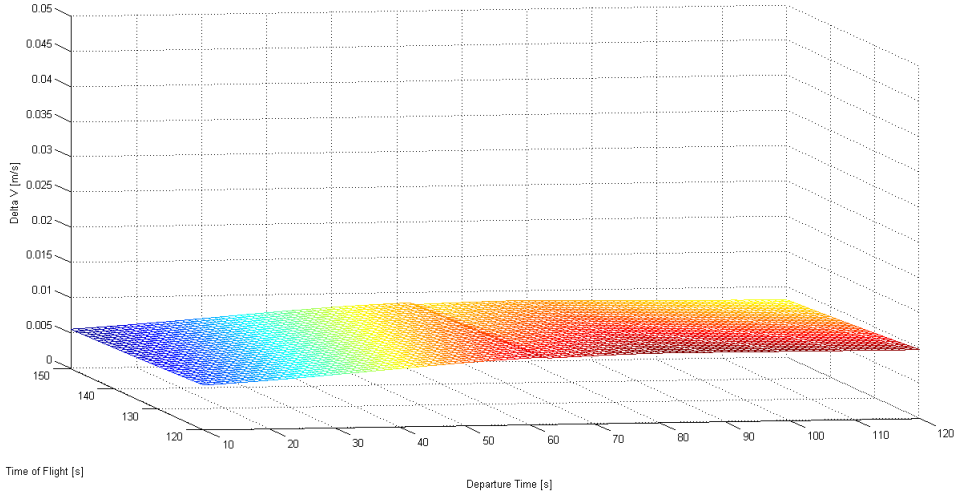

Figure 5.9: Transfer orbit porkchop: Simulation 2

5.4.3 Orbital parameters disturbance

A satellite in orbit around the Earth experiences small perturbations of its keplerian orbit, such as acceleration due to the irregular distribution of the planetary mass, due to atmospheric drag and solar pressure and other massive disturbing neraby and far bodies. Each of these perturbations is sufficient to cause significant errors on the prediction of satellite position based on the assumption of Keplerian orbit.
The perturbation forces here included in the model considered are limited to their in-plane components as the frictionless table cannot transmit the vehicle actions normal to the table itself. The effect of this limitation has repercussions on the right ascension of the ascending node and on the inclination of the orbital plane that remain constant. Therefore the matrices A_i and A_Ω described in subsection 5.3.5 can be evaluated only once for the entire simulation while the other must be updated at every step.
Another consideration is that given the large number of variables involved in the forces and torques computation[5] to scale all size involved in a meaningful way turns out to be unprofitable; therefore $\underline{r}$ and $\underline{v}$ are reported to the real dimension, to compute the actual forces and torques and just afterwards the scaling mechanism is applied taking advantage of f, g and h previously computed 5.4.1. Thus the breadth of these perturbation is coherent with the laboratory facility.

Atmospheric drag perturbation

These perturbation effects are significant for satellites in low orbit. The disturbance acceleration can be easily computed by:

$$\begin{aligned} F_T &= -Dcos(\gamma) \\ F_R &= -Dsin(\gamma) \end{aligned} \tag{5.36}$$

Remembering that D is the aerodynamic drag always directed in the opposite direction of the velocity vector while γ is the flight path angle:

$$D = \frac{1}{2m}\rho A|\underline{v}|^2 C_D \tag{5.37}$$

while $sin(\gamma) = \frac{esin(\nu)}{\sqrt{1+e^2+2ecos(\nu)}}$ and $cos(\gamma) = \frac{1+ecos(\nu)}{\sqrt{1+e^2+2ecos(\nu)}}$.
Atmospheric density is modeled with the classic exponential model:

$$\rho = \rho_0 e^{-\left(\frac{h-h_0}{H}\right)} \tag{5.38}$$

where ρ_0, h_0 and H are tabulated depending on the height h [9].

Irregular mass distribution: the J2 effect

The asphericity of Earth effects are here limited to the contribution of the first zonal armonics J2 in the the Earth's gravitational potential [1].

[5] The perturbation caused by magnetic field or the calculation of the Sun position is considered using the Julian date.

$$\begin{aligned} F_T &= -\mu J_2 R^2 \tfrac{3}{r^4} sin^2(i) sin(u) cos(u) \\ F_R &= -\mu J_2 R^2 \tfrac{3}{r^4} \left(\tfrac{1}{2} - \tfrac{3}{2} sin^2(i) sin^2(u)\right) \end{aligned} \tag{5.39}$$

where $J_2 \approx 1082.63 \cdot 10^{-6}$, R is the Earth's equatorial radius, $u = \omega + \nu$ at current location of the satellite and i is the (constant) inclination of the orbital plane.

Solar pressure perturbation

A real pressure is generated by the solar photons impact on the surface of the satellite, and its value is:

$$P_{sr} = \frac{\varphi_{sr}}{c} \tag{5.40}$$

where $\varphi_{sr} = 1367.6\ [W/m^2]$ is the solar flux while $c = 3 \cdot 10^8 [m/s]$ is the light speed. Obviously, this pressure acts only when the satellite is in sunlight, and then it depends on the relative position of the sun at the current time.
The disturbance acceleration is given by:

$$\underline{a}_{ps} = -P_{sr} C_r \frac{A}{m} \frac{\underline{r}_\odot - SAT}{|\underline{r}_\odot - SAT|} \tag{5.41}$$

where $C_r = 1 + \beta$ is the spacecraft reflectivity and it is always between 0 and 2. In case of the satellite is exposed to the solar lights the pressure will be decomposed into the radial and transverse direction:

$$\left\{ \begin{array}{c} F_R \\ F_T \\ 0 \end{array} \right\} = A_\nu T\left(i, \Omega, \omega\right)^T \underline{a}_{ps} \tag{5.42}$$

with A_ν presented in 5.3.5, while $T\left(i, \Omega, \omega\right)^T$ is the same as in equation 5.57 and 5.58. The next pictures show the radial and transverse forces that acts during both simulations:

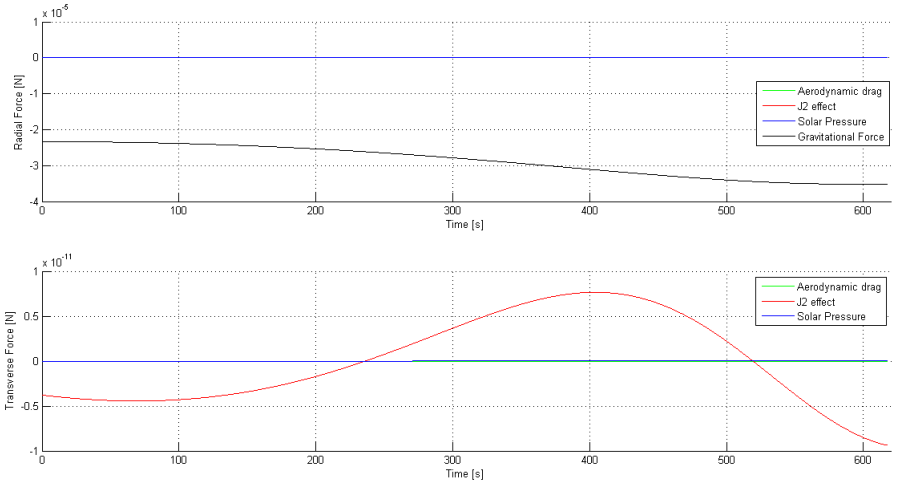

Figure 5.10: Scaled perturbation forces: TF - Simulation 1 - Controller PD

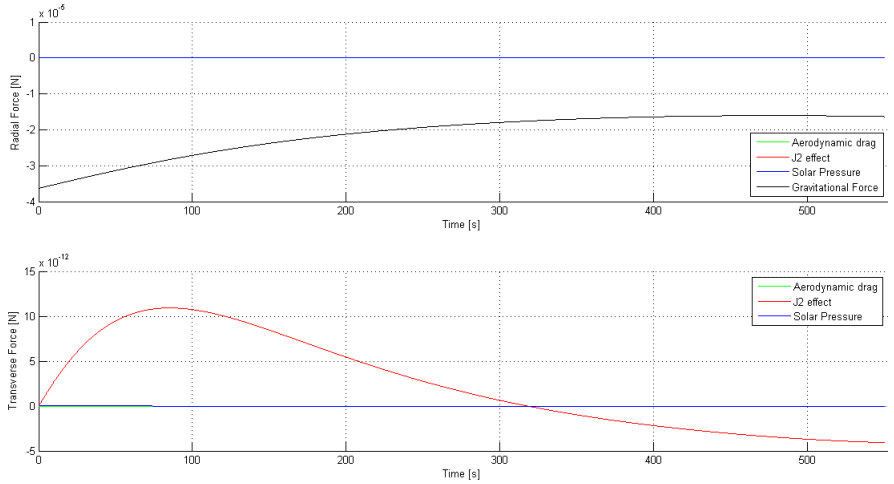

Figure 5.11: Scaled perturbative forces: TF - Simulation 2 - Controller PD

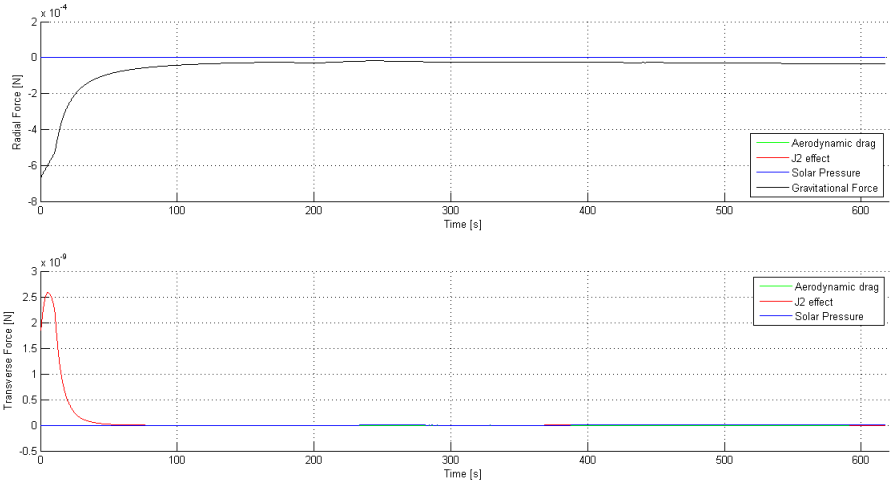

Figure 5.12: Scaled perturbative forces: SF - Simulation 1 - Controller PD

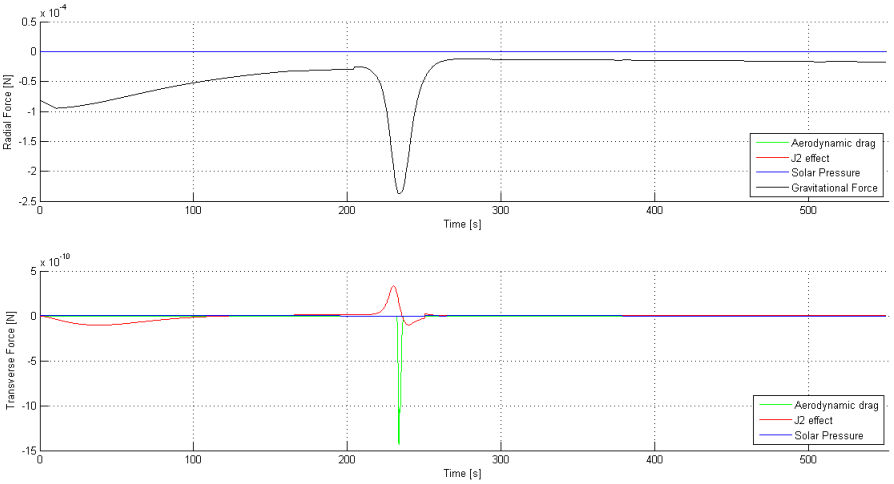

Figure 5.13: Scaled perturbative forces: SF - Simulation 2 - Controller PD

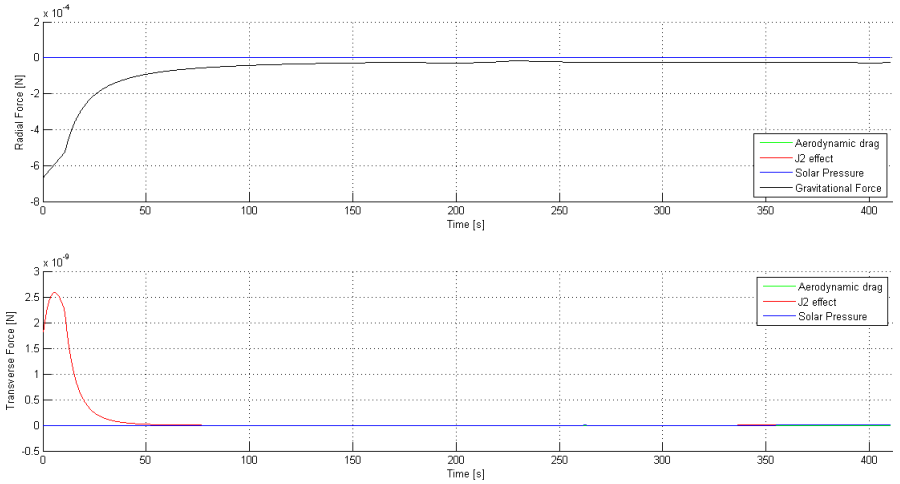

Figure 5.14: Scaled perturbative forces: SF - Simulation 1 - Controller LQR

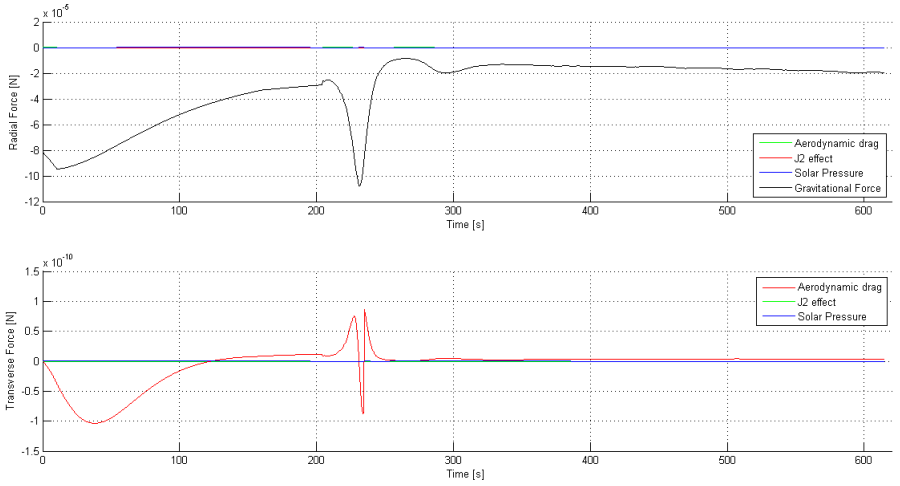

Figure 5.15: Scaled perturbative forces: SF - Simulation 2 - Controller LQR

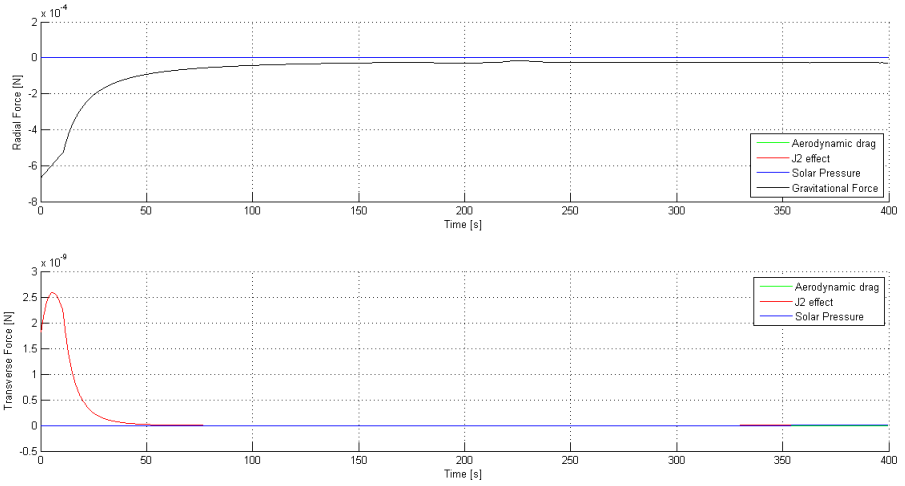

Figure 5.16: Scaled perturbative forces: SF - Simulation 1 - Controller NL

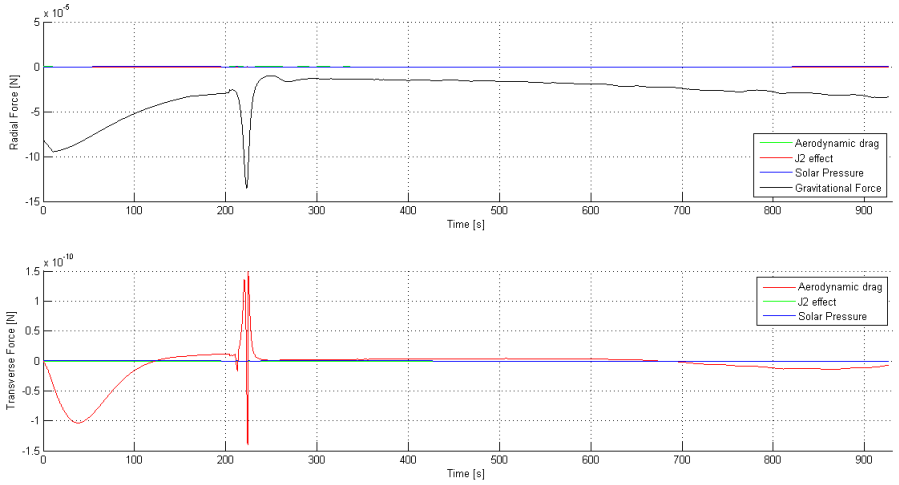

Figure 5.17: Scaled perturbative forces: SF - Simulation 2 - Controller NL

Concerning the radial direction, it's obvious that the gravitational force results greater than the other perturbative forces. As for the trasverse force the J2 effect results important in simulation 1, but in simulation 2 the atmospheric drag become the gratest. This happens because in the docking phase during the alignment with the TF, the chaser has to perform maneuvers that led it to approach the center of the table, leading it even at lower altitude than its parking orbit. At least it could also get to lower altitudes than the Earth's radius, causing the birth of senseless gravitational and aerodynamic forces, see figures 5.13,5.15 and 5.17.

5.4.4 Perturbation torques

The motion of a satellite around its center of mass is triggered by different perturbation torques whose size is specified in the following paragraphs. To the scope of this work the only torque of interest is around the Z axis of the satellite that is coincident as can be seen from section 5.3.5 with Z axis of the table [5].

The gravity gradient perturbation

The gravitational torque exists because of the presence of the various onboard elements that are at different distances from the center of the earth and are therefore subject to gravity forces differently directed.
Given the satellite position in geocentric equatorial reference $\underline{r}$ it's possible to determine the torque due to gravity gradient:

$$\left\{ \begin{array}{c} C_1 \\ C_2 \\ C_3 \end{array} \right\} = A_\alpha A_\omega^T T\left(i, \Omega, \omega\right) \frac{\underline{r}}{|\underline{r}|} \tag{5.43}$$

$$T_g = \frac{3\mu}{|\underline{r}|^3} \left(I_y - I_x\right) C_1 C_2 \tag{5.44}$$

The magnetic field perturbation

The Earth's magnetic field can be presented schematically at the first order as generated by a magnetic dipole whose axis is tilted of 11.5 [deg] respect to the Earth rotation axis.

$$T_m = \underline{m} \wedge \underline{B} \tag{5.45}$$

where $\underline{m}$ is the magnetic induction due to residual currents on the satellite, while $\underline{B}$ is the intensity of the magnetic field at a generic point P and is proportional to $R^3 H_0/|\underline{r}|^3$ with $\underline{r}$ distance to P from the center of the Earth, while $H_0 = \sqrt{(g_1^0)^2 + (g_1^1)^2 + (h_1^1)^2}$ is the intensity of magnetic dipole computed with g_1^0, g_1^0, h_1^1 which are tabulated in the IGRF of the current year, instead R is the Earth's equatorial radius.

$$\underline{B} = \frac{R^3 H_0}{\underline{r}^3} \left[3\left(\underline{\hat{m}} \cdot \underline{\hat{r}}\right) \underline{\hat{r}} - \underline{\hat{m}}\right] \tag{5.46}$$

By defining the right ascension of the Earth $\alpha_m = \alpha_{G0} + \frac{d\alpha_G}{dt}(t - t_0) + \varphi_m$, where α_{G0} is the right ascension of Greenwich at time t_0, $\frac{d\alpha_G}{dt}$ the Earth's rotation speed and the dipole orientation with

$$\vartheta_m = arccos\left(\frac{g_1^0}{H_0}\right) \tag{5.47}$$

$$\varphi_m = arctan\left(\frac{h_1^1}{g_1^1}\right) \tag{5.48}$$

The local direction $\hat{m}$ can be obtained:

$$\hat{m} = \left\{ \begin{array}{c} sin(\vartheta_m)cos(\alpha_m) \\ sin(\vartheta_m)sin(\alpha_m) \\ cos(\vartheta_m) \end{array} \right\} \tag{5.49}$$

The atmospheric drag perturbation

The interaction between the spacecraft and the atmosphere generates an aerodynamic forces on the satellite. This forces that generate a torque around the center of mass is not negligible under 700[km] altitude.

$$T_d = \sum \underline{r}_{Li} \wedge F_{ai} \tag{5.50}$$

This equation is valid only for those sides for which $\underline{N_i} \cdot \underline{v} > 0$ where $underline(v)$ is the velocity vector while:

$$\underline{\underline{N}} = A_\alpha \begin{bmatrix} 1 & 0 & -1 & 0 \\ 0 & 1 & 0 & -1 \\ 0 & 0 & 0 & 0 \end{bmatrix} \tag{5.51}$$

Therefore setting $[\underline{r}_{L1}, \underline{r}_{L2}, \underline{r}_{L3}, \underline{r}_{L4}] = L_c \underline{\underline{N}}$ where L_c is the distance from the center of mass to the geometric center of the generic face and the force F_{ai} which depends on the drag coefficient C_D, on the air density computed once again with the exponential model (see 5.38), on the speed of flight and in addition on the area of i-th face.

$$F_{ai} = \frac{1}{2} C_D \rho |\underline{v}|^2 \left(\underline{N_i} \cdot \underline{v}\right) \underline{\hat{v}} A_i \tag{5.52}$$

So the disturbance torque due to 5.50 is known..

5.4.5 The solar pressure perturbation

Some faces of the satellite may be in shadow because they are opposite to the sides directly irradiated by sunlight, others may be only partially illuminated, so this contributes to the birth of a torque who instantaneously depend on the satellite attitude and on the relative position of the sun.

$$T_s = \sum \underline{r}_{Li} \wedge \underline{F_{si}} \tag{5.53}$$

where the force F_{si} can be computed from the knowledge of unit vectors $\hat{S}$ and $\hat{N}_i$, representing the satellite-Sun direction and the direction normal to the i-th face respectively.

$$F_{si} = -A_i P_{sr} \left[(1 - c_s) \hat{S} + 2 \left(c_s cos(\vartheta_i) + \frac{1}{3} c_d \right) \hat{N}_i \right] cos(\vartheta_i) \tag{5.54}$$

were $\vartheta_i = arccos(\underline{\hat{S}} \cdot \underline{\hat{N}_i})$

The atmospheric and Earth radiation perturbations

A satellite orbiting around the earth can be in solar eclipse but will never be saved from terrestrial and atmospheric radiation. The method of calculating the forces is quite similar to the previous while the value of radiation pressure of Earth P_{er} and atmospheric P_{ar} depend on the satellite altitude.

$$F_{si} = -A_i \left(P_{er} + P_{ar}\right) \left[\left(1 - c_s\right) \underline{\hat{S}_e} + 2 \left(c_s cos(\vartheta_i) + \frac{1}{3} c_d\right) \underline{\hat{N}_i}\right] cos(\vartheta_i) \tag{5.55}$$

The unit vector $\hat{S}_e$ indicates the direction of satellite-Earth, while c_s and c_d are defined in table 5.1.
In the following figures the computed perturbation torques are presented.

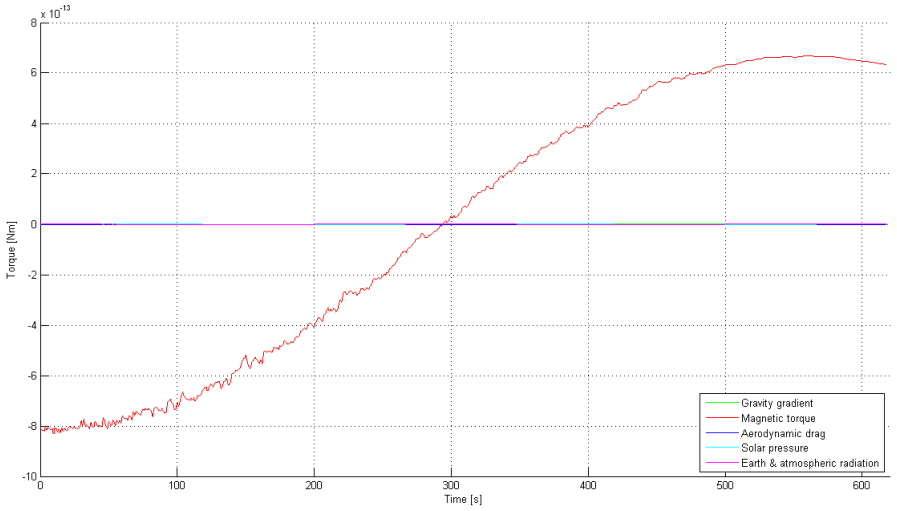

Figure 5.18: Scaled perturbative torques: TF - Simulation 1 - Controller PD

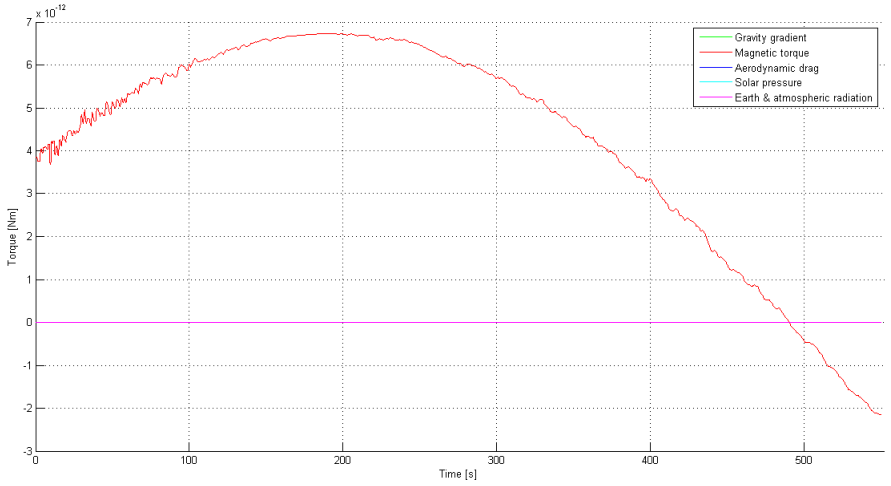

Figure 5.19: Scaled perturbative torques: TF - Simulation 2 - Controller PD

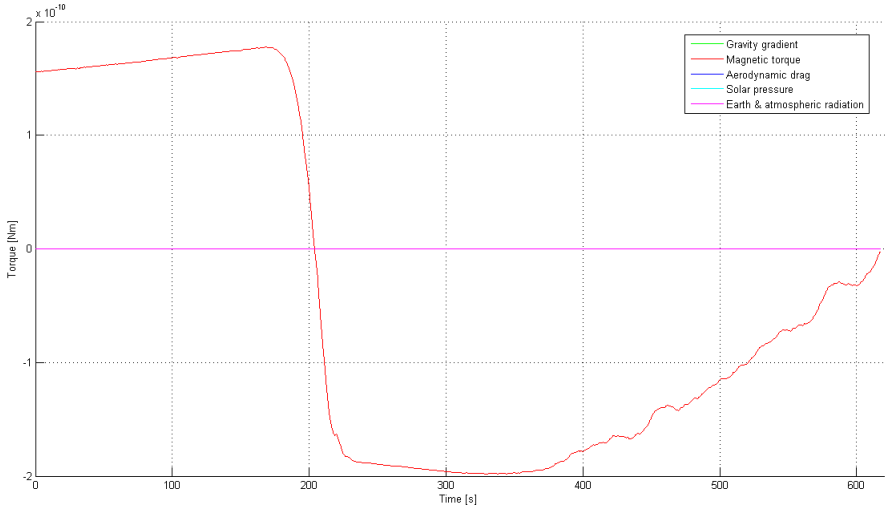

Figure 5.20: Scaled perturbative torques: SF - Simulation 1 - Controller PD

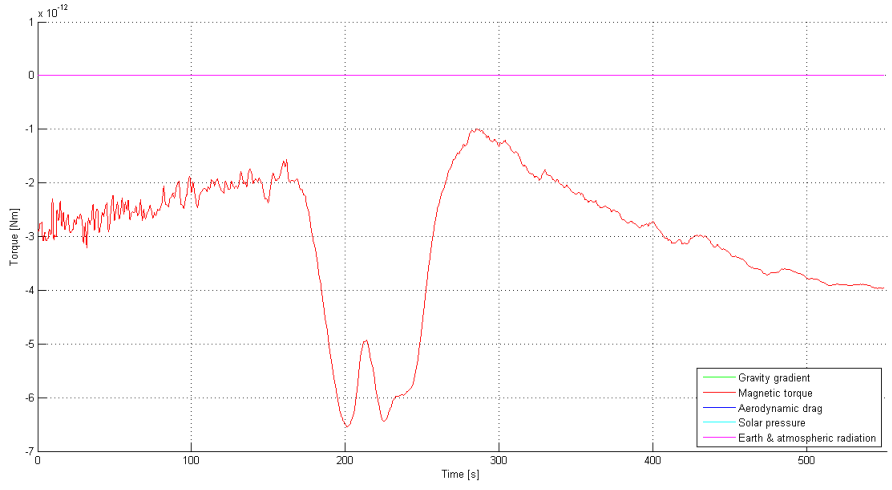

Figure 5.21: Scaled perturbative torques: SF - Simulation 2 - Controller PD

It's possible to see that the scaled perturbative torques are really negligible, despite the magnetic field perturbation is an order of magnitude greater than other disturbances.

5.4.6 Orbits propagation

The position of both satellites in geocentric equatorial reference system can be obtained by the initial kepelrian parameters. The state of each vehicle can be mapped into te table reference system by exploitng rotation matrices presented in 5.3.5. In particular:

$$p = a(1 - e^2) \tag{5.56}$$

$$\begin{Bmatrix} r_I \\ r_J \\ r_K \end{Bmatrix} = \frac{p}{1 + ecos(\nu)} T\,(i, \Omega, \omega)^T \begin{Bmatrix} cos(\nu) \\ sin(\nu) \\ 0 \end{Bmatrix} \tag{5.57}$$

$$\begin{Bmatrix} v_I \\ v_J \\ v_K \end{Bmatrix} = \sqrt{\frac{\mu}{p}}\, T\,(i, \Omega, \omega)^T \begin{Bmatrix} -sin(\nu) \\ e + cos(\nu) \\ 0 \end{Bmatrix} \tag{5.58}$$

By using s and c respectively on behalf of sin and cos $T\,(i, \Omega, \omega)^T$ matrix can be defined:

$$T\,(i, \Omega, \omega)^T = \begin{bmatrix} c(\Omega)c(\omega) - s(\Omega)s(\omega)c(i) & -c(\Omega)s(\omega) - s(\Omega)c(\omega)c(i) & s(\Omega)s(i) \\ s(\Omega)c(\omega) + c(\Omega)s(\omega)c(i) & -s(\Omega)s(\omega) + c(\Omega)c(\omega)c(i) & -c(\Omega)s(i) \\ s(\omega)c(i) & -c(\omega)s(i) & c(i) \end{bmatrix}.$$

Then in the table reference:

$$\begin{Bmatrix} x_{TABLE} \\ y_{TABLE} \\ 0 \end{Bmatrix} = A_i A_\Omega \begin{Bmatrix} r_I \\ r_J \\ r_K \end{Bmatrix} \tag{5.59}$$

$$\begin{Bmatrix} \dot{x}_{TABLE} \\ \dot{y}_{TABLE} \\ 0 \end{Bmatrix} = A_i A_\Omega \begin{Bmatrix} v_I \\ v_J \\ v_K \end{Bmatrix} \tag{5.60}$$

Both orbits are then propagated by numerical integration of perturbed Keplerian motion. In the followings details on the two different vehicle dynamic histories are offered.

Target Flyer orbit

The motion of the TF is supposed to be affected by the gravitational forces, by the disturbance forces on the orbital parameters[6] and by the perturbation torques on attitude.

$$\begin{Bmatrix} \ddot{r}_I \\ \ddot{r}_J \\ \ddot{r}_K \end{Bmatrix}_{TF} = A_\Omega^T A_i^T A_{\omega_{TF}}^T A_{\nu_{TF}}^T \begin{Bmatrix} -\frac{\mu}{|\underline{r}_{TF}|^2} + F_R \\ F_T \\ 0 \end{Bmatrix}_{TF} \tag{5.61}$$

[6]Note that the forces considered are only the radial and transverse component because in the laboratory facility it's impossible to generate forces normal to the table. The consequence of this restriction, as has been explained in subsection 5.4.3, is to have Ω and i fixed in time.

Smart Flyer orbit

Smart Flyer dynamics experiences the perturbation and gravitational forces too, but, the impulsive forces for the transfer from its own orbit to the TF current position must be added in t_1 and t_2.

$$\left\{ \begin{array}{c} \ddot{r}_I \\ \ddot{r}_J \\ \ddot{r}_K \end{array} \right\}_{SF} = A_\Omega^T A_i^T A_{\omega_{SF}}^T A_{\nu_{SF}}^T \left\{ \begin{array}{c} -\frac{\mu}{|\underline{r}_{SF}|^2} + F_R + F_{R\ \Delta V_1} + F_{R\ \Delta V_2} \\ F_T + F_{T\ \Delta V_1} + F_{T\ \Delta V_2} \\ 0 \end{array} \right\}_{SF} \tag{5.62}$$

5.5 Final Docking phase manoeuvres

After the transfer orbit phase the Smart Flyer starts final rendezvous operations defined *closing* and *final approach*.

5.5.1 The closing phase: Sighting

Within the closing phase, as soon as the first manoeuvre, when the transfer ends, will be a rotation of 360 deg is planned, to look for and catch the TF with the camera on the SF. As reported in 3.11 the camera's field of view is wide (about 70 [deg]) despite that the speed necessary to perform this maneuver is limited by the speed of the onboard software to analyze the acquired images, this to avoid that in the analysis time between two subsequent image TF crosses the camera field of view without be seen. A speed of about 5 [deg/s] would give a calculation time to the PC104+ of 14 [s] and in the worst conditions it assures that the TF catching occurs within a minute from the start of the manoeuvre.

5.5.2 The closing phase: Initial approach

Having the target vehicle tracked the SF starts the approaching where the target point will depend on the relative location and attitude. The angle α_{TF-SF} is firstly defined as the angle between the x-axis of the SF and the x-axis of TF positive counterclockwise, the ϑ angle is also introduced as the angle between the x-axis of SF and the vector that joins target with chaser. Generally it's possible to consider two cases that are represented in figure 5.22.

1. Case 1: $\vartheta - \frac{pi}{2} \leq \alpha_{TF-SF} \leq \vartheta + \frac{pi}{2}$.

   The SF approaches TF from behind and to align with it must turn around it. The target point is then defined as follows:

$$\begin{array}{c} \beta_1 = \alpha_{TF-SF} + 80\frac{\pi}{180} \\ \beta_2 = \alpha_{TF-SF} - 80\frac{\pi}{180} \end{array} \tag{5.63}$$

$$\left\{ \begin{array}{c} x_{error1} \\ y_{error1} \end{array} \right\} = \left\{ \begin{array}{c} x_{TF-SF} \\ y_{TF-SF} \end{array} \right\} + \left[\begin{array}{cc} cos(\beta_1) & -sin(\beta_1) \\ sin(\beta_1) & cos(\beta_1) \end{array} \right] \left\{ \begin{array}{c} 0.6 \\ 0 \end{array} \right\} \tag{5.64}$$

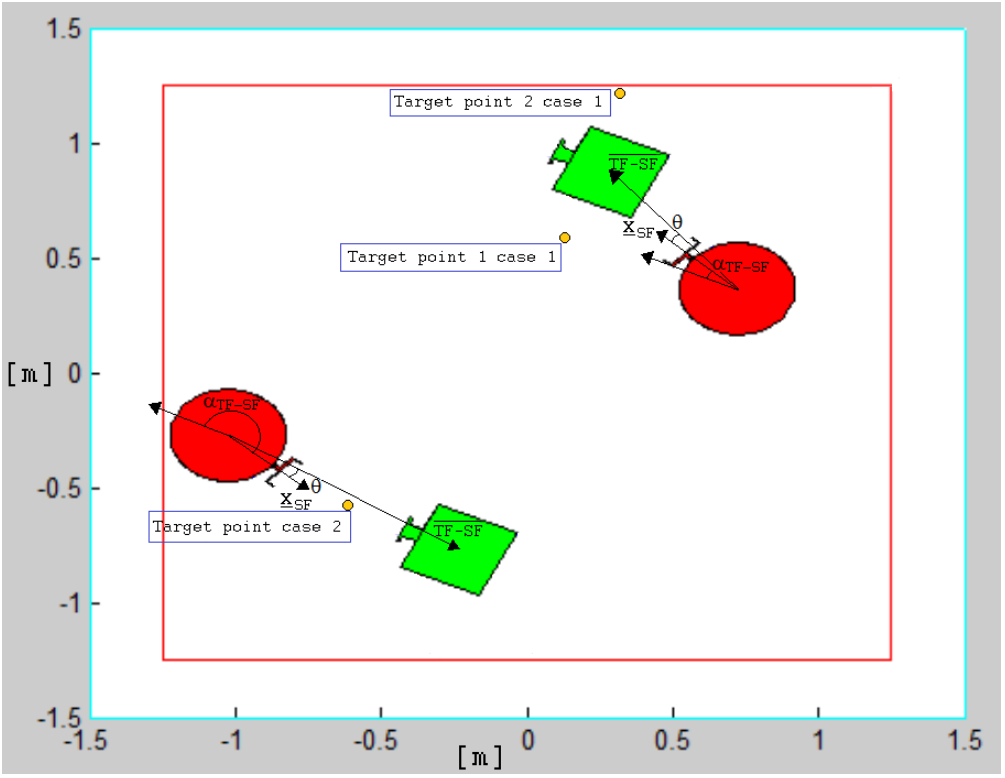

Figure 5.22: Target point choice: TF (green), SF (red)

$$\begin{Bmatrix} x_{error2} \\ y_{error2} \end{Bmatrix} = \begin{Bmatrix} x_{TF-SF} \\ y_{TF-SF} \end{Bmatrix} + \begin{bmatrix} cos(\beta_2) & -sin(\beta_2) \\ sin(\beta_2) & cos(\beta_2) \end{bmatrix} \begin{Bmatrix} 0.6 \\ 0 \end{Bmatrix} \tag{5.65}$$

The solution that will present the smallest $\sqrt{x_{error}^2 + y_{error}^2}$ will correspond to the shortest path to align with the target; referring to figure 5.22 the trajectory point chosen by the software in case 1 is the target point 1.

Note that in order to minimize the collisions risk to pass at a distance between centroids of 60 [cm] has been imposed that is equivalent to a distance of about 15 [cm] between the appendices of the two robots.

2. Caso 2: $\alpha_{TF-SF} > \vartheta + \frac{pi}{2} \vee \alpha_{TF-SF} < \vartheta - \frac{pi}{2}$.

   This case includes all remaining possible relative positions between the DF and the TF: in fact in this condition it's possible to align the flyers without turning around the target.

$$\beta = \alpha_{TF-SF} \tag{5.66}$$

$$\begin{Bmatrix} x_{error} \\ y_{error} \end{Bmatrix} = \begin{Bmatrix} x_{TF-SF} \\ y_{TF-SF} \end{Bmatrix} + \begin{bmatrix} cos(\beta) & -sin(\beta) \\ sin(\beta) & cos(\beta) \end{bmatrix} \begin{Bmatrix} 0.65 \\ 0 \end{Bmatrix} \tag{5.67}$$

The 65[cm] chosen in this case assure a that there would be a distance of 20[cm] between the plier and the target plate, this will be the end point of the approach maneuver and once reached it is possible to pass to the final docking.

The attitude error, is always equal to ϑ, so the chaser looses sight of TF.
A note on the velocity error is required: the speed of the target is not part of the set of measurements, therefore the discrete derivative of the error can be computed; the same is valid for the error on the spin rate.

5.5.3 Alignment and final docking

Final alignment should be done (once it is reached the target point of the case 2 with a tolerance of 1 [cm]) very slowly so to reduce the risk of collisions, which in reality would bring Target to drift away from the chaser and could also cause the fall from the table of one of the two robots. When the relative distance and the attitude are those suitable for docking with a tolerance of 1 [cm] position and 1 [deg] on attitude the plier can be activated.

5.5.4 Linear actuator thrust compensation

For the conservation of momentum, the linear motor that closes the clamp will cause a reaction that will separate the SF (which does not exchange any binding reaction with the table) from the ideal position for docking. SF should therefore compensate this disturbance with the fans that will provide, more than the action required from the controller to maintain relative distance, attitude and gravitational forces, also a force in X_{SF} direction (since the clamp is directed like the camera) to compensate also this effect. When the chaser starts the plier closing the docking mission is at the end, so

Controller	**Time Simulation 1 [s]**	**Time Simulation 2 [s]**
PD	564	542
LQR	594	825
Non-linear	387	876

Table 5.5: Linear motor activation

from table 5.5 it's clear that the Nonlinear and the PD controller are the fast one in simulation 1 and 2 respectively.
It is also important to stop the generation of this force before the motor is turned off because being already tied the two satellites there will be no risk of separation, while if it were also provided for an instant after the closure of the clamp, the clash would be inevitable.

5.6 Collision Avoidance Manoeuvre

5.6.1 Flyers collision

A dangerous situation may occur if the when the chaser, while following the target, impacts with it. Fortunately the low speeds involved are not dangerous for the collision itself, but its consequence would be to push the target out of the table with a force that the actuators activated by the anti-falling module (see 5.6.2) fail to prevent it.
It is therefore important to avoid this situation by acting directly on the path planning software: the relative distance measured with the chaser onboard camera is checked to be greater (or at most equal to) than the distance between the two flyers when the clamp and target plate are perfectly aligned for docking: about 60 [cm] (see figure 5.23). So an imaginary limit of 60 [cm] radius is created around the TF center of mass that the chaser is forbidden from crossing.

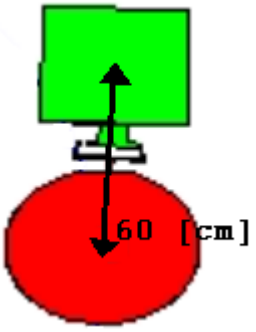

Figure 5.23: Minimum distance between flyers

5.6.2 Fall avoidance manoeuvre

The motion field is limited to the size of the table which is 9 square meters. To avoid the flyers to down from the frictionless plane, a virtual margin of 25 [cm] at the edges has been created, so that at least the center of mass of the flyer will be far from the edge of the table up to 25 [cm]. When this border is exceeded, the anti-fall module creates a force in the opposite direction along which the virtual edge was exceeded. This force will add to the orbital and to the control forces, and will be proportional to the distance from the virtual limit (see the red line in figure 5.22).

$$\begin{aligned} F_x &= \begin{cases} -K_a\,(x_F - 1.25) & x_F > 1.25 \\ 0 & -1.25 \leq x_F \leq 1.25 \\ -K_a\,(x_F + 1.25) & x_F < -1.25 \end{cases} \\ F_y &= \begin{cases} -K_a\,(y_F - 1.25) & y_F > 1.25 \\ 0 & -1.25 \leq y_F \leq 1.25 \\ -K_a\,(y_F + 1.25) & y_F < -1.25 \end{cases} \end{aligned} \tag{5.68}$$

where the gain K_a has been taken equal to 0.5.

5.7 Actuators

The analysis refers to the revisited actuators configuration of 3.3, where only four fans are considered really necessary for control (figure 5.3). Thus the thrust of the chaser will be reduced by a factor of $\frac{\sqrt{2}}{2}$.
As can be seen in figures 5.2 and 5.3 both vehicles have the same number and same clockwise numeration of fans, so the link between current and generated forces is the same as reported in 5.72.

5.7.1 The calibration

As already mentioned, those fans are not born as actuators; therefore no Thermaltake calibration curves are avaiable. A calibration campaign has been performed to map the different input current levels into force: table 5.6, already reported in section 3.3.

	Measured Force[N]			
Power [W]	**Measure 1**	**Measure 2**	**Measure 3**	**Measure 4**
0	0	0	0	0
0.84	0.023544	0.022563	0.023544	0.025506
1.2	0.054936	0.054936	0.060822	0.05886
1.8	0.095157	0.097119	0.089271	0.10791
2.4	0.135378	0.126549	0.133416	0.131454
3	0.164808	0.157941	0.164808	0.159903
3.6	0.184428	0.184428	0.184428	0.192276
4.2	0.217782	0.21582	0.214839	0.216801
4.8	0.238383	0.23544	0.238383	0.236421
5.4	0.2668326	0.272718	0.266832	0.262908
5.64	0.275661	0.276642	0.276642	0.273699

Table 5.6: Thrust supplied by the Thermaltake fans

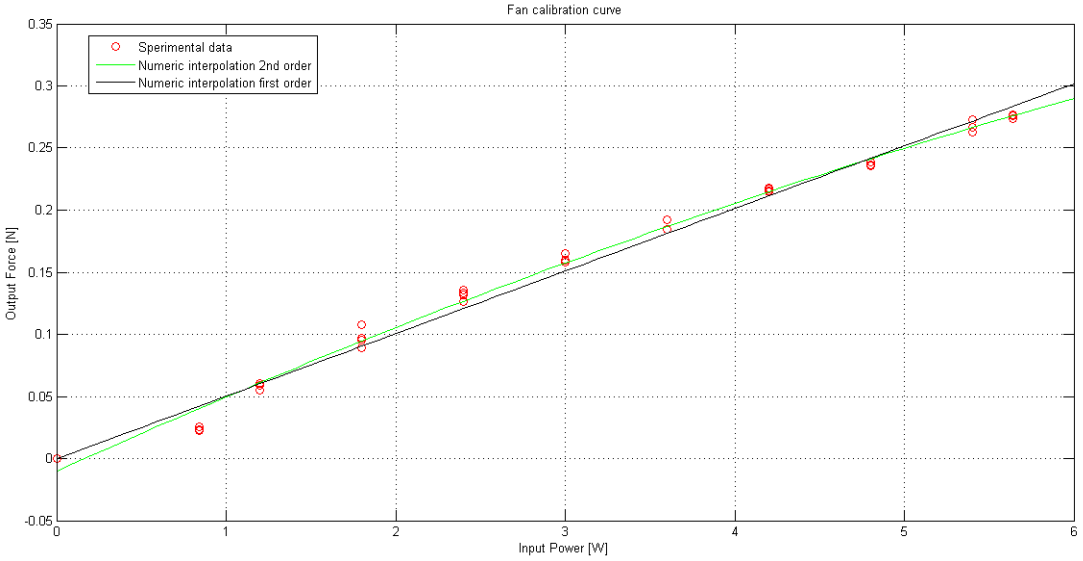

Figure 5.24: Fans calibration curve

As can be seen from figure 5.24 the ideal calibration curve is a second order polynomial: $F = K_1P^2 + K_2P + K_3$ where $K_1 = -0.0019$, $K_2 = 0.0617$, $K_3 = -0.0102$. Thus assuming a constant voltage of 12 [V], the control variable is the current to feed the individual fan in order to generate the necessary control forces.
To take into account the disturbance introduced by the actual behaviour of the fans a second order polynomial is considered in the actuator block, while a straight line through the origin is applied into the controller module; therefore $F(t) = K_{FAN}\ V\ I(t)$ where $K_{FAN} = 0.0503$.

5.7.2 The actuators dynamic

To be more consistent with the real device behaviour, the fan dynamics must be modeled too within the simulator; that allows veryfing that the controller bandwidth is adapted to the actuators bandwidth. To this end the inertial and damping characteristics of the fans, and also the constant of proportionality between the torque and the input current are needed. The fan dynamic system is:

$$J_{FAN}\ddot{\vartheta} + D_{FAN}\dot{\vartheta} = C_{FAN} \tag{5.69}$$

where

- $\vartheta, \dot{\vartheta}$ and $\ddot{\vartheta}$ are respectively rotation, angular velocity and angular acceleration of the fan;
- $C_{FAN} = K_m I_{FAN} \neq 0$ when the fan is on, while is null when the fan is off. It is the torque of the electric motor inside the fan;
- I_{FAN} is the current supplied to the fan;
- J_{FAN} is the inertia of the fan;
- D_{FAN} is the damping factor;
- K_m is the constant between the torque applied and the current supplied.

The force generated by each fan can be obtained as follows:

$$F_{FAN} = K_f \dot{\vartheta} \tag{5.70}$$

where:

- K_f is the constant factor between the angular velocity and the thrust supplied;
- F_{FAN} is the force supplied to the flyer.

The unknown parameters of the models are identified by a fitting procedure with data coming from two different sets of measurements during fan transient, and shown in table 5.7.

J_{FAN}	$1.25 \cdot 10^{-5}[m^2kg]$
D_{FAN}	$1.4 \cdot 10^{-5}[m^2kg/s]$
K_m	$0.0021[Nm/A]$
K_f	$0.0032[kg/m/s]$

Table 5.7: Dynamic fans parameters

Writing in the state system notation:

$$\begin{gathered} \ddot{\vartheta} = -\frac{D_{FAN}}{J_{FAN}}\dot{\vartheta} + \frac{K_m}{J_{FAN}} I_{FAN} \\ F_{FAN} = K_f \dot{\vartheta} \end{gathered} \tag{5.71}$$

The comparison between the measured and analytical results is shown in figures 5.26 and 5.27.

As can be seen from the plots, the measured data show some dispersion that can be reproduced in the simulator by introducing a random noise in the input current amplitude equal to 10 [mA]: this value coincides with the DC-DC ripple value.
As soon as the forces generated by each fan it is possible to determine the forces and torques in the local reference system (centered in the flyer) by simple algebraic manipulations:

$$u = \frac{\sqrt{2}}{2} \begin{bmatrix} -1 & 1 & 1 & -1 \\ 1 & 1 & -1 & -1 \\ a & -a & a & -a \end{bmatrix} \begin{bmatrix} F_{FAN1} \\ F_{FAN2} \\ F_{FAN3} \\ F_{FAN4} \end{bmatrix} \tag{5.72}$$

where a represents the distance that works for the force generated by each fan figure 5.25.

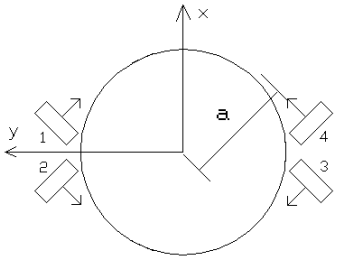

Figure 5.25: Actuators geometric parameter

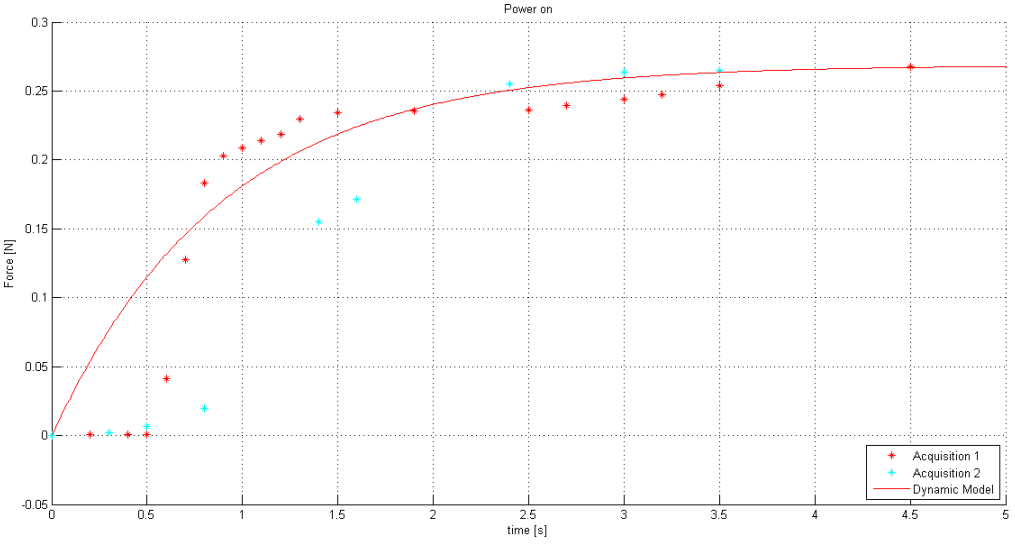

Figure 5.26: Fan power on curve

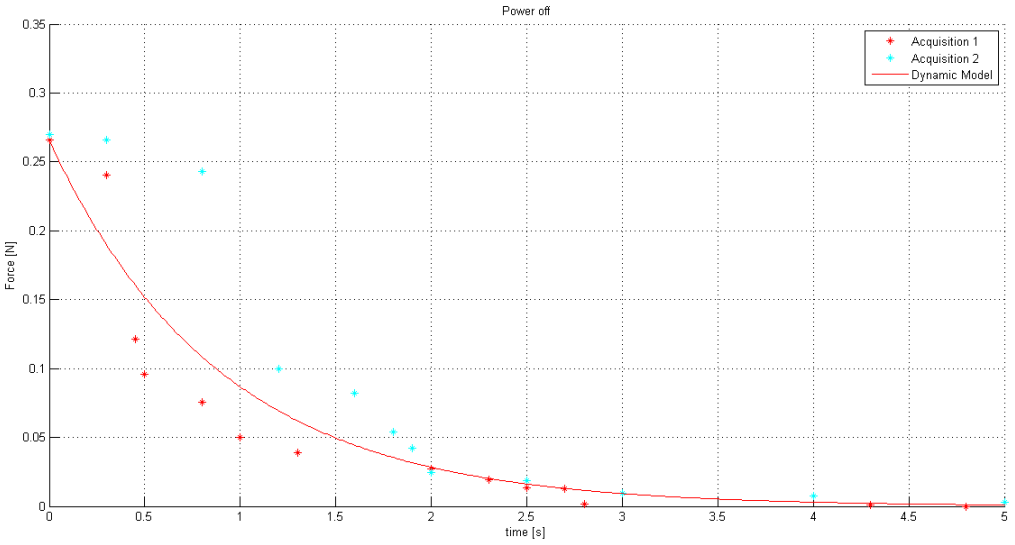

Figure 5.27: Fan power off curve

The following figures show the comparison among the three forces here defined:

- required: forces required by the controller;
- modulated: forces that would be produced if the actuators were ideal after currents modulation, coincident with control actions required by the controller;
- real: forces actually supplied by the fans, taking into account the transients and random fluctuations of the input current for different simulations.

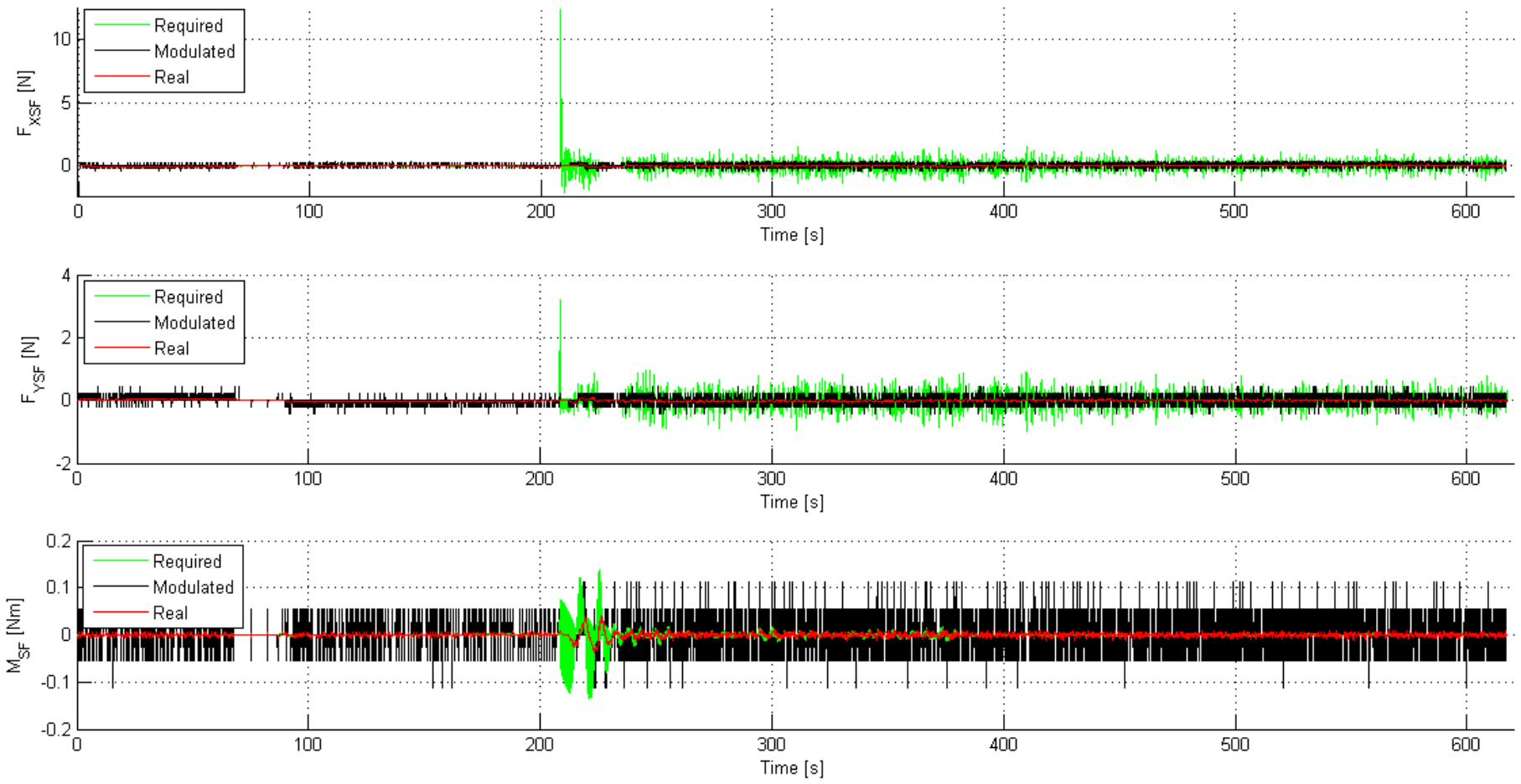

Figure 5.28: Comparison among the required, modulated and real forces: SF - Simulation 1 - Controller PD

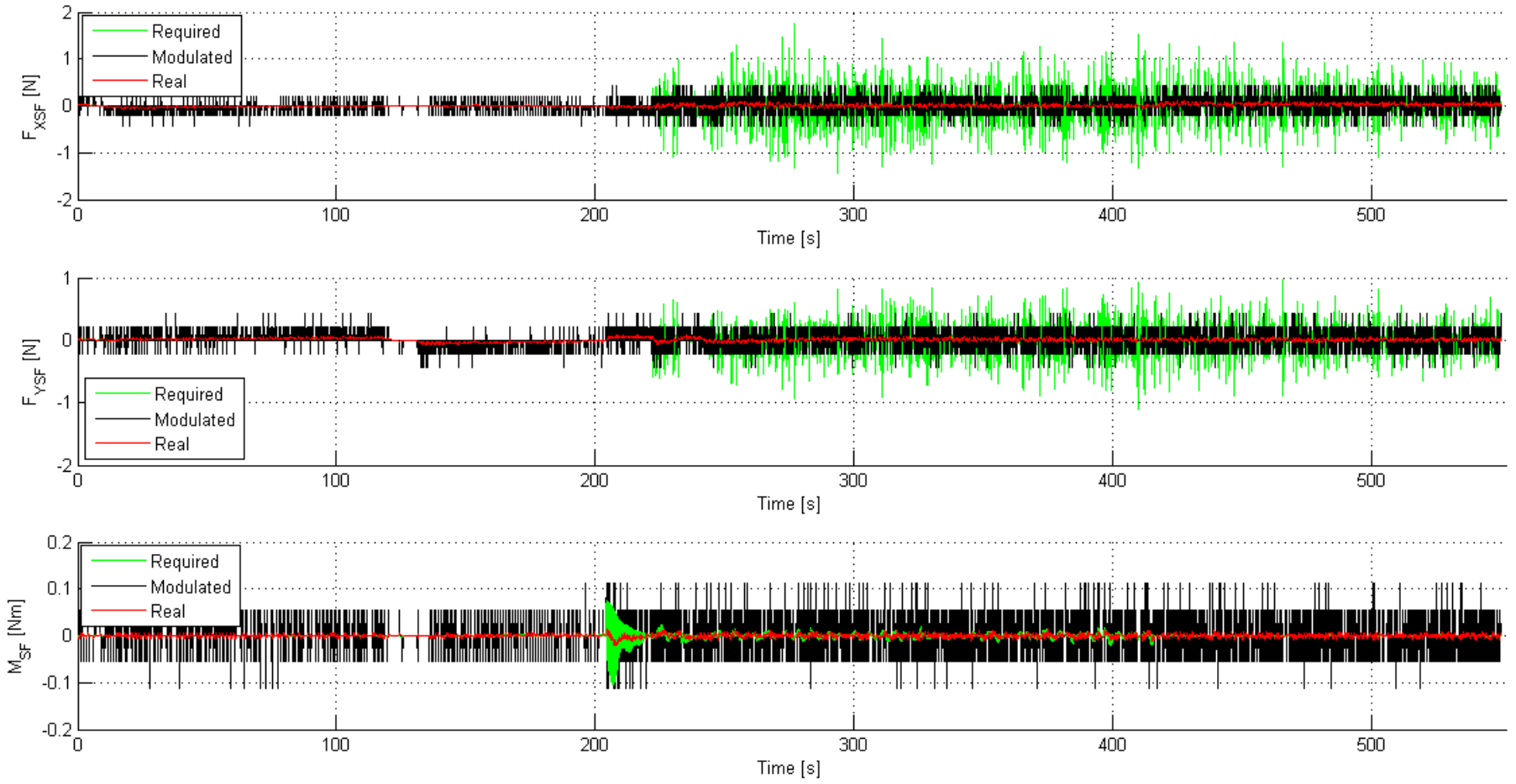

Figure 5.29: Comparison among the required, modulated and real forces: SF - Simulation 2 - Controller PD

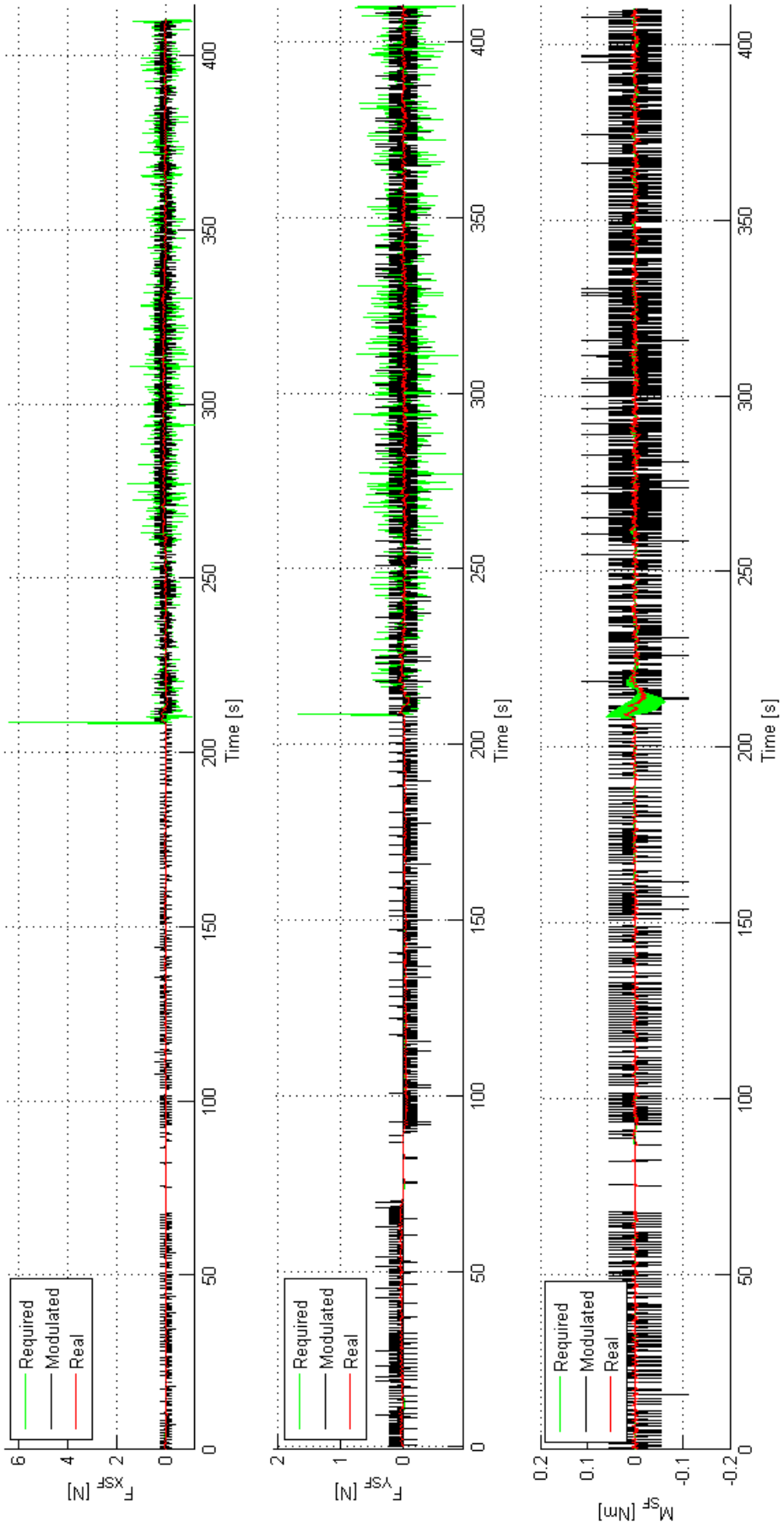

Figure 5.30: Comparison among the required, modulated and real forces: SF - Simulation 1 - Controller LQR

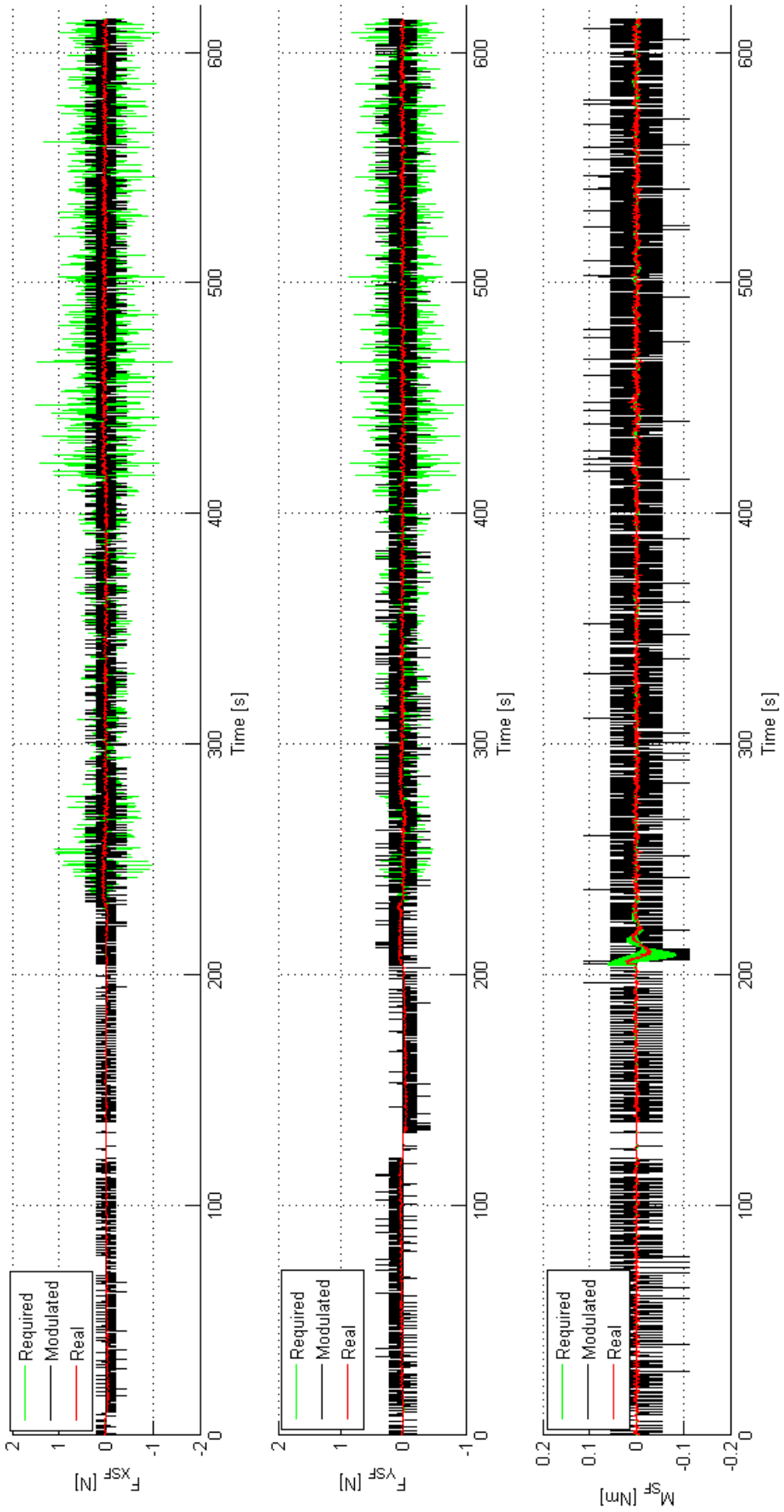

Figure 5.31: Comparison among the required, modulated and real forces: SF - Simulation 2 - Controller LQR

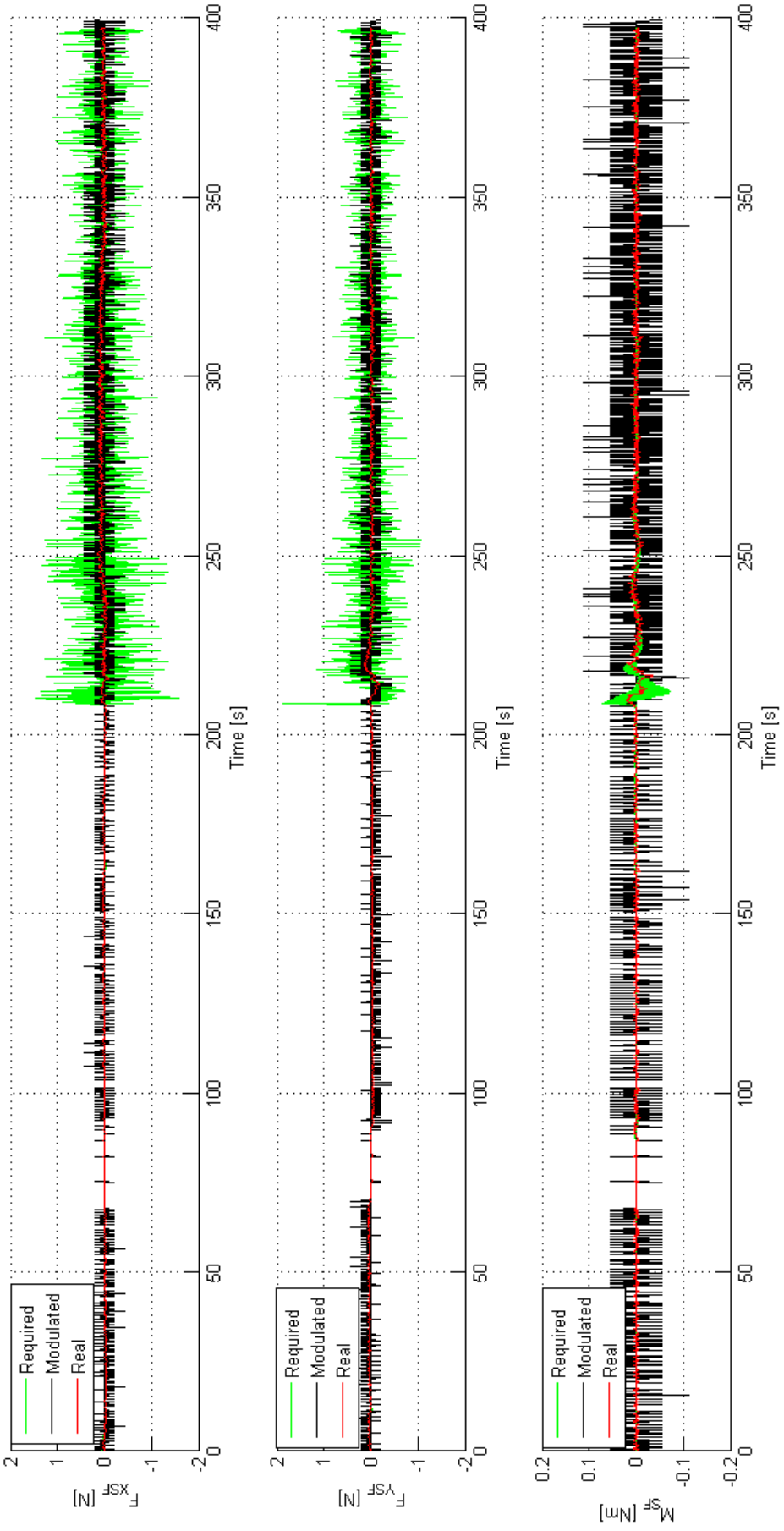

Figure 5.32: Comparison among the required, modulated and real forces: SF - Simulation 1 - Controller NL

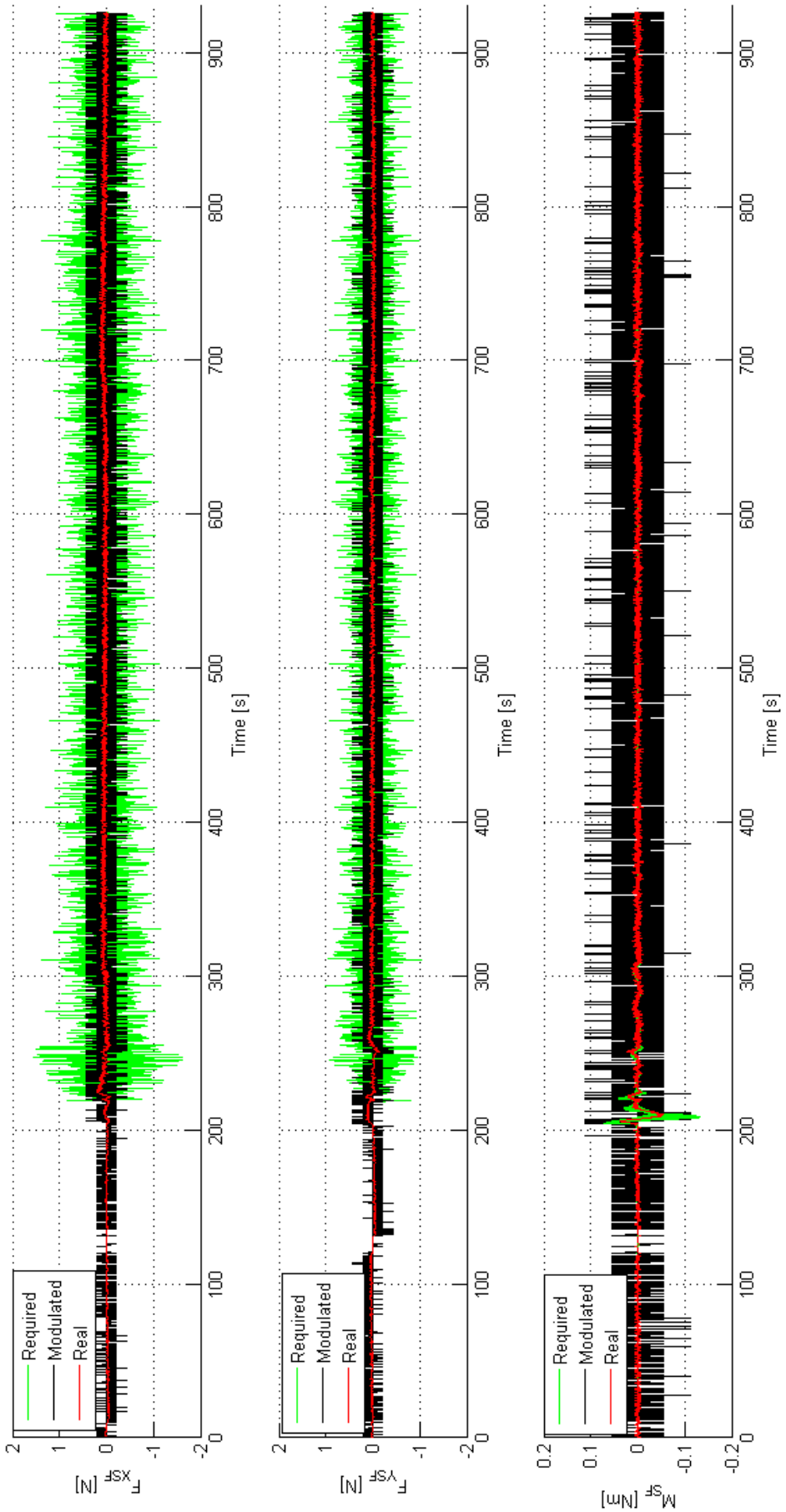

Figure 5.33: Comparison among the required, modulated and real forces: SF - Simulation 2 - Controller NL

From the figures 5.28, 5.29, 5.30, 5.31, 5.32 and 5.33 it's possible to observe that forces greater than the actuator skills are required when the transfer manoeuvre starts. But thanks to the width modulation the same effect can be achieved leaving the fans turned on for more than one pulse 5.14.2.

5.8 The navigation

The sensor module has been already described in subsection 3.1.6 and its provide to the calculation of SF and TF position. Such data are also filtered and propagated by the recursive filter described in 5.8.1.

5.8.1 Recursive filter

This filter, to be run on the desktop PC, is designed to propagate and filter the output of the fixed camera[7]. As said in the subsection 3.1.6 a $f_{ACQcamera} = 1\ [Hz]$ has been selected in order to be conservative compared todata offered by literature [17].
The philosophy of this filter is based on finding a curve (whose order depends on the order of the filter) that minimizes the error between the measures generally contaminated by noise with zero mean, and the curve itself, using a least squares technique. The basic steps of implementation include the computation of the residue Res_k at each step.

$$Res_k = x_k^{meas} - \hat{x}_{k-1} - \hat{\dot{x}}_{k-1}dt - \frac{1}{2}\hat{\ddot{x}}_{k-1}dt^2 \tag{5.73}$$

where x_k^{meas} is the position measured at k-th instant, and $\hat{x}_{k-1}$, $\hat{\dot{x}}_{k-1}$, $\hat{\ddot{x}}_{k-1}$ are filtered positions, velocities and accelerations at the previous step. Then it's possible to propagate the filter status taking into account the residual at the current step and the previous output:

$$\begin{aligned} \hat{x}_k &= \hat{x}_{k-1} + \hat{\dot{x}}_{k-1}dt + \tfrac{1}{2}\hat{\ddot{x}}_{k-1}dt^2 + K_{1k}Res_k \\ \hat{\dot{x}}_k &= \hat{\dot{x}}_{k-1} + \hat{\ddot{x}}_{k-1}dt + K_{2k}Res_k \\ \hat{\ddot{x}}_k &= \hat{\ddot{x}}_{k-1}dt^2 + K_{3k}Res_k \end{aligned} \tag{5.74}$$

where $K_{1k} = \frac{3\left(3k^2-3k+2\right)}{k(k+1)(k+2)}$, $K_{2k} = \frac{18(2k-1)}{k(k+1)(k+2)dt}$ and $K_{3k} = \frac{60}{k(k+1)(k+2)dt^2}$, derived by simple algebraic operations [10].

In the following figures the comparison among the real positions and attitude, those detected by the camera and those filtered by the recursive filter is reported. The values are expressed in the inertial frame: see 5.3.3.

[7]Do not be deceptive the fact that the camera has an high acquisition frequency, because what implies a slowdown in the flyers status estimation is the software that will process the image.

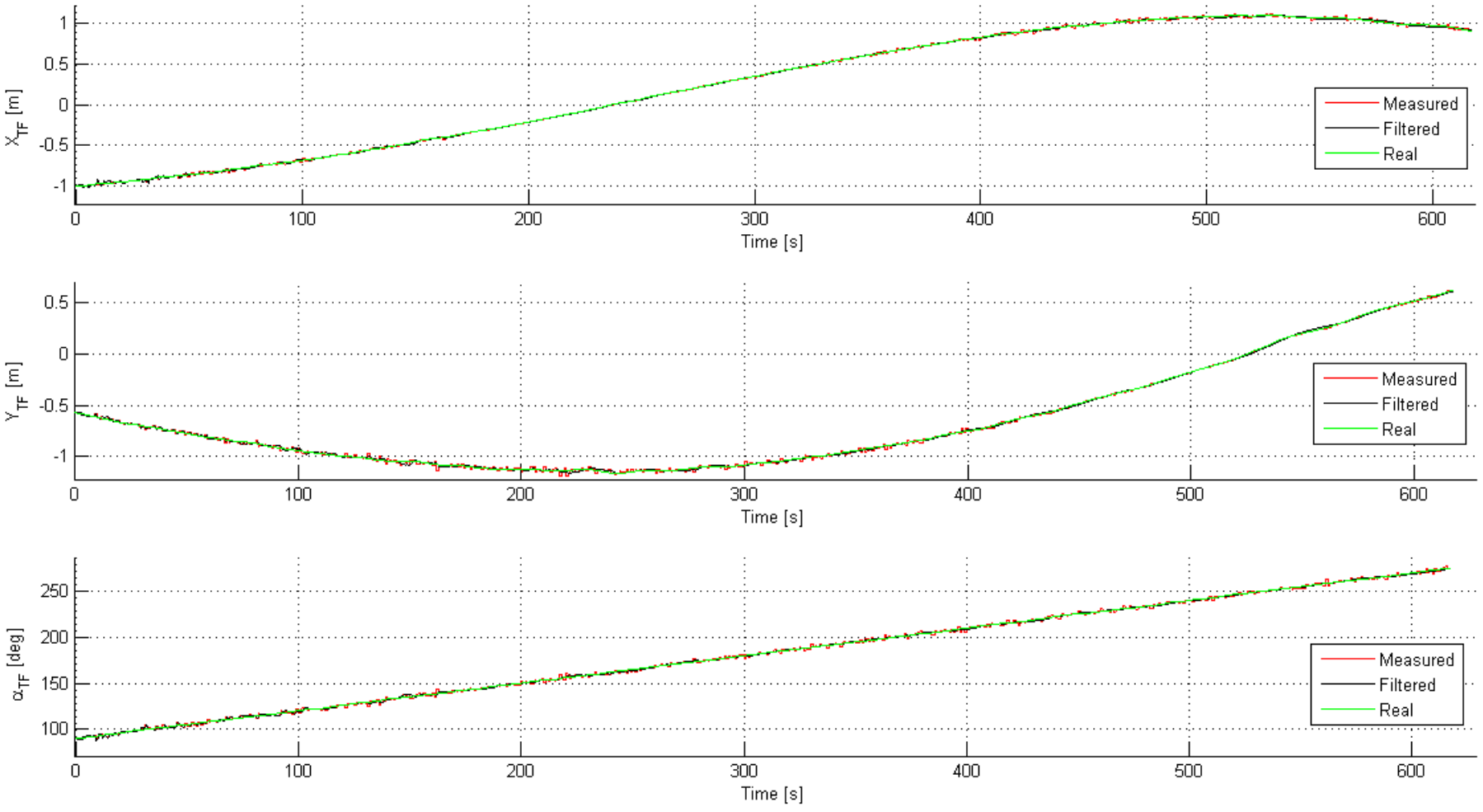

Figure 5.34: Comparison among real and filtered position and attitude: TF - Simulation 1 - Controller PD

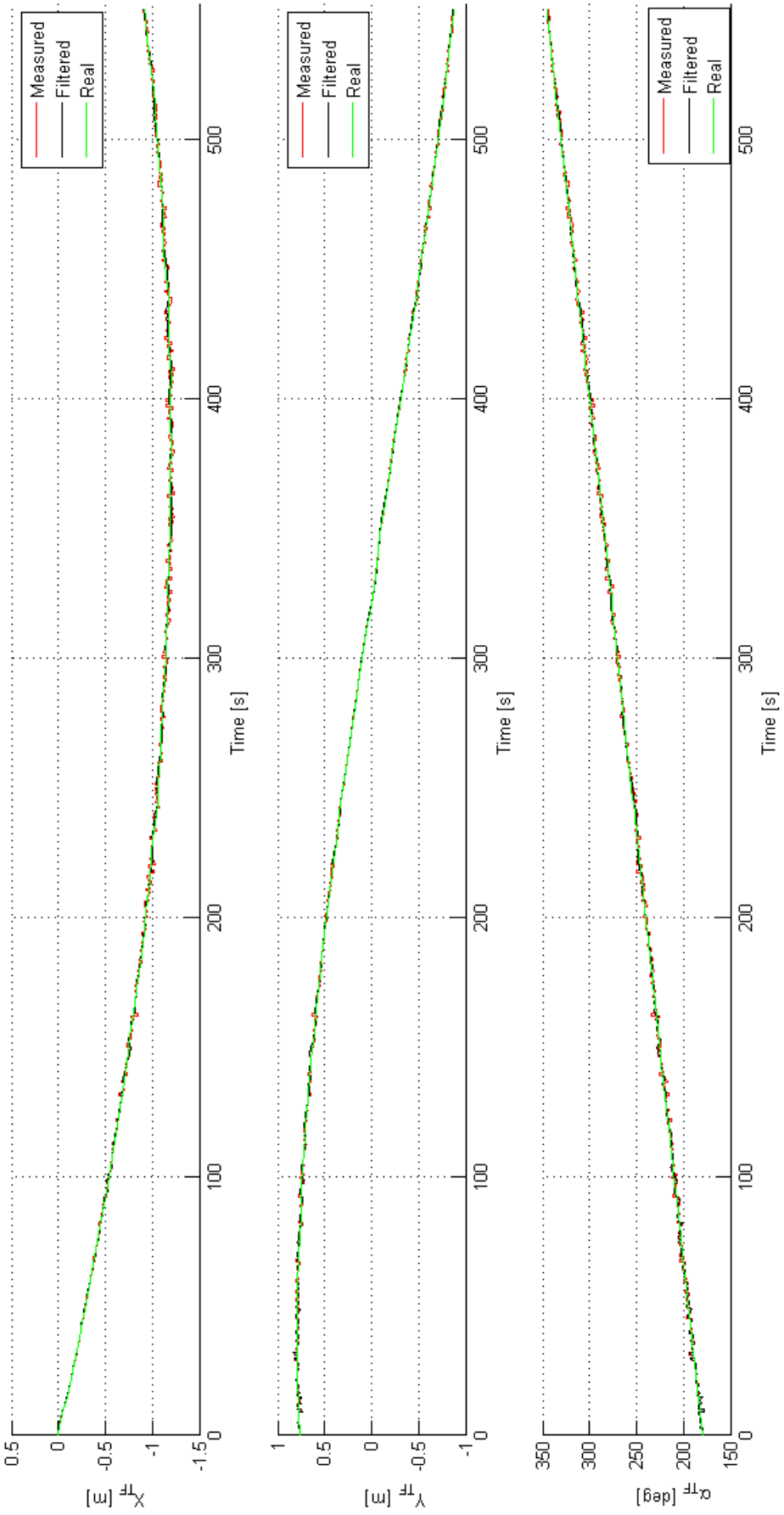

Figure 5.35: Comparison among real and filtered position and attitude: TF - Simulation 2 - Controller PD

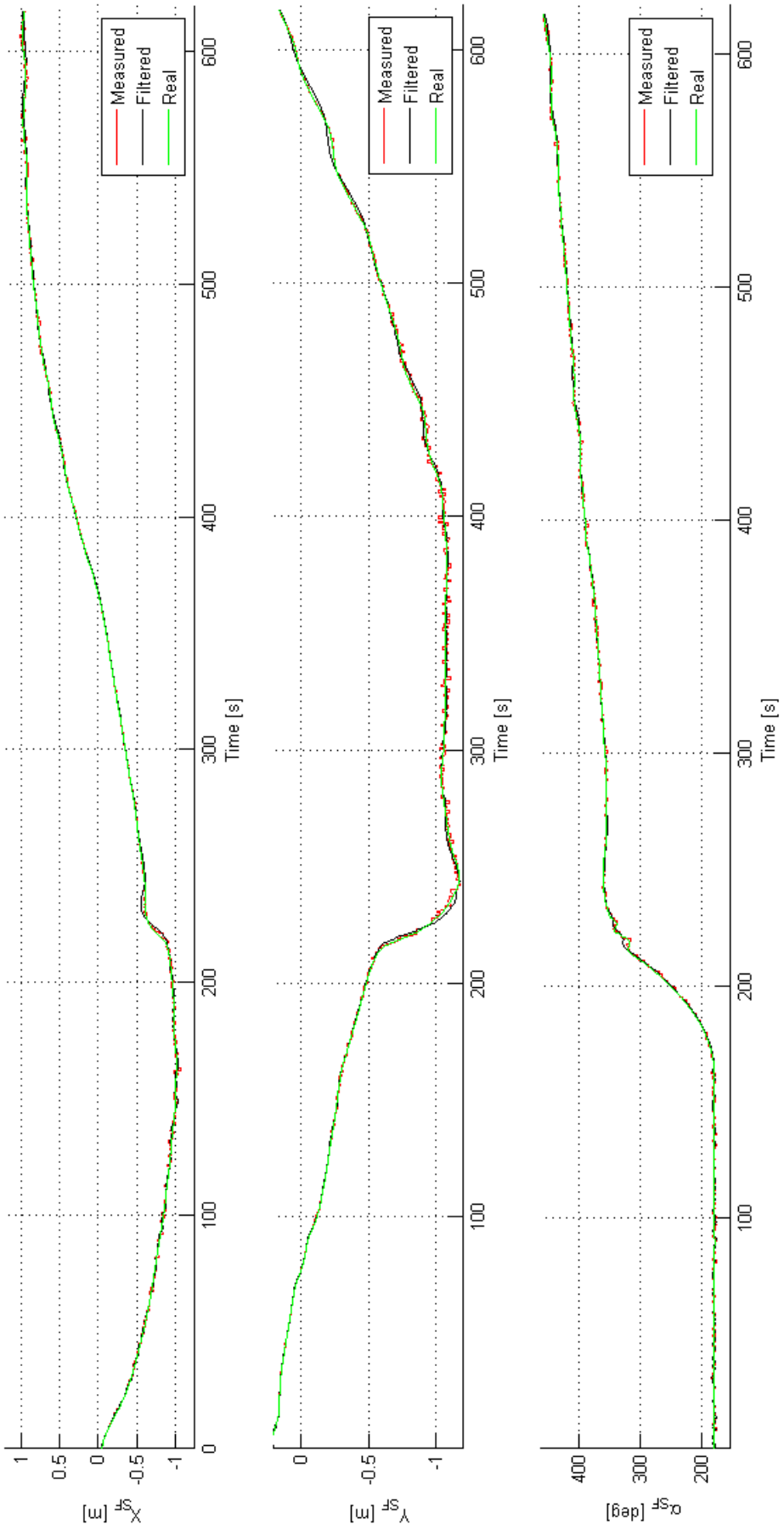

Figure 5.36: Comparison among real and filtered position and attitude: SF - Simulation 1 - Controller PD

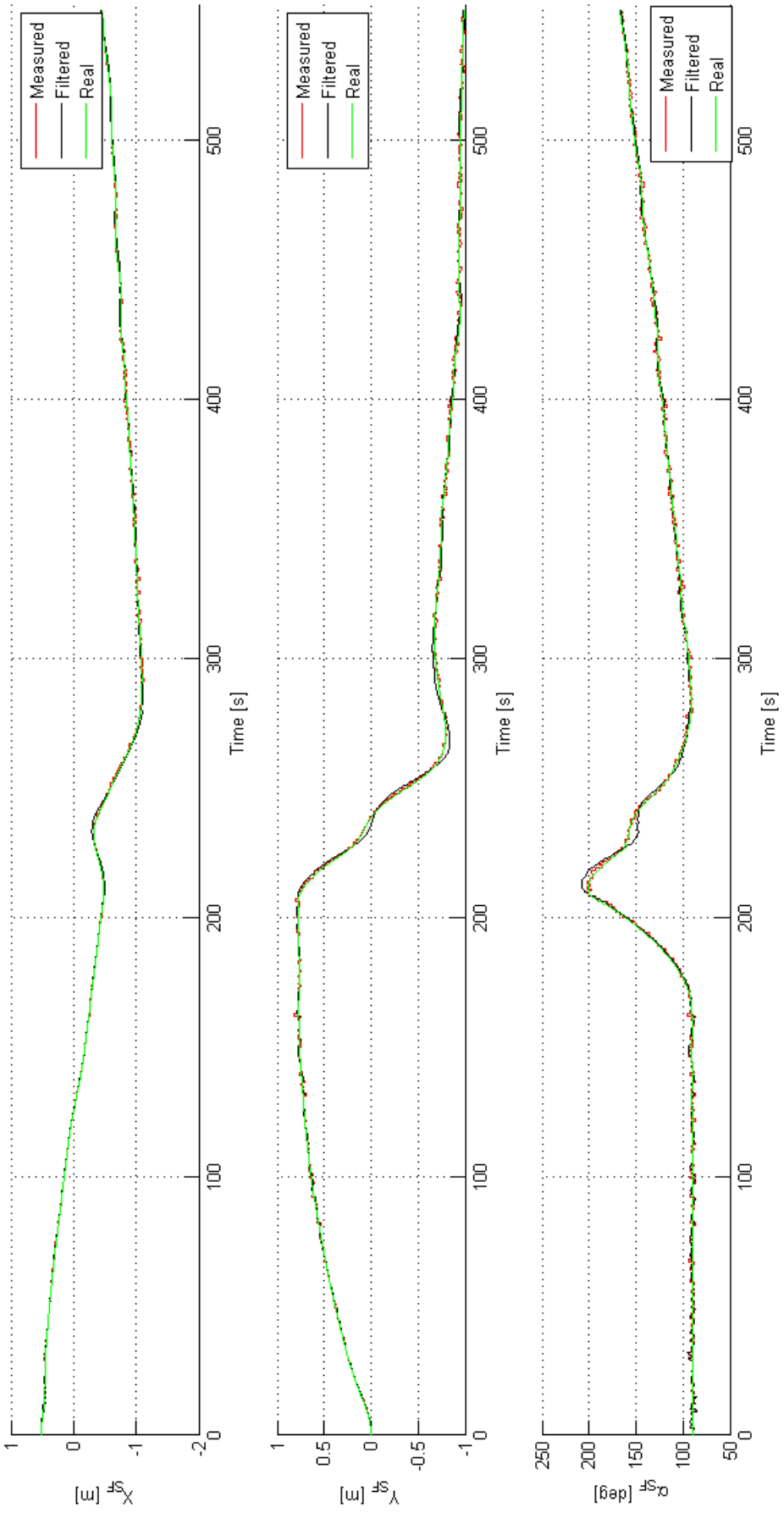

Figure 5.37: Comparison among real and filtered position and attitude: SF - Simulation 2 - Controller PD

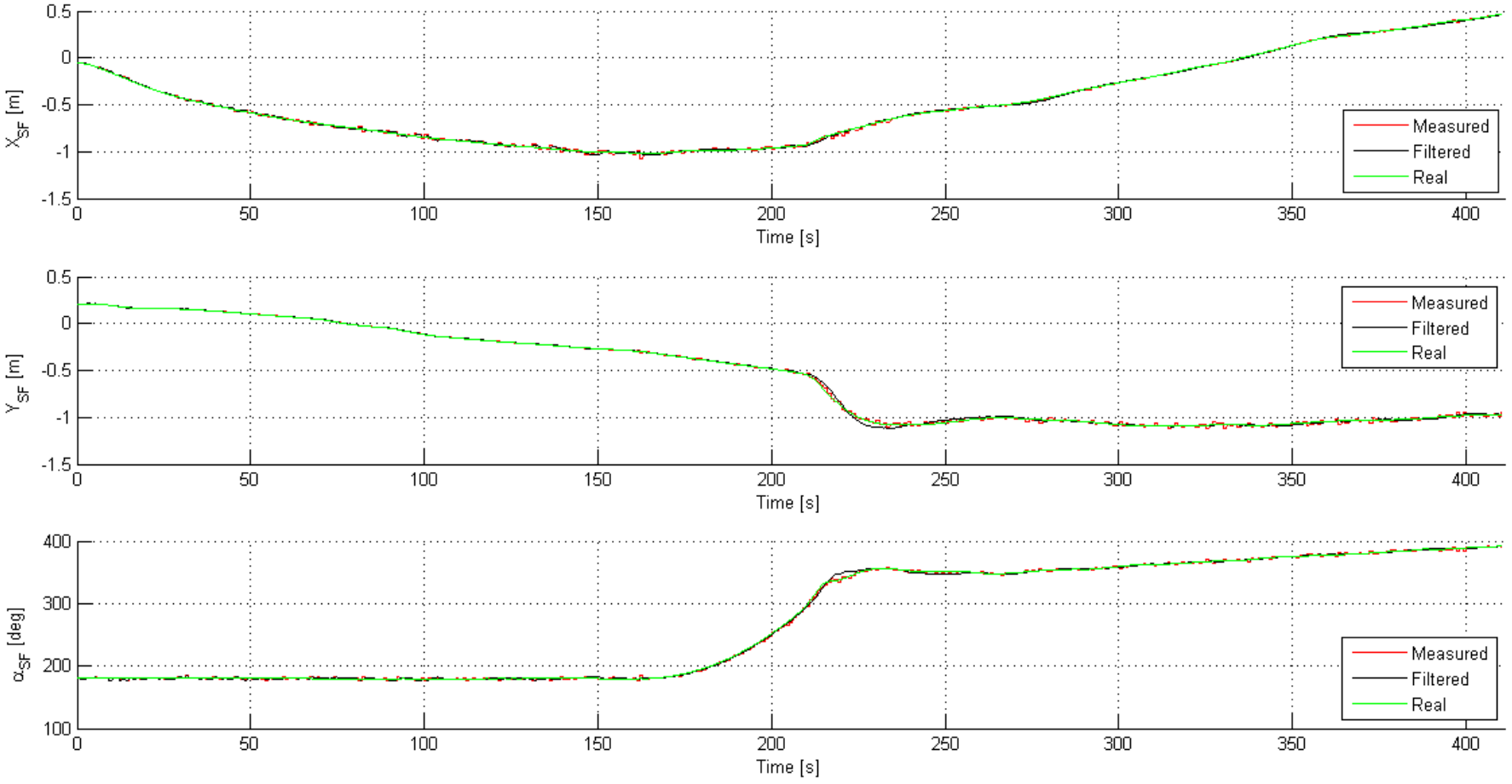

Figure 5.38: Comparison among real and filtered position and attitude: SF - Simulation 1 - Controller LQR

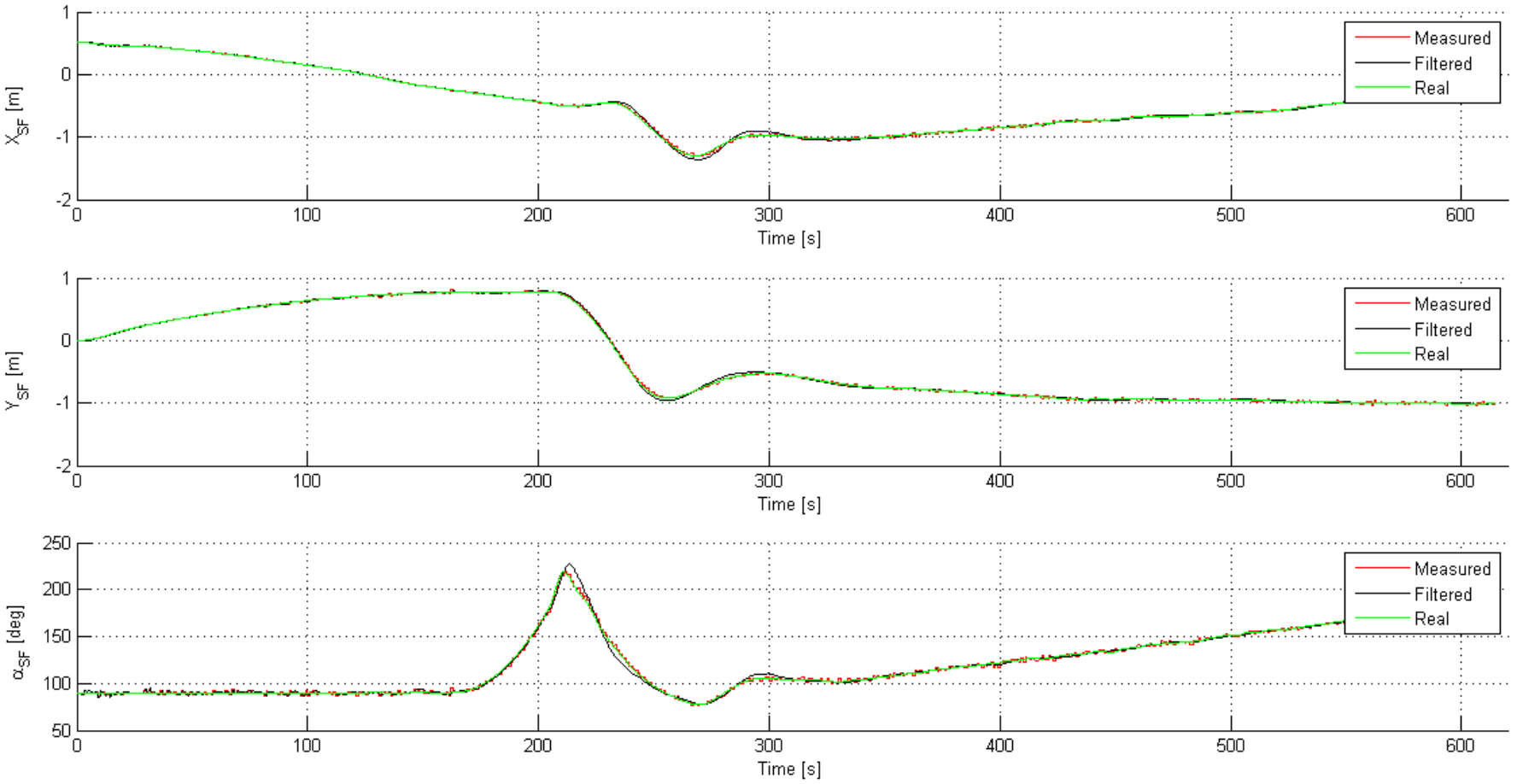

Figure 5.39: Comparison among real and filtered position and attitude: SF - Simulation 2 - Controller LQR

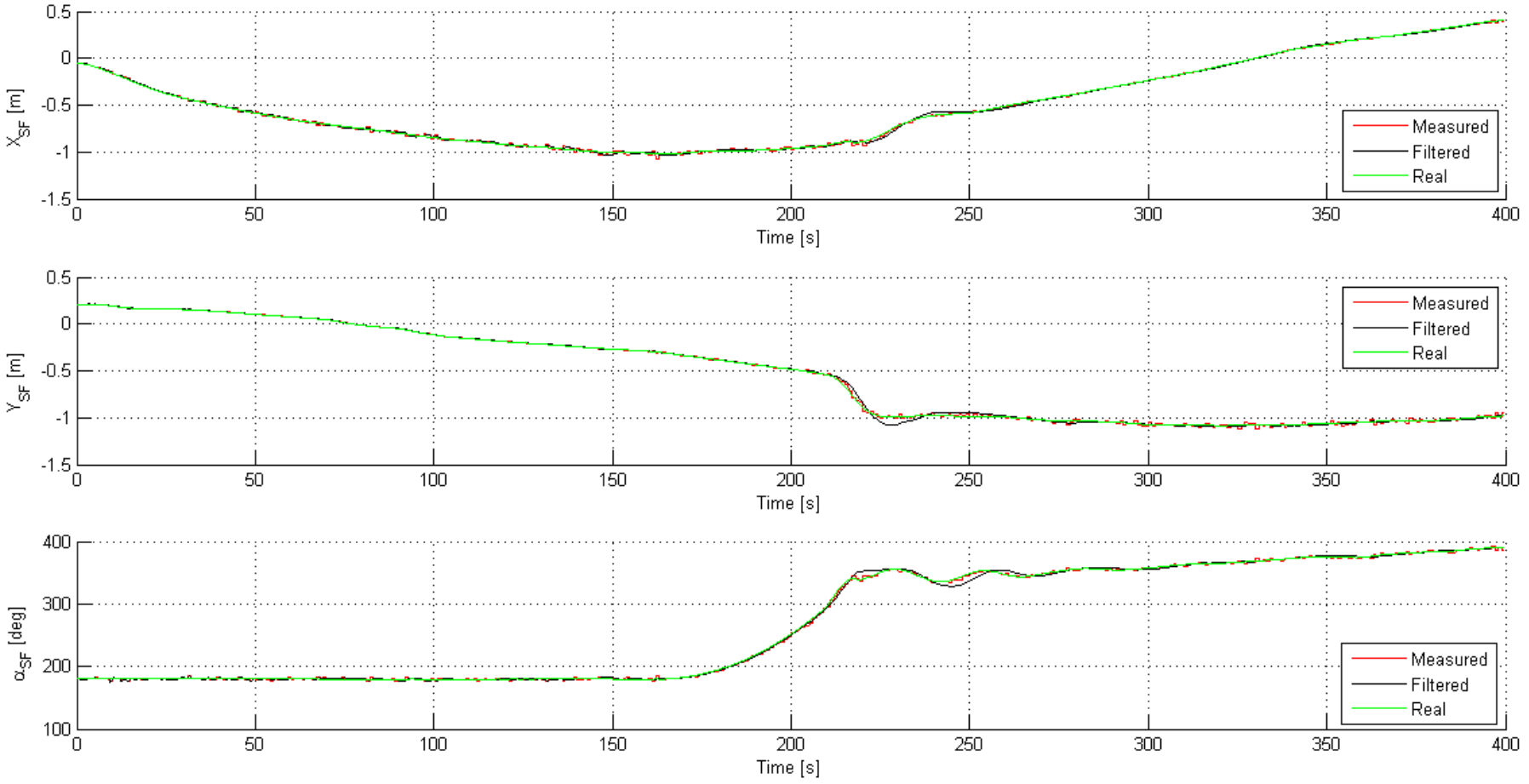

Figure 5.40: Comparison among real and filtered position and attitude: SF - Simulation 1 - Controller NL

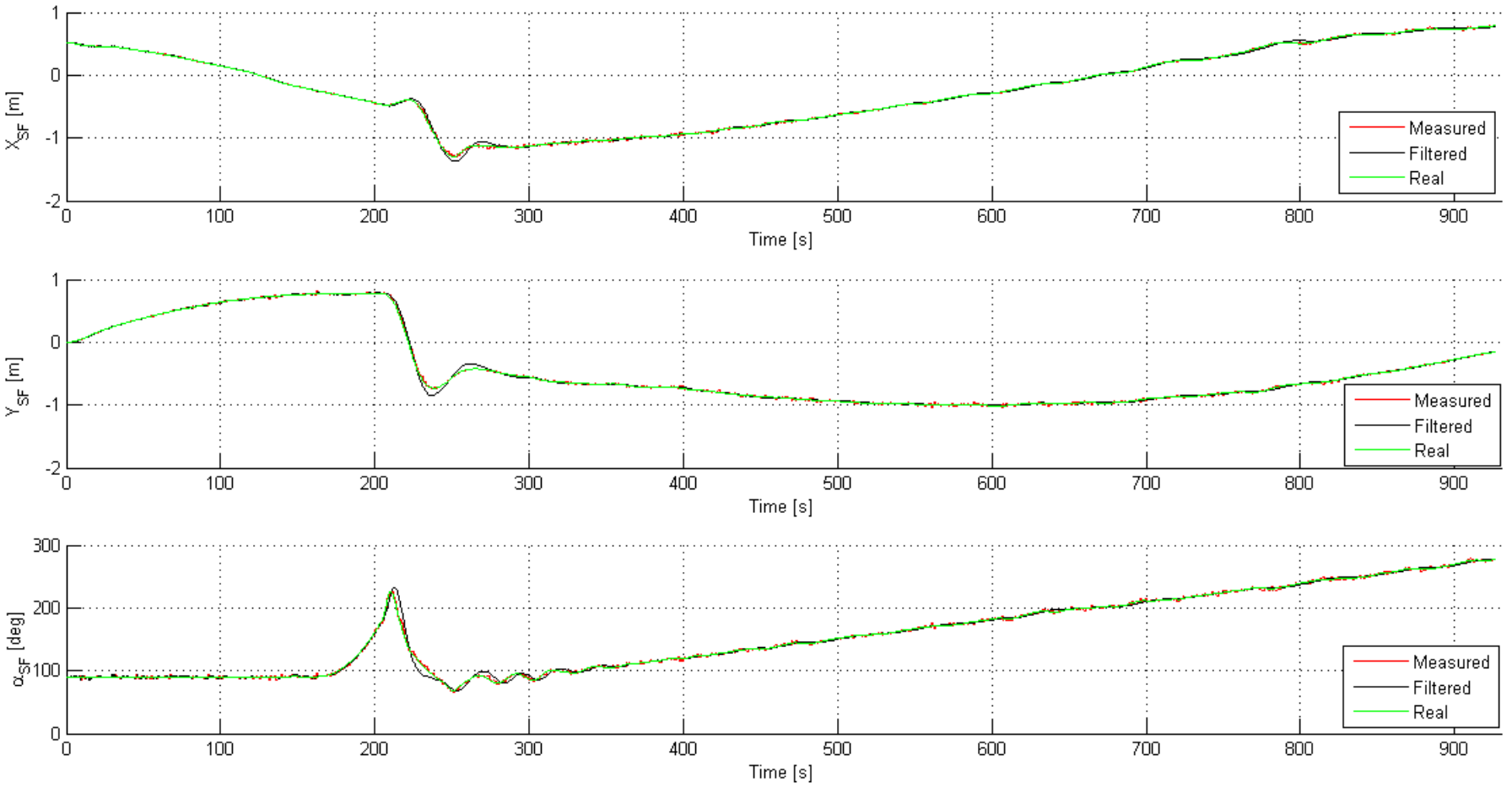

Figure 5.41: Comparison among real and filtered position and attitude: SF - Simulation 2 - Controller NL

5.8.2 The Relative position sensor

The chaser in addition to receive data from the fixed camera (subsection 3.1.6) has another visual system (whose characteristics are reported in table 3.11) necessary to determine the relative state. In practice by acquiring an image of the Target flyer the onboard software can reconstruct relative attitude and distance. The algorithm will be explained in the section 6.1.2, but since there is no transfer via wireless, and having to process a single image at a time can be considered, a sampling time of 0.2 [s] has been assumed, according to literature [17].
The webcam used to esteem the relative position is described in table 3.11.

Unlike what happens for the inertial camera, in this case the recursive filter after the camera can be avoided as because every 2 control actions[8] the image processing software supplies a new measure of the state, therefore the computational load of the filter can be avoided.
In the following figures the trend of the real and measured state, in the different simulations is shown. The values in the following plots are expressed in the chaser reference system 5.3.

[8]It points out that the bandwidth of the controller is 10 [Hz].

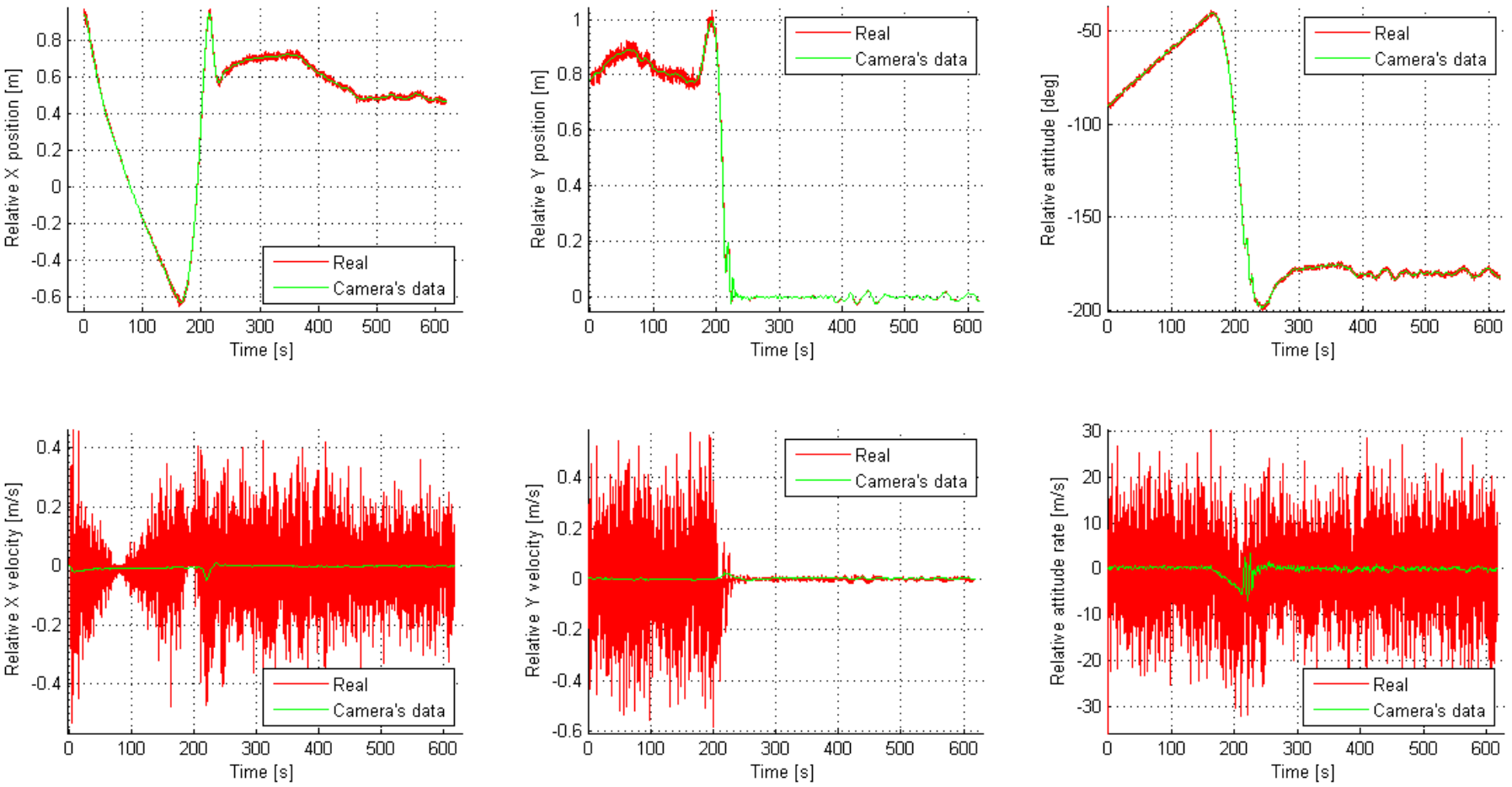

Figure 5.42: Comparison between relative state measured and real: Simulation 1 - Controller PD

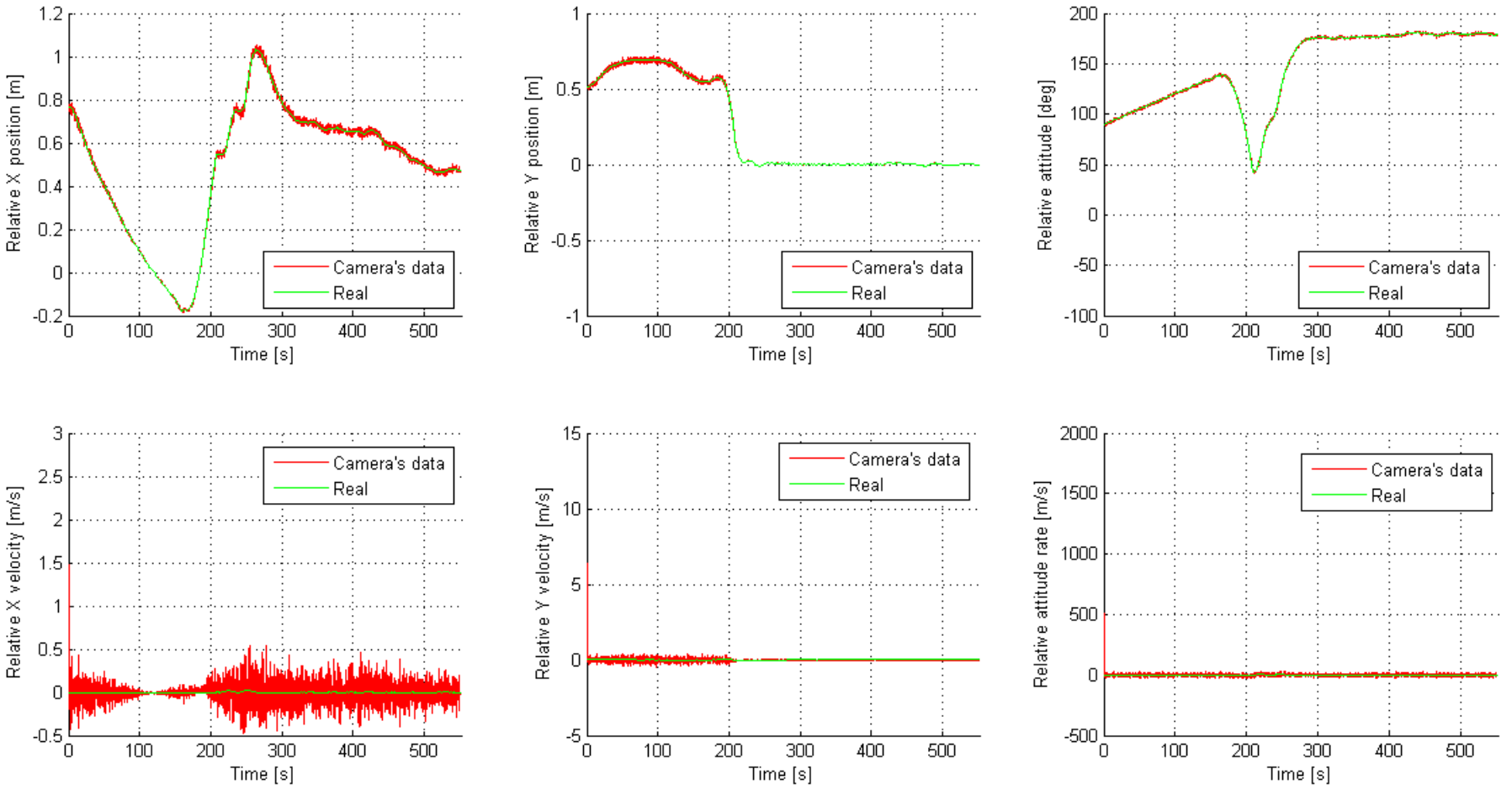

Figure 5.43: Comparison between relative state measured and real: Simulation 2 - Controller PD

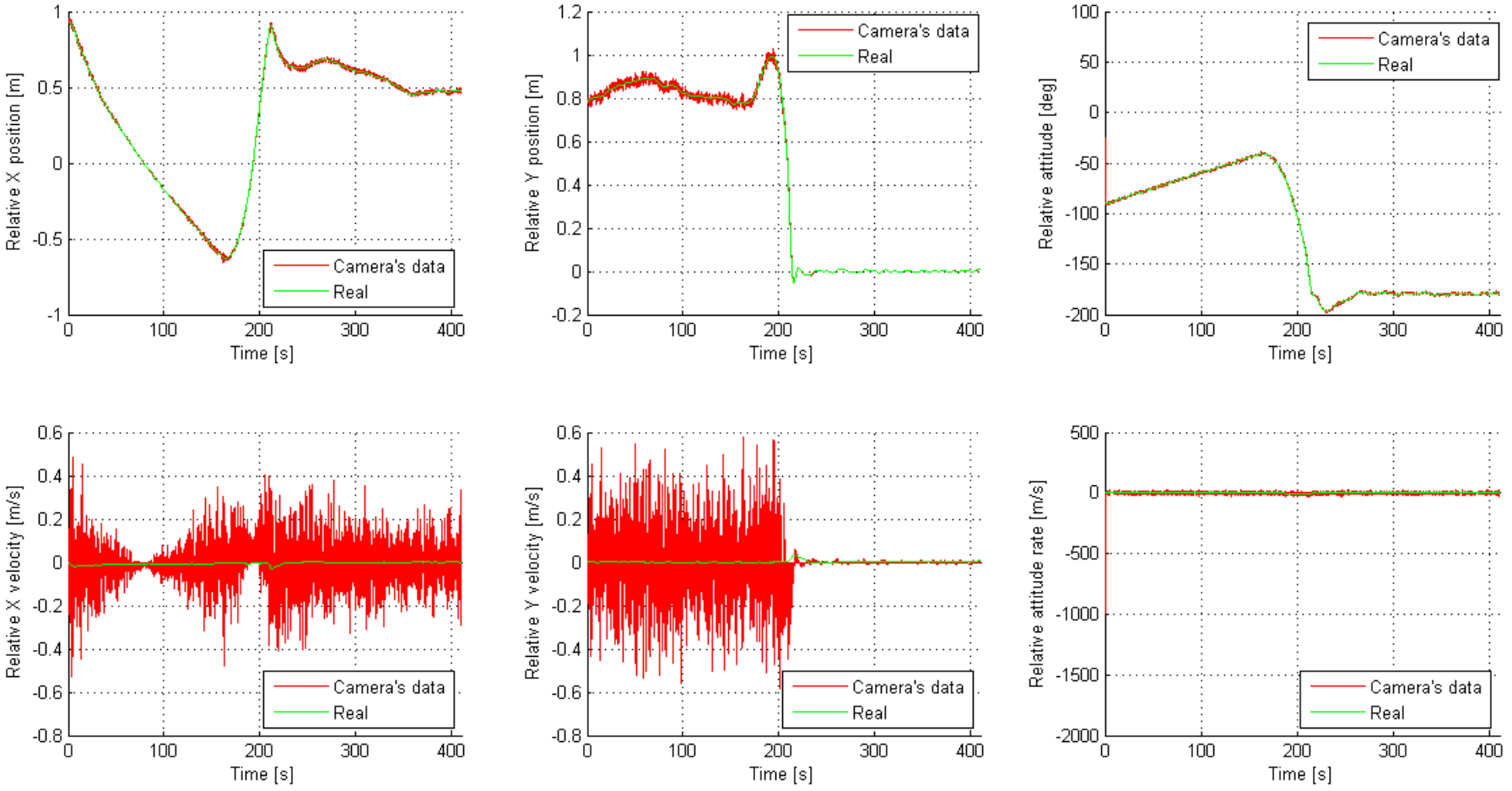

Figure 5.44: Comparison between relative state measured and real: Simulation 1 - Controller LQR

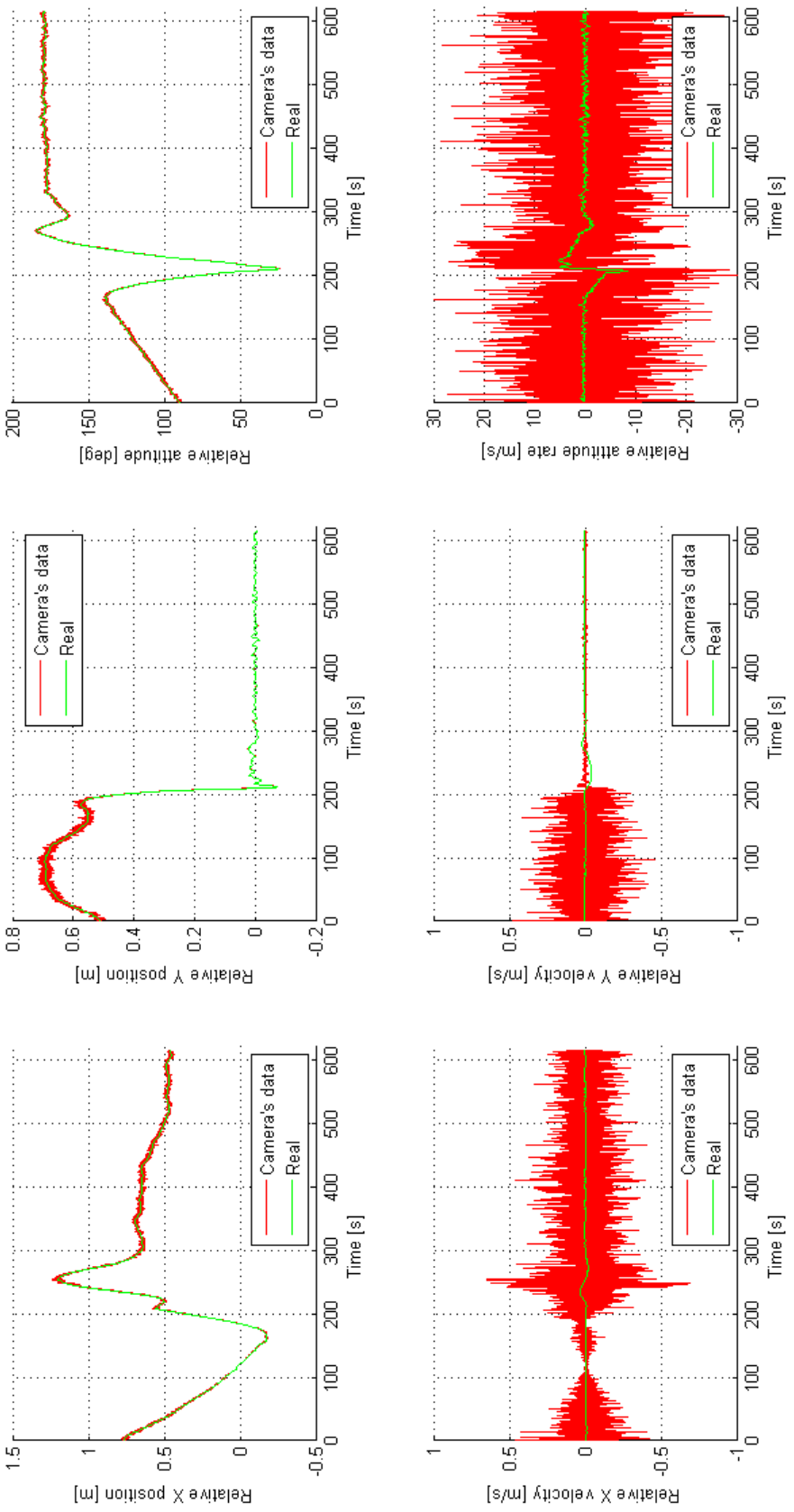

Figure 5.45: Comparison between relative state measured and real: Simulation 2 - Controller LQR

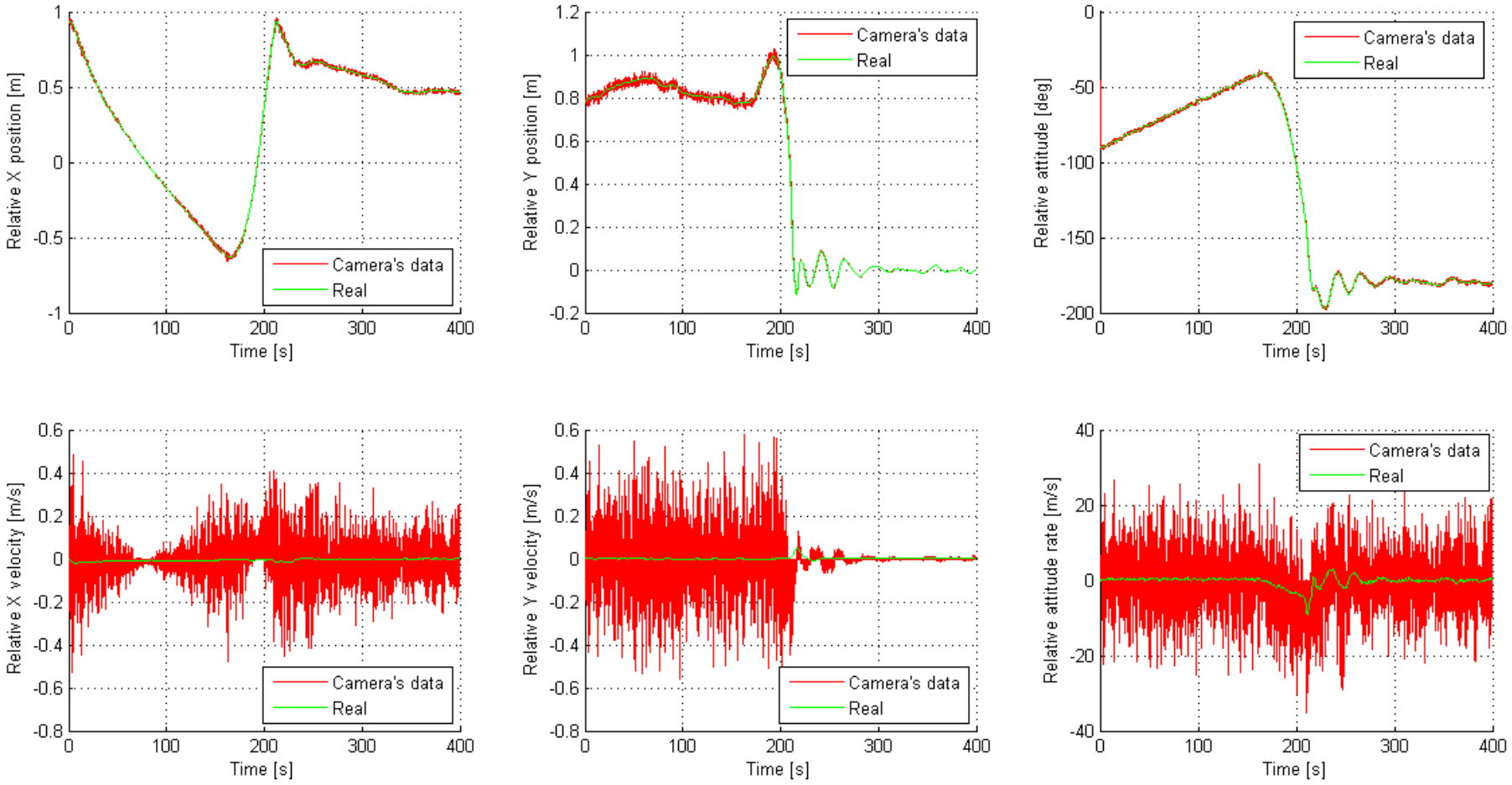

Figure 5.46: Comparison between relative state measured and real: Simulation 1 - Controller NL

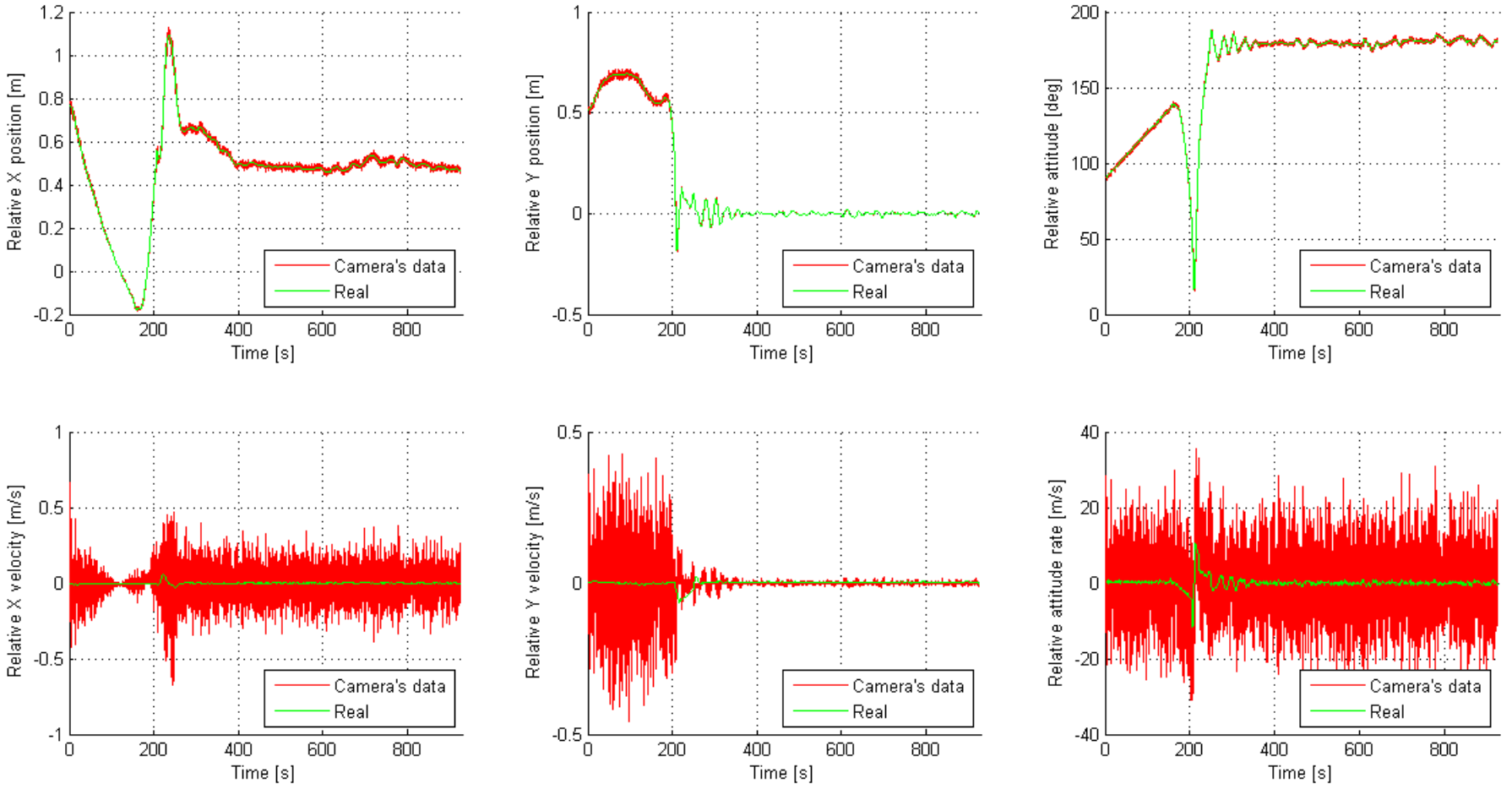

Figure 5.47: Comparison between relative state measured and real: Simulation 2 - Controller NL

The X and Y components is referred to the distance between the two flyers center of mass; for this reason when the docking has been completed the distance between the two center of mass: $d = \sqrt{X^2 + Y^2}$ is about 0.5 [m]. For the relative attitude the optimal condition in order to successfully complete the docking manoeuvre is 180 deg, see 5.3 and 5.2.
Concerning the relative velocity, they are not directly measured. In fact they have been computed with a numerical derivative, that cause such fluctuations. However such fluctuations does not compromise the docking mission, because the relative error on the velocity (and angular velocity) is obtained directly from a numerical derivative of the position (and attitude) error.

5.9 Kinematics

The attitude of both flyers, of the plane motion is easily described by the only angle α which has been described in 5.3.1 and 5.3.2. The kinematics can be represented by the cosines attitude matrix that will have the following form:

$$A_\alpha = \begin{bmatrix} cos(\alpha) & -sin(\alpha) & 0 \\ sin(\alpha) & cos(\alpha) & 0 \\ 0 & 0 & 1 \end{bmatrix} \tag{5.75}$$

This matrix is the transpose [9] of that used in section 5.3.5, because it allows to pass from the local flyer reference to the inertial one.

5.10 The Dynamics

The vehicles dynamic is very simple as only rigid motions occur, that take place all in the plane of the table. From the actuators forces, modeled in 5.7, it's possible to compute the acceleration of the flyers taking into account the acceleration noise given by the concavity of the table, discussed in section 2.1.1: figure 5.48: at each point of the plan it is possible to calculate the acceleration a_{dx} and a_{dy} by simply projecting the gravity acceleration for the local table inclination.
So the calculation of this slope depends on the position of the flyer, note which one can evaluate the table local deflection in Z direction according to the relation:

$$z = -\left| 2.0 \cdot 10^{-4} sin\left(\frac{2\pi x}{3}\right) sin\left(\frac{2\pi y}{3}\right) \right|. \tag{5.76}$$

where x, y, and z are the coordinates in the inertial reference. Considering the table splitted into 4 quadrants depending on where the flyer is, it is possible to join that point with the center of the quadrant that has the maximum deflection of $-0.2[mm]$ and determine the inclination as that of the segment so established.

Thus the equations that govern the system dynamic are:

[9] Being orthogonal matrices transposed and reverse match.

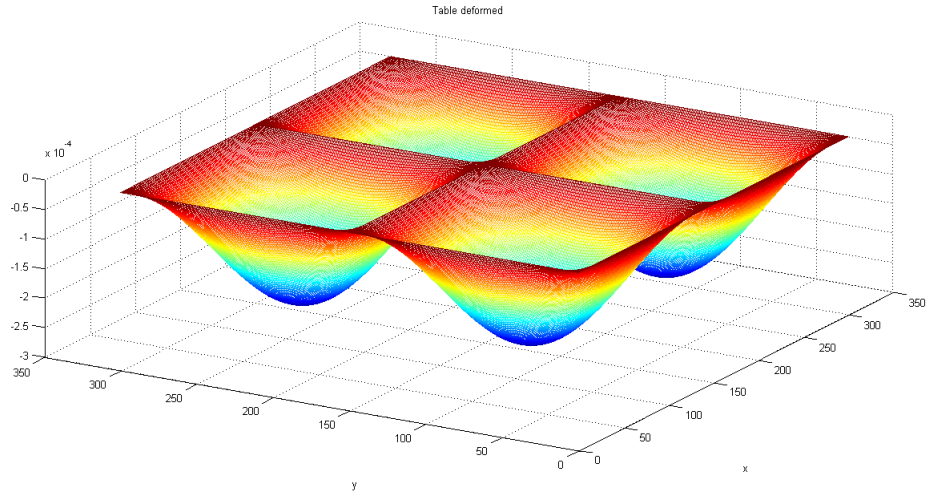

Figure 5.48: Table concavity

$$\begin{aligned} m_F a_x &= F_x + m_F a_{Dx} \\ m_F a_y &= F_y + m_F a_{Dy} \\ I_F \ddot{\vartheta} &= M \end{aligned} \tag{5.77}$$

where m_F and I_F are respectively the mass and inertia of the flyer in question.
Actually, only for the Smart Flyer, an additional force has to be considered, when the linear actuator is activated to close the clamp (see subsection 5.5.4). At that moment, the force is generated for the principle of action and reaction, in the $-X$ direction of the chaser local system, that thrust will move away from its target position the chaser. This force will depend on the torque generated by the electric motor and then on the power supply to it.

5.11 Kalman Filter

After modeling the real vehicle components, the implementation of the digital system that closes the control loop has been performed.
Because of the noise on the measurements, introduced by the tracking software and the lack of velocity information an observer module must included in the chain. A Kalman filtering technique has been here selected.
The Kalman filter is a statistical tool that allows variables estimation, including those non-measurable, from measured values of some quantities associated with them and from the dynamic model of the system. It is based on some fundamental assumptions, such as dependence of the current system state only from the state at previous time (first order Markovian process) and the linearity of this dependence [11].
Two relations must be identified to set the kalman filter: the state and the measurement equation. The equation of state expresses the relationship between the state parameters at two subsequent epochs and represents the mathematical model chosen to describe

the analyzed phenomenon. The measure equation instead binds the state parameters to measures of quantities related to them. Both equations must be linear.
The Kalman filter is divided into two parts: first, the *filtering*, determines the best estimate of the parameters at current time using the measures until the present time, the second phase, called *smoothing*, allows to determine the best estimate of the parameters at previous moments, taking into account the measures until the last time. The estimators are optimal in the Wiener−Kolmogorov sense, so have minimal variance and are normally distributed. The optimality is guaranteed but only until the assumptions in the model are valid. To ensure stability of the Kalman filter only the conditions of observability (or at least of detectability) of the uncontrolled system are required.
It was thought then to use an observer status, which can improve the quality of measurements. The base concept of this filter is to attribute certain percentage of reliability to the measures and the remaining to the dynamic model [10]. This level of trust is placed in the filter through the matrices Q and R that are respectively the covariance matrices of disturbances on the state and noise on measurements.
Taking filter status $x = \left\{x_F \; y_F \; \alpha_F \; \dot{x_F} \; \dot{y_F} \; \dot{\alpha_F} \; \dot{\vartheta}_1 \; \dot{\vartheta}_2 \; \dot{\vartheta}_3 \; \dot{\vartheta}_4\right\}^T$ where x_F e y_F are the components of the position the flyer expressed in the local reference system, α_F is the attitude, $\dot{x_F}$ and $\dot{y_F}$ are the velocity components of flyers expressed always in the local system $\dot{\alpha_F}$ is the spin speed, while $\dot{\vartheta}_1 \; \dot{\vartheta}_2 \; \dot{\vartheta}_3 \; \dot{\vartheta}_4$ are the rotation speed of the 4 fans, each of which is the state variable of the actuator dynamic system. As filter outputs only position, attitude, velocity and angular speed of the flyer[11] have been exploited: $y = \{x_F \; y_F \; \alpha_F\}^T$. Therefore the filter is:

$$\begin{aligned} \dot{x} &= Ax + Bu \\ y &= Cx + Du \end{aligned} \tag{5.78}$$

where

$$A = \begin{bmatrix} 0 & 0 & 0 & 1 & 0 & 0 & 0 & 0 & 0 & 0 \\ 0 & 0 & 0 & 0 & 1 & 0 & 0 & 0 & 0 & 0 \\ 0 & 0 & 0 & 0 & 0 & 1 & 0 & 0 & 0 & 0 \\ 0 & 0 & 0 & 0 & 0 & 0 & -\frac{\sqrt{2}K_f}{2m_F} & \frac{\sqrt{2}K_f}{2m_F} & \frac{\sqrt{2}K_f}{2m_F} & -\frac{\sqrt{2}K_f}{2m_F} \\ 0 & 0 & 0 & 0 & 0 & 0 & \frac{\sqrt{2}K_f}{2m_F} & \frac{\sqrt{2}K_f}{2m_F} & -\frac{\sqrt{2}K_f}{2m_F} & -\frac{\sqrt{2}K_f}{2m_F} \\ 0 & 0 & 0 & 0 & 0 & 0 & \frac{\sqrt{2}K_f a}{2I_F} & -\frac{\sqrt{2}K_f a}{2I_F} & \frac{\sqrt{2}K_f a}{2I_F} & -\frac{\sqrt{2}K_f a}{2I_F} \\ 0 & 0 & 0 & 0 & 0 & 0 & -\frac{D_{FAN}}{J_{FAN}} & 0 & 0 & 0 \\ 0 & 0 & 0 & 0 & 0 & 0 & 0 & -\frac{D_{FAN}}{J_{FAN}} & 0 & 0 \\ 0 & 0 & 0 & 0 & 0 & 0 & 0 & 0 & -\frac{D_{FAN}}{J_{FAN}} & 0 \\ 0 & 0 & 0 & 0 & 0 & 0 & 0 & 0 & 0 & -\frac{D_{FAN}}{J_{FAN}} \end{bmatrix} \tag{5.79}$$

[10] Actually the dynamics of the system is very well known, because the only disturbances that weren't modeled is the viscous friction due to air and the aerodynamic drag, although this will be very small since the velocities involved are low.

[11] Before passing the measure to filter the camera inertial measures should be rotated in the local reference system of the flyer.

$$B = \begin{bmatrix} 0 & 0 & 0 & 0 \\ 0 & 0 & 0 & 0 \\ 0 & 0 & 0 & 0 \\ 0 & 0 & 0 & 0 \\ 0 & 0 & 0 & 0 \\ 0 & 0 & 0 & 0 \\ \frac{K_m}{J_{FAN}} & 0 & 0 & 0 \\ 0 & \frac{K_m}{J_{FAN}} & 0 & 0 \\ 0 & 0 & \frac{K_m}{J_{FAN}} & 0 \\ 0 & 0 & 0 & \frac{K_m}{J_{FAN}} \end{bmatrix} \tag{5.80}$$

$$C = \begin{bmatrix} 1 & 0 & 0 & 0 & 0 & 0 & 0 & 0 & 0 & 0 \\ 0 & 1 & 0 & 0 & 0 & 0 & 0 & 0 & 0 & 0 \\ 0 & 0 & 1 & 0 & 0 & 0 & 0 & 0 & 0 & 0 \end{bmatrix} \tag{5.81}$$

$$D = \begin{bmatrix} 0 & 0 & 0 \\ 0 & 0 & 0 \\ 0 & 0 & 0 \end{bmatrix} \tag{5.82}$$

where all the parameters of the fans were already described in chapter 5.7, and m_F e I_F are respectively the mass and inertia of the flyer. The input vector u represents the current sent to the fans.

It should be intuitive the preference of considering the state vector measurement reported into the body frame, instead of the inertial reference system: that trick avoids to insert a trascendent dependency of accelerations from control actions provoked by the attitude matrix[12].

To start the filter information about the statistical characteristics of measurement noise and disturbances on the state are needed.. These quantities are well known as fas as software simulations run, since the disturbances are modeled as white noise, but in the real experiment to vary these quantities by trial until a correct reconstruction of the state is obtained is a more correct procedure.

$$R = \rho \begin{bmatrix} \sigma_{ax} & 0 & 0 \\ 0 & \sigma_{ay} & 0 \\ 0 & 0 & \sigma_{\omega} \end{bmatrix} \tag{5.83}$$

[12]In this case, the system became nonlinear and its solution would be more complicate.

$$Q = \begin{bmatrix} 1 & 0 & 0 & 0 & 0 & 0 & 0 & 0 & 0 & 0 \\ 0 & 1 & 0 & 0 & 0 & 0 & 0 & 0 & 0 & 0 \\ 0 & 0 & 1 & 0 & 0 & 0 & 0 & 0 & 0 & 0 \\ 0 & 0 & 0 & 0 & 0 & 0 & 0 & 0 & 0 & 0 \\ 0 & 0 & 0 & 0 & 0 & 0 & 0 & 0 & 0 & 0 \\ 0 & 0 & 0 & 0 & 0 & 0 & 0 & 0 & 0 & 0 \\ 0 & 0 & 0 & 0 & 0 & 0 & 0 & 0 & 0 & 0 \\ 0 & 0 & 0 & 0 & 0 & 0 & 0 & 0 & 0 & 0 \\ 0 & 0 & 0 & 0 & 0 & 0 & 0 & 0 & 0 & 0 \\ 0 & 0 & 0 & 0 & 0 & 0 & 0 & 0 & 0 & 0 \end{bmatrix} \tag{5.84}$$

where $\sigma_{ax} = 0.1$, $\sigma_{ay} = 0.1$, $\sigma_{\omega} = 0.1$ and ρ is a parameter that is used to restore consistency between the size of R and those of Q and is taken equal to 1.
Some further manipulations of the matrices of the system are required to map the continuous problem 5.78 in the discrete time domain:

$$\begin{gathered} A_k = I + A \cdot dt + \frac{(A \cdot dt)^2}{2!} + ... \\ B_k = \int_0^{dt} A_k \cdot B d\tau \\ Q_k = \int_0^{dt} A_k \cdot Q \cdot A_k^T d\tau \end{gathered} \tag{5.85}$$

where dt is the sampling time of the Kalman filter in simulation that has been put at $0.1[s]$ (the same as the controller). The matrices C, D and R remain unchanged even in the transition to discrete domain.
The last information necessary to start the Kalman filter is on the covariance matrix of errors between the actual state and the estimated at initial time. This matrix will be updated at every step of the filter and therefore an error on its initial estimate does not affect the convergence of the filter, for this reason it is initialized with the identity matrix.
The discrete-time Kalman filter algorithm is based on three basic steps:

$$\begin{gathered} P_k^- = A_k P_{k-1}^+ A_k^T + Q_k \\ K_k = P_k^- (C_k^T) \left(C_k P_k^- C_k^T + R \right)^{-1} \\ P_k^+ = (I - K C_k) P_k^- \end{gathered} \tag{5.86}$$

Now by weighting with the matrix K_k the value of the predicted variable by propagation of the state, with the error on the current measure::

$$\begin{gathered} x_{k+1} = A_k x_k + B_k u_k + K_k (y_k - C_k x_k - D u_k)) \\ y_{k+1} = C_k x_{k+1} + D u_k \end{gathered} \tag{5.87}$$

But the problem to insert in the observer module also the table disturbance[13] still remains. To cope with that problem, the acceleration due to the table thanks to the state x_{k+1} just estimated is computed and then corrected at every step with the double

[13]In addition to the table disturbance there would be, only for the SF, there is the effect of recoil due to activation of the clamp, but this effect is easily considered by integrating one or two times the force (constant) generated by the linear motor, in order to obtain the correction position or velocity component along the x axis of the local flyers.

integration of the acceleration disturbance over time (projected into the body frame) for the position and with single integration for the velocity.
The following figures show the relation between the actual and estimated positions and velocities for the two flyers in the two simulations.

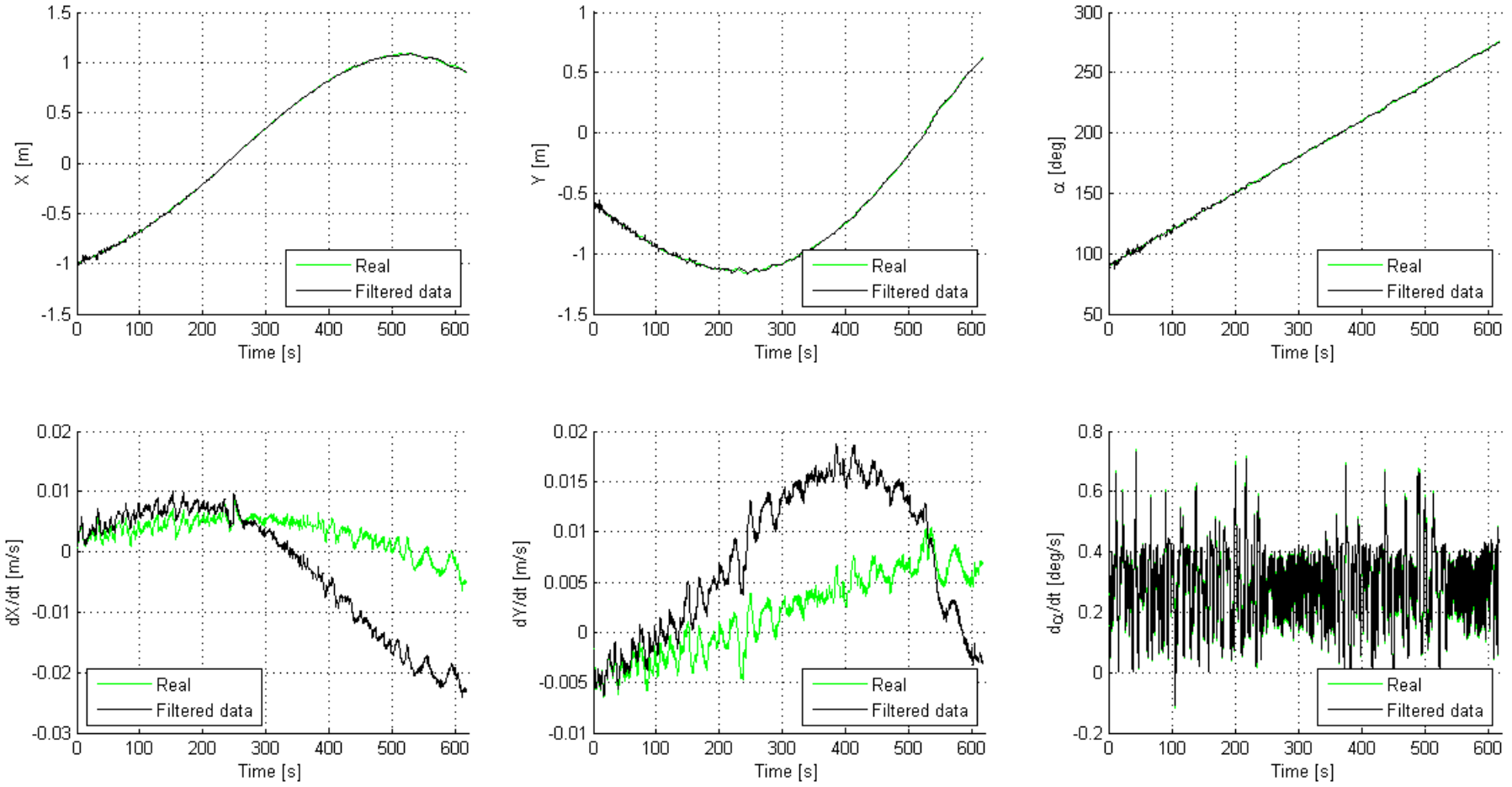

Figure 5.49: Comparison among the real and estimated state: TF - Simulation 1 - Controller PD

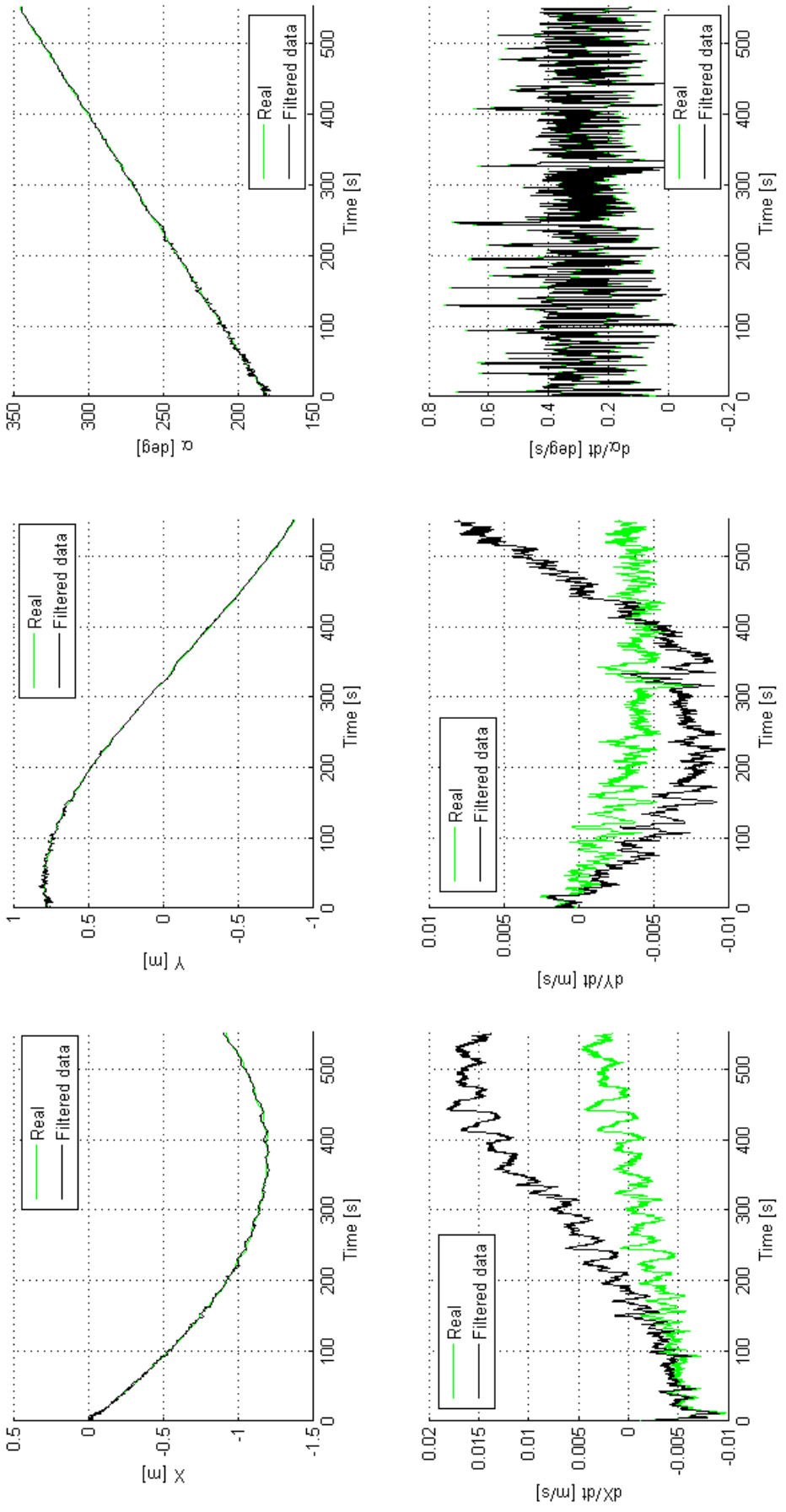

Figure 5.50: Comparison among the real and estimated state: TF - Simulation 2 - Controller PD

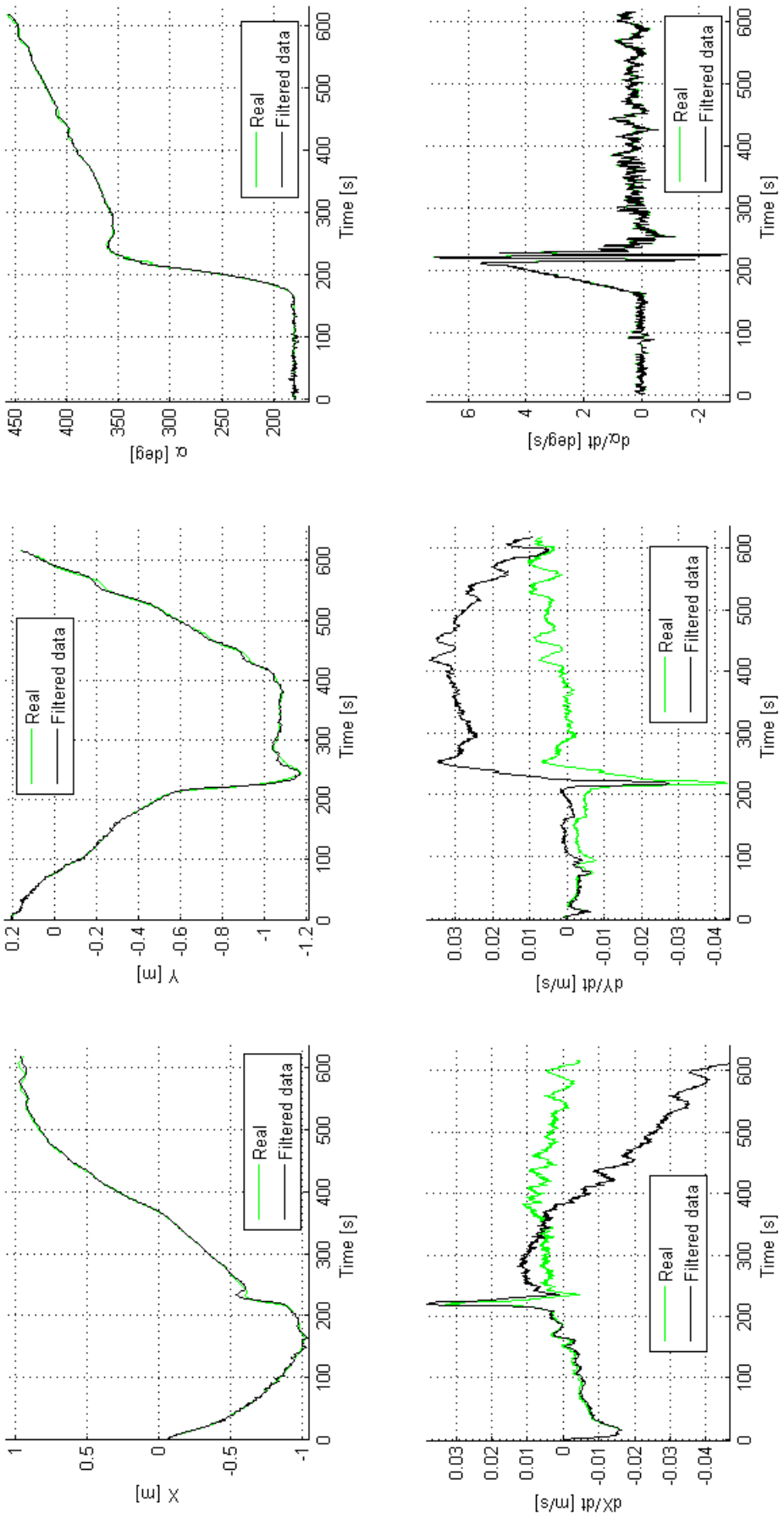

Figure 5.51: Comparison among the real and estimated state: SF - Simulation 1 - Controller PD

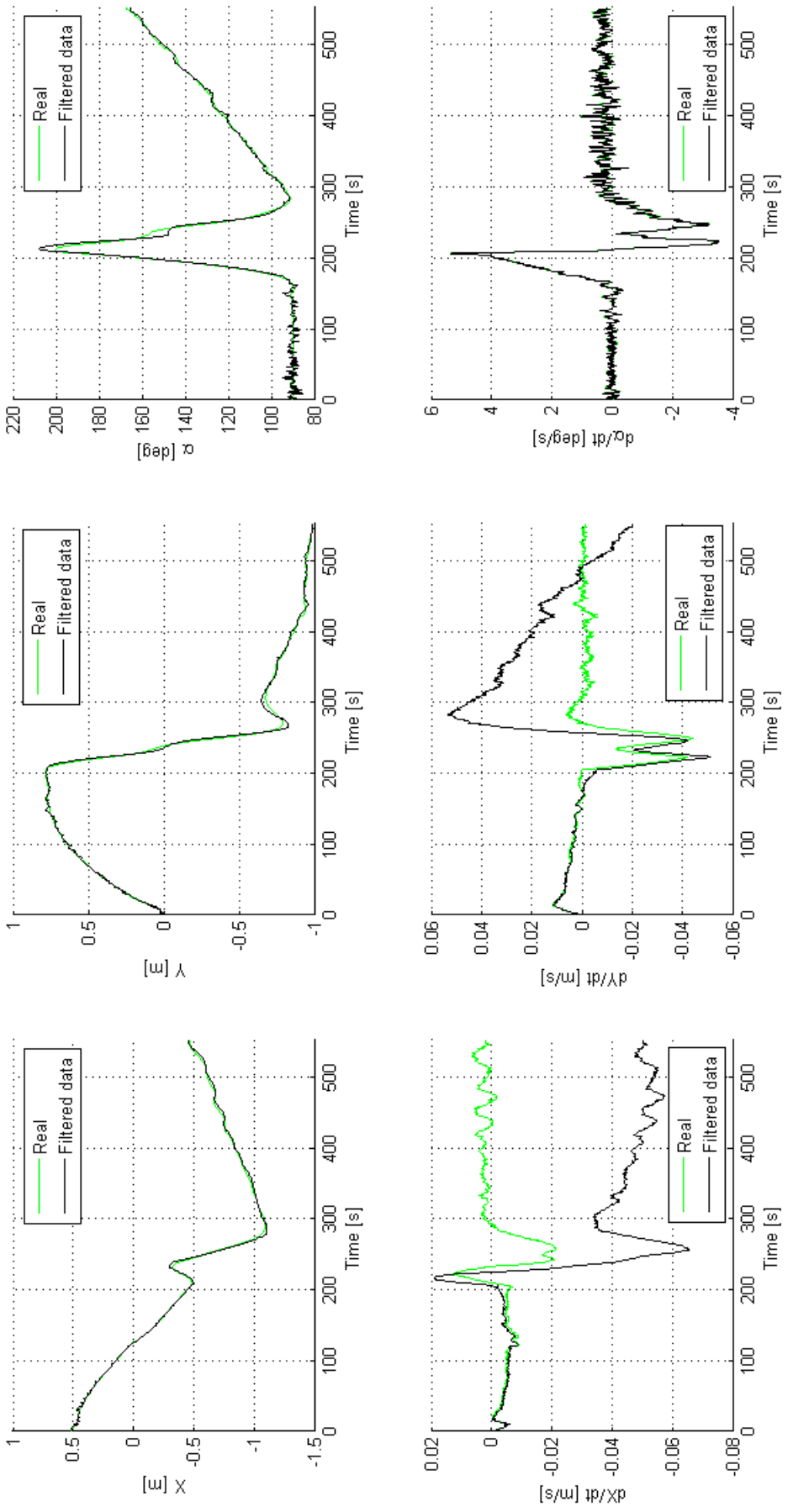

Figure 5.52: Comparison among the real and estimated state: SF - Simulation 2 - Controller PD

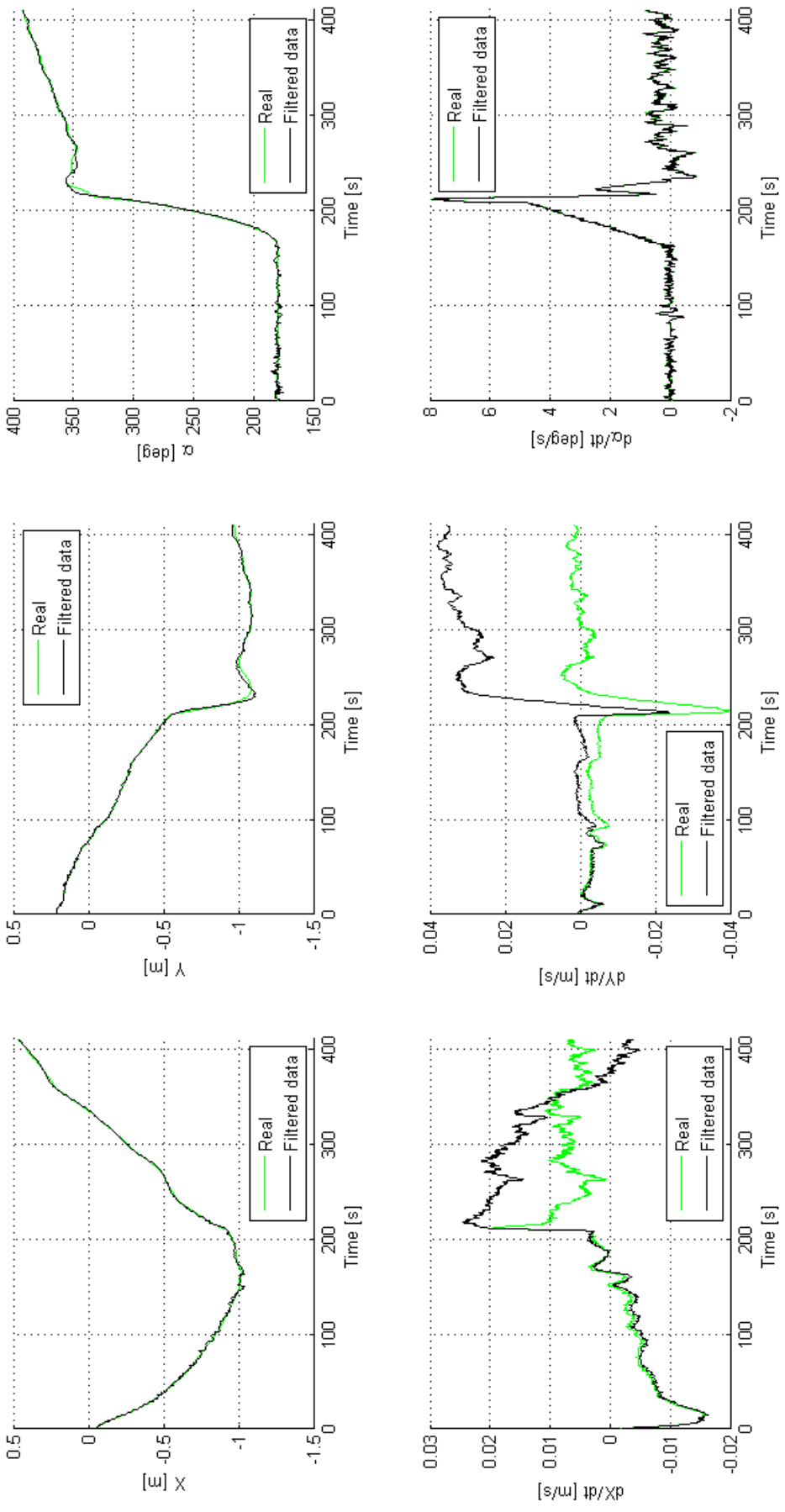

Figure 5.53: Comparison among the real and estimated state: SF - Simulation 1 - Controller LQR

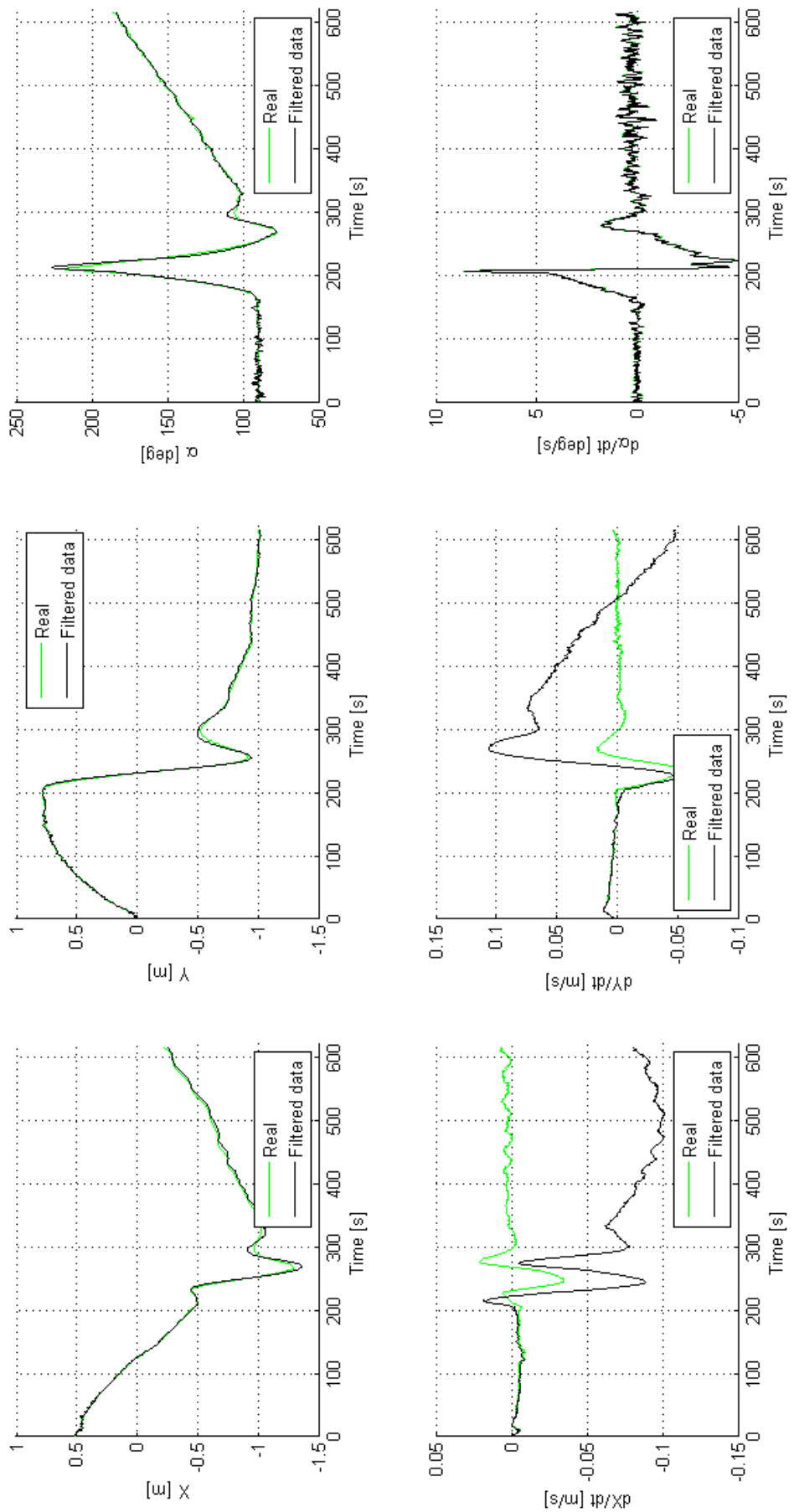

Figure 5.54: Comparison among the real and estimated state: SF - Simulation 2 - Controller LQR

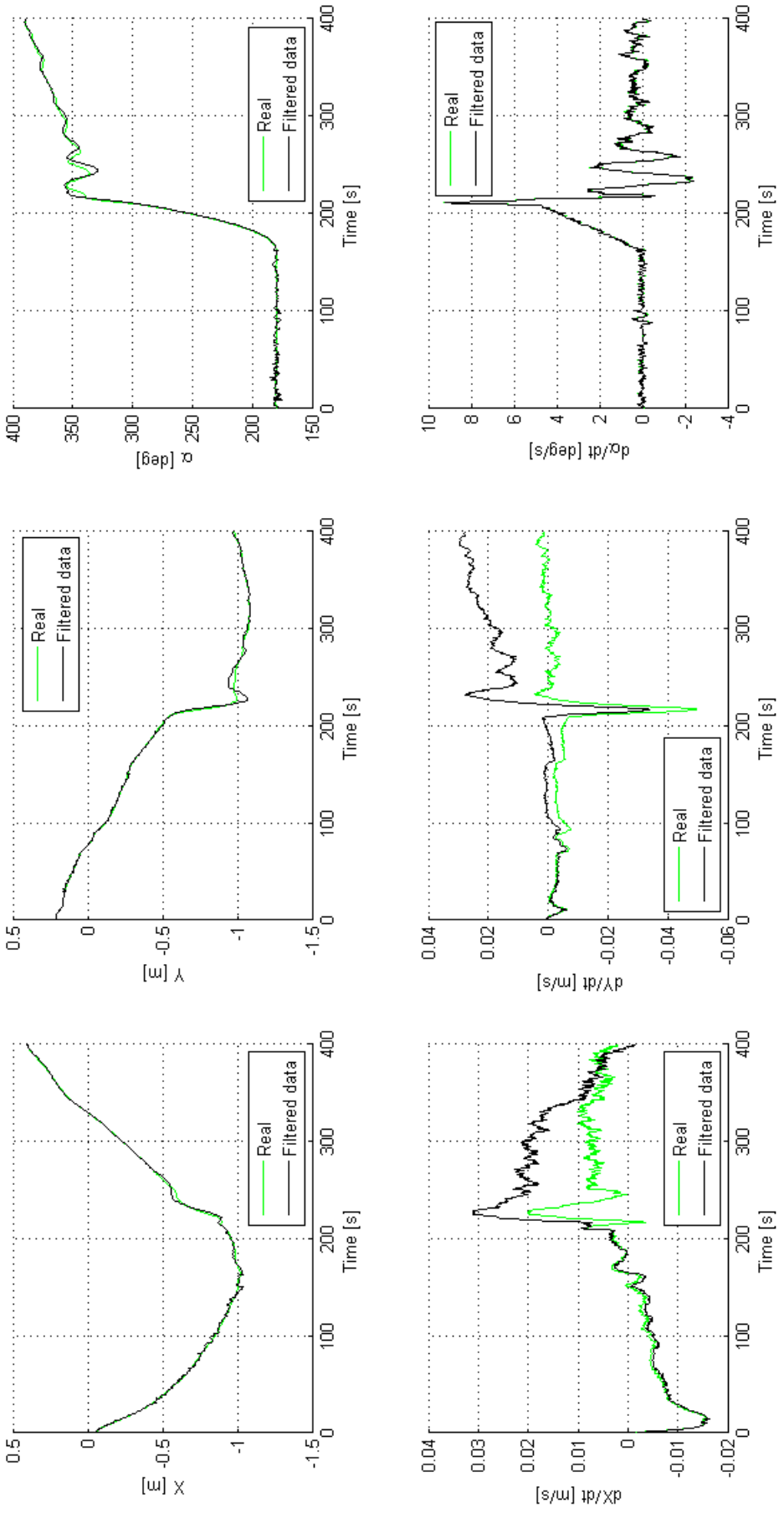

Figure 5.55: Comparison among the real and estimated state: SF - Simulation 1 - Controller NL

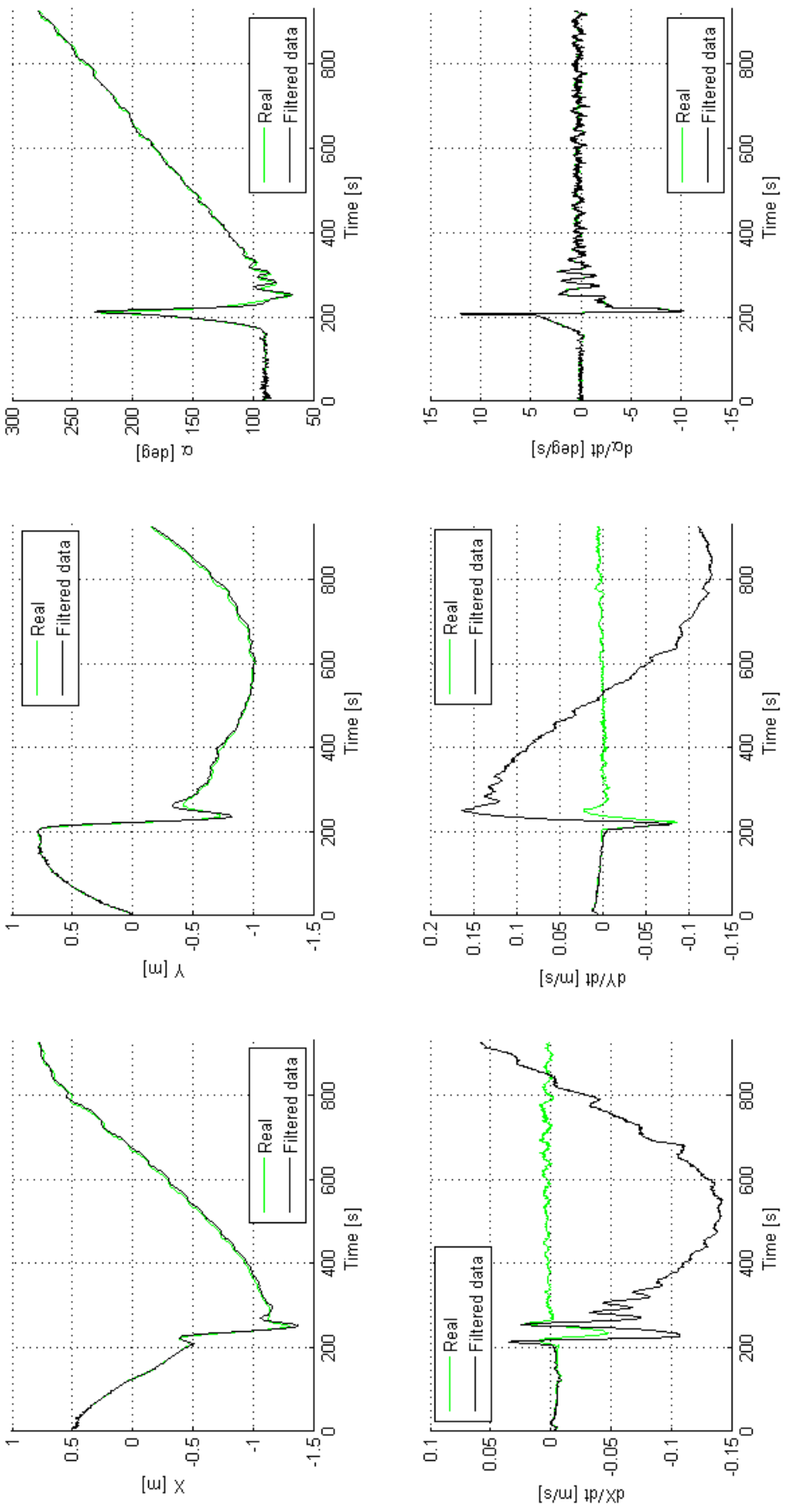

Figure 5.56: Comparison among the real and estimated state: SF - Simulation 2 - Controller NL

The Kalman filter results show good propagation and filtering property for the position vector, attitude and angular velocity. While concerning the velocity vector, its components are still noisy. Probably an appropriate changing in the weight matrix could reduce the problem. Despite this noise, the implemented controllers successfully complete the docking mission: see 5.13.

5.12 Target Flyer controller

The low accuracy requirements on the TF position and the simplicity of the trajectory that it will follow (see 5.6 and 5.7), mean that for the control of this system is sufficient a proportional controller, so with the control forces proportional to error according to the gains matrix:

$$G_{Orbital}^{TF} = \begin{bmatrix} 0.65 & 0 & 0 & 5 & 0 & 0 \\ 0 & 0.65 & 0 & 0 & 5 & 0 \\ 0 & 0 & 0.01 & 0 & 0 & 0.35 \end{bmatrix} \tag{5.88}$$

The control forces are then computed by writing $u = -G(x - x_{target}) = G(x_{target} - x)$. It should be remembered that the control variables are not directly forces but the currents to be supplied to the fans, so it is necessary to realize a distribution and saturation software that can ensure the desired forces and torques. This application is discussed in detail in chapter 5.14. Moreover, the necessary forces are not exactly those obtained by the relation $u = G(x_{target} - x)$ for the simple fact that these are defined in the inertial reference system, and therefore must rotate through the cosines matrix.

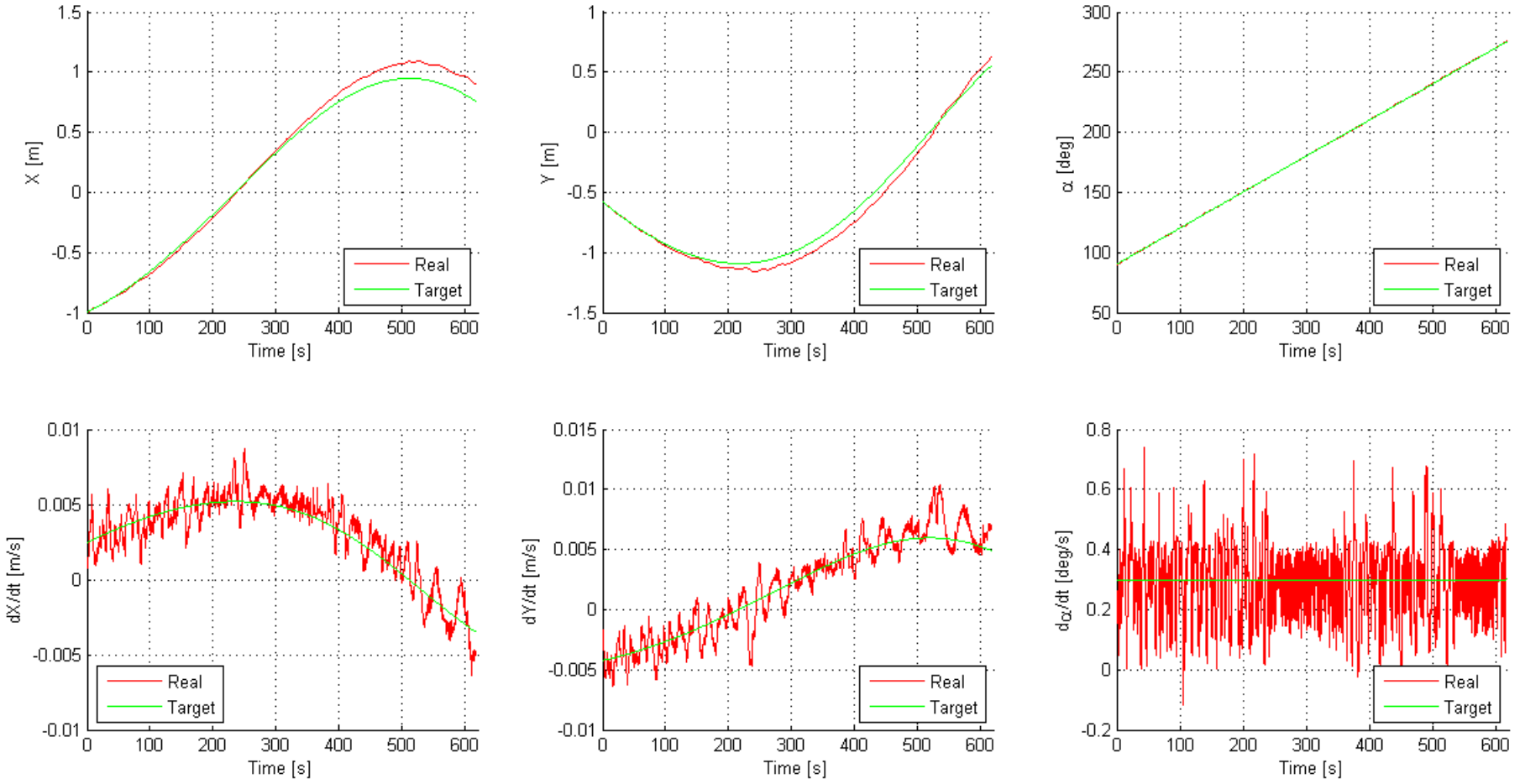

Figure 5.57: Comparison among the real and target state: TF - Simulation 1 - Proportional Controller

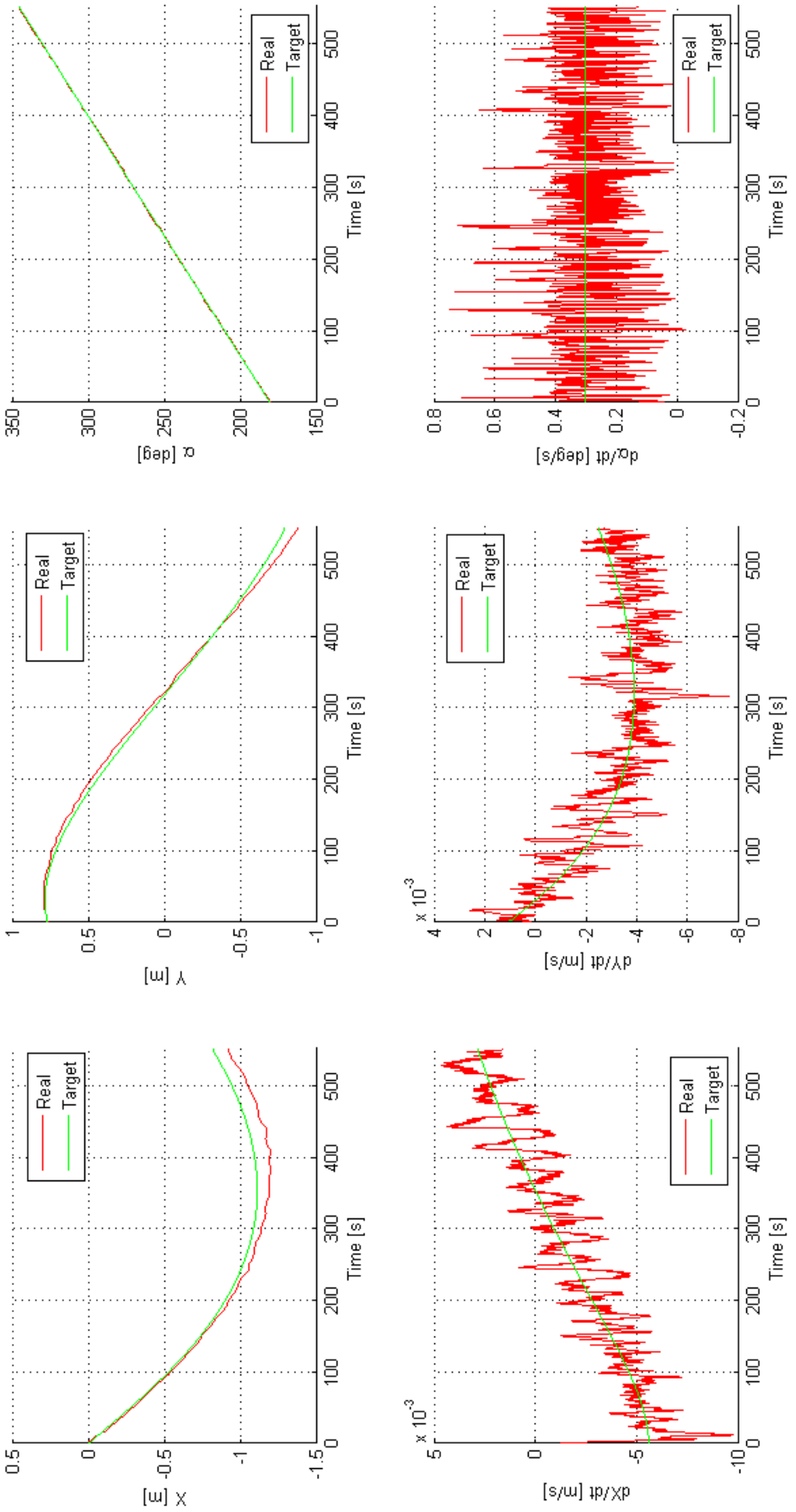

Figure 5.58: Comparison among the real and target state: TF - Simulation 2 - Proportional Controller

In the figures 5.57 and 5.58 it's possible to observe that a simple proportional controller is sufficient to simulate orbital dynamic.

5.13 Smart Flyer controller

Different control startegies have been considered to identfy the best suited for the current application. However, these controllers have to require a limited number of steps to ensure that the limited power of the SF onboard computer precludes the pursuit of its goal.
Before proceeding to summarize the different control methods of the chaser the reachability (or stabilizability) in the system must be checked. The reachability matrix is computed as:

$$K_R = \begin{bmatrix} B & AB & A^2B & ... & A^{n-1}B \end{bmatrix} \tag{5.89}$$

with $n = 6$ while $B = \begin{bmatrix} 0 & 0 & 0 \\ 0 & 0 & 0 \\ 0 & 0 & 0 \\ \frac{1}{m_{SF}} & 0 & 0 \\ 0 & \frac{1}{m_{SF}} & 0 \\ 0 & 0 & \frac{1}{I_{SF}} \end{bmatrix}$ and $A = \begin{bmatrix} 0 & 0 & 0 & 1 & 0 & 0 \\ 0 & 0 & 0 & 0 & 1 & 0 \\ 0 & 0 & 0 & 0 & 0 & 1 \\ 0 & 0 & 0 & 0 & 0 & 0 \\ 0 & 0 & 0 & 0 & 0 & 0 \\ 0 & 0 & 0 & 0 & 0 & 0 \end{bmatrix}$.

The rank of K_R is 6, so it will be completely accessible and it is therefore possible to assign all eigenvalues of the closed loop system via the state feedback.
As it is going to be described below the chaser has to different operating conditions: from the simple orbital transfer, to the alignment with the target until the final docking, and in this three phases the controllers has different needs and must ensure different performances. It is therefore necessary to vary its properties by acting on some decision parameters.

- During the transfer orbit, the controller must be simply able to track a given trajectory without restrictive requirements of precision, so a proportional controller will suffice. The gains matrix chosen is:

$$G^{SF}_{Orbital} = \begin{bmatrix} 0.5 & 0 & 0 & 5 & 0 & 0 \\ 0 & 0.5 & 0 & 0 & 5 & 0 \\ 0 & 0 & 0.01 & 0 & 0 & 0.35 \end{bmatrix} \tag{5.90}$$

- Only in special missions can happen that at the end of the transfer orbit, the chaser before starting the final approach should make manoeuvres to get around the target in order to align with it, and in these cases the error status can vary greatly, generating high control forces. Nevertheless, the alignment phase is still one of the stages of docking and thus the same controller used in the final approach is exploited, perhaps with a matrix of gains that generates more cautious control actions.

- In the final approach phase the error varies very little around zero, therefore the gains will be high in order to generate appropriate control forces.

The controllers described in the following paragraphs refer to the alignment phase and to the final approach, because like has been showed for the Target flyer to simulate a scaled orbital motion a simple proportional controller is sufficient.

5.13.1 PD controller

The simplest controller that can be achieved is the proportional-derivative. The success of these regulators is related to several factors:

1. highly effectiveness in regulating a wide range of processes;
2. relative simplicity of calibration;
3. the poor performance of many control systems are caused by the sensors and actuators problems such as bad calibration, filtering noise, hysteresis, etc., and with these problems, the role of control law can become modest, so there is less motivation to seek more sophisticated controller than PD [24].

In summary, this type of controllers have success because they represent a solution not easily overcome, generally in the ratio efficacy/cost. PD control laws are composed of combinations of elementary actions of control: the proportional action and derivative. This last action deserves a little consideration: the derivative action is complementary to the integral one (because it is originally null) but deriving also the components of signals at high frequencies and affected by noise, the derivative action can cause excessive moving of actuators, with premature wear, and possible troubles to the process. Therefore, the presence of noise on the measurement signals condition the use of fans and could be useful to associate to the control law a low-pass filter that limits the gain at high frequency. Therefore the noise amplification level is limited by introducing a first order filter, with the following transfer function:

$$F(s) = \frac{1}{1 + sT_D/N} \tag{5.91}$$

with N between 5 and 30.
Actually in the ADS the excessive movement of the actuators is limited by the fact that the control actions are modulated in amplitude as is described in section 5.14.2. So the fans are activated only when the integral of the required current exceeds a certain threshold, so in this case the low pass filter on derivative action becomes useless.
In this way the transfer function of the controller takes the form:

$$PD(s) = K^{SF}\left(1 + sT_D\right) \tag{5.92}$$

while the discrete control action becomes:

$$\underline{u_k} = K^{SF}\left(e_k + T_D\frac{(e_k - e_{k-1})}{dt}\right) \tag{5.93}$$

Where it has been used $T_D = 0.015$ for both the alignment and final docking phase:

$$K^{SF}_{Align.} = \begin{bmatrix} 0.1 & 0 & 0 & 3 & 0 & 0 \\ 0 & 0.1 & 0 & 0 & 3 & 0 \\ 0 & 0 & 0.1 & 0 & 0 & 0.7 \end{bmatrix} \tag{5.94}$$

$$K^{SF}_{Docking} = \begin{bmatrix} 0.65 & 0 & 0 & 3 & 0 & 0 \\ 0 & 0.65 & 0 & 0 & 3 & 0 \\ 0 & 0 & 0.1 & 0 & 0 & 0.12 \end{bmatrix} \tag{5.95}$$

Unlike the orbital phase in this two phases the error is generated in the body frame system, so the control actions must not be rotated. It is absolutely required to properly distribute the forces to the four fans, so to get the current to be supplied (see section 5.14).

The synthesized controller, however, does not take into account the acceleration of interference due to concavity of the table; it is possible to compensate these disorders by purifying the control forces. As soon as the state (estimated by the Kalman filter) the table deflection at the point where the chaser is can be estimated, as described in section 5.10. Then the control forces applied are:

$$\underline{\widetilde{u}_k} = \underline{u_k} - m_{SF} B_d a_d \tag{5.96}$$

where $B_d = \begin{bmatrix} 1 & 0 & 0 \\ 0 & 1 & 0 \\ 0 & 0 & 0 \end{bmatrix}$ while $a_d = \begin{Bmatrix} a_{dx} \\ a_{dy} \\ 0 \end{Bmatrix}$.

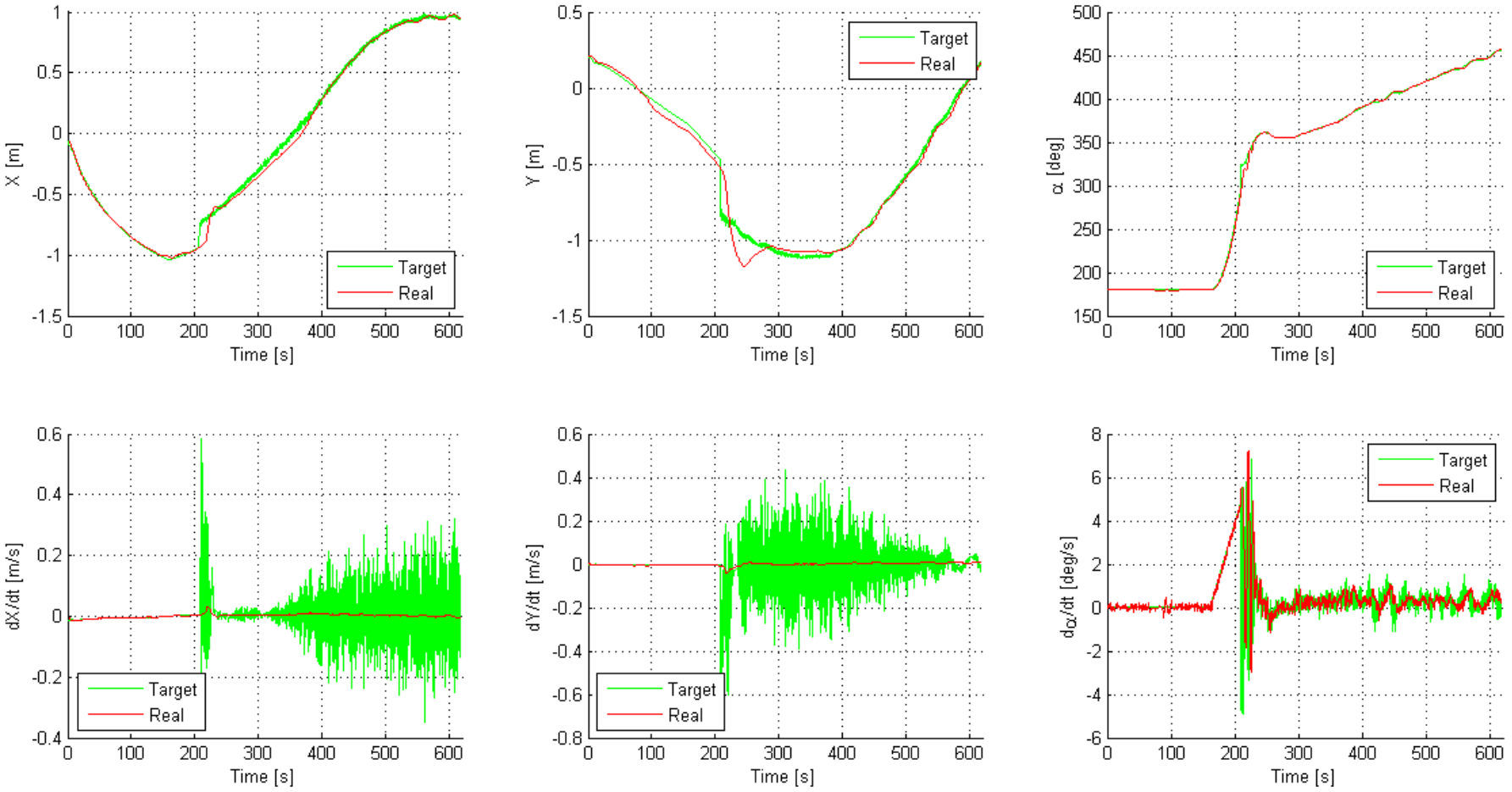

Figure 5.59: Target and real state: SF - Simulation 1 - Controller PD

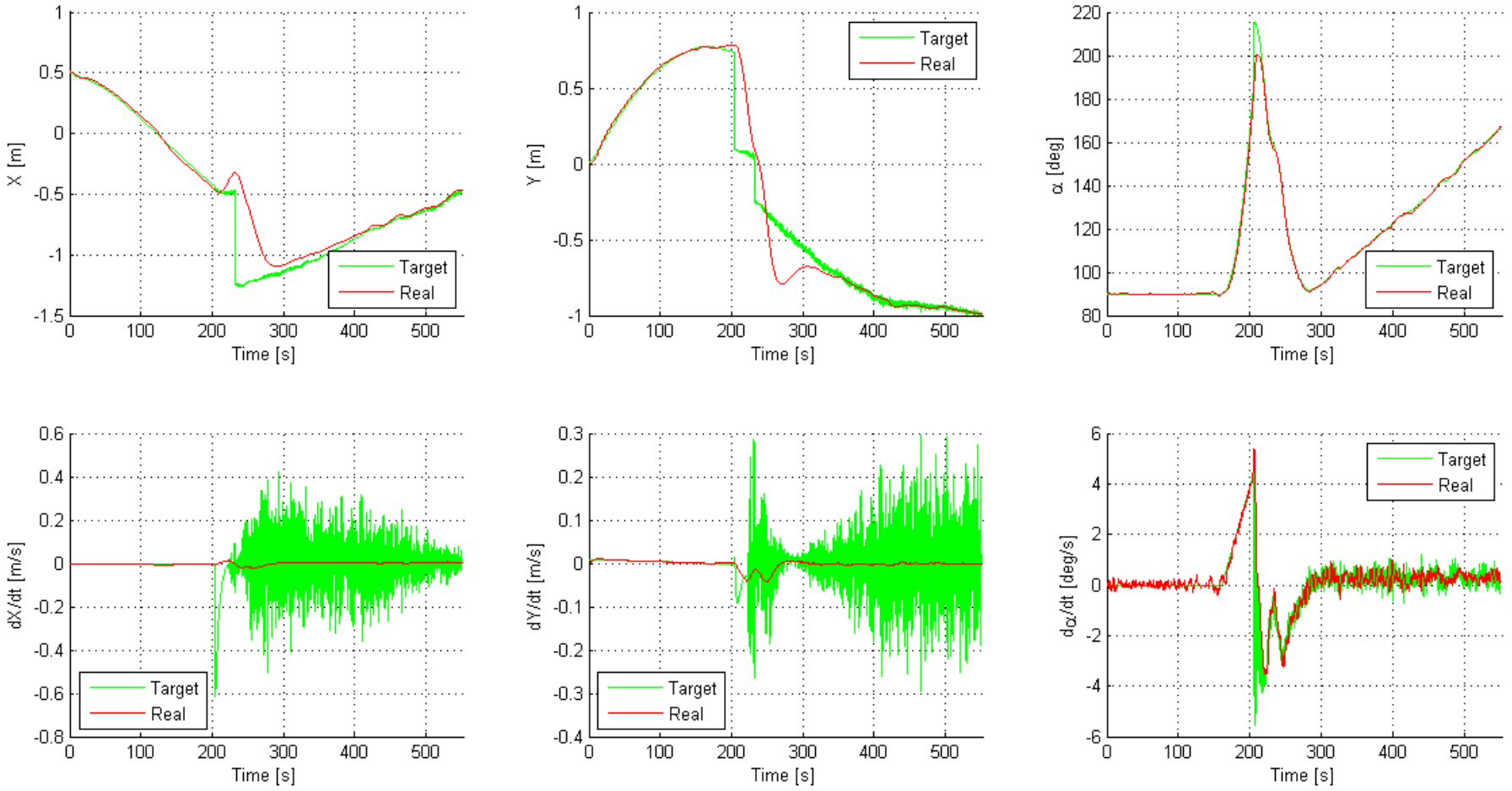

Figure 5.60: Target and real state: SF - Simulation 2 - Controller PD

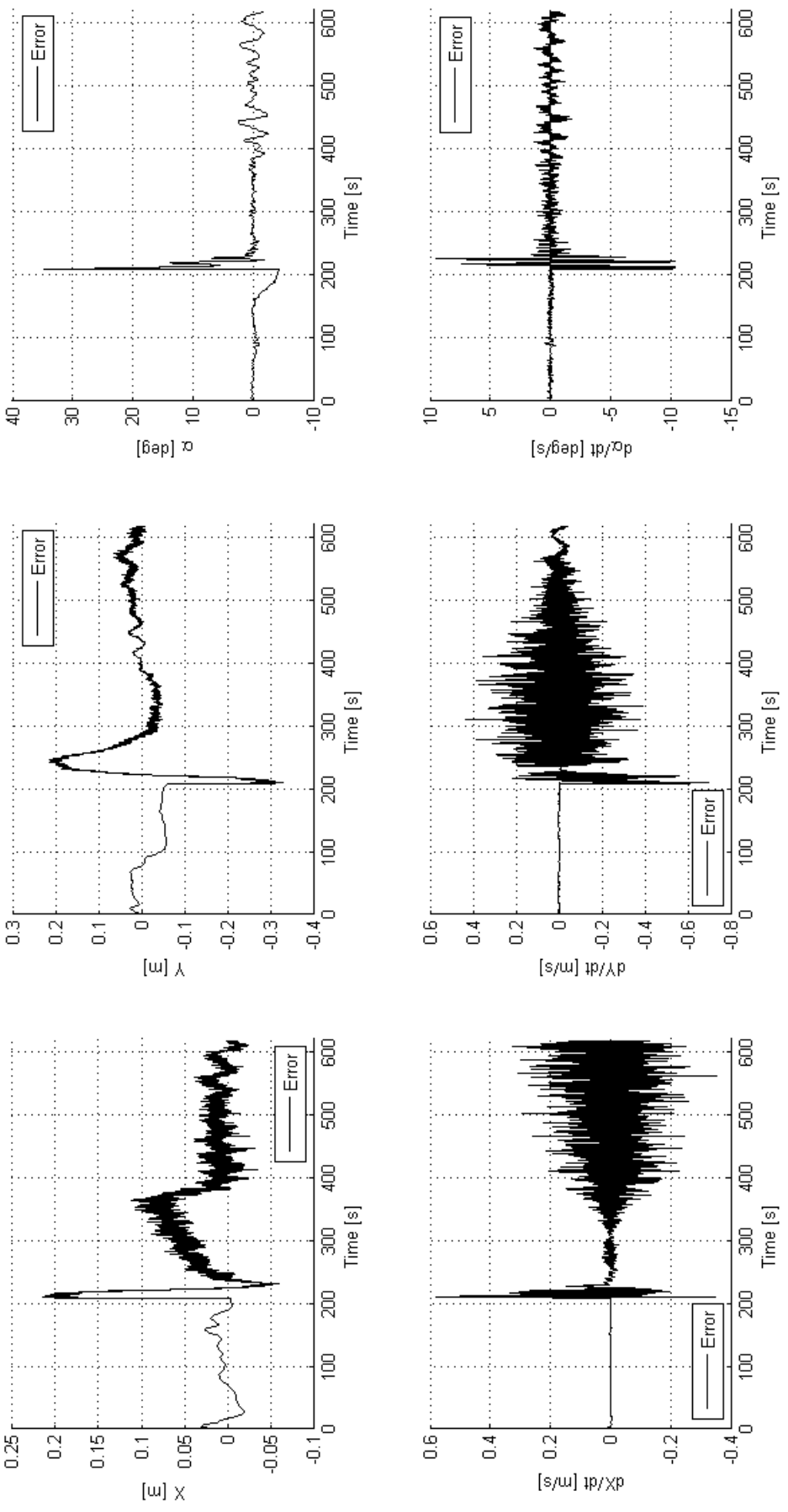

Figure 5.61: Error between target and real state: SF - Simulation 1 - Controller PD

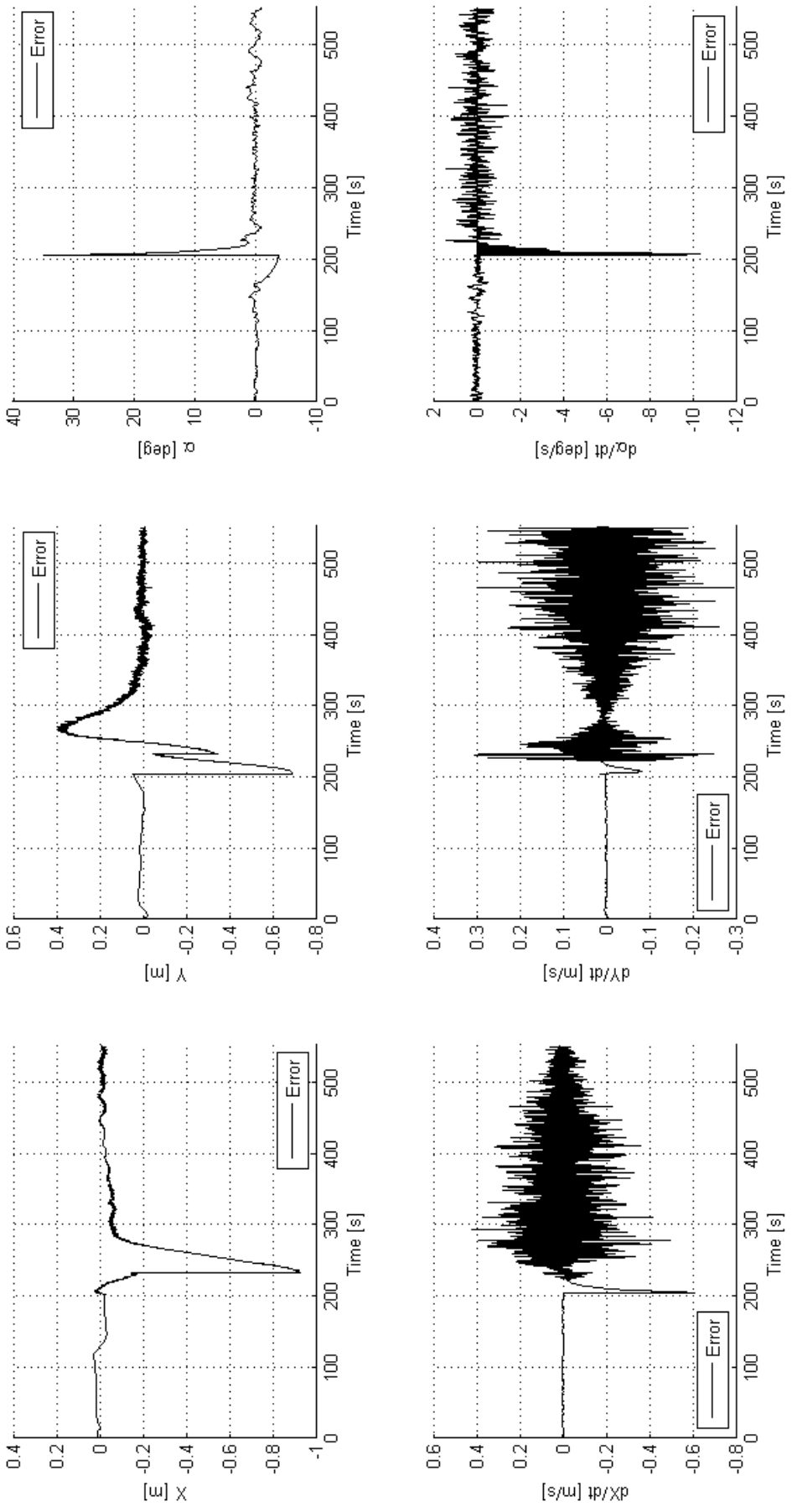

Figure 5.62: Error between target and real state: SF - Simulation 2 - Controller PD

The results reported in the figures above show that the PD controller enables to follow its target path during the transfer phase. When the docking controller is activated (about at 220 s) a quick error increase is reasonable. This error increase is reduced with the time and the fluctuations in velocity vector are caused by the numerical derivative of the relative position measures, and also by the fact that the position measures are not filtered by the Kalman filter.

5.13.2 Linear quadratic regulator

As an alternative the linear quadratic regulator has been considered. This technique it tries to minimize the quadratic cost function subject to the boundary condition defined by the dynamics of the system $\dot{x} = Ax + Bu$ introduced by Lagrange multipliers [14].

$$F = \frac{1}{2}\int_0^{dt} \left(x^T Q x + u^T R u + 2\lambda^T \left(Ax + Bu - \dot{x}\right)\right) d\tau \tag{5.97}$$

The first term in the cost function 5.97 is the norm of the error state, while the second term is a generalization of the energy system, where Q and R are respectively a positive semidefinite matrix and a positive definite matrix of appropriate size (in this case Q is a 6x6 and R is a 3x3). For a known theorem, the stabilizing solution can be obtained under the strictly constraint of asymptotic stability of the uncontrolled system, while in absence of such property it should have accessibility (stabilizability) for the pair A, B and observability (or least detection) for the pair A, C_z. Thus in the case of Smart Flyer, which is an unstable, but fully accessible system it is sufficient to choose the matrix Q so that the C_z obtained as the factorization of Q (see 5.98 where W_{zz} is the matrix with which to weigh the required performance) ensures at least the detectability of the pair A, C_z.

$$Q = C_z^T W_{zz} C_z \tag{5.98}$$

Then the feedback matrix is:

$$G = R^{-1} B^T P \tag{5.99}$$

where P is the solution of algebraic Riccati 5.100.

$$PA + A^T P - PRP + Q = 0 \tag{5.100}$$

The main problem consists in determining the Q and R matrix. It is actually only to determine the matrix Q, because only the relative magnitudes of the elements of Q and R changes the control. Therefore R has been chosen equal to ρI_{3x3} where $\rho = 10$

while $Q_{Allin.} = \begin{bmatrix} 0.1 & 0 & 0 & 0 & 0 & 0 \\ 0 & 0.1 & 0 & 0 & 0 & 0 \\ 0 & 0 & 0.1 & 0 & 0 & 0 \\ 0 & 0 & 0 & 0 & 0 & 0 \\ 0 & 0 & 0 & 0 & 0 & 0 \\ 0 & 0 & 0 & 0 & 0 & 0.5 \end{bmatrix}$ $Q_{Docking} = \begin{bmatrix} 2 & 0 & 0 & 0 & 0 & 0 \\ 0 & 2 & 0 & 0 & 0 & 0 \\ 0 & 0 & 0.1 & 0 & 0 & 0 \\ 0 & 0 & 0 & 0 & 0 & 0 \\ 0 & 0 & 0 & 0 & 0 & 0 \\ 0 & 0 & 0 & 0 & 0 & 0.5 \end{bmatrix}$

It is known that in the cost function 5.97 R and Q matrices in practice represent the *price* of variables $\underline{x}(t)$ and $\underline{u}(t)$. If Q is relatively large compared to R, the optimization procedure provides a state $\underline{x}(t)$ relatively small compared to the input $\underline{u}(t)$ (since high amplitudes of$\underline{x}(t)$ are *expensive*). This corresponds to prefer the control speed than the limit in the required force. Vice versa if Q is relatively small compared to R, priority is given to the limitations of control.
For the system in exam, in particular, is necessary to reduce the control action in order to avoid the fans saturation. With this choice the following matrices of state feedback have been obtained:

$$G_{Align.} = \begin{bmatrix} 0.1 & 0 & 0 & 1.789 & 0 & 0 \\ 0 & 0.1 & 0 & 0 & 1.789 & 0 \\ 0 & 0 & 0.1 & 0 & 0 & 0.324 \end{bmatrix} \tag{5.101}$$

$$G_{Docking} = \begin{bmatrix} 0.447 & 0 & 0 & 3.783 & 0 & 0 \\ 0 & 0.447 & 0 & 0 & 3.783 & 0 \\ 0 & 0 & 0.1 & 0 & 0 & 0.324 \end{bmatrix} \tag{5.102}$$

The control forces are thus defined as:

$$\underline{u_k} = -G\underline{e_k} \tag{5.103}$$

Also in this case the note done while discussing the PD controller applies: the forces can be purified with the disturbances generated from the table:

$$\underline{\widetilde{u}_k} = \underline{u_k} - m_{SF} \begin{bmatrix} 1 & 0 & 0 \\ 0 & 1 & 0 \\ 0 & 0 & 0 \end{bmatrix} \begin{Bmatrix} a_{dx} \\ a_{dy} \\ 0 \end{Bmatrix} \tag{5.104}$$

However, it remains the problem of getting the two forces and torque, so determined by the 4 fans available, avoiding of course the saturation: it is an underdetermined problem, whose solution is described in chapter 5.14.

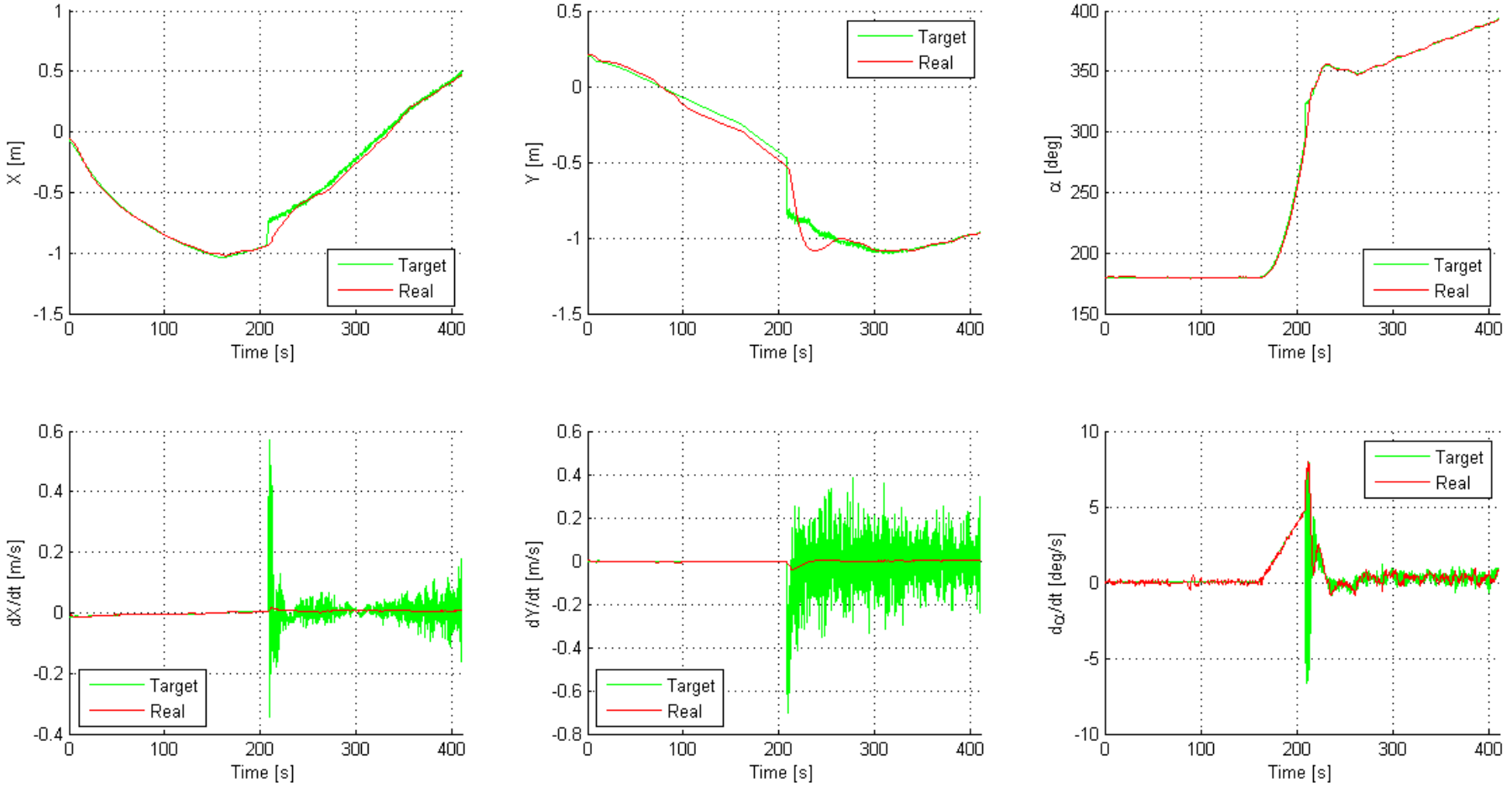

Figure 5.63: Target and real state: SF - Simulation 1 - Controller LQR

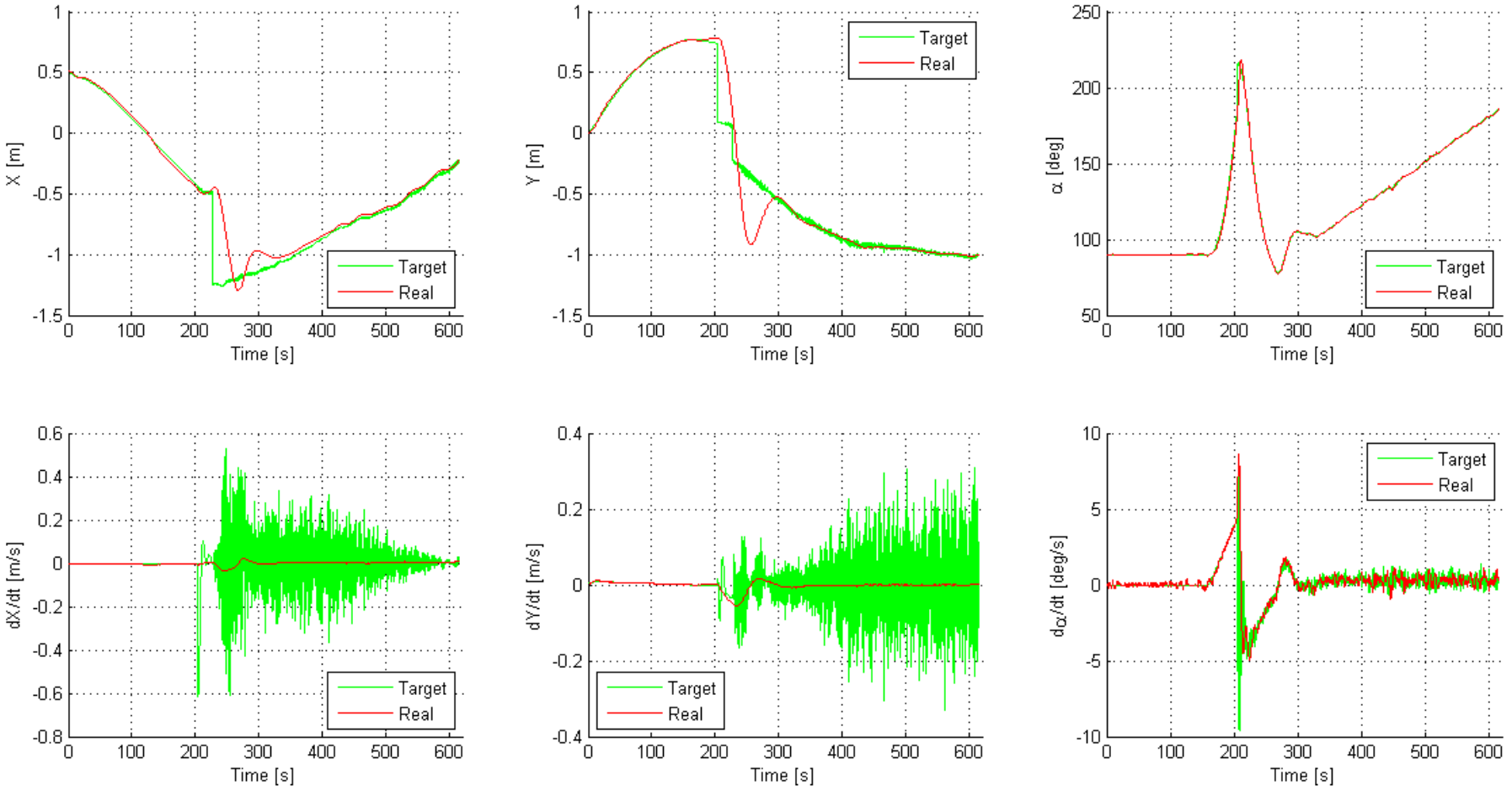

Figure 5.64: Target and real state: SF - Simulation 2 - Controller LQR

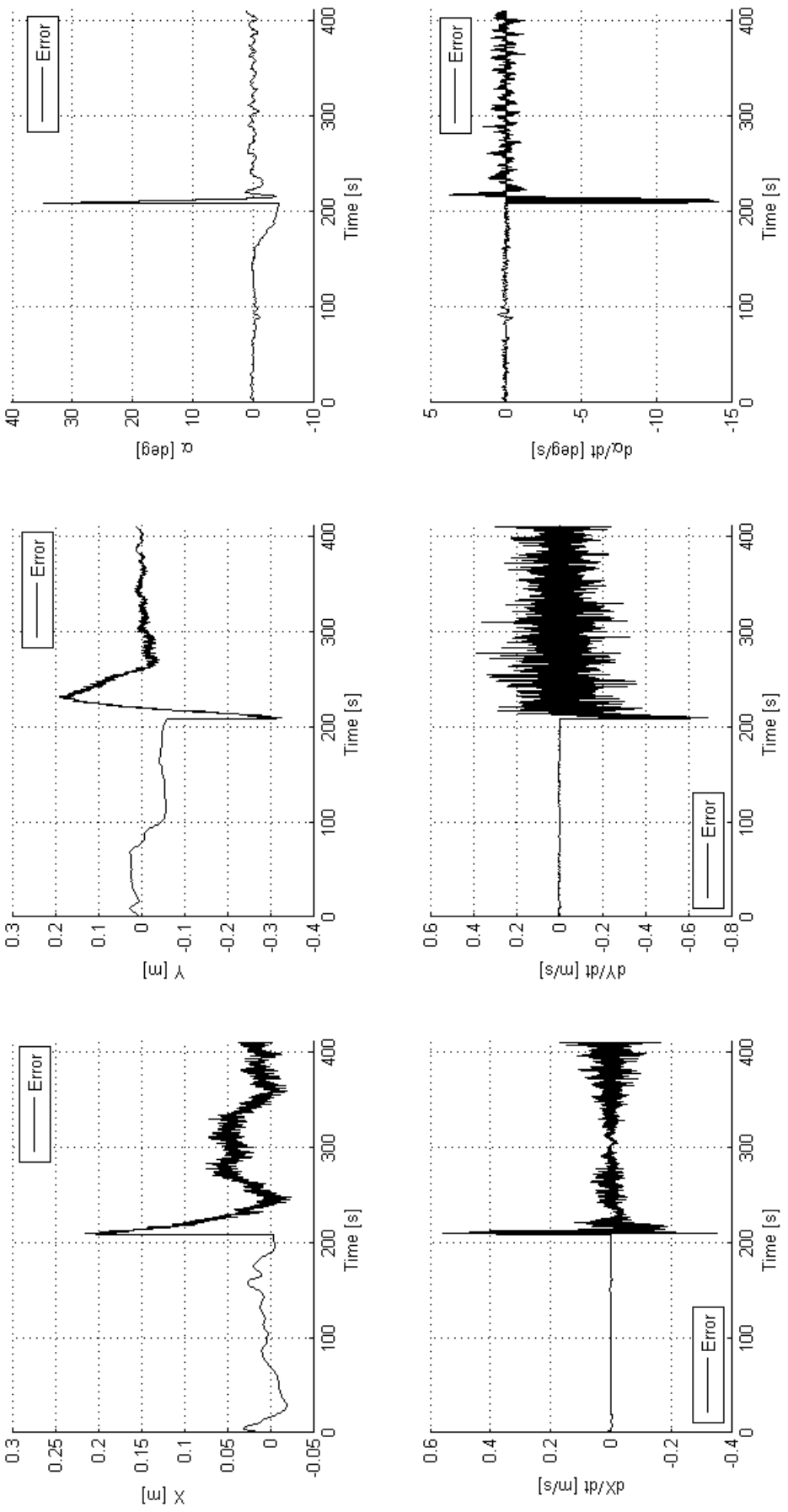

Figure 5.65: Error between target and real state: SF - Simulation 1 - Controller LQR

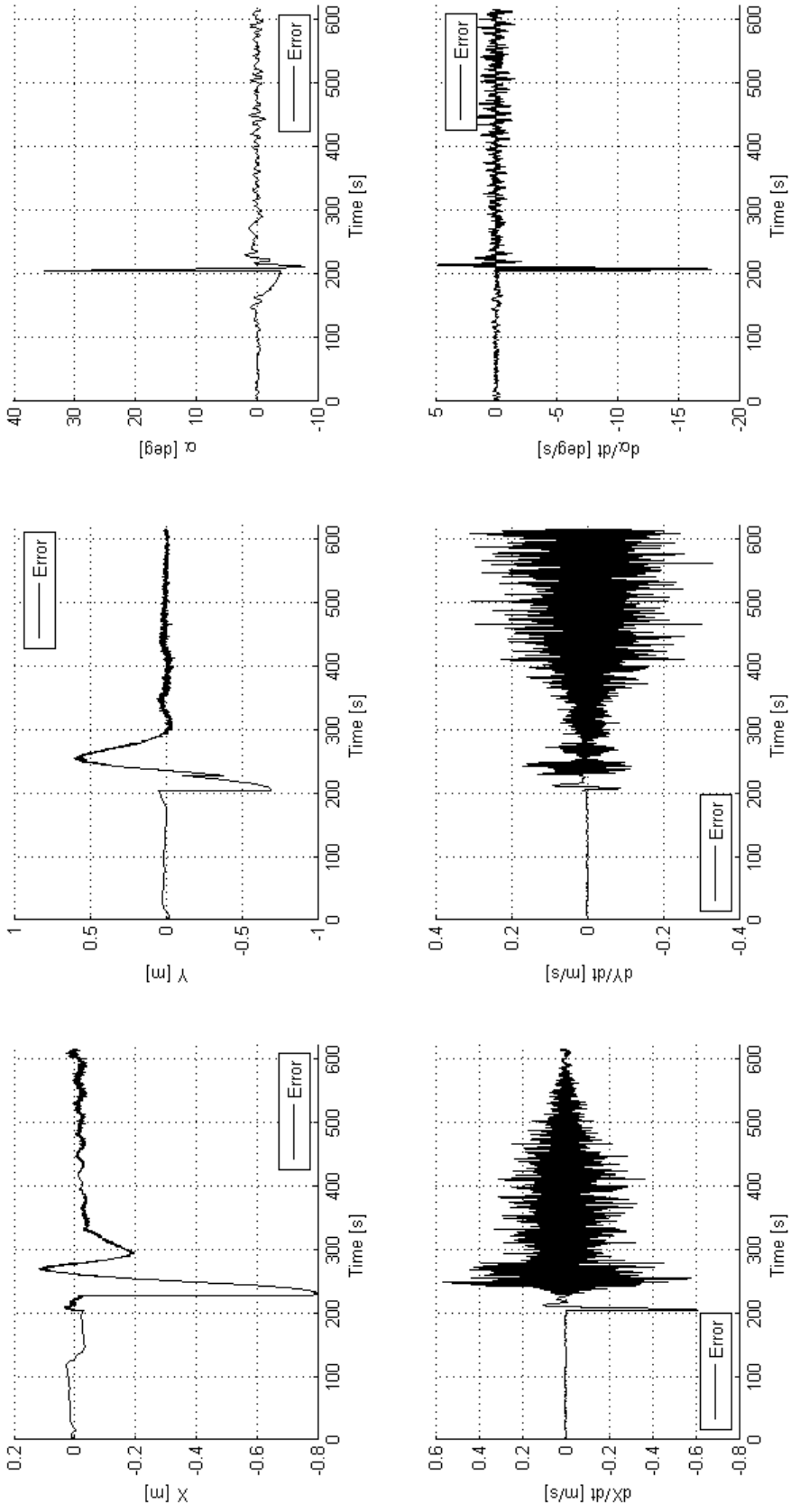

Figure 5.66: Error between target and real state: SF - Simulation 2 - Controller LQR

Te LQR controller performs the docking with less fluctuation than PD controller but takes more time to complete the mission in both simulations: see 5.8. The problem on the velocity vector fluctuation still remains but such fluctuations don't give fluctuating control forces because the controller output pass through the PWM module that calculate the integral of the required current and turn on the fan only when a fixed threshold is crossed: see 5.14.2.

5.13.3 Non linear controller

The last method here considered for the control implementation is based on a non-linear control law. The laws most commonly used include an array of gains that vary either with the exponential error or its root. Those laws have the advantage that their authority varies depending on that the system is either away or close to the desired condition.
The nonlinear control law that gave the best results in all simulations done follows:

$$\underline{u_k} = G \left(\begin{bmatrix} e^{-|e_{kx}|} & 0 & 0 & e^{-|e_{k\dot{x}}|} & 0 & 0 \\ 0 & e^{-|e_{ky}|} & 0 & 0 & e^{-|e_{k\dot{y}}|} & 0 \\ 0 & 0 & 0 & 0 & 0 & 0 \end{bmatrix} + \begin{bmatrix} 0 & 0 & 0 & 0 & 0 & 0 \\ 0 & 0 & 0 & 0 & 0 & 0 \\ 0 & 0 & \sqrt{|e_{k\alpha}|} & 0 & 0 & \sqrt{|e_{k\dot{\alpha}}|} \end{bmatrix} \right) \underline{e_k} \tag{5.105}$$

The constants in the G matrix are chosen so that the desired forces are achievable by the actuators:

$$G = \begin{bmatrix} \frac{g_{xy}}{g_k} & 0 & 0 & \frac{1}{g_k} & 0 & 0 \\ 0 & \frac{g_{xy}}{g_k} & 0 & 0 & \frac{1}{g_k} & 0 \\ 0 & 0 & \frac{g_\alpha}{g_c} & 0 & 0 & \frac{1}{g_c} \end{bmatrix} \tag{5.106}$$

where $g_{xy} = 0.04$, $g_a = 0.15$, $g_c = 2$ e $g_k = 0.2$.
Please note that for the nonlinear controller implemented is not necessary to distinguish between alignment phase and final docking because its authority ois variable and so with a single controller it's possible to manage the entire docking process.
Again it's valid the same reasoning done for the two previous controllers on the fact that these forces may be purified with the contribution of disturbance generated from the table deflection:

$$\widetilde{u}_k = u_k - m_{SF} \begin{bmatrix} 1 & 0 & 0 \\ 0 & 1 & 0 \\ 0 & 0 & 0 \end{bmatrix} \begin{Bmatrix} a_{dx} \\ a_{dy} \\ 0 \end{Bmatrix} \tag{5.107}$$

The last fundamental step is to translate the desired forces to the currents to be generated, for which the reader can consult the section 5.14.

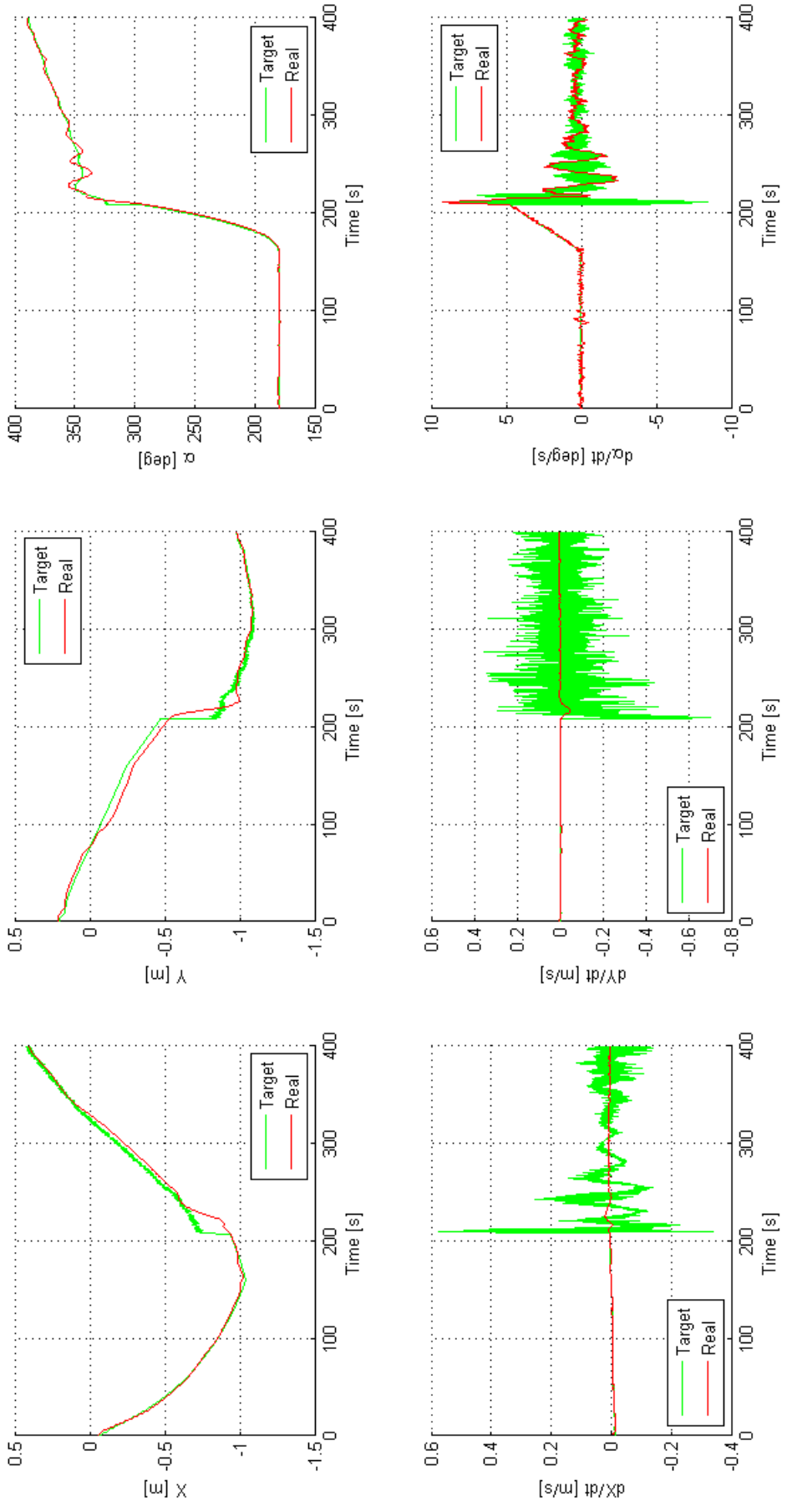

Figure 5.67: Target and real state: SF - Simulation 1 - Controller NL

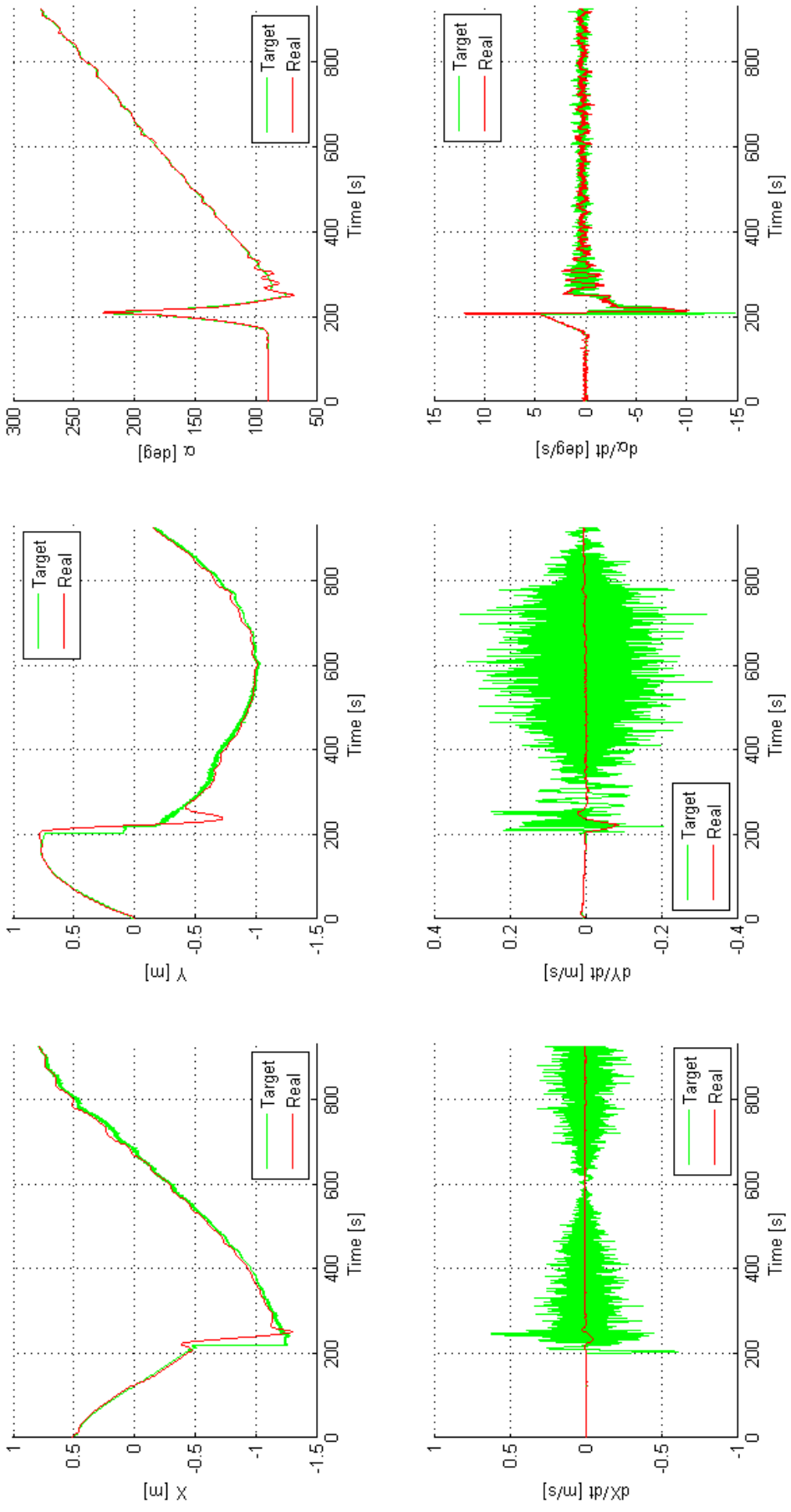

Figure 5.68: Target and real state: SF - Simulation 2 - Controller NL

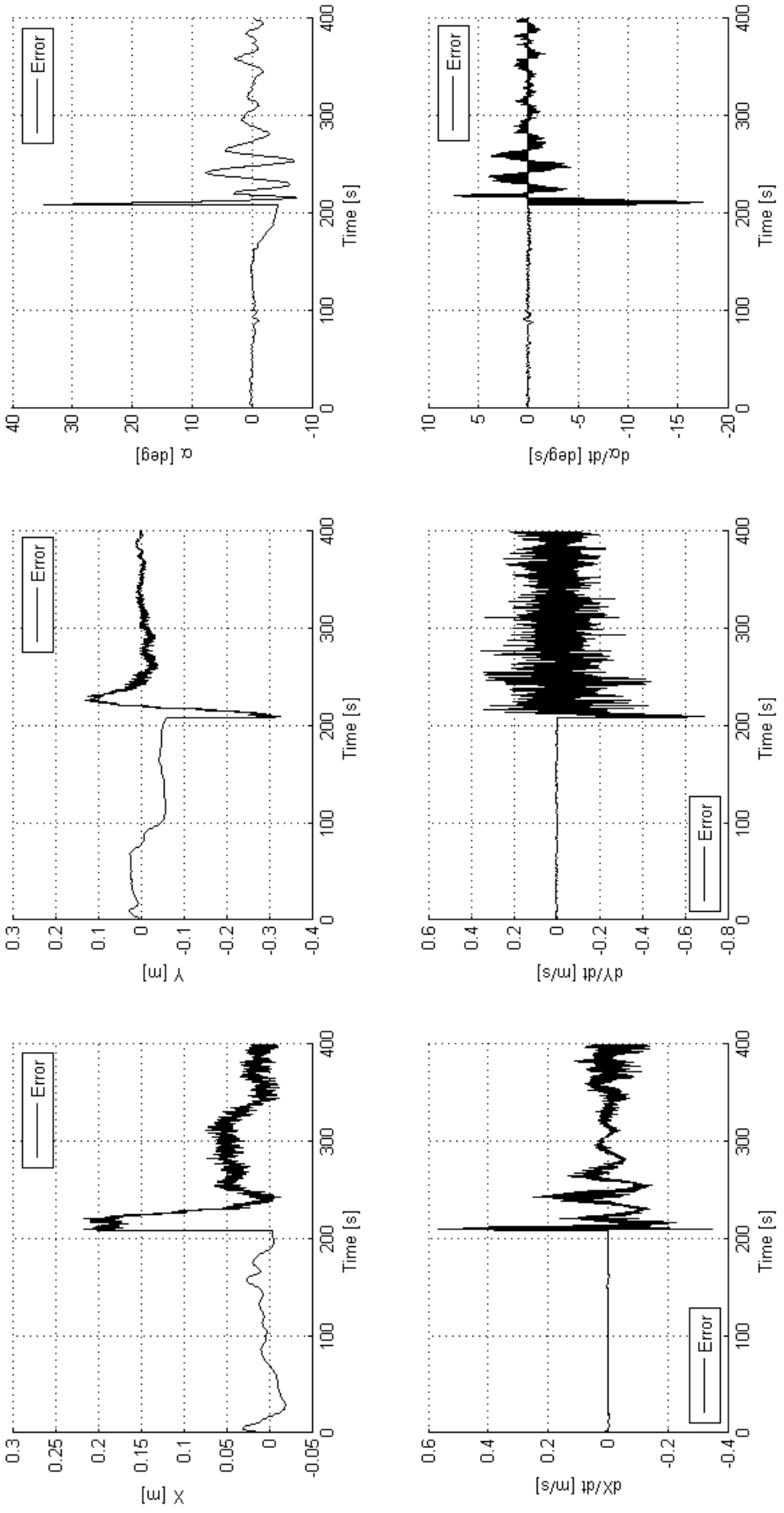

Figure 5.69: Error between target and real state: SF - Simulation 1 - Controller NL

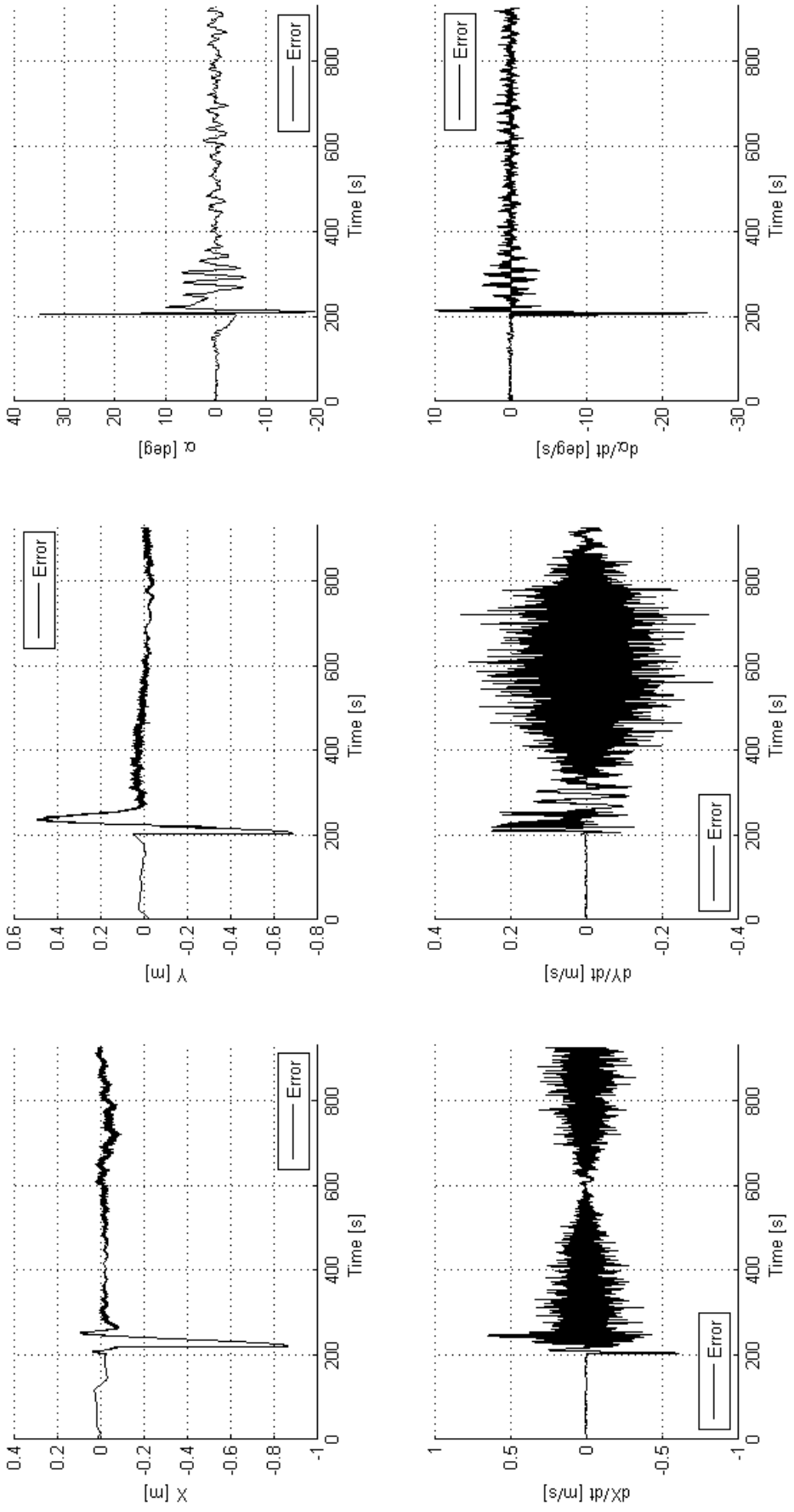

Figure 5.70: Error between target and real state: SF - Simulation 2 - Controller NL

The results for the Nonlinear controller has shown its great adaptability to control different phases of the mission. It is also the fastest in the first simulation but it is also the last one in the second simulation see 5.8. The velocity fluctuation problem as described in the section 5.13.2 does not translate in the control force fluctuation thanks to the PWM module (see 5.14.2).
The comparison between the 3 controllers is reported in section 5.16, where the performances used for the regulator choice are presented.

5.14 The Control law actuation

The controller control forces must be translate in currents to send to the actuators. In this chapter will be described how are considered the controller outputs and in which way they are modulated in order to avoid the fans saturation.

5.14.1 Currents distribution

At each step the underdetermined problem in5.108 must be solved.

$$\begin{bmatrix} F_x \\ F_y \\ M \end{bmatrix} = \frac{\sqrt{2}}{2} K_{FAN} V \begin{bmatrix} -1 & 1 & 1 & -1 \\ 1 & 1 & -1 & -1 \\ a & -a & a & -a \end{bmatrix} \begin{bmatrix} I_{FAN1} \\ I_{FAN2} \\ I_{FAN3} \\ I_{FAN4} \end{bmatrix} \tag{5.108}$$

where $K = 0.0503\ [N/W]$ is the proportionality constant between the power supplied to the fans and the force generated, and $V = 12[V]$ is the supply voltage. The currents distribution must takes into account that that to generate the two forces and the desired torque only 3 fans have to be active. In fact it's always possible to identify the direction of the resultant force and as a consequence to choose two fans; afterwards, chose 2 fans, depending on the sign of the desired torque the third fan is selected. Therefore underdetermined system 5.108 is reduced to a linear system as, at each step a column of the rectangular matrix is deleted and the corresponding current is set null.

5.14.2 Pulse width modulation

The pulse width modulation, is a type of modulation in which the information is encoded as duration of each signal pulse.
The duration of each pulse can be expressed in relation to the period between two successive pulses, entailing the concept of *duty cycle*. A duty cycle of 0% indicates a pulse of zero duration (no signal), while a ratio of 100% indicates that the pulse ends when the next begins.
The pulse width modulation is widely used also to adjust the electrical power sent to a load such as the fans of both flyers. As it is possible to guess, with a zero duty cycle the transferred power is zero, while with 100% the value of transferred power is equal to that in the case of circuit modulation absence.
This technique drastically reduces the power dissipated by the limiter circuit. In a PWM circuit whenever the transistor leads the slippage at its ends is minimum, while

whenever it doesn't, the current is nulled; in both cases the power loss is minimal.
For the fans activation the following modulation law has been created:

$$\begin{array}{c} \int_0^{t+dt} \tilde{I}(\tau)\ dt - \int_0^t I(\tau)\ dt\ \geq\ U_C\ \Rightarrow\ I(t+dt) = I_{MAX} \\ \int_0^{t+dt} \tilde{I}(\tau)\ dt - \int_0^t I(\tau)\ dt\ <\ U_C\ \Rightarrow\ I(t+dt) = 0 \end{array} \tag{5.109}$$

where $\tilde{I}(t)$ is the current required by the fan controller for the generic fan and $I(t)$ is the actually controlled current. Thus the only parameter to choose is the threshold value U_C which will be logically linked to the duration *duty cycle*. The optimum value for this parameter is $U_C = \frac{dt \cdot I_{MAX}}{2}$.
In figures the comparison between the current required by the regulator and that actually controlled to the four fans of the two flyers during the different simulations.

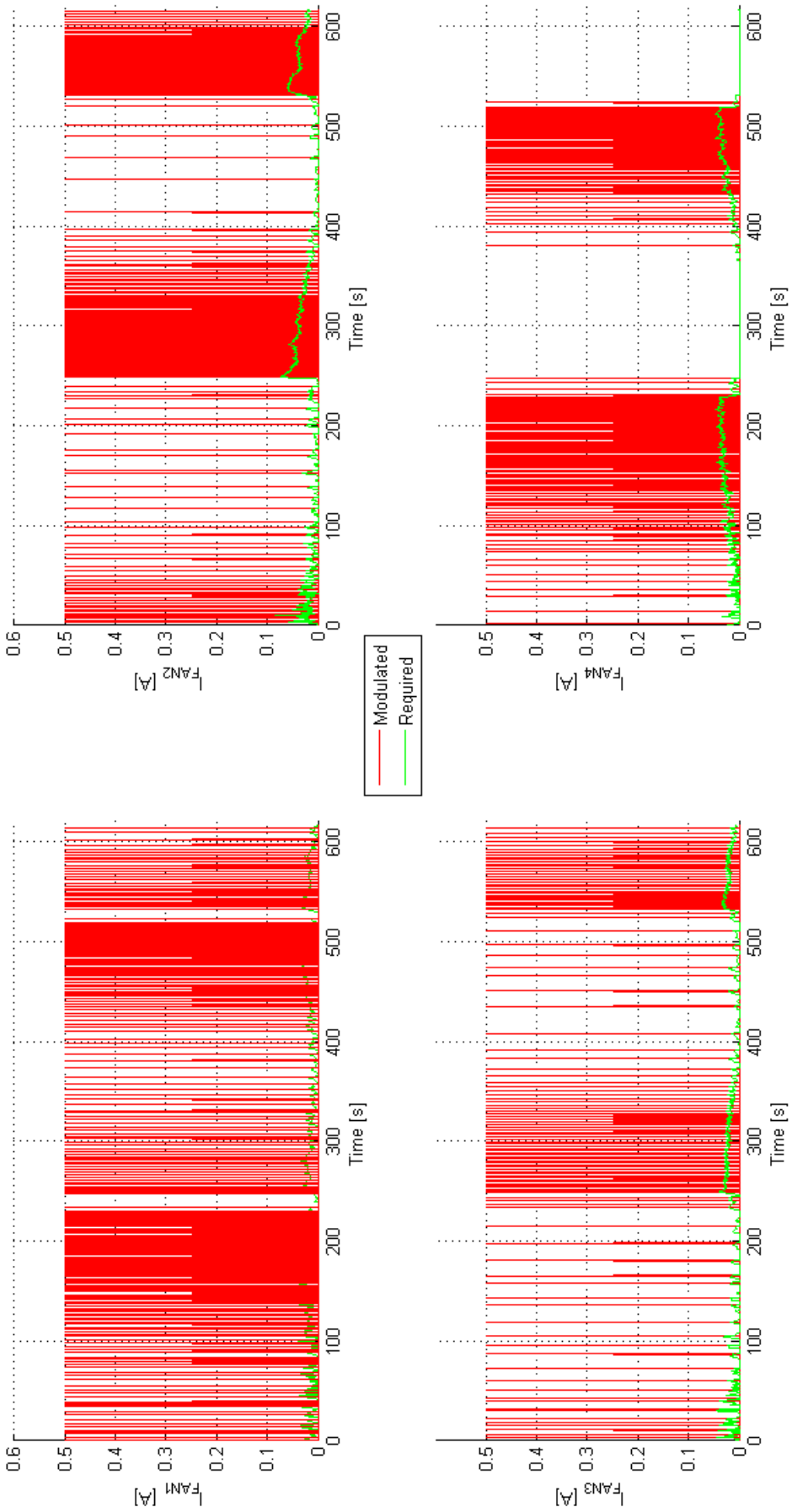

Figure 5.71: Required current VS modulated current: TF - Simulation 1 - Controller PD

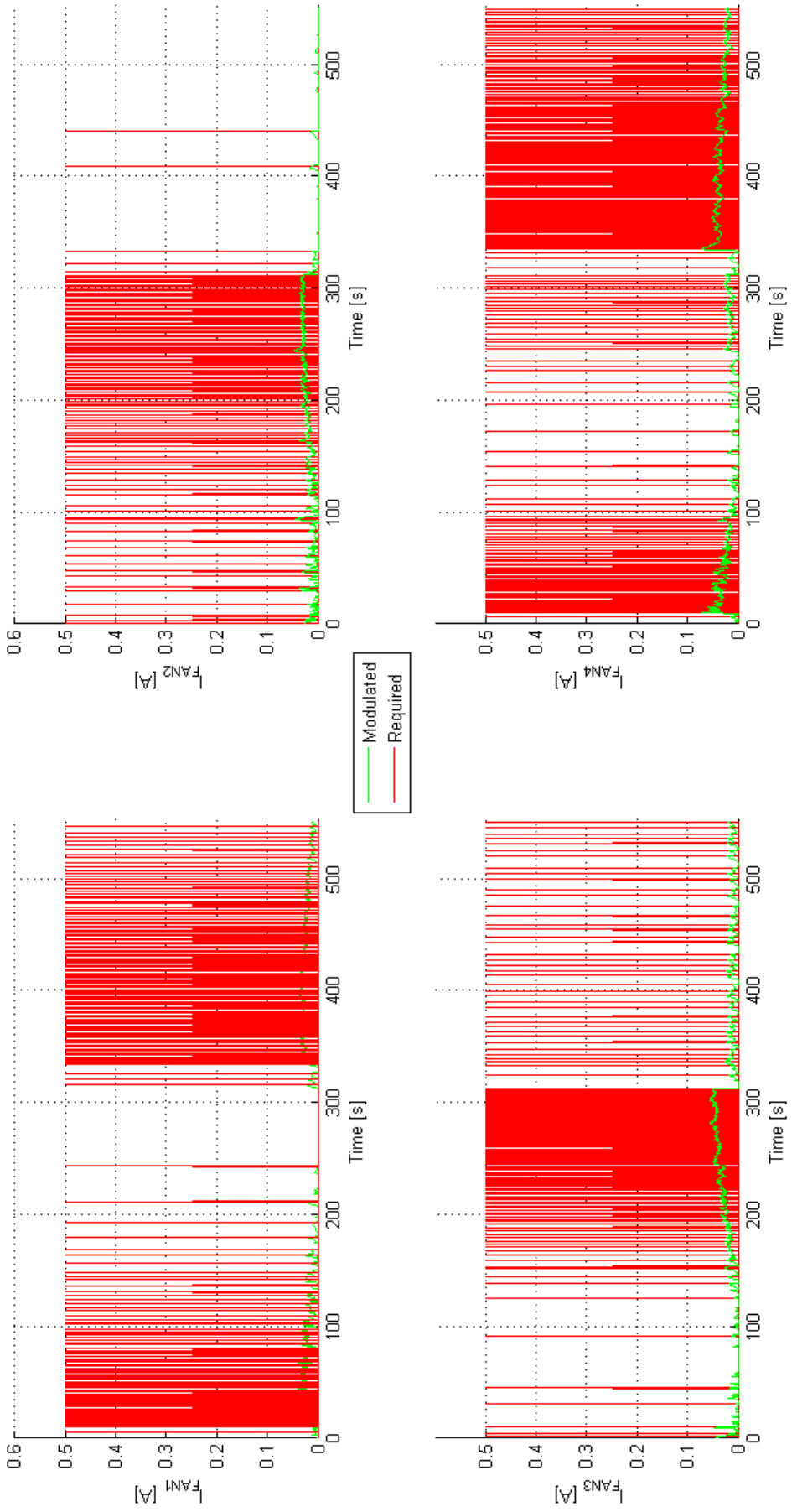

Figure 5.72: Required current VS modulated current: TF - Simulation 2 - Controller PD

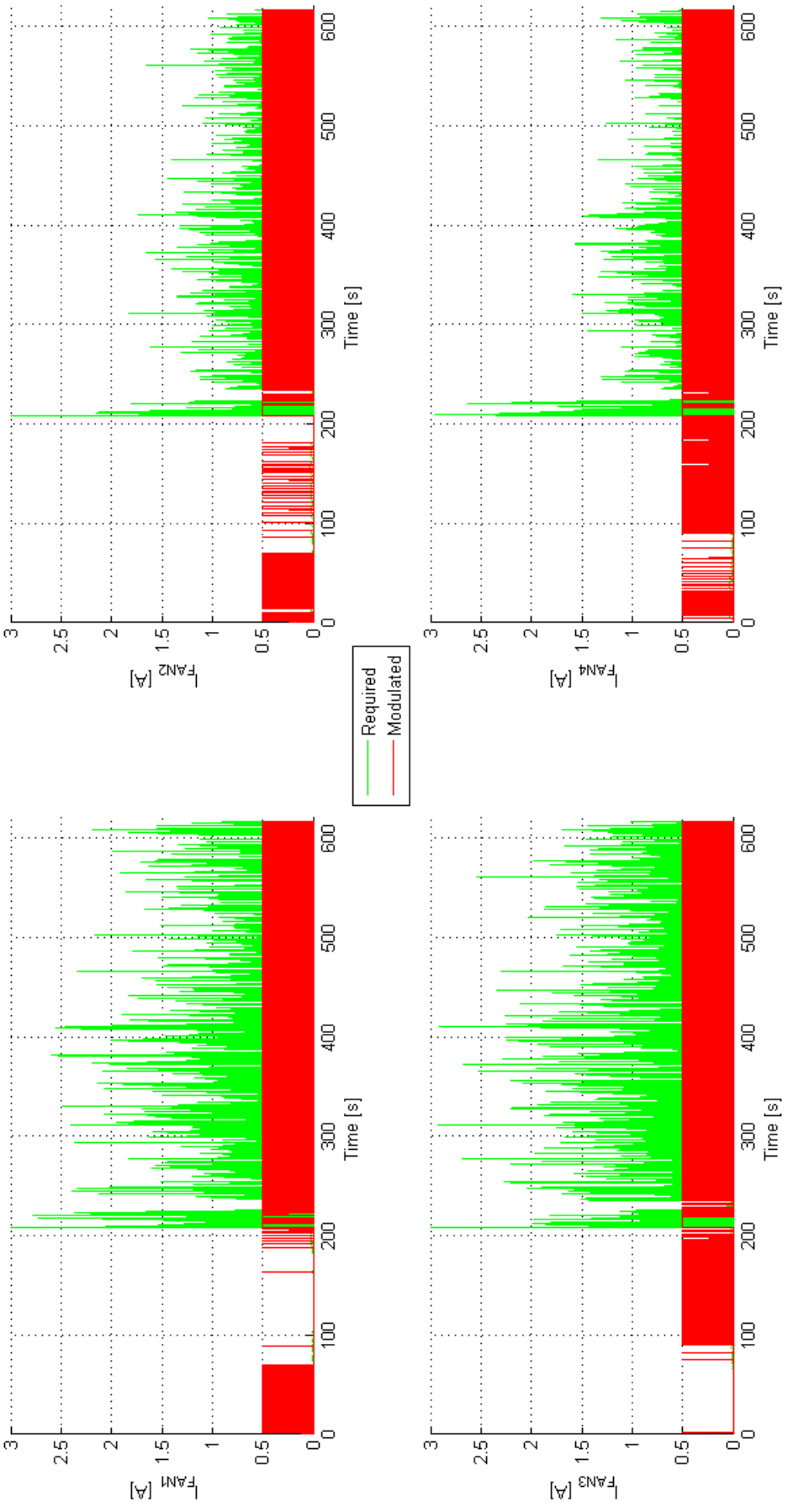

Figure 5.73: Required current VS modulated current: SF - Simulation 1 - Controller PD

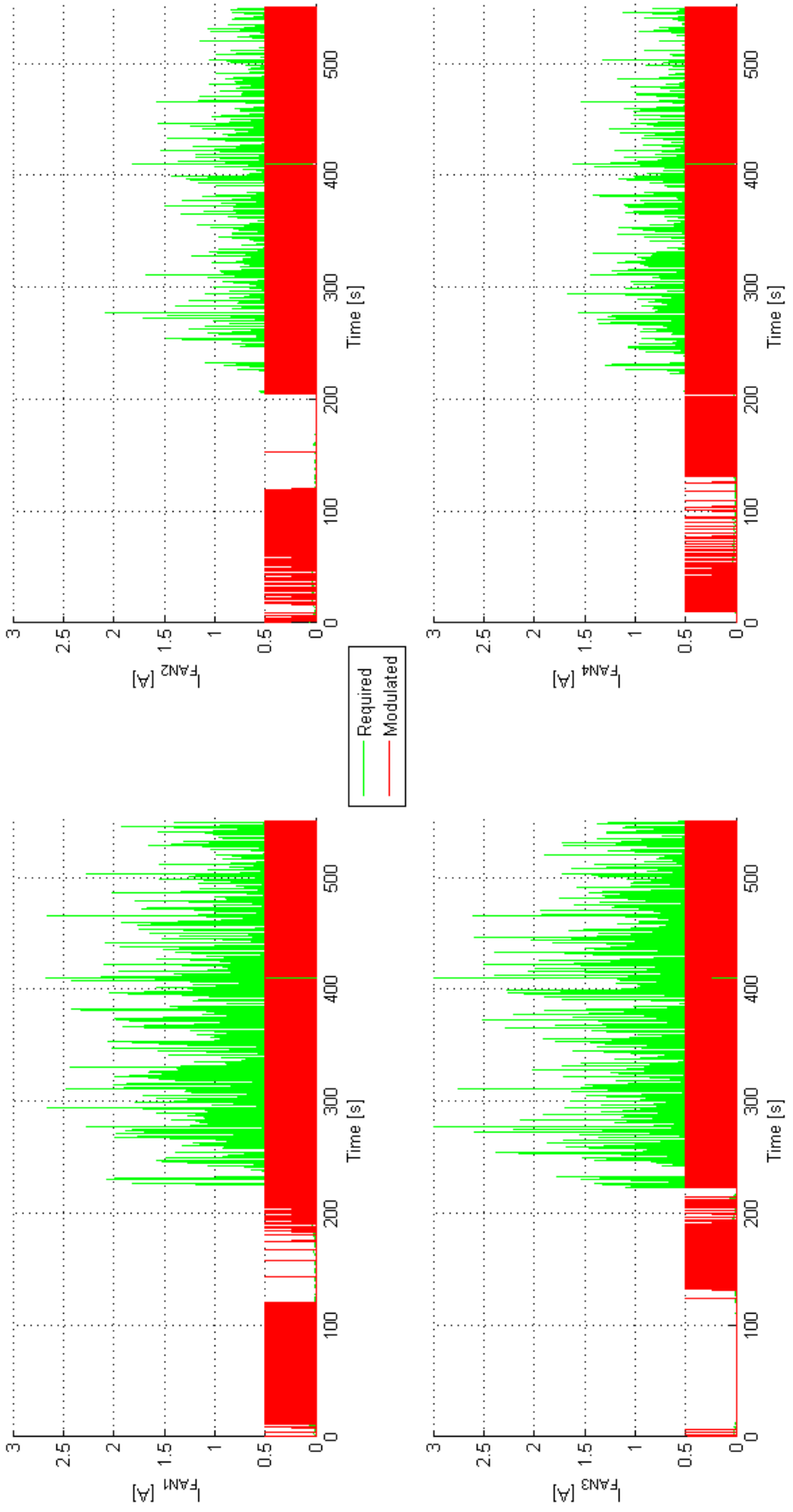

Figure 5.74: Required current VS modulated current: SF - Simulation 2 - Controller PD

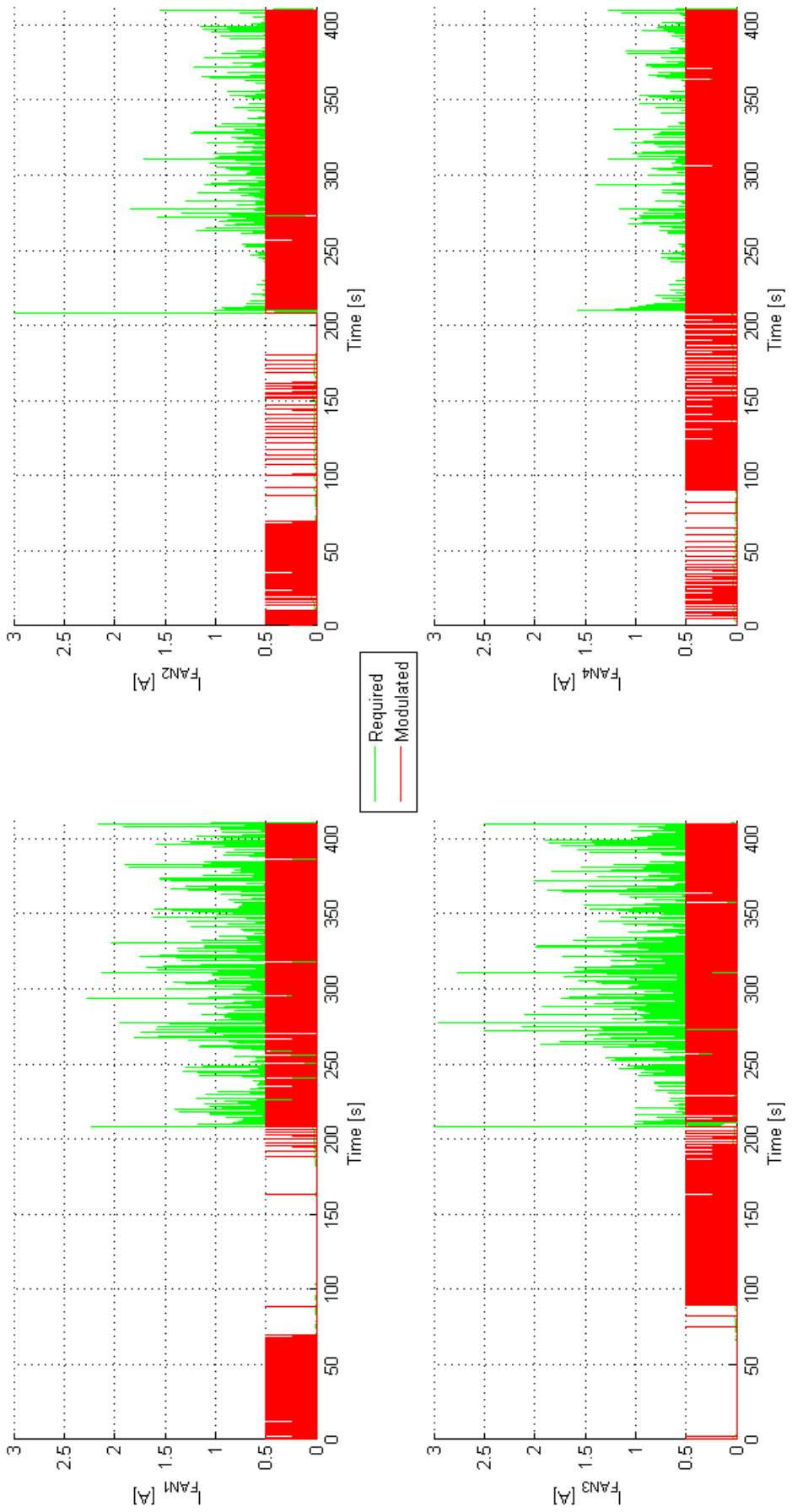

Figure 5.75: Required current VS modulated current: SF - Simulation 1 - Controller LQR

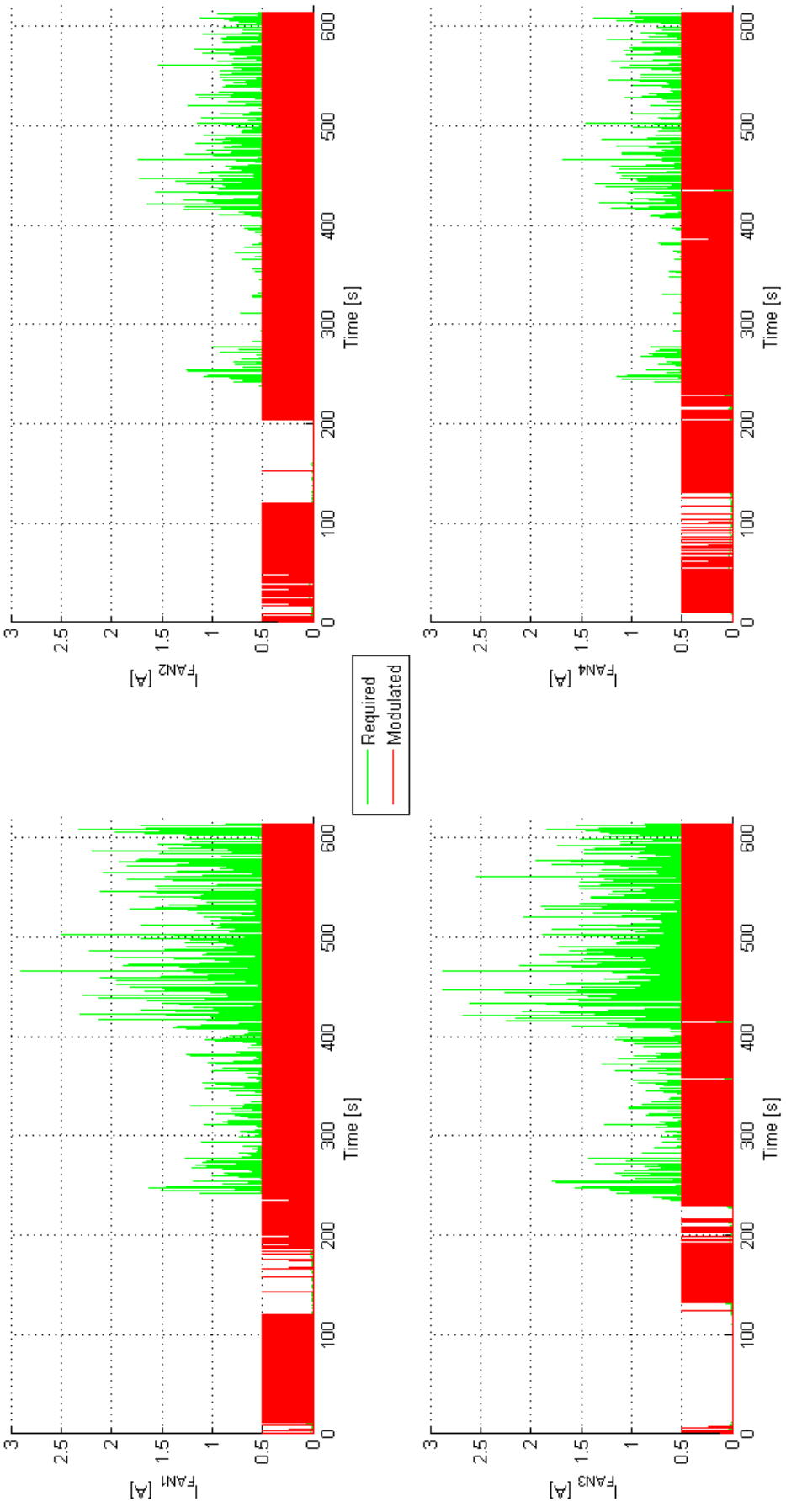

Figure 5.76: Required current VS modulated current: SF - Simulation 2 - Controller LQR

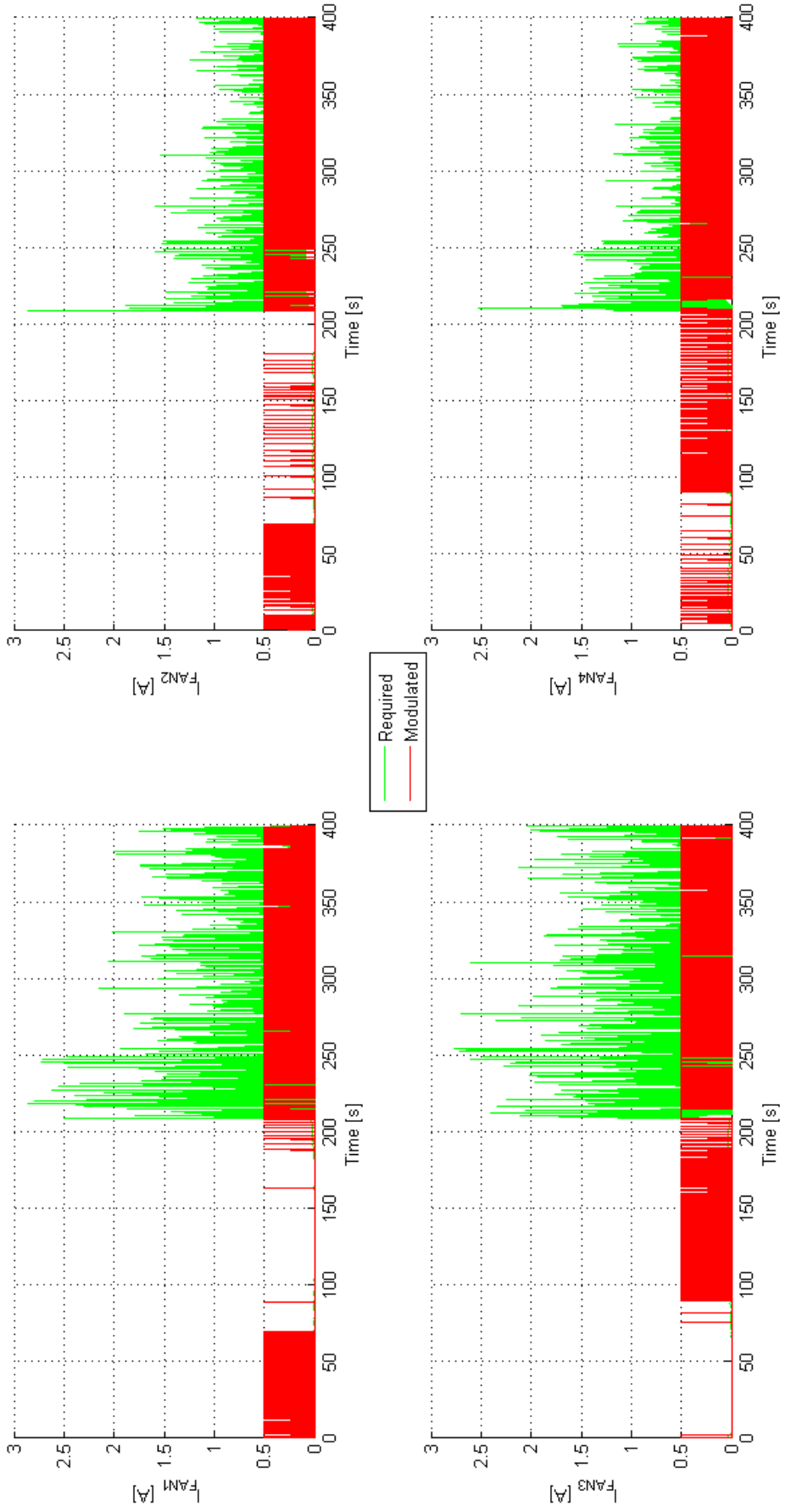

Figure 5.77: Required current VS modulated current: SF - Simulation 1 - Controller NL

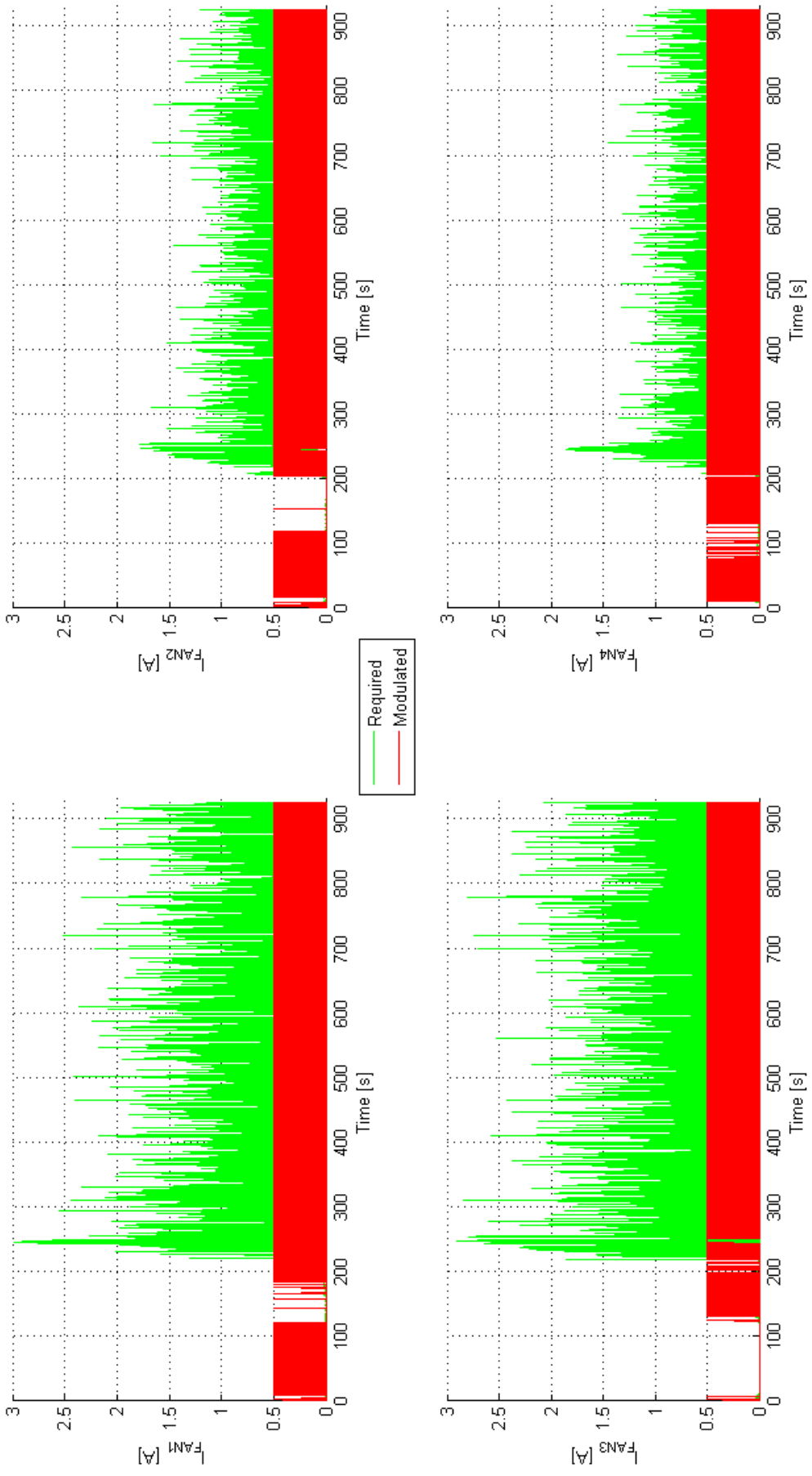

Figure 5.78: Required current VS modulated current: SF - Simulation 2 - Controller NL

The PWM allows to reproduce in the chaser control chain the same effect given by a control forces that the actuators aren't able to supply. Moreover this modulation model prevents that the velocity fluctuation in the relative velocity (obtained performing a discrete derivative of the measured position) can propagate itself in the actuator forces. Therefore pulse width modulation after the controller module has filtering properties.

5.15 ADS limits

5.15.1 Perturbation torques and forces

As can be seen in figures 5.18,5.19,5.20,5.21 the magnitude of these disturbance effects can not be reproduced with the actuators available. Moreover, these perturbation is negligible compared to those that will act in the experimental stage, and that it could not be modeled, such as real drag rather than the actual behavior of the instruments used and the misalignment of the air bearings.
Therefore it was decided not to reproduce these perturbations in the experimental phase with the idea of lightening the computational load of the on-board computer.

5.15.2 Simulator limits

Within the experiment to be done two distinct phases clearly appear: the first is the transfer orbit, where it is very important the orbital mechanics of the two flyers, while the second is the docking phase that also provides for the alignment phase. In this last phase what is very important is the relative mechanics of the two vehicles, but the gravitational forces are still reproduced. It can happen that during the alignment with the TF, the chaser has to perform maneuvers that led it to approach the center of the table, leading it even at lower altitude than its parking orbit. At least it could also get to lower altitudes than the Earth's radius, causing the birth of senseless gravitational and aerodynamic forces. What is just described can be seen clearly in figures 5.13,5.15 and 5.17.
It's necessary be aware that in some particular initial conditions the simulation may fail because the term $1/r^3$ in gravitational forces tends to ∞ with r that tends to 0. A solution to the problem, may be to vary slightly the gains of the controller before starting the simulation, depending on the type of mission.

5.16 Chaser control law choice

In choosing the controller to implement on the PC104+, of the chaser satellite, a table with various selection criteria that will be considered has been created.:

- $t_{DOCKING}$: Time employed to complete the docking. The simulation is considered finished when the chaser remain at least 30 seconds in the target position with a maximum error of 1 [cm];
- S_{MAX}: Maximum value in the variable given in superscript;

- S_∞:Maximum oscillation in the variable given in superscript during the final approach.

	PD	**LQR**	**NL**	**PD**	**LQR**	**NL**
Simulation	**1**			**2**		
$t_{DOCKING}[s]$	594	624	**417**	**572**	885	906
$S^x_{MAX}[m]$	**0.21**	**0.21**	0.22	-0.92	**-0.8**	-0.86
$S^y_{MAX}[m]$	-0.33	**-0.325**	-0.33	-0.69	-0.69	-0.69
S^α_{MAX}[deg]	34.7	34.7	34.7	34.9	34.9	34.9
$S^{\dot{x}}_{MAX}[m/s]$	0.58	**0.56**	0.57	-0.61	-0.61	-0.61
$S^{\dot{y}}_{MAX}[m/s]$	-0.69	-0.69	-0.69	0.33	0.33	0.33
$S^{\dot{\alpha}}_{MAX}$[deg/s]	**-10.4**	-14.1	-17.5	**-10.3**	-17.5	-26
$S^x_\infty[m]$	±**0.025**	±0.035	±0.034	±**0.04**	±**0.04**	±0.045
$S^y_\infty[m]$	±0.02	± **0.01**	±0.011	±**0.025**	±**0.025**	±0.047
S^α_∞[deg]	±2	±**1**	±2.8	±1.1	±**1**	±2.2
$S^{\dot{x}}_\infty[m/s]$	±0.3	±0.17	±**0.14**	±0.17	±**0.15**	±0.32
$S^{\dot{y}}_\infty[m/s]$	±**0.05**	±0.29	±0.23	±0.29	±0.33	±**0.11**
$S^{\dot{\alpha}}_\infty$[deg/s]	±**1**	±1.3	±1.4	±**0.8**	±1.5	±2.1

Table 5.8: Performance of implemented controllers

As shown in table 5.8 the PD controller allows to conclude quickly the simulation 2 but is also the slowest in the simulation 1, and also in the other parameters PD and NL are either the best or worst. Instead the LQR when isn't the best solution is always between the other two.

On the other hand the great adaptability of the non linear controller, does not require two different gain matrices to control the final phases of alignment and docking, because the gains for this controller depends of the error itself. This adaptability is paid with a greater complexity in the controller architecture and operations involved, which certainly increase the computational cost.

Even the simple PD controller requires the calculation of the discrete derivative of the error at each step, and even if it is faster than the nonlinear controller, it is slower than the LQR, for which the complexity in the synthesis of the gain matrix, that could be done once before the simulation, and could also be performed on an external computer. Obtained this in fact, the LQR is reduced to a proportional controller, where control actions are the product of the gains matrix for the vector error. For this reason the LQR this will be the primary solution, but in any case the other two controllers could be used because they complete the mission successfully.

Chapter 6

Computer Vision

The estimation of the three dimensional orientation and position of an object from its images has been an active topic of study in Computer Vision. Image-based attitude estimation methods find applications in autonomous navigation, robot sensing and vehicle docking.

To the scope of this work relative attitude and position information about the target spacecraft is used for closed-loop guidance and control of the chaser satellite during the final approach phase. The camera vision sensor mounted on the chaser can provide the images of the target features, which can be further processed to derive the pose information.
The library used for the computer vision phase of this work is the OpenCV, that stands for Open Source Computer Vision Library. It being developed at Intel since 1999, written in C/C++ and contains over 500 functions [62].

6.1 Relative position and attitude determination

6.1.1 Existing algorithms

Nowadays available software in this field are mainly based on triangularization algorithms which ask for at least 3 points in the TF frame, and at least one must be out of the TF face plane. In this way not only position and attitude can be analytically computed on board the chaser, but also a lot of approximated algorithms may be exploited. The first problem is that in the laboratory facility no devices to identify the target is available[1], so the sighting phase 5.5.1 should be done via webcam with the S.U.R.F. recognition.
S.U.R.F. that means Speeded Up Robust Features is a robust image detector and descriptor, first presented by Herbert Bay in 2006, that can be used in computer vision tasks like object recognition or 3D reconstruction [26]. It is partly inspired by the SIFT descriptor [42]. The standard version of SURF is several times faster than SIFT. SURF is based on sums of approximated 2D Haar wavelet responses and makes an efficient use of integral images. As basic image features it uses a Haar wavelet approximation of the determinant of Hessian blob detector [32]. Obviously the SURF process allows to

[1] Such as laser with cornercube reflectors, LIDAR etc.

recognize a planar image while for attitude determination, a marker, that can be either a system of LEDs or an image that should not be planar, is needed.
In fact if the problem was limited to track only three points of light a standard approximate algorithm available in the literature would have been simply applied [34], [35], [36], [37], [38], to derive relative position and attitude. In this application a feature that identify uniquely the flyer put on the TF and to be recognized by the chaser is needed, the LEDs possibly already on the TF, can be exploited to this end by the SF.
The second problem is that the features on TF face are planarly placed; therefore, to finalize the localization a LED out of the face plane can be used:

- two features inclined compared to the face of the target at 45 [deg], with LEDs placed at the corner of images, figure 6.1.1;
- two parallel features but at different levels, and place at least two LEDs on the image belonging to the TF face plane and one on the other, figure 6.1.2.

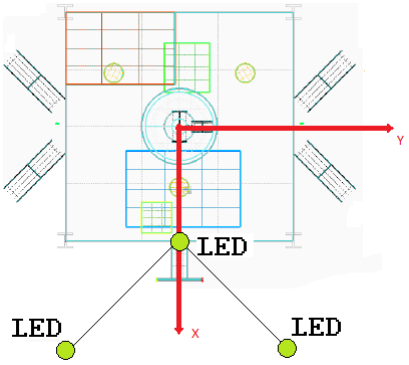

6.1.1: Skewed features

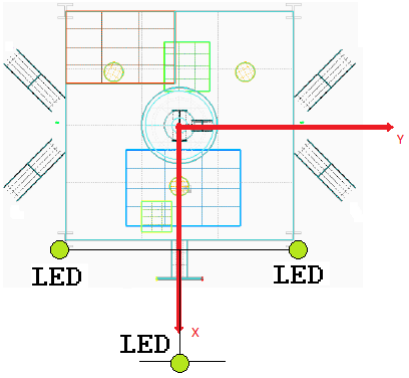

6.1.2: Parallel features

Figure 6.1: Feature out of the plane disposition

The two features skewed in the first case may seem superfluous but in fact with a single image it's possible to have situations where the relative attitude is only 45 deg and the chaser's view direction is perfectly parallel to the plane of the feature: whenever this situation occurs the chaser cannot correctly catch the target.As far as the second alternative is concerned, it would happen that the out-of-plane feature partially blinds the other, so the SF experiences more difficulty in recognition of both images.
In addition both solutions also have other significant drawbacks: first of all that if for each face of TF two no coplanar images should be placed, there is an increase in size and weight [2]; the second is certainly that the search and analysis on a the frame captured by the camera of two features makes the initialization operation for tracking very slow. Actually, multiple images on the same face of the target vehicle may be avoided if the TF section of the structure of the TF is at least hexagonal, with a logo on each side,

[2]The weight increases because inevitably it is necessary to give stiffness to the system to steady out of the plane.

but the high computational cost required for the recognition of two (or possibly three) feature remains high and the risk is to begin to track points that at the end of the algorithm initialization actually do not belong to the Target flyer, figure 6.2.

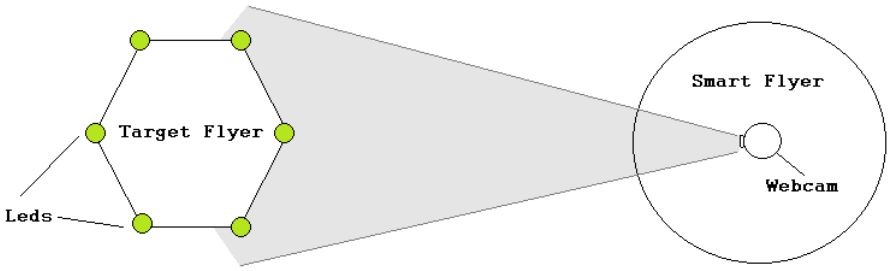

Figure 6.2: TF with hexagonal section and SF field of view

6.1.2 Attitude determination based on 2D Feature recognition

To cope with aspects underlined in the previous subsection an approximate algorithm has been developed in this work that can determine the relative attitude and position of the TF by using only a planar image (see figure 6.3).

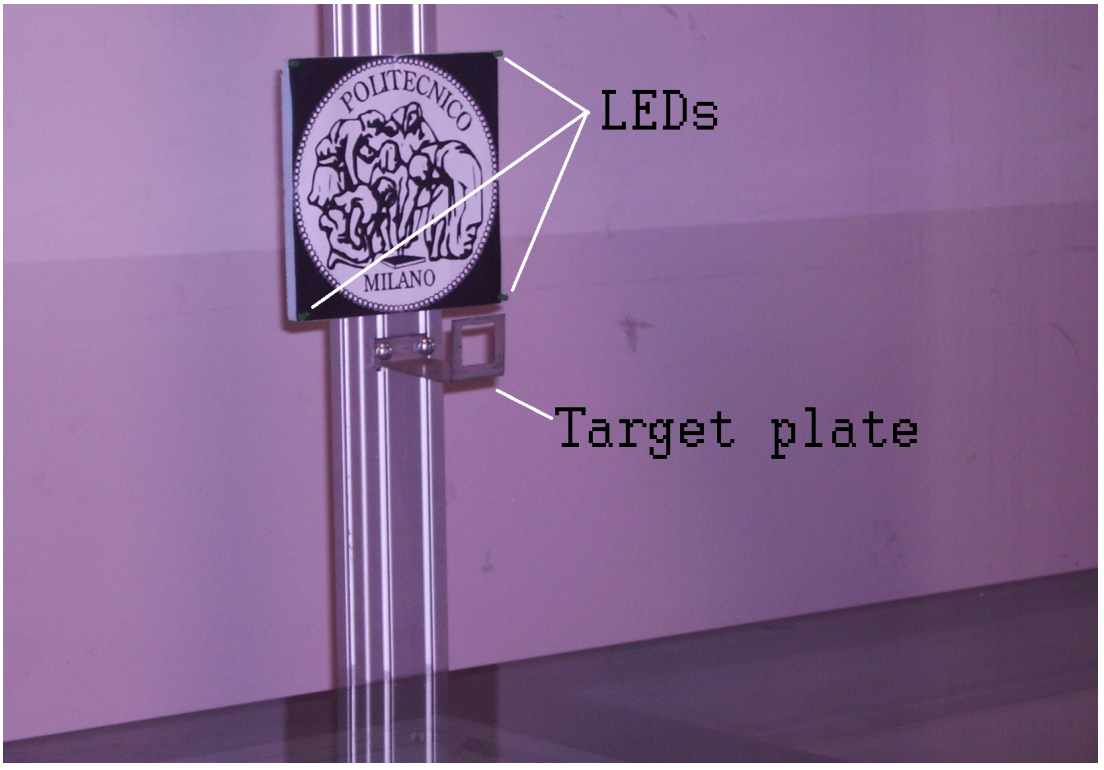

Figure 6.3: 2D feature and target plate

The software implemented on the chaser PC104+ computer uses the feature recognition only to engage the target and to fix the corners, then starts with the tracking of

that corners that coincide with the LEDs position[3], figure 6.3. The OpenCV function used for the feature extraction is the *ExtractSURF* that extracts Speeded Up Robust Features from an image while for tracking the LEDs *CalcOpticalFlowPyrLK* that is the same used for the inertial position calculation section 6.2. As soon as the TF is engaged, the relative attitude and position determination starts. Figure 6.4 reports the selected reference frame to deal with the current state determination..

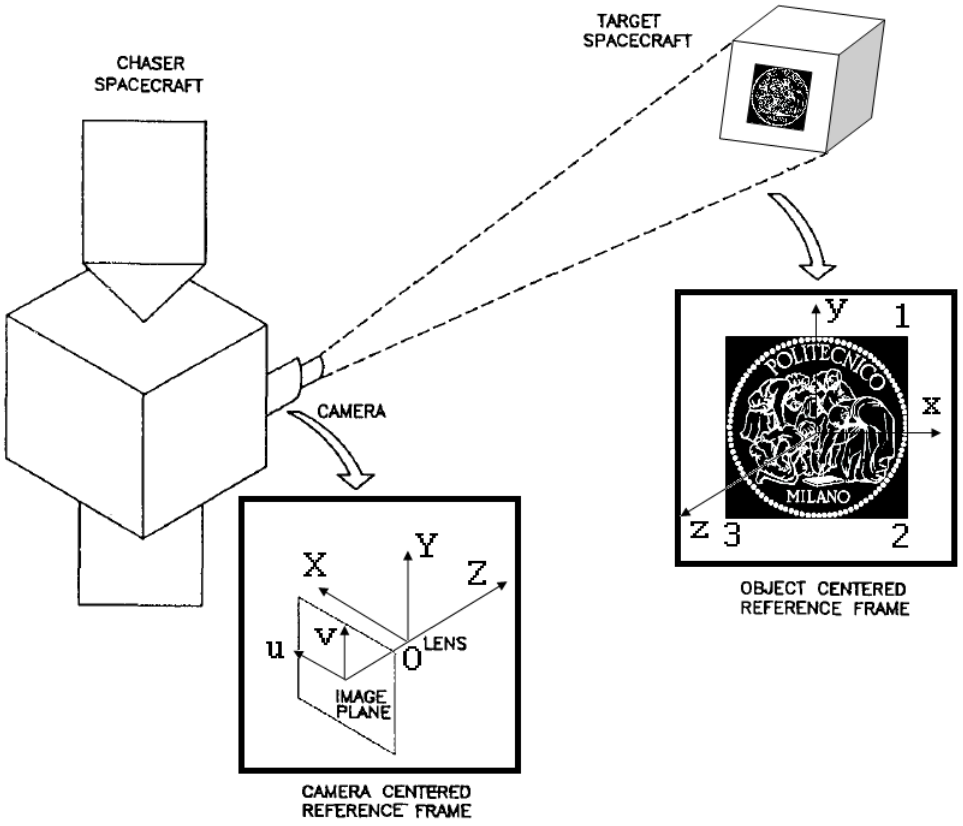

Figure 6.4: Reference system involved in 2D feature recognition

To the set of the three points needed to reconstruct the state vector a fourth point has been added, located at the center of the feature shown in fig 6.4. That point is also the reference frame center (o).

From the similarity relations 6.1, it's possible to obtain $2n$ equation where n is the number of points in the object picture that are considered.

$$\begin{aligned} Z_i u_i &= X_i f \\ Z_i v_i &= Y_i f \end{aligned} \tag{6.1}$$

where f is the focal length of the camera, that is equal to $6 \cdot 10^{-3}[m]$. The vector between the center of the camera reference frame and the center of the object reference frame can be expressed:

[3]The LEDs are necessary because the tracking function give better results with bright pixels.

$$\underline{Oo} = \left\{ \begin{array}{c} P \\ Q \\ R \end{array} \right\} \tag{6.2}$$

In addition other $3n$ equations derived from the classical equation set used to translate and rotate a reference frame, can be considered:

$$\begin{aligned} X_i &= A_{11}x_i + A_{12}y_i + A_{13}z_i + P \\ Y_i &= A_{21}x_i + A_{22}y_i + A_{23}z_i + Q \\ Z_i &= A_{31}x_i + A_{32}y_i + A_{33}z_i + R \end{aligned} \tag{6.3}$$

where A_{ij} are the coefficient of the cosine matrix that uniquely define the relative attitude.
The algorithm exploits points only in the image plane; therefore their z_i coordinate nulls. So for the moment the A_{i3} are not unknown quantity, and are available $5n$ equation with $3n + 6$ unknown quantity. In order to close the problem 3 points shown in figure 6.4 are used..
Actually also P, Q, R components are unknown terms, but for them it's possible to write:

$$\begin{aligned} X_4 &= P \\ Y_4 &= Q \\ Z_4 &= R \end{aligned} \tag{6.4}$$

$$\begin{aligned} Rv_4 &= Qf \\ Ru_4 &= Pf \end{aligned} \tag{6.5}$$

So the only approximation used in this process deals with the esteem of D that is the module of the Oo vector:.

$$D = \sqrt{P^2 + Q^2 + R^2} \tag{6.6}$$

In fact from experimental analysis it's possible to demonstrate that D is a function of the ratio of the real area and its projection on the image plane and of the minimum angle between two consecutive sides of the logo. This last dependence allows to esteem the distance more accurately even when the relative attitude is greater than 30 deg.

$$D = f\left(\frac{A_{real}}{A_{proj}}, \beta\right) \tag{6.7}$$

So by knowing value of D and using the 6.6 and 6.5 it's possible to obtain P, Q, and R. Then with the 6.1 and 6.3 it's possible to obtain all the X_i, Y_i, Z_i and A_{ij} with $i = 1, 2, 3$ while $j = 1, 2$.
The last three unknown quantities could be found thanks to the normalization property in the cosine matrix:

$$\begin{aligned} A_{11}^2 + A_{12}^2 + A_{13}^2 &= 1 \\ A_{21}^2 + A_{22}^2 + A_{23}^2 &= 1 \\ A_{31}^2 + A_{32}^2 + A_{33}^2 &= 1 \end{aligned} \tag{6.8}$$

The problem is that in this way it's possible to determine A_{13}, A_{23}, A_{33} with a sign vagueness. Actually it's sufficient to know the sign of only one between the 3 unknown coefficients, because the other two can be extract by the orthogonality property of the cosine matrix.

$$\begin{aligned} A_{11}A_{21} + A_{12}A_{22} + A_{13}A_{23} &= 0 \\ A_{11}A_{31} + A_{12}A_{32} + A_{13}A_{33} &= 0 \\ A_{21}A_{31} + A_{22}A_{32} + A_{23}A_{33} &= 0 \end{aligned} \tag{6.9}$$

Finally it's absolutely possible to know the sign of A_{33} because if the relation for a point 5 that has $x_5 = 0, y_5 = 0, z_5 \neq 0$ is taken into account, the equation 6.10 for this point becomes:

$$\begin{aligned} X_5 &= A_{13}z_5 + P \\ Y_5 &= A_{23}z_5 + Q \\ Z_5 &= A_{33}z_5 + R \end{aligned} \tag{6.10}$$

but seeing that the point 5 must be in front of the image plane[4] $Z_5 < R$ so $A_{33} < 0$. In fact a positive value of A_{33} would mean that the camera can't observe the feature because it would be behind the image plane. Experimental results given by this software are reported in the section 6.3.

6.2 Inertial position and attitude determination

For the inertial position and attitude determination of the both flyers a fixed camera has been placed at 2.35 [m] on the table, as discussed in subsection 3.1.6 and depitched in figure 3.2. This camera is cabled with a desktop PC which, via wireless, trasmits their absolute position and attitude to the vehicles themselves.

6.2.1 Object Tracking Software

The software developed uses another OpenCV funtion called *CalcOpticalFlowPyrLK* that calculates the optical flow for a sparse feature set using the iterative Lucas-Kanade method with pyramids [25]. So the users must set the point to track that are 2 for each flyer (and correspond with the led position) and knowing the table corners position in pixel reference system is possible with simple algebraic manipulation to esteem the actual position.

6.3 Experimental results

From experimental test it as been deduced that the dependence among the distance, the ratio between the real and the projected feature area and the minimum β angle is

[4]Because if it is behind the camera can't see that point.

not linear. In fact a frontal image acquisition revealed that the dependence among D and A_{real}/A_{proj} is parabolic, as shown in figure 6.5.

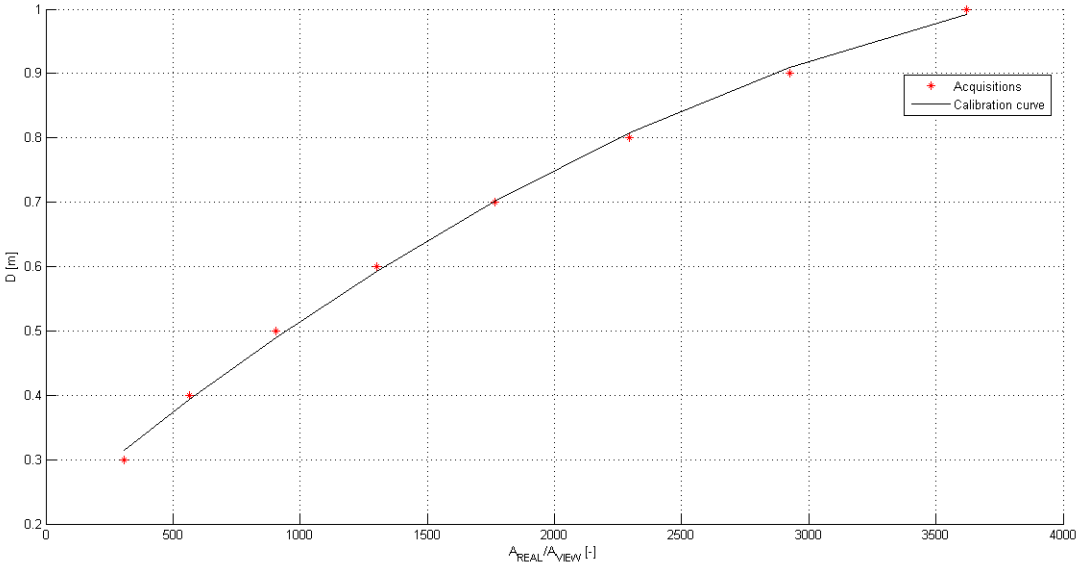

Figure 6.5: Calibration curve between D and A_{real}/A_{proj}

As a second testing campaign, images at fixed distance but with different inclinations have been acquired and the relation between D and β has been identified, as reported in figure 6.6.

So the distance D can be estimated with the following expression:

$$D_{estim} = (s_1\beta + s_2) \cdot \left(k_1 \left(\frac{A_{real}}{A_{proj}} \right)^2 + k_2 \frac{A_{real}}{A_{proj}} + k_3 \right) \tag{6.11}$$

where $s_1 = 3.0240, s_2 = -3.6647, k_1 = 3.3 \cdot 10^{-8}, k_2 = 3.3 \cdot 10^{-4}, k_3 = 0.2159$. In the figures below the consistency between the model and the real data is shown.

Figure 6.8 highlights that the maximum error is less than 8.5% and it happens in the forth measure when the target feature is at 1.22 [m] or in measure 11 when the target is so close to the camera that part of the feature is out of the image plane.

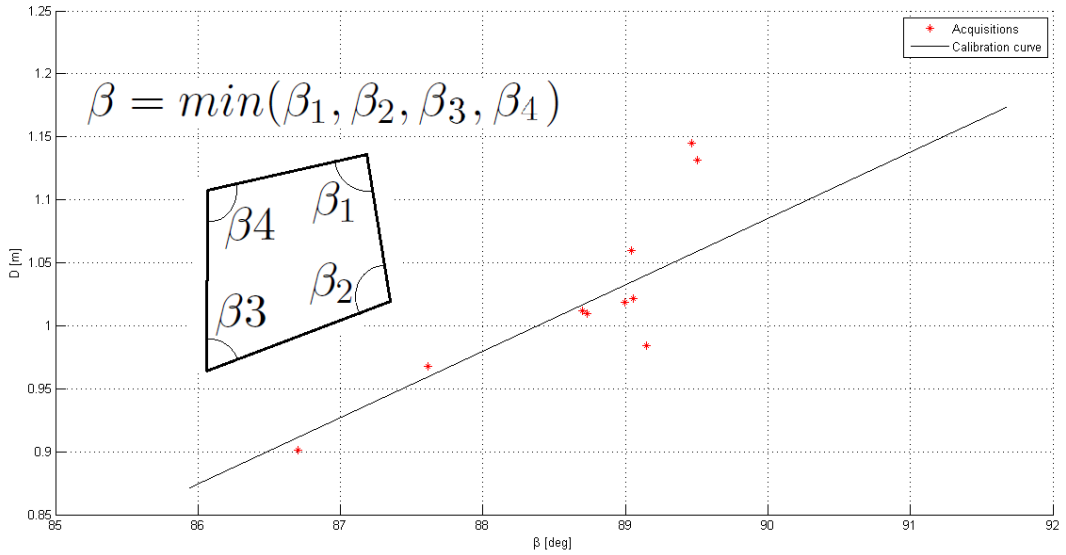

Figure 6.6: Calibration curve between D and β

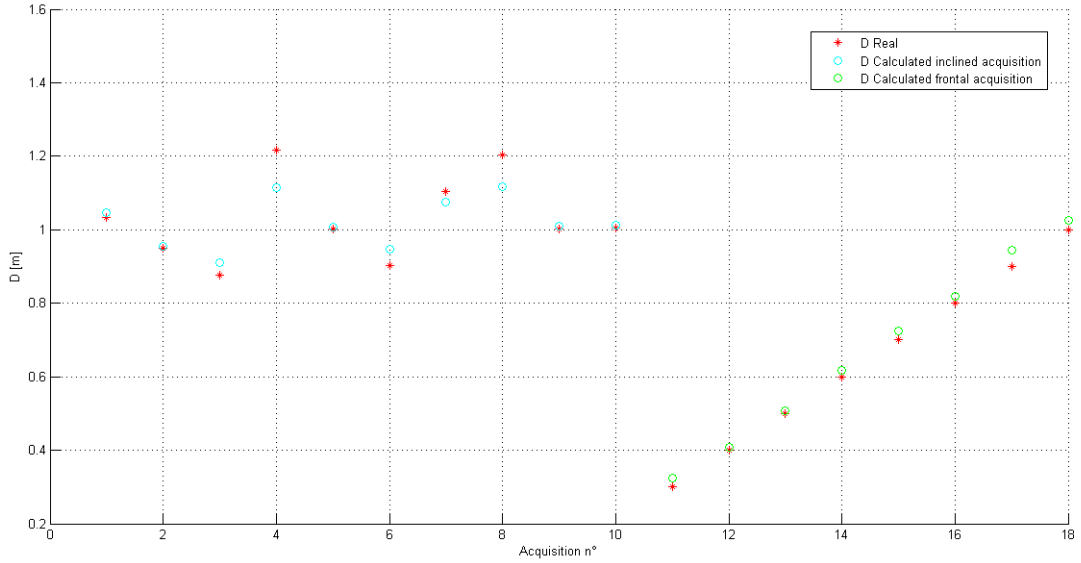

Figure 6.7: Real and estimed distances

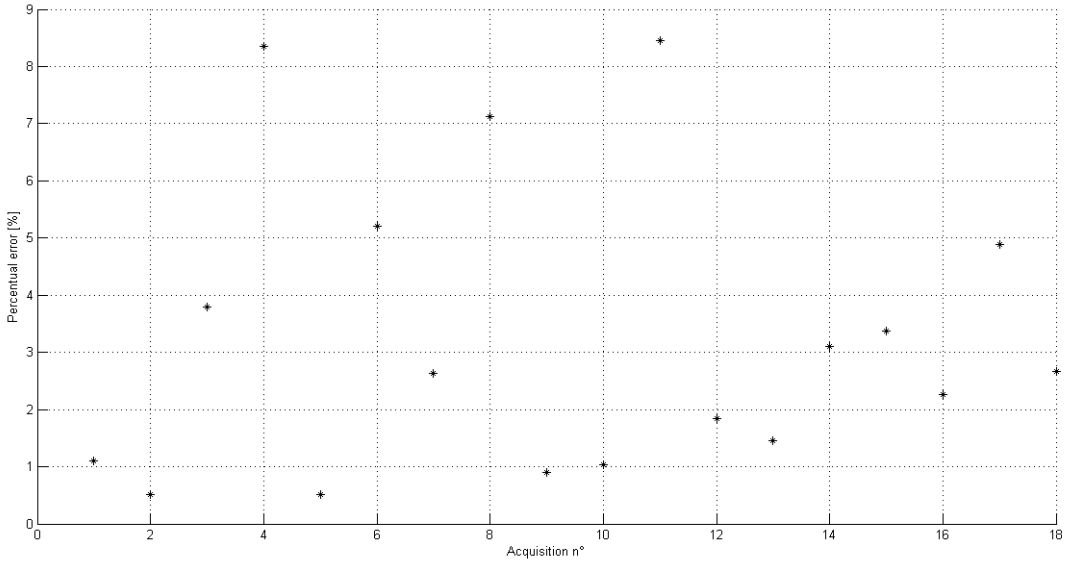

Figure 6.8: Percentual error between estimed and real distances

In the following tables the estimation of P, Q, R and the attitude angle with its errors are listed.

	Real			**Estimated**		
Measure	**P [m]**	**Q [m]**	**R [m]**	**P [m]**	**Q [m]**	**R [m]**
1	0	-0.006	1.034	0.0016	-0.0082	1.0453
2	0	-0.013	0.950	0.0015	-0.0165	0.9548
3	0	-0.036	0.877	0.0014	-0.0342	0.9099
4	0	-0.0015	1.217	0.0017	0	1.1154
5	0	0.05	1.0	0.0016	0.0582	1.0047
6	0	0.05	0.9	0	0.0593	0.9465
7	0	-0.1	1.1	-0.0017	-0.0956	1.0712
8	0	-0.1	1.2	0.0017	-0.0925	1.1146
9	0	-0.059	1.0	0.0032	-0.0616	1.0088
10	0.053	-0.063	1.000	0.0475	-0.0681	1.0103
11	0	0	0.3	0	0.0036	0.3254
12	0	0	0.4	$6.38 \cdot 10^{-4}$	0.0038	0.4073
13	0	0	0.5	$7.95 \cdot 10^{-4}$	0.0040	0.5073
14	0	0	0.6	0	0.0048	0.6186
15	0	0	0.7	0	0.0045	0.7236
16	0	0	0.8	0.0013	0.0038	0.8180
17	0	0	0.9	-0.0015	0.0044	0.9440
18	0	0	1.0	0.0016	0.0048	1.0266

Table 6.1: Real and estimated P, Q, and R

	Real			Estimated		
Measure	α_x **[deg]**	α_y [°]	α_z [°]	α_x [°]	α_x [°]	α_x [°]
1	15	180	0	13.12	175.00	-0.45
2	20	180	0	16.88	175.17	0.09
3	20	180	0	18.60	180.25	-0.57
4	-10	180	0	-5.87	174.15	0.53
5	0	180	0	-9.36	184.32	-0.65
6	0	180	0	6.59	194.89	-0.35
7	0	180	180	0.09	185.19	180.02
8	0	180	90	5.64	174.58	90.53
9	0	180	-45	-0.92	170.25	-41.36
10	0	180	30	-6.97	176.33	28.26
11	0	180	0	0.003	179.18	0.28
12	0	180	0	1.40	181.39	0.20
13	0	180	0	-1.11	176.66	0.20
14	0	180	0	-4.92	176.63	-0.03
15	0	180	0	-4.45	177.67	-0.67
16	0	180	0	-2.86	174.14	0.35
17	0	180	0	-11.54	175.73	-0.45
18	0	180	0	-4.47	179.93	0

Table 6.2: Real and estimated attitude angle

Figures 6.9, 6.10 and 6.11 give the comparison between the real and estimed inertial position and attitude.

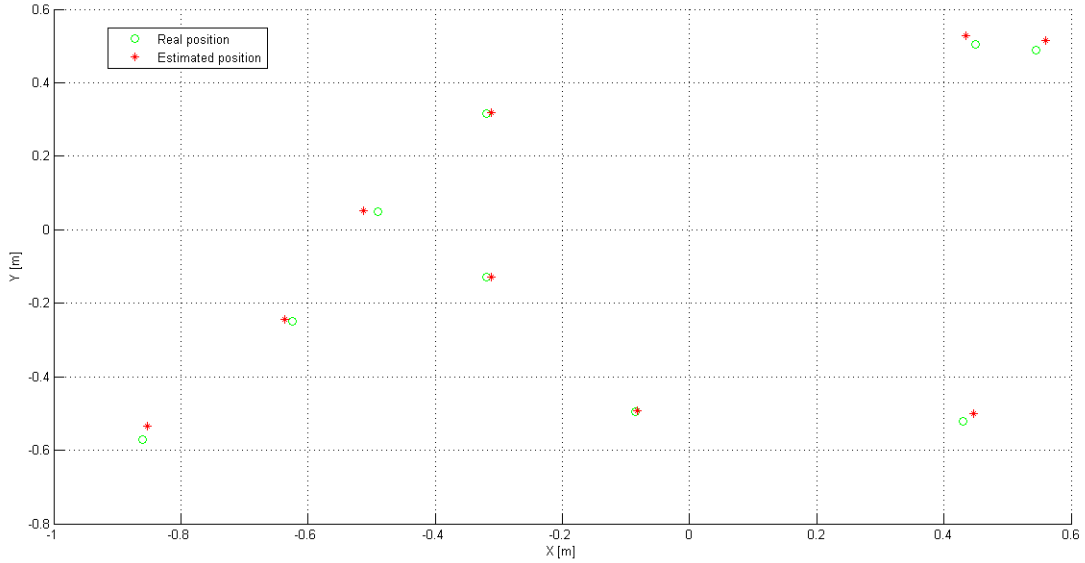

Figure 6.9: Absolute position estimated with the inertial positioning system

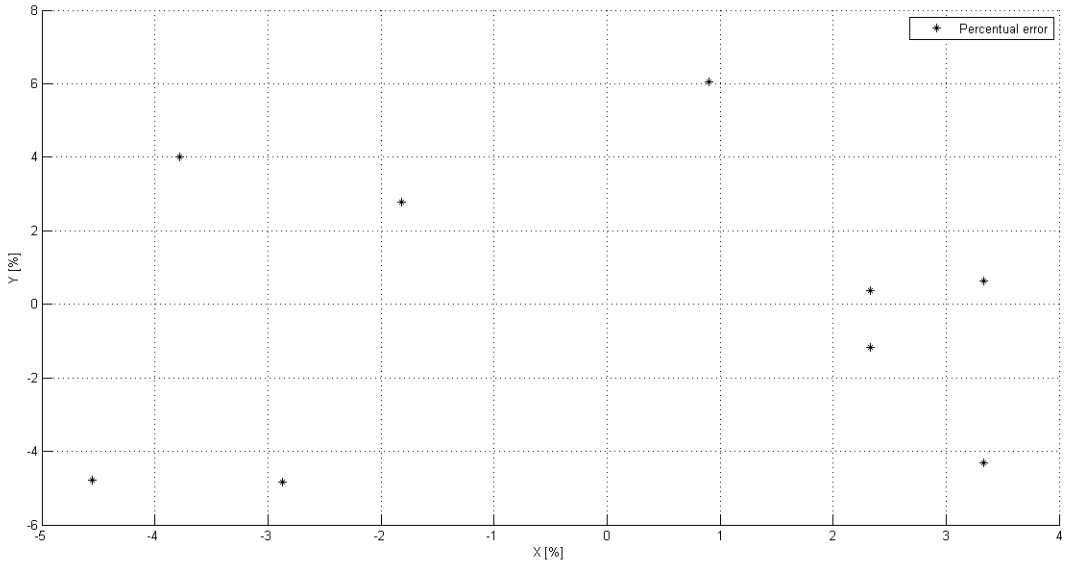

Figure 6.10: Percentual error on the absolute position estimated

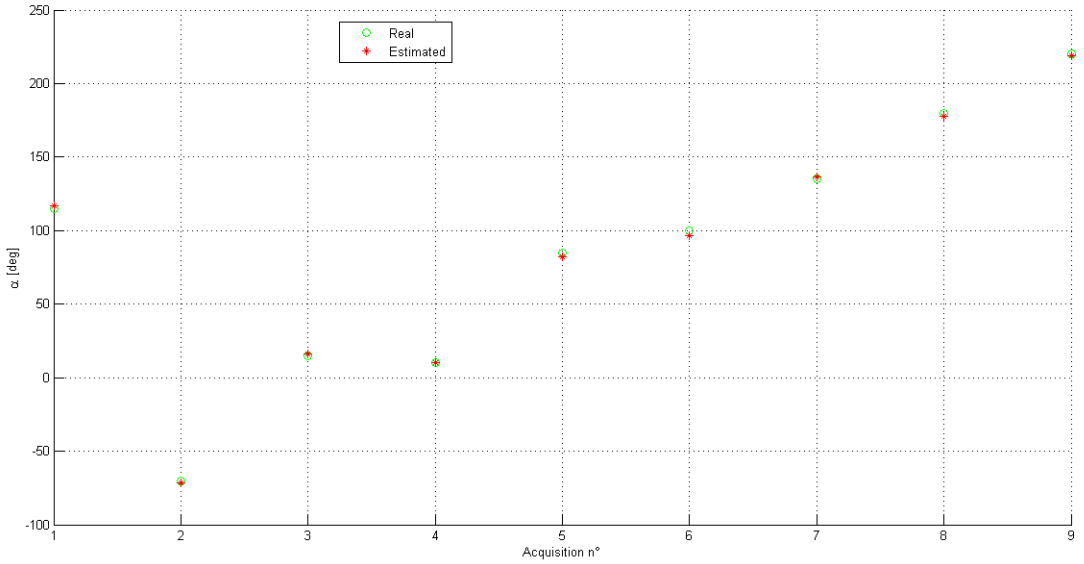

Figure 6.11: Comparison between real and estimated attitude

The error committed by the tracking software increases with the distance of the flyer from the center of the table, like it's possible to see in figure 6.10, this is probably caused by the curvature of the camera lens.

Chapter 7

Conclusions

7.1 Summary

The goal of this work were to upgrade the laboratory facility for proximity maneuvering in space simulation and to develop an Autonomous Docking Simulator (A.D.S.) to support a critical selection of the guidance navigation and control strategy to be put on board the tesbed. According to the first goal, some variations have been applied to the test bed; in particular the number of actuators has been reduced with a benefic effect on the power saving of about 6W and on the system mass of about 4 kg. The actuation architecture has been simplified too: the PIC board has been replaced by only 4 analogical output channel, with an integrated circuit lighter and with a lower power consumption.
The docking mechanism has been kept but improved, to overcome some annoying limitations, while the male passive palte has been built.
The hardware architecture to supply the vehicles with state vectors information has been completely rearranged, and a solution with assisted navigation camera has been selected and implemented. The inertial positioning system based on the fixed camera acquisition allow to perform an accurate navigation which error doesn't depend on the time. Moreover the calibration of this sensor is faster than accelerometers and gyroscopes, it doesn't require power, mass or space allocation onboard and in the real scenario its measures can be replaced with the GPS data.
The relative navigation the chaser must accomplish to chase the target vehicle, is still done through computer vision but the CCD camera has been replaced with a webcam with an evident mass and power saving on about 0.3kg and 2.4 [W] respectively.

The heavy stirrups that supported the Pulnix camera can be eliminated as consequence of the USB webcam use, in order to gain a $0.67[kg]$ mass.
The total mass gained with the Smart Flyer improvements is about 2.3 kg while the power margin is approximately 9 W.
The second vehcile has been sized as far as possible as a clone of the first veichle; target robot has an USB webcam too, to allow future formation flyng skills.
The second part of the work dealt with the development of the ADS. The simulator focused on different control solutions and a comparison campaign among results ob-

tained from simulations on similar scenarios with different controllers has been carried out. The a posteriori analysis revealed that a best choice does not exist, because all controllers allow to complete the docking manouvre safely and precisely. As far as the convergence speed and fluctuation criteria are considered to trade off the controllers, the PD and non linear controller turned out to have the extremely good and extremely bad performances. The LQR while never being the best, it always stays between the others.
On the other hand the great adaptability of the non linear controller, does not require two different gain matrices to control the final phases of alignment and docking, because the gains for this controller depend on the error itself. This adaptability is paid with a greater complexity in the controller architecture and operations involved, which certainly increase the computational cost.
Even the simple PD controller requires the calculation of the discrete derivative of the error at each step, and even if it is faster than the nonlinear controller, it is slower than the LQR, for which the complexity in the synthesis of the gain matrix, that could be done once before the simulation, and could also be performed on an external computer. As soon as the gain matrix is computed, the LQR is reduced to a proportional controller, the control actions are the product of the gains matrix for the vector error. For this reason the LQR has been chosen as the baseline solution, and has been implemented onboard.
The GNC chain asked, of course, for the state determination too: to this end a preference has been given to vision based algorithms, both for inertial and relative navigation. The computer vision software realized allow the feature recognition in order to engage the target and the tracking of LEDs to calculate the relative attitude and position.
Today the relative attitude estimation softwares use a non-planar marker, but to avoid the use of alternative system to sight the target a new algorithm has been designed based on the attitude and relative position estimation from a planar image on the Target Flyer; the maximum determination error is about 8.5% that occurs when the relative distance is greater than 1.2 [m].
The tracking software for the inertial navigation system has presented a position error about 5% and an attitude error of 3 deg.
The fixed camera data fused with the Discrete Kalman Filter were proven to provide navigation solutions up to 2 centimeter accuracy.
The testbed's supporting architecture, in terms of new inertial positioning system, new method to control the actuators thrust and the control strategies has been developed to the point where future endeavors can focus far more attention to the onboard software enhancement, optimizing the C++ code written in order to reduce computational cost.

7.2 Future development

Unfortunately, a autonomous docking experimental campaign didn't take place within this thesis period because of a malfunctioning in the acquisition board available.
The software to maneuvering to dock with the target has been designed and imple-

mented on board the chaser. To successfully accomplish the experimental tests some furterh hardware upgrade is required:

1. a new acquisition board with at least 4 analog outputs and 1 analog input, provided with an ISA, PCI or USB communication bus;
2. the SF onboard computer upgrade by replacing the the 1432 CPU with the 1433 acquired for the Target Flyer that doesn't need an high computational power;
3. the completion of the Target Flyer assembly and its software configuration.

Concerning the experimental test in addition to the docking manouvre, a formation flyng experiment can be conducted. Thanks to the artificial vision system available even on Target Flyer Formation Flying reconfiguration maneuvering, can be also tested.

Appendix A

ADS details

The Smart Flyer and Target Flyer control chain are reported in figure A.1. In the Smart Flyer regulator two controllers can be observed. The *Enable controllers* module decide which controller has to be enabled. The choice depends by the time, indeed only when the transfer phase is completed the docking controller is activated.
During the parking and transfer phases the orbital controller follow the scaled orbital position and velocity vector, that are subject to the gravitational and perturbative forces and torques, while the docking controller is turned off. When the transfer is ended the docking controller starts with the sighting manoeuvre but gravitational and perturbative forces and torques, in open loop, are still reproduced. In fact the orbital controller in the docking phase generates directly forces and torques knowing the dynamic model of the actuators.
In the Target Flyer regulator only orbital controller is used, and it follow the scaled orbital position and velocity vector, that are subject to the gravitational and perturbative forces and torques, for all the simulation time.
The figure A.3 represents the graphics interface of the ADS simulator developed.

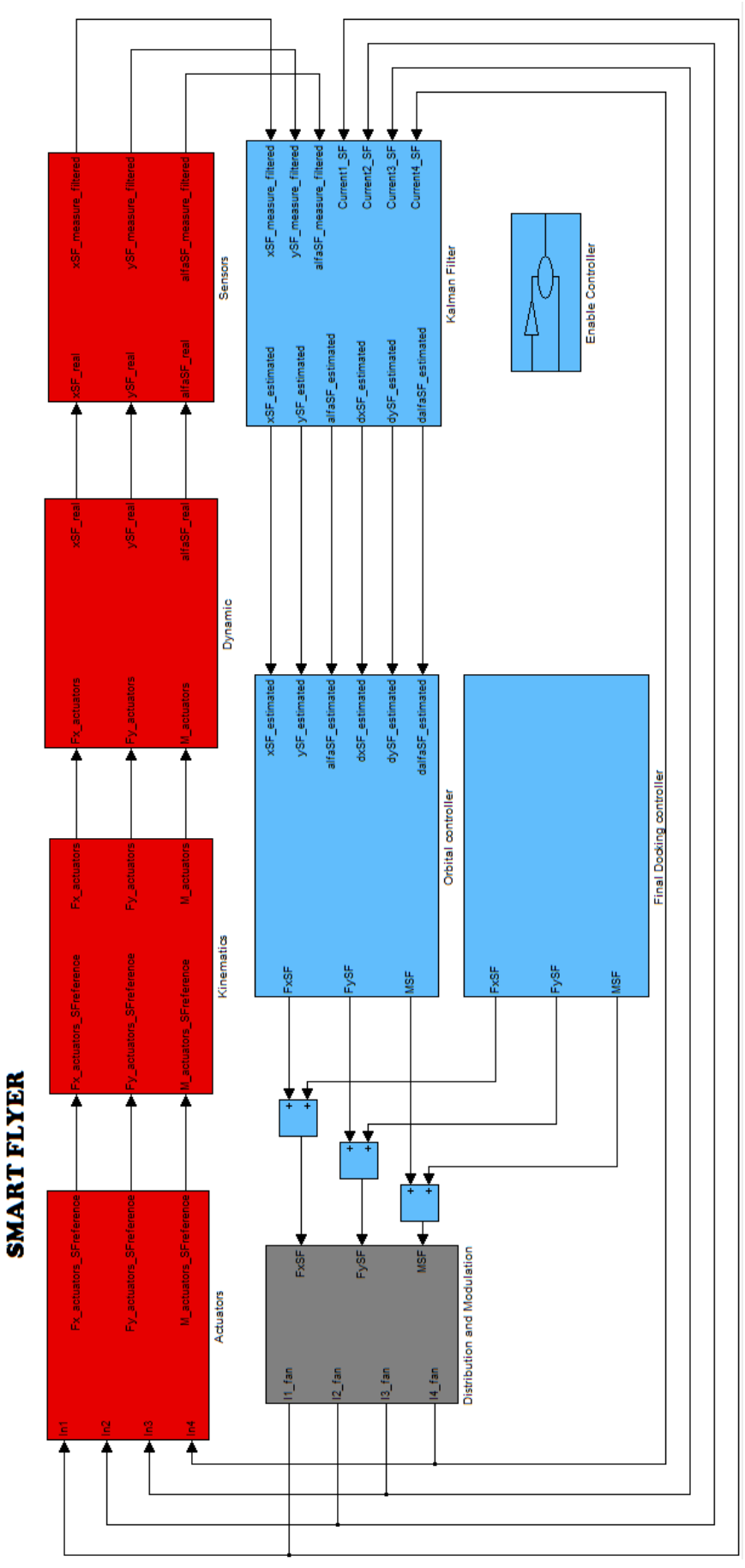

Figure A.1: Smart Flyer control chain

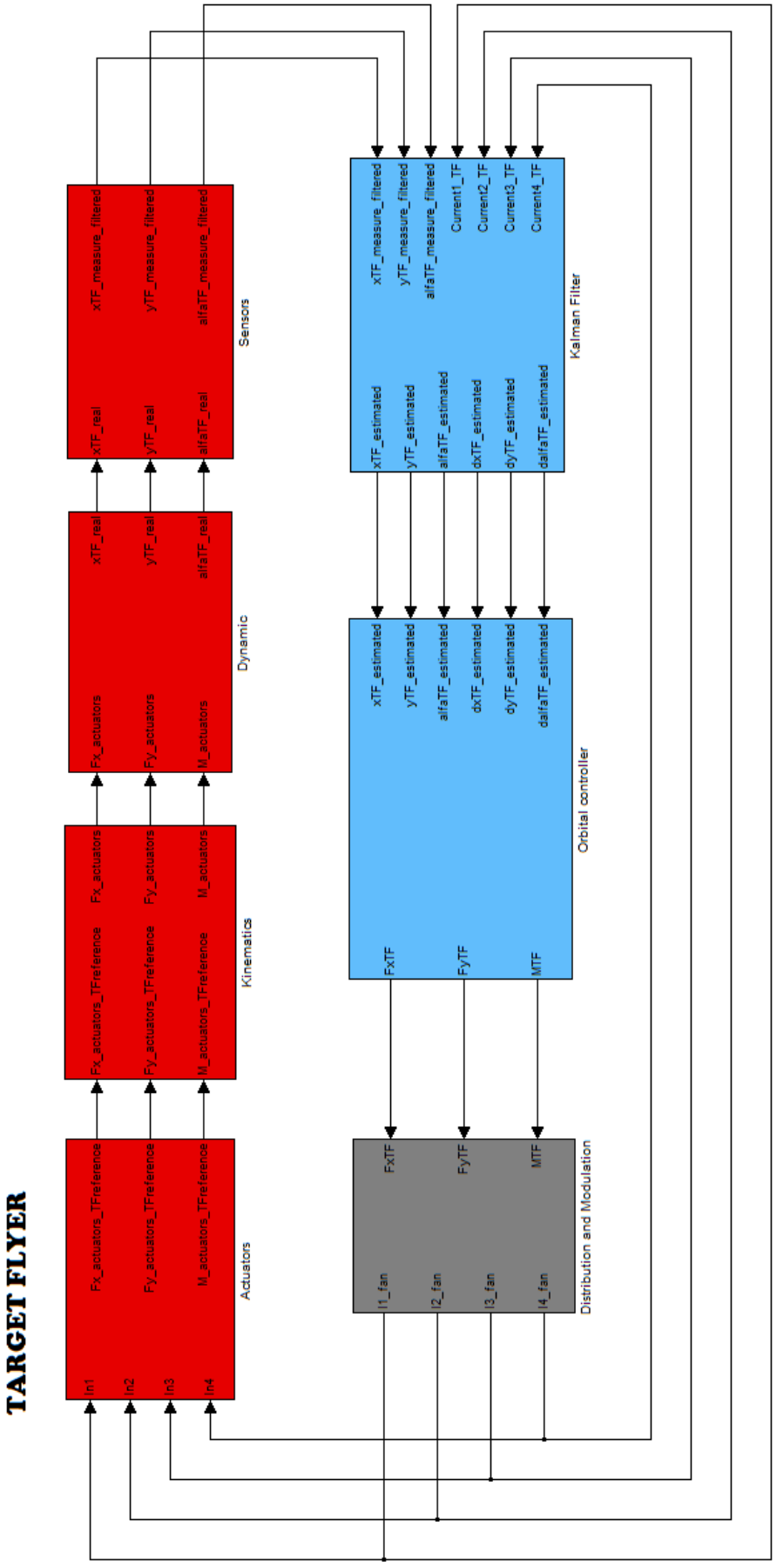

Figure A.2: Target Flyer control chain

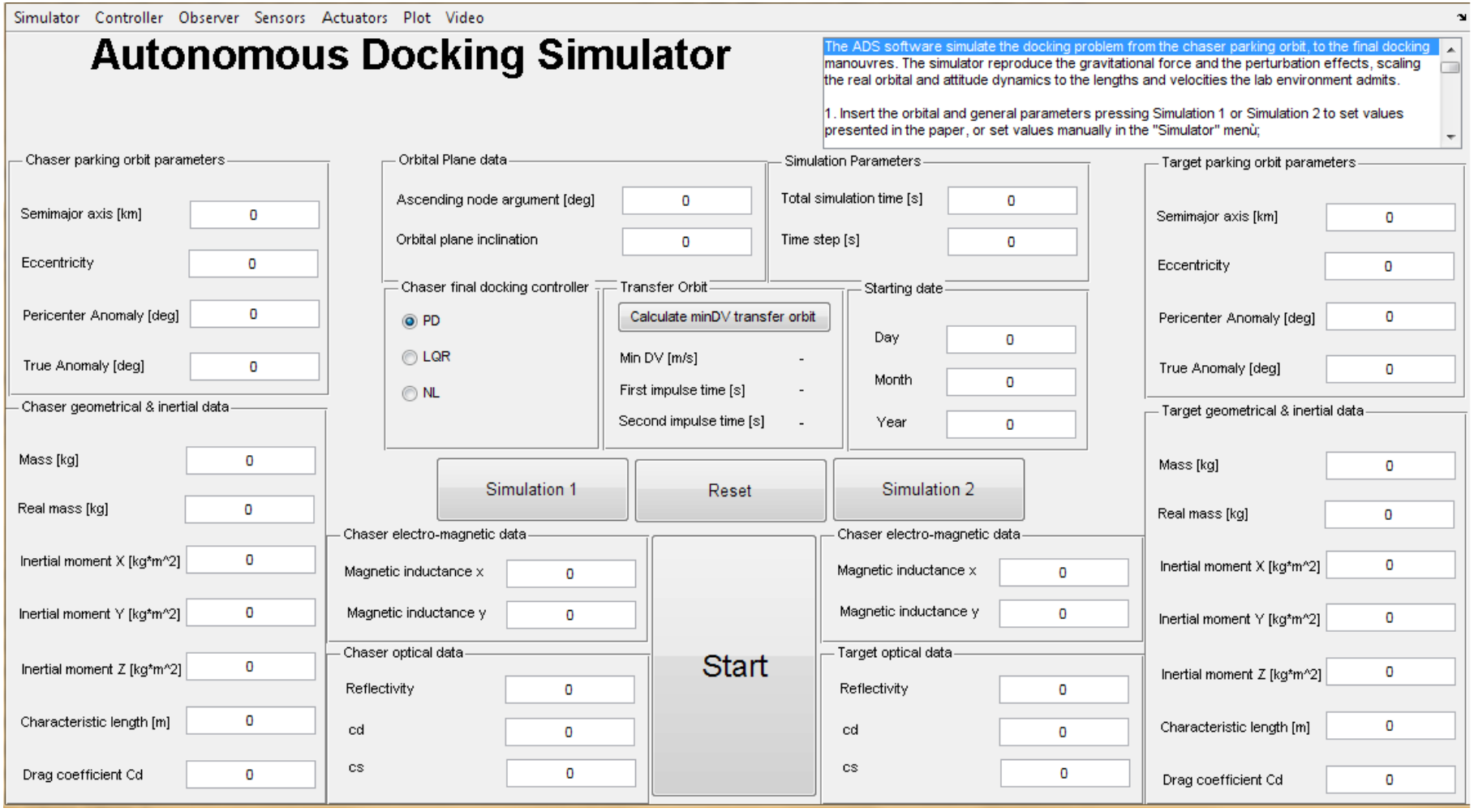

Figure A.3: ADS graphics interface

Bibliography

[1] D. A. Vallado, *Fundamentals of Astrodynamics and Applications*, Space Technology Library, Dordrecht 2001.

[2] M. Torluccio, C. Francesco, *Smart Flyer: Sviluppo hardware con pianificazione di traiettoria e controllo di manovre in microgravitá simulata*, Politecnico di Milano, Anno Accademico 2006-2007.

[3] M. Borgonovo, *Verifica di un dimostratore di sistema di navigazione per il prelievo di campioni di suolo planetario*, Politecnico di Milano, Anno Accademico 2003-2004.

[4] A.G. Ledebuhr, L.C. Ng, M.S. Jones, B.A. Wilson, *Micro-Satellite Ground Test Vehicle for Proximity and Docking Operations Development*, Lawrence Livermore National Laboratory, Livermore 2000.

[5] James R. Wertz and Robert Bell, *Autonomous Rendezvous and Docking Technologies - Status and Prospects*, Microcosm Inc., SPIE AeroSense Symposium 2003.

[6] K. Maachida, Y. Toda, T. Iwata, *Maneuvering and Manipulation of Flying Space Telerobotics System*, MITI, Tsukuba, 1992.

[7] Alessandro Carlini, Mirna Marcuccio, *Apparato sperimentale per la simulazione dinamica di un mini-robot flottante con applicazione spaziale*, Politecnico di Milano, Anno Accademico 2002-2003.

[8] J. R. Wertz, *Spacecraft attitude determination and control*, Kluver Academic Publisher, Dordrecht, 1990.

[9] G. Mengali, A. A. Quarta, *Fondamenti di meccanica del volo spaziale*, Edizioni Plus, Università di Pisa, 2001.

[10] P. Zarchan, H. Musoff, *Fundamentals of Kalman Filtering. A pratical approach*, Paul Zarchan Editor-in-Chief, AIAA 2000.

[11] AGARD, *Pratical aspects of Kalman filtering implementation*, North Atlantic Treaty Organization, Neuilly sur Seine 1976.

[12] AGARD, *Kalman filter integration of modern guidance and navigation systems*, North Atlantic Treaty Organization, Neuilly sur Seine 1989.

[13] M.S. Grewal, A.P. Andrews, *Kalman filtering theory and practice using Matlab*, John Wiley and sons, New York 2001.

[14] B. Friedland, *Advanced control system*, Prentice-Hall, 1st edition 1996.

[15] P. Rocco, *Automatica: Ingegneria Aerospaziale*, Politecnico di Milano, 2001.

[16] A. Huster, *Relative position sensing by fusing monocular vision and inertial rate sensor*, Stanford University, Stanford 2003.

[17] M. Romano, D.A. Friedman, T.J. Shay *Laboratory experimentation of autonomous spacecraft approach and docking to a collaborative target*, Celest Mechanic Dynamic Astrodynamic, article no. DOI 10.1007/s10569-009-9240-3, 2009.

[18] T.J. Shay *Design and fabrication of a planar autonomous spacecraft simulator with docking and fluid transfer capability*, U.S. Naval Postgraduate School, Monterey 2005.

[19] D.A. Friedman *Laboratory experimentation of autonomous spacecraft docking using cooperative vision navigation*, U.S. Naval Postgraduate School, Monterey 2005.

[20] R. Bevilacqua, J. S. Hall, M. Romano *Multiple spacecraft rendezvous maneuvers by differential drag and low thrust engines*, U.S. Naval Postgraduate School, Monterey 2005.

[21] M. Pizzighella, *Autonomous RendezVous Planner Approach*, Politecnico di Milano, Anno Accademico 2006-2007.

[22] M. Campanella, *Elaborazione di immagini e controllo di una unità autonoma nella esplorazione di superfici planetarie*, Politecnico di Milano, Anno Accademico 2002-2003.

[23] D.H. Titterton, J.L. Weston, *Strapdown Inertial Navigation Technology*, Paul Zarchan Editor-in-Chief, Lexington 2004.

[24] G. Magnani, *Tecnologie dei sistemi di controllo*, McGraw-Hill, Milano 2000.

[25] Z. W. Chen, C. C. Chiang, Z. T. Hsieh, *Extending 3D Lucas Kanade tracking with adaptive templates for head pose estimation*,Springer, Verlag 2009.

[26] Herbert Bay, Tinne Tuytelaars, Luc Van Gool, *SURF: Speeded Up Robust Features*, ETH Zurich, Zurich 2004.

[27] G. Panin, A. Knoll, *Fully Automatic Real-Time 3D Object Tracking using Active Contour and Appearance Models*,Journal of multimedia vol. 1, No. 7, 2006.

[28] H. Y. Kim, S. A. de Araújo, *Grayscale Template-Matching Invariant to Rotation, Scale, Translation, Brightness and Contrast*, M.S. Thesis, Escola Politécnica, Universidade de São Paulo, 2007

[29] Adolf Florian, *How-to build a cascade of boosted classifiers based on Haar-like features*, OpenCV's Rapid Object Detection conference, 2003

[30] M. Taiana, *3D model-based tracking with one omnidirectional camera and particle filters*, M.S. Thesis, Politecnico di Milano, 2007.

[31] Naotoshi Seo, *Tutorial: OpenCV haartraining (Rapid object detection with a cascade of boosted classifiers based on haar like features)*, http://note.sonots.com/SciSoftware/haartraining.html, 2008.

[32] H. Bay, A. Ess, T. Tuytelaars, L. Van Gool, *Speeded-Up Robust Features (SURF)*,http://www.vision.ee.ethz.ch/ surf/, 2008.

[33] *OpenCV Documentation*, 2009.

[34] N.K. Philip, M.R. Ananthasayanam, *Relative position and attitude estimation and control schemes for the final phase of an autonomous docking mission of spacecraft*, Acta Astronautica, Bangalore, 2003.

[35] R. Mukundan, K.R. Ramakrishnan, *A quaternion solution to the pose determination problem for rendezvous and docking simulations*, IMACS, Bangalore, 1995.

[36] R. Mukundan, K.R. Ramakrishnan, *An iterative solution for object pose parameters using image moments*, Indian Institute of Science, Bangalore, 1996.

[37] P. Wlezek, A. Maccato, R. J. P. deFigueiredo, *Pose estimation of three-dimensional objects from single camera images*, University of California, Irvine, 1995.

[38] Zhang Shijie, Liu Fenghua, Cao Xibin, He Liang, *Monocular vision-based two-stage iterative algorithm for relative position and attitude estimation of docking spacecraft*, Chinese Journal of Aeronautics, Harbin, 2009.

[39] Z. Jia, A. Balasuriya, S. Challa, *Vision based data fusion for autonomous vehicles target tracking using interacting multiple dynamic models*, Computer Vision and Image Understanding, Shanghai, 2006.

[40] C. Schlaile, O. Meister, N. Frietsch, C. Kessler, J. Wendel, G. F. Trommer, *Using natural features for vision based navigation of an indoor-VTOL MAV*, Universität Karlsruhe, Karlsruhe, 2009.

[41] T. Heimonen, J. Heikkila, *Monocular point based pose estimation of artificial markers by using evolutionary computing*, University of Oulu, Karlsruhe, 2007.

[42] Y. Wang, Z. Bin, Y. Ge, *The Invariant Relations of 3D to 2D Projection of Point Sets*, Journal of Pattern Recognition Research, Vol 3, No 1, 2008

[43] M. Osadchy, Y. Le Cun, M. L. Miller, *Synergistic face detection and pose estimation with energy-based models*, University of Haifa, Israel, 2006.

[44] H. Jang, G. Kim, H. Choi, *Position and pose computation of a moving camera using geometric edge matching for visual SLAM*, Soongsil University, Korea, 2004.

[45] C. H. Wu, S. J. Horng, C. F. Wen, Y. R. Wang, *Fast and scalable computations of 2D image moments*, Image and Vision Computing, Taiwan, 2007

[46] A. Criminisi, I. Reid, A. Zisserman, *Single view metrology*, Department of Engineering Science, University of Oxford, Oxford 2002

[47] Y. Oshman, A. Carmi, *Attitude estimation from vector observations using genetic algorithms-embedded quaternion particle filter*, Journal of guidance, control and dynamics vol. 29, no. 4, July-August 2006.

[48] C. C. J. Ho, N. H. McClamroch, *Autonomous spacecraft docking using a computer vision system*, Proceedings of the 31st conference of decision and control, Tucson, Arizona, 1992.

[49] K. T. Alfriend, H. Schaub, *Dynamics and control of spacecraft formations: challenges and some solutions*, Journal of the Astronautical Sciences Vol. 48, no. 2, April-September, 2000, pag. 249-267.

[50] http://www.sci.univr.it/fusiello *Visione Artificiale: appunti delle lezioni*, Dipartimento di Informatica, Andrea Fusiello, Università di Verona, 2002.

[51] http://www.eurotech.com

[52] http://www.zarm.uni-bremen.de/space-science/aerospace-control-systems/projects/students/luvex/

[53] http://arl.stanford.edu

[54] http://www.russianspaceweb.com/mir.html

[55] http://www.darpa.mil

[56] http://www.afrl.af.mil

[57] http://www.nasa.gov/missionpages/dart/main/index.html

[58] http://www.sensoray.com

[59] http://www.scidyne.com

[60] http://www.nelsonair.com

[61] http://www.thermaltakeusa.com

[62] http://www.intel.com/technology/computing/opencv/